



HAL
open science

Correlative microscopy of III-nitride nanostructures : application to photonics

Ioanna Dimkou

► **To cite this version:**

Ioanna Dimkou. Correlative microscopy of III-nitride nanostructures : application to photonics. Quantum Physics [quant-ph]. Université Grenoble Alpes [2020-..], 2021. English. NNT : 2021GRALY018 . tel-03508249

HAL Id: tel-03508249

<https://theses.hal.science/tel-03508249>

Submitted on 3 Jan 2022

HAL is a multi-disciplinary open access archive for the deposit and dissemination of scientific research documents, whether they are published or not. The documents may come from teaching and research institutions in France or abroad, or from public or private research centers.

L'archive ouverte pluridisciplinaire **HAL**, est destinée au dépôt et à la diffusion de documents scientifiques de niveau recherche, publiés ou non, émanant des établissements d'enseignement et de recherche français ou étrangers, des laboratoires publics ou privés.

THÈSE

Pour obtenir le grade de

DOCTEUR DE L'UNIVERSITE GRENOBLE ALPES

Spécialité : **NANOPHYSIQUE**

Arrêté ministériel : 25 mai 2016

Présentée par

Ioanna DIMKOU

Thèse dirigée par **Eva MONROY**, Université Grenoble Alpes,
codirigée par **Lorenzo RIGUTTI**, Université de Rouen,
et coencadrée par **Adeline GRENIER**

préparée au sein du **Laboratoire d'Electronique et
de Technologie de l'Information (LETI - CEA)**
dans l'**École Doctorale Physique**

**Microscopie corrélative des nanostructures
de nitrures d'éléments III : application à la
photonique**

**Correlative Microscopy of III-Nitride
Nanostructures: Application to Photonics**

Thèse soutenue publiquement le **1 Octobre 2021**,
devant le jury composé de :

Madame Catherine BOUGEROL

DIRECTRICE DE RECHERCHE, CNRS DELEGATION ALPES
Présidente

Monsieur Olivier DURAND

PROFESSEUR DES UNIVERSITES, INST NAT SC APPLIQ RENNES
Rapporteur

Monsieur Mathieu KOCIAK

DIRECTEUR DE RECHERCHE, CNRS DELEGATION ILE-DE-FRANCE SUD
Rapporteur

Madame Rachel OLIVER

PROFESSEUR, UNIVERSITY OF CAMBRIDGE
Examinatrice

Monsieur Martin EICKHOFF

PROFESSEUR, UNIVERSITÄT BREMEN
Examineur

Monsieur Frédéric DE GEUSER

CHARGE DE RECHERCHE, CNRS DELEGATION ALPES
Invité



Acknowledgments

On October 25th 2018, I started my thesis at the CEA, Leti in Grenoble in the Nanocharacterization Platform (PFNC) in collaboration with the the group of “Nanophysique et Semiconducteurs (NPSC)” at IRIG and with the University of Rouen, GPM. First, I would like to express, from the bottom of my heart, my deep gratitude towards to **Anne Charrier** and thanks to her I chose this PhD and she is always next to me to give me the best guidance and support. Then I would like to thank all the people with whom I have interacted and who have helped and welcomed me during these three years.

I would like to thank the supervisors, **Eva Monroy**, **Lorenzo Rigutti** and **Adeline Grenier** for guiding me over the past three years and for putting at my disposal all the means that allowed me to carry out the thesis in very good conditions.

I would like to thank **Nevine Rochat** for training me to CL and to make me have a critical look in science and to reply all my curious questions during our discussions that have helped me a lot to improve my understanding.

A huge thank to the directors **Nicolas Lhermet** for giving me his trust and his support and **Nicolas Chevalier** for source of limitless inspiration and your guidance having discussions for my future plans and my career as well as **Vincent Delaye**.

I would also like to thank the best administrative staff I have ever met, **Carmelo Castagna** for all his help in navigating the administration of CEA.

I would like to extend my thanks to all the members of the jury for accepting to serve as the jury, despite their busy schedules.

I would like to thank our fruitful collaborators from the University of Rouen, namely **Jonathan Houard** and **Pradip Dalapati** for their valuable contributions.

I sincerely thank **David Cooper**, **Enrico Di Russo** and **Aidan Rooney** for their valuable work, comments and discussions. I am very thankful for all my colleagues here at CEA-Leti in the building 51B: **Julie** always with a big smile and ready to reply my silly questions, **Florian** for training with the TEM and discussion, **Lucas** with your state of big calm in the lab, **Younes** with his endless support, **Paul**, **Vitomir**, **Manon** et **Patrice**, **Théodore**.

I am very thankful for all my colleagues at IRIG C5: **Anjali**, **Maria Spies**, **Vincent**, **Ali**, **Sergi**, **Jane**, **Remy**, **Alexandre**, **Raouia**, **Mattheo**, **Thibaut**, **Saransh**, **Saptarshi**, **Akhil**, **Marion**, **Mada**, **Akanksha**, **Romain**. Also thanks to **Bruno Gayral** and **Regis Andre** for their support and the interesting discussions in the lab.

Special thanks to my professors in Greece who teach me to be good scientist enriching my ethics in my studies. Κ. **Μανωλη Νικολαιδη**, κ. **Σπύρο Νικολαιδη**, κ. **Στέλιο Σίσκο**, κ. **Κώστα Σιώζιο** και κ. **Νικό Βουρουτζή** σας ευχαριστώ. J’aimerais remercier ma meilleure professeure de français κ. **Ελένη Γκίνου**.

Special thanks to my friends: **Gabriele** and **David**, **Pauline**, **Danae**, **Vivi**, **Filareti**, **Maria**, **Niko** and **Georgios Tsoulis** for their constant support and adventures that we share. My lovely family in France: **Didier**, **Nathalie**, **Laura**, **Mathieu**, **Isabelle**, **Christiane**, **Gisèle** and **Jean-Pierre** je vous remercie infiniment.

A big thanks to my greek family for being there always: **νονά μου**, **μαμά**, **μπαμπά**, **Σταυρούλα**, **Θανάση** και **Ελένη** σας ευχαριστώ για όλα.

*Finally, I would like to thank my spouse **Michaël** for helping me get through all the difficulties.*

Résumé

Ce mémoire porte sur les activités de recherche pendant ma thèse dans la période 2018-2021. Ce manuscrit est complètement écrit en anglais et ces quelques pages résument en français les problématiques et les expériences menées ainsi que leurs résultats étant organisés de cette façon :

Le **chapitre 1** illustre la motivation, les objectifs ainsi que l'organisation du manuscrit.

Le **chapitre 2** introduit les propriétés générales des semi-conducteurs à base de nitrure III; de leur structure cristalline, leur propriétés structurales, élastiques à leurs propriétés électroniques. En particulier, nous concentrons notre attention sur les nanostructures avec une croissance (i) planaire de boîtes quantiques auto-assemblées (QD) et (ii) de boîtes quantiques auto-assemblées dans un nanofil. De plus, nous faisons une introduction aux phénomènes de contraintes hydrostatiques et uniaxiales.

Le **chapitre 3** présente les techniques expérimentales et la méthodologie de simulation utilisées dans cette thèse. Nous commençons par le processus de croissance utilisant l'épitaxie par faisceau moléculaire assistée par plasma. Un diffractomètre d'électrons à haute énergie par réflexion in-situ dans le bâti de croissance permet de suivre et contrôler en temps réel la croissance. Ensuite, nous présentons les différentes techniques de caractérisation utilisées. En particulier, nous avons étudié la morphologie et la structure de nos échantillons en utilisant la diffraction des rayons X et la microscopie à force atomique. Les propriétés optiques ont été évaluées par des techniques de photoluminescence et de cathodoluminescence. La distribution chimique et quantitative des espèces est déterminée par sonde atomique tomographique. Une attention particulière est portée au système de tomographie sonde atomique qui intègre la spectroscopie de micro-photoluminescence in-situ. Nous décrivons également la préparation des échantillons intrinsèque à la technique de sonde atomique tomographique, effectuée par microscopie électronique à balayage couplée avec faisceau d'ions focalisé. Enfin, ce chapitre fournit des informations sur les méthodes de simulation utilisées pour modéliser la structure de bande de nos échantillons. Ces simulations prennent en compte les paramètres structuraux et chimiques issus des techniques expérimentales.

Le **chapitre 4** concerne la conception et caractérisation de super-réseaux de boîtes quantiques $\text{Al}_x\text{Ga}_{1-x}\text{N}$ ($0 \leq x < 1$) séparées par une barrière d'AlN, polaires azote auto-assemblées le long de nanofils de GaN. Leur domaine d'application est la réalisation de sources UV à pompage électronique. Il existe une demande particulière pour des dispositifs à semi-conducteurs émettant dans la plage ultraviolette (UV) autour de 254 nm pour la désinfection et purification de l'eau. Une alternative prometteuse pour la fabrication de lampes UV hautement efficaces et respectueuses de l'environnement repose sur l'injection d'électrons dans des nanostructures d'AlGaN/AlN à l'aide d'un canon à électrons miniaturisé. Dans ce chapitre, nous décrivons les conditions de croissance pour obtenir une densité élevée de nanofils non coalescents et améliorer l'uniformité de la hauteur le long du substrat. Nous estimons que le super-réseau de nanofils est suffisamment long pour collecter les paires électron-trou générées par

un faisceau d'électrons avec une tension d'accélération de 5 kV, valeur typique pour empêcher l'émission de rayons X. Nous évaluons systématiquement les performances optiques des super-réseaux GaN/Al_xGa_{1-x}N assemblés dans les nanofils pour différentes épaisseurs de boîtes/barrières et teneurs en aluminium dans les boîtes. Ces études sur structure nanofil sont complétées par la comparaison de leur émission optique avec des super-réseaux planaires GaN/ Al_xGa_{1-x}N de même périodicité. Les rendements quantiques internes sont mesurés dans des conditions d'injection faibles et pour des densités de puissance d'excitation plus élevées. Enfin, nous étudions l'efficacité quantique externe de ces structures sous pompage optique.

Le **chapitre 5** présente les travaux menés sur des nanostructures InGaN/GaN à base de boîtes quantiques d'InGaN, formant la région active de dispositifs émettant dans le domaine spectral visible tels que des diodes électroluminescentes, diodes laser ou émetteurs monophotoniques. Pour mieux comprendre les performances optiques de ces nanostructures, il est nécessaire de corrélérer leurs signatures optiques aux propriétés structurales et chimiques. Dans cette optique, la sonde atomique tomographique assistée par laser (La-APT) a permis d'accéder à une cartographie 2D quantitative de la fraction d'In en site III. Les avancées instrumentales récentes de cette technique offrent également la possibilité d'enregistrer simultanément le spectre de photoluminescence de l'échantillon étudié. Nous rapportons ici les résultats d'une étude corrélative d'un empilement de boîtes quantiques d'InGaN, combinant la caractérisation chimique et optique à haute résolution, respectivement par La-APT et micro-photoluminescence in-situ (PAP) et cathodoluminescence ex-situ. Nous montrons que les informations structurales et chimiques extraites de ces techniques permettent la modélisation de la structure de bande de ces nanostructures; à partir desquelles peuvent être extrait différents paramètres physiques. Ces simulations de la structure électronique sont basées sur des équations de Poisson-Schrödinger et effectuées à partir du logiciel commercial Nextnano³. Celui-ci a été adapté aux calculs de structures de boîtes quantiques. La corrélation entre la signature chimique et optique s'effectue par comparaison directe entre longueur d'onde d'émission expérimentale et simulée. L'excellent accord entre l'émission expérimentale et simulée, lors de cette étude, permettent de valider les modèles physiques utilisés pour les simulations électroniques de ces nanostructures à base d'InGaN/GaN.

Lors de l'expérience de PAP (Photonic Atom Probe), il a été possible de résoudre l'émission de boîtes quantiques uniques situés dans les 9 couches de boîtes quantiques les plus proches du substrat. Les lignes de boîtes quantiques uniques affichent un décalage spectral vers le rouge pendant l'expérience, attribué à la relaxation de la contrainte élastique provoquée par l'évaporation du matériau. Notre étude donne une image des boîtes quantiques de Stranski-Krastanov InGaN très différente du système GaN/AlN. L'épaisseur de la couche de mouillage InGaN est plus épaisse que la partie des boîtes qui dépasse au-dessus de la couche, et la fraction molaire d'indium dans la couche de mouillage est inférieure à celle des points. Cette croissance perturbée de Stranski-Krastanov s'explique par l'effet tensioactif de l'indium favorisant la croissance planaire.

Le **chapitre 6** illustre les derniers résultats obtenus lors de cette thèse sur l'analyse corrélée d'un système InGaN/GaN, à base de boîtes quantiques d'InGaN. Il est constitué de trois empilements

d'InGaN/GaN crûs à différentes températures; chaque empilement étant constitué de trois couches de boîtes quantiques d'InGaN séparées par une barrière de GaN. La diminution de la température du substrat pendant la croissance entraîne une augmentation de la densité de défauts structurels. Cependant, les premières couches boîtes quantiques se comportent comme des pièges à défauts ponctuels non radiatifs, de sorte que l'intensité de luminescence augmente vers la surface malgré la densité plus élevée de dislocations de filetage. Lors de l'analyse de ce système par PAP, il a été possible d'isoler l'émission optique d'une seule boîte quantique provenant de la couche de boîte quantique la plus proche de la surface. La seule ligne BQ a affiché un décalage spectral au cours de l'expérience confirmant la relaxation de la contrainte élastique due à l'évaporation du matériau.

Le **chapitre 7** résume le travail accompli, les principales réalisations et présente certaines perspectives de ce travail.

Table of contents

ACKNOWLEDGMENTS	1
RESUME	3
CHAPTER 1: CONTEXT AND MOTIVATION.....	11
1.1. III-NITRIDE SEMICONDUCTORS FOR OPTOELECTRONICS.....	11
1.2. ATOM PROBE TOMOGRAPHY FOR III-NITRIDES.....	12
1.3. TARGETS	13
1.4. ORGANIZATION OF THE MANUSCRIPT	14
CHAPTER 2: NITRIDE SEMICONDUCTORS.....	17
2.1. CRYSTAL STRUCTURE AND POLARITY	17
2.2. ELASTIC PROPERTIES	20
2.3. SPONTANEOUS AND PIEZOELECTRIC POLARIZATION.....	22
2.4. ELECTRONIC PROPERTIES.....	23
2.5. HYDROSTATIC AND UNIAXIAL STRESS	25
2.6. INTRODUCTION TO SEMICONDUCTOR HETEROSTRUCTURES	27
CHAPTER 3: EXPERIMENTAL METHODS	31
3.1. EPITAXIAL GROWTH	31
3.1.1. PLASMA-ASSISTED MOLECULAR BEAM EPITAXY	31
3.1.2. GROWTH OF III-NITRIDES.....	36
3.1.2.1. PLANAR LAYERS.....	36
3.1.2.2. NANOWIRES.....	38
3.1.2.3. INGAN QUANTUM DOTS.....	40
3.2. PHOTOLUMINESCENCE	43
3.3. CATHODOLUMINESCENCE	45
3.4. X-RAY DIFFRACTION	48
3.5. ATOMIC FORCE MICROSCOPY	49
3.6. DUAL SCANNING ELECTRON MICROSCOPY / FOCUSED ION BEAM	52
3.7. ATOM PROBE TOMOGRAPHY	55
3.7.1. LASER-ASSISTED APT	56
3.7.2. PHOTONIC ATOM PROBE	60
3.7.3. 3D RECONSTRUCTION OF THE VOLUME EVAPORATED.....	61

3.8. NEXTNANO SIMULATIONS	64
CHAPTER 4: ALGAN/ALN NANOWIRES FOR ELECTRON-PUMPED ULTRAVIOLET SOURCES	67
4.1. INTRODUCTION TO UV EMITTERS: MOTIVATION	67
4.2. DESCRIPTION OF THE ELECTRON-PUMPED UV LAMP	69
4.3. WHY NANOWIRES?	70
4.4. TARGET STRUCTURE	71
4.5. GROWTH CONDITIONS	73
4.6. GAN/ALN NWS	75
4.6.1. STRUCTURAL PROPERTIES	77
4.6.2. OPTICAL PROPERTIES	79
4.6.3. BAND PROFILE SIMULATIONS	82
4.6.4. CATHODOLUMINESCENCE MEASUREMENTS	84
4.7. TOWARDS SHORTER WAVELENGTHS: $Al_xGa_{1-x}N/ALN$	87
4.7.1. STRUCTURAL PROPERTIES	87
4.7.2. OPTICAL PROPERTIES	89
4.8. EXTERNAL QUANTUM EFFICIENCY	91
4.9. CONCLUSION	92
CHAPTER 5: CORRELATIVE-MICROSCOPY INVESTIGATION OF INGAN/GAN QDS	95
5.1. MOTIVATION	95
5.2. CHARACTERIZATION OF THE AS-GROWN SPECIMEN	96
5.2.1. GROWTH PROCEDURE	97
5.2.2. STRUCTURAL CHARACTERIZATION	97
5.2.3. OPTICAL SPECTROSCOPY	101
5.3. CHARACTERIZATION OF THE APT SPECIMEN	104
5.3.1. STRUCTURAL AND EX-SITU OPTICAL CHARACTERIZATION	104
5.3.2. PHOTONIC ATOM PROBE ANALYSIS	107
5.3.3. CHEMICAL ANALYSIS BY ATOM PROBE TOMOGRAPHY	113
5.3.4. MODELING THE QUANTUM DOT STRUCTURE	114
5.3.5. SAMPLE UNIFORMITY AND REPRODUCIBILITY OF THE RESULTS	116
5.4. CONCLUSIONS AND PROSPECTS	118
CHAPTER 6: EFFECT OF STRUCTURAL AND POINT DEFECTS ON INGAN/GAN QDS	121
6.1. INTRODUCTION	121

6.2. DESCRIPTION OF THE AS-GROWN SAMPLE AND PROPERTIES	122
6.3. CHARACTERIZATION OF THE FIELD EMISSION TIP.....	125
6.3.1. PHOTONIC ATOM PROBE ANALYSIS.....	125
6.3.2. CHEMICAL ANALYSIS BY ATOM PROBE TOMOGRAPHY	128
6.4. DISCUSSION: EFFECT OF EXTENDED AND POINT DEFECTS	131
6.5. CONCLUSIONS	132
CHAPTER 7: CONCLUSIONS AND PERSPECTIVES	133
7.1. ALGAN/ALN QUANTUM DOTS IN NANOWIRES.....	133
7.2. INGAN/GAN STRANSKI-KRASTANOV QDS.....	134
BIBLIOGRAPHY	137
SCIENTIFIC CONTRIBUTIONS.....	157
JOURNAL ARTICLES	157
CONFERENCES	157
GLOSSARY	159

Chapter 1: Context and motivation

1.1. III-nitride semiconductors for optoelectronics

AlN, GaN and InN with wurtzite crystalline structure are the keystone of blue and green optoelectronics. III-nitride ternary compounds present a direct band gap which can be tuned from the near infrared to the UV region (from 0.69 eV for InN to 6.2 eV for AlN)^{1,2}, with the possibility of fabricating type-I heterostructures^{3,4}. The wide band gap of gallium nitride (GaN) makes this material suitable not only as a light emitting source but also for applications involving high temperature or requiring low noise. GaN and its alloys have a high potential for power electronics, competing with SiC in power devices such as transistors, thyristors or rectifiers. Ultraviolet solar-blind photodetectors based on AlGaIn have applications in early missile threat warning, chemical and biological threat detection, flame detection, and UV environmental monitoring. There are some other conceivable applications for III-nitrides such as surface acoustic wave generation, acousto-optic modulators, PH sensors or devices that utilize negative electron affinity⁵.

Compared with bulk materials, low-dimensional materials such as nanowires (NWs) or quantum dots (QDs) can have different electrical and optical properties due to the strong confinement of charge carriers. Motivated by exploring the properties derived from low dimensionality, and in search for a new material platforms for future generation electronic and photonic devices, tremendous efforts have been devoted in the past two decades to the study of semiconductor NWs and quantum dots, with remarkable progress in their integration in light emitters, solar energy conversion devices, transistors, and biosensors^{6–12,12–21}.

The usefulness of III-nitrides in optoelectronics does not stop in the blue/green, but it can also be extended to longer wavelengths (yellow/red range) as well as to shorter wavelengths (UV range). AlGaIn-based light-emitting diodes (LEDs) are expected to be employed in UV for disinfection, replacing conventional sources (mercury lamps) due to their inherent non-toxicity, fast switching and longer lifetime.^{22,23} However, the performance of UV LEDs is not at the level of arc lamps. Laboratories report record LED external quantum efficiencies (EQE) close to 20% at 275 nm²⁴, yet commercial devices exhibit efficiencies lower than 1%. The limitations are mostly attributed to doping, asymmetric carrier transport, light extraction and metal contacting.

Moreover, there still remain challenges for LEDs to be competitive in terms of performance and manufacturing costs. One of the critical technical challenges to be addressed for visible high-brightness and high-power operation of LEDs is a phenomenon commonly referred to as the efficiency droop, which is observed as a reduction in emission efficiency with increasing injection current under high current density conditions. The origin of the efficiency droop for longer wavelengths was previously suspected to be related to high defect densities in combination with alloy inhomogeneities causing carrier delocalization from localized states in the active region of light emitters^{25,26}. A lot of published works have suggested several causes of the efficiency droop, including Auger recombination

processes^{27–30}, carrier spill-over^{31,32}, and limited hole transport^{33,34}.

In order to provide a solution for these well-identified problems, a key challenge is to correlate the optical and structural properties of III-nitride materials and nanostructures, to reach a full understanding of 3D phenomena at the nanometer scale. A similar situation occurs in the case of intentionally created QD structures,³⁵ whose optical signature can only be predicted by getting access to the 3D structure and chemical distribution with a resolution close to the atomic scale.^{36,37} Thanks to correlation of different experimental techniques applied on the same nano-object, we are able to establish a one-to-one correspondence between the optical, chemical and the structural properties. A number of correlative studies have been performed in the past few years on single nano-objects of different nature, composition, size, and geometry, providing a deeper and deeper insight into the interplay between their structure and their optical properties. These studies were mostly based on the complementary use of transmission electron microscopy (TEM) correlated with different ex situ^{38–43} or in situ^{44–47} optical spectroscopy techniques. In this direction, laser-assisted atom probe tomography (La-APT) is a valuable alternative providing 3D chemical information.^{48,49}

1.2. Atom probe tomography for III-nitrides

The atom probe was introduced at the 14th Field Emission Symposium in 1967 by Erwin Wilhelm Müller and J. A. Panitz. It combined a field ion microscope with a mass spectrometer having a single particle detection capability and as they have mentioned in their publication⁵⁰: “... *We believe we now have a powerful tool for alloy research since we can determine, quite easily, short range order, discrete visibility of atomic species⁵¹, and other related items of interest. Finally, the chemical nature of interstitials, segregations, and precipitates will be open to direct experimental observation and analysis*”⁵⁰. APT⁵² is an analytical technique allowing the 3D reconstruction of the elemental composition of a nanoscale sample with sub-nanometer spatial resolution. This is made possible through the controlled field evaporation of single atoms from a field emission tip with an apex radius lower than 100 nm and through their analysis by means of a position- and time-of-flight-sensitive detector⁵³. In the last generation of atom probes, the field evaporation is triggered by a femtosecond laser⁵⁴, enabling the analysis of semiconducting⁵⁵ and insulating samples^{56–59}. Furthermore, the possibility of analyzing the luminescence in situ during the La-APT measurement (the so-called photonic atom probe⁶⁰ or PAP technique) allows linking the emission lines to the atomic layers that are evaporated.⁶¹ However, quantitative La-APT of III-nitrides faces some particular challenges since the result depends on experimental parameters such as the electric field at the sample surface, the laser pulse energy and the sample temperature.⁶² Initially, sample preparation proved challenging, with some damage to the QWs observed in the APT⁴⁸ and attributed to knock-on damage during the deposition of a protective Pt coating in the FIB.

During APT studies of III-nitrides, it became evident that the technique does not generally yield an accurate measurement of the elemental composition. Due to the relatively high rate of success for the

analyses and to the straightforward interpretation of their mass spectra, III-N materials have become a model system for the study of compositional biases in APT, which may occur in a much broader class of compounds. Studies conducted on III-N materials highlighted the need to further explore the field evaporation behavior of compound semiconductors in order to (i) assess whether there is a bias in the compositional measurement, (ii) understand the physical mechanisms inducing any bias and (iii) correct said bias, if possible.

APT applied to III-nitrides has already lead to a number of interesting results. For InGaN QWs, the identification indium clustering was demonstrated by Galtrey et al.⁶³ and Tang et al.⁶⁴. Here, it is pointed out that strong luminescence is possible from InGaN QWs in the absence of indium clustering or regions of high indium concentration. Aminci et al.^{65,66} have demonstrated the experimental evidence of Mg clusters in doped GaN where the correlation between APT and electron holography has allowed the direct link between the nm-scale spatial distribution and the electrical activity of Mg dopants. Demonstration of luminescence from an APT tip containing tens of InGaN QWs⁶⁷ was achieved showing influence of interface fluctuations on radiative recombination. It was also studied the effect of stacking faults (SFs) formed along the c-plane on the optical properties of an InGaN non-polar MQW system extracted from the side facets of a c-axis NW. A correlative study involving scanning transmission electron microscopy (STEM), atom probe tomography (APT), μ PL and simulations showed that the contribution of cubic inclusions to the transition energies must be taken into account in order to achieve good understanding of the optical properties of multi-quantum wells (MQWs). The luminescence from an APT tip containing GaN/AlN QDs was first studied by Mancini et al.⁶⁸. The results indicated that holes effectively localize at interface fluctuations at the bottom of the QD, decreasing the extent of the wave function and the band-to-band transition energy. They also represent an important step toward the correlation of the 3D atomic scale structural information with the optical properties of single light emitters based on quantum confinement.

1.3. Targets

The target of this thesis is the development of an original method for the characterization of III-nitride nanostructures by means of correlating APT with their optical performance.

During the first year of my PhD, I was trained in molecular beam epitaxy (MBE) of III-nitrides and I performed an exhaustive investigation of AlGaIn/AlN QDs inserted in NWs for the implementation of the active region of electron-beam pumped UV sources. In this study, I combined the design of the nanostructures, theoretical modeling, accurate characterization and extensive PL and CL studies.

The next two years, I focused on APT studies of InGaIn QDs. The shift to In containing nanostructures was motivated by the requirement of higher PL intensity in the photonic atom probe system, to perform correlated studies. The reduced band gap of InGaIn/GaN in comparison to AlGaIn/AlN results in more efficient excitation, which facilitated this exploratory studies. The target here was to attain a full correlation of optical, chemical and structural characterization of single InGaIn

QDs, to better understand the chemical distribution and its effect on the properties of the single QD emission.

1.4. Organization of the manuscript

The manuscript is organized in seven chapters. Besides this context chapter, chapters 2 and 3 are introductory, and chapters 4, 5 and 6 present and discuss the experimental results. A last chapter draws conclusions and proposes perspectives for future studies.

Chapter 2 is an introduction to the general properties of III-nitride semiconductors, describing their crystal structure, structural and elastic properties that can explain electronic and optical performance. In particular, we focus our attention on nanostructures such as the planar growth of self-assembled QDs and QD systems in the self-assembling NW. In addition, we make an introduction to the phenomena of hydrostatic and uniaxial stresses.

Chapter 3 deals with the experimental techniques and the simulation methodology used in this thesis. We start with the process of epitaxial growth using plasma-assisted molecular beam epitaxy (PAMBE). Then, we present the different characterization techniques used. In particular, we studied the morphology and structure of our samples using X-ray diffraction and atomic force microscopy (AFM), and the optical properties were evaluated by photoluminescence and cathodoluminescence techniques. We also describe sample preparation using dual scanning electron microscopy (SEM) / focused ion beam (FIB), and chemical characterization by La-APT. Particular attention is paid to the atomic probe tomography system which integrates in-situ micro-photoluminescence spectroscopy. Finally, this chapter provides information on the simulation methods used to model our samples.

Chapter 4 contains the design and characterization of nitrogen polar $\text{Al}_x\text{Ga}_{1-x}\text{N}/\text{AlN}$ ($0 \leq x \leq 0.1$) QD superlattices integrated along GaN NWs for application in pumped UV sources. There is a particular demand for semiconductor devices emitting in the ultraviolet (UV) range around 254 nm for application in the disinfection and purification of water. A promising alternative for manufacturing highly efficient and environmentally friendly UV lamps relies on the injection of electrons into AlGaN/AlN nanostructures using a miniaturized electron gun. In this chapter, we first describe the growth conditions and we systematically evaluate the optical performance of GaN/AlN superlattices on NWs for different thicknesses of dots/barriers and the effect of incorporating Al into the dots.

Chapter 5 describes the InGaN/GaN QD nanostructures forming the active region of III nitride emitters in the visible spectral range. In order to understand the optical performance of these QD nanostructures, it is necessary to obtain a direct correlation of the distribution of the alloy and the optical characteristics. Studies using La-APT offer the possibility of simultaneously recording the photoluminescence spectrum of the sample studied. We report here the results of a correlative study of a stack of InGaN / GaN QDs, combining high-resolution chemical and optical characterization by La-APT and in-situ micro-photoluminescence and comparing to ex-situ cathodoluminescence. We

demonstrate that the structural information extracted from these techniques allow precise modeling of these nanostructures, obtaining excellent agreement with optical measurements. During the La-APT experiment, it was possible to resolve the emission of single QDs located in the 9 layers of QDs closest to the substrate.

Chapter 6 illustrates the results of a correlative microscopy study of three InGaN / GaN QD stacks grown at different substrate temperatures, each stack consisting of 3 QD layers. Decreasing the temperature of the substrate during growth leads to an increase in the density of structural defects. However, the first QD layers behave as non-radiative point defect traps, so that the luminescence intensity increases towards the surface, despite the higher density of thread dislocations. In atomic probe tomography experiments combined with in situ micro-photoluminescence, it was possible to isolate the optical emission of a single QD located in the highest QD stack, closer to the surface of sample. The single line QD displayed a spectral shift during the experiment confirming the relaxation of the elastic stress due to the evaporation of the material.

Chapter 7 summarizes the work accomplished and the main achievements and presents some perspectives of this work.

Chapter 2: Nitride semiconductors

In this chapter, we present some of the characteristics of III-nitride semiconductors for both ternary and binary materials. This chapter covers the structural, elastic and electronic properties which can explain the optical performance. We discuss the difference between hydrostatic and uniaxial stress and its effects on the crystal. Finally, we focus our attention on nanostructures such as QWs, QDs and quantum wires and describe the effect of quantum confinement on the density of states.

2.1. Crystal structure and polarity

III-nitride semiconductors (GaN, AlN, InN and their ternary and quaternary alloys) occur in three crystallographic configurations: hexagonal wurtzite, cubic zinc-blende and cubic rocksalt. Depending on the substrate and growth conditions, epitaxial III-nitrides are either wurtzite or zinc-blende crystals, and it is also possible to have the co-existence of these two phases. The zinc-blende phase of GaN has cubic symmetry with atoms having tetrahedral coordination. **Figure 2.1(a)** illustrates this phase consisting of two face-centered cubic structures shifted by $u=1/4[111]$, with both metal and nitrogen atoms occupying appropriate sites. As a consequence, the stacking periodicity is ABCABC along the $[111]$ axis. This kind of nitrides can be grown by MBE mostly on cubic substrates such as (001)3C-SiC⁶⁹ or (001) GaAs⁷⁰.

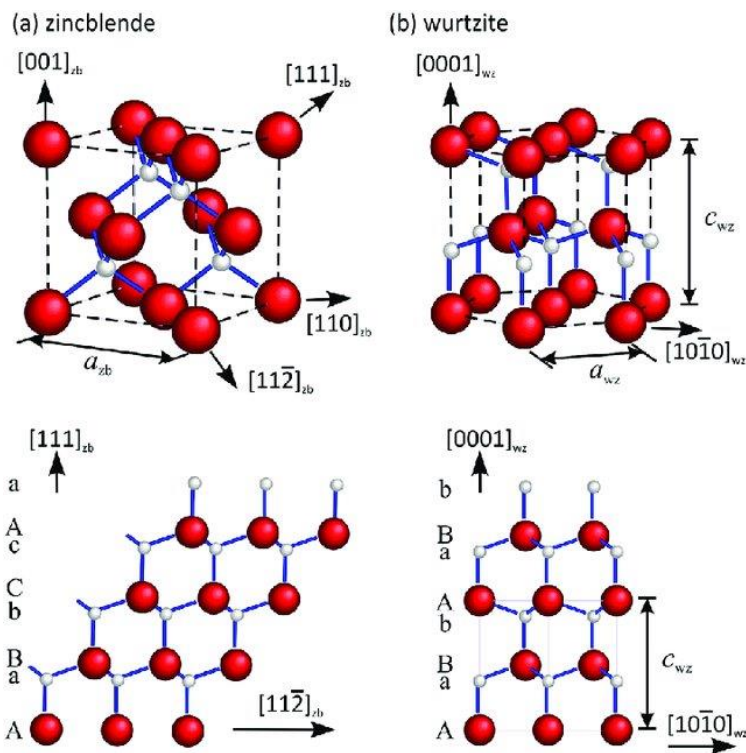


Figure 2.1: Crystal structure of (a) zinc-blende and (b) wurtzite GaN. The projections show the different stacking sequences of the close packed planes of Ga (red) and N (white) atoms. ⁷¹

In this work, we will focus on the wurtzite phase, as it is the most thermodynamically stable and finds applications in most III-nitride based devices. The wurtzite GaN phase shows hexagonal symmetry, the atoms are tetrahedrally coordinated and the orientation of the tetrahedra in subsequent layers is rotated by an angle of 60° around the $\langle 0001 \rangle$ axis. The lattice consists of two merged hexagonal sublattices (HCP) that are composed of group-III metal and nitrogen atoms, respectively, as it is shown in **Figure 2.1(b)**. Therefore, the stacking periodicity along the $[0001]$ axis is ABAB.

The wurtzite structure can be described by two lattice parameters a and c , and the internal parameter u . The basal plane lattice parameter, which is the edge length of the basal plane hexagon, is conventionally depicted by a and the axial lattice parameter, perpendicular to the basal plane, is conventionally described by c , which is the unit cell height. The u parameter is defined as the anion-cation bond length divided by the c lattice parameter.

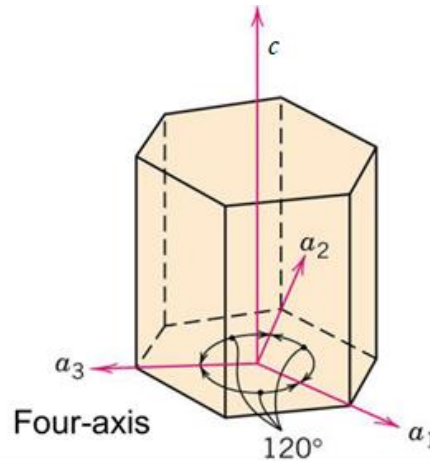


Figure 2.2: Hexagonal unit cell.

In the hexagonal system, the crystallographic directions and planes are named after four Miller-Bravais indices $\{h, k, i, l\}$. The notation of these indices is assigned to the three base vectors \vec{a}_1 , \vec{a}_2 , and \vec{a}_3 , and the out of plane vector \vec{c} , as it is shown in **Figure 2.2**. The three base vectors are separated by an angle of 120° . The direction of the vectors \vec{a}_1 , \vec{a}_2 , \vec{a}_3 and \vec{c} are $[2\bar{1}\bar{1}0]$, $[\bar{1}2\bar{1}0]$, $[\bar{1}\bar{1}20]$ and $[0001]$, respectively. It must be remembered that $\vec{a}_1 + \vec{a}_2 + \vec{a}_3 = \vec{0}$ and $h+k+i=0$. The lattice parameters of the materials used in this work are indicated in the **Table 2.1**.^{72,73}

	InN	GaN	AlN
c (Å)	5.72	5.185	4.982
a (Å)	3.542	3.189	3.112
c/a	1.612	1.626	1.6
u	0.377	0.377	0.382

Table 2.1: Lattice parameters of binary InN, GaN, AlN compounds.^{72,73}

The lattice parameters a and c of the ternary compounds with formula $A_xB_{1-x}N$ can be calculated using Vegard's law:

$$a_{A_xB_{1-x}N} = x * a_{AN} + (1 - x) * a_{BN} ; c_{A_xB_{1-x}N} = x * c_{AN} + (1 - x) * c_{BN} \quad (2.1)$$

Figure 2.3 illustrates some crystallographic planes with special importance in nitrides which are the polar c-plane (0001), the non-polar planes a ($11\bar{2}0$) and m ($10\bar{1}0$).

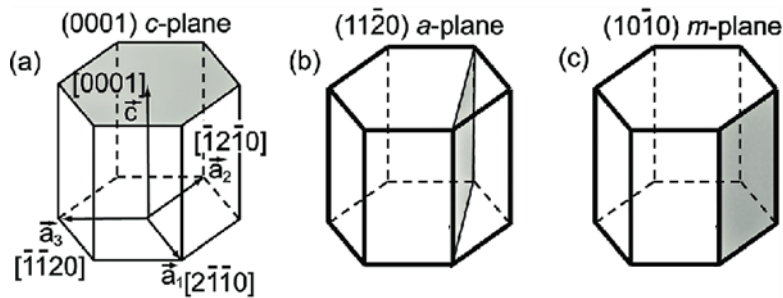


Figure 2.3: Schematic views of (a) polar c-plane, (b) and (c) nonpolar a- and m-planes, respectively.⁷⁴

The hexagonal wurtzite structure is not centrosymmetric this means that directions $[0001]$ and $[000\bar{1}]$ are not equivalent. A good example to understand the crystal polarity is studying the crystalline structure of GaN shown in **Figures 2.4**.

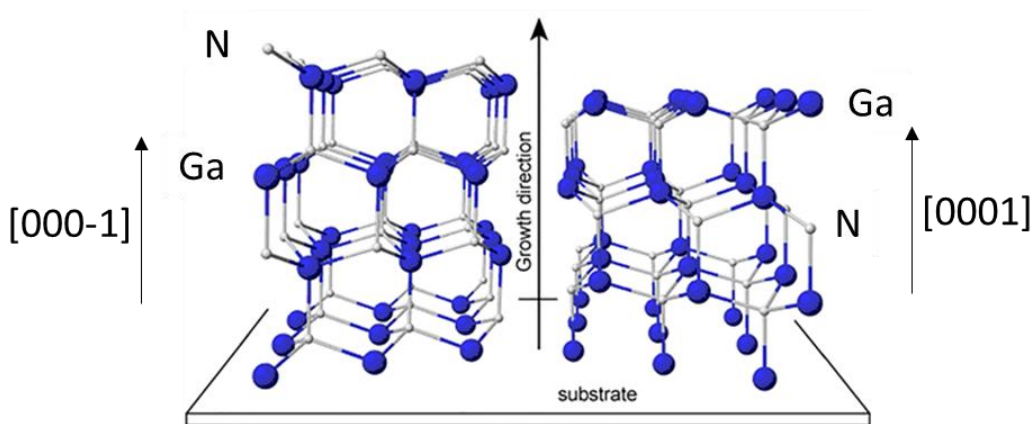


Figure 2.4 : Crystal structure of GaN illustrating Ga-polar orientation (right) and N-polar orientation (left) grown along the $[0001]$ crystallographic axes.⁷⁵

The Ga polarity in GaN wurtzite structure is defined by the direction of the vector pointing from Ga to N atoms along the c-axis $[0001]$. Conversely, The N polarity is defined by the direction of the vector from N to Ga atoms along c-axis. The (0001) face of the crystal is called Ga-face and the $(000\bar{1})$ face is called N-face. The two faces present important differences in surface morphology, chemical reactivity and growth conditions. Metal polar structures are more chemically stable than their nitrogen polar counterparts. In the case of growth on hexagonal SiC, the polarity of the substrate can impose the polarity of the III-N structure that is grown. Thus, a growth on (0001) face SiC will give a metal face structure. On the contrary, N-polar deposition can be done on $(000\bar{1})$ face SiC substrate.⁷⁶ In the case

of GaN grown on silicon or sapphire by MBE, its polarity depends on the substrate preparation and the nature of the buffer layer. N-polar GaN presents often rougher surface in comparison to Ga-polar GaN, since the growth window that favors two-dimensional growth is larger in the latter.^{76,77} **Figure 2.5** presents the visualization of GaN polarity by TEM observation.⁷⁵

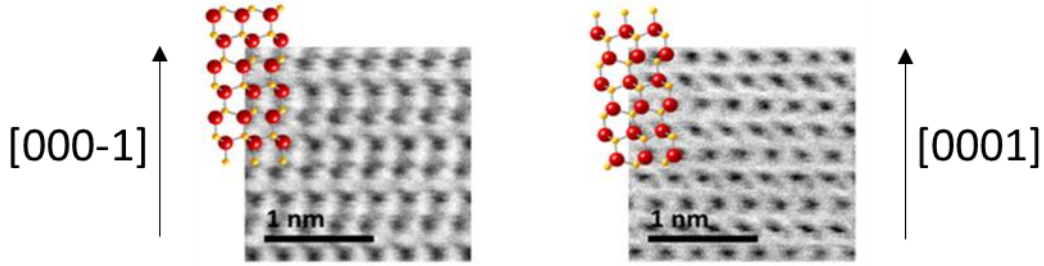


Figure 2.5 : Scanning TEM annular dark field images images of a GaN film (right) and GaN NW (left) showing aligned columns of N atoms (yellow) and Ga atoms (red). As the growth axis is oriented towards the top of the page for both systems, the film is Ga-polar and the NW is N-polar.

2.2. Elastic properties

For the III-nitride layers grown on commonly oriented templates with c-plane as a growth plane, strain arises because of the equibiaxial crystal lattice mismatch between the layer and template materials. In the semiconductor crystal, stress ($\sigma_{i,j}$) and strain ($\varepsilon_{k,l}$) are linked by Hooke's law:

$$\sigma_{i,j} = \sum_{k,l} C_{i,j,k,l} \varepsilon_{k,l} \quad (2.2)$$

where $C_{i,j,k,l}$ is the fourth-order elastic tensor. For the strain, we introduce the indices {1,2,3,4,5,6}, which are respectively the pairs of indices {xx,yy,zz,yz,zx,xy}:

$$\left\{ \begin{array}{l} \varepsilon_1 = \varepsilon_{xx} \\ \varepsilon_2 = \varepsilon_{yy} \\ \varepsilon_3 = \varepsilon_{zz} \\ \varepsilon_4 = \varepsilon_{yz} + \varepsilon_{zy} \\ \varepsilon_5 = \varepsilon_{zx} + \varepsilon_{xz} \\ \varepsilon_6 = \varepsilon_{xy} + \varepsilon_{yx} \end{array} \right.$$

In the same way for the stress, we have:

$$\left\{ \begin{array}{l} \sigma_1 = \sigma_{xx} \\ \sigma_2 = \sigma_{yy} \\ \sigma_3 = \sigma_{zz} \\ \sigma_4 = \sigma_{yz} + \sigma_{zy} \\ \sigma_5 = \sigma_{zx} + \sigma_{xz} \\ \sigma_6 = \sigma_{xy} + \sigma_{yx} \end{array} \right.$$

The elastic module or second-order tensor can be represented by a 6x6 stiffness matrix. For a crystal of hexagonal symmetry, this matrix contains six elastic modules, of which five are independent, as given in **Equation 2.3**:

$$C_{ij} = \begin{pmatrix} C_{11} & C_{12} & C_{13} & 0 & 0 & 0 \\ C_{12} & C_{11} & C_{13} & 0 & 0 & 0 \\ C_{13} & C_{13} & C_{33} & 0 & 0 & 0 \\ 0 & 0 & 0 & C_{44} & 0 & 0 \\ 0 & 0 & 0 & 0 & C_{44} & 0 \\ 0 & 0 & 0 & 0 & 0 & \frac{1}{2}(C_{11}-C_{12}) \end{pmatrix} \quad (2.3)$$

The theoretical values of the parameters C_{ij} for III-nitrides used in this work are reported below.

	C_{11} (GPa)	C_{12} (GPa)	C_{13} (GPa)	C_{33} (GPa)	C_{44} (GPa)	Ref.
InN	271	124	94	200	46	78
GaN	396	144	100	392	91	78
	367	135	103	405	95	79
AlN	398	140	127	382	96	78
	396	137	108	373	116	79

Table 2.2 : Theoretical stiffness constants of InN, GaN and AlN.

Performing Brillouin or Raman scattering, we can determine experimentally the elastic stiffness constants. However, in many cases there are still differences between the theoretical and experimental data due to the difficulties of growing high quality crystals. To compare the theory, experimental values of the parameters C_{ij} are summarized in **Table 2.3**.

	C_{11} (GPa)	C_{12} (GPa)	C_{13} (GPa)	C_{33} (GPa)	C_{44} (GPa)	Ref.
GaN	374	106	70	379	101	80
	390	145	106	398	105	81
AlN	411	149	99	389	125	82
	410	140	100	390	120	83

Table 2.3 : Experimental stiffness constants of GaN and AlN.

Given Hooke's law (**Equation 2.2**), it is possible to calculate the strain induced in a layer, knowing the stress distribution. During epitaxial growth, non-polar nitrides encounter anisotropic in-plane stress, which results in anisotropic distortion of the wurtzite unit cell.⁸⁴ On the contrary, during heteroepitaxy of planar III-nitrides along the <0001> direction, the in-plane stress is uniform ($\sigma_{11} =$

$\sigma_{22} = \sigma$) and there is no stress along the \bar{c} -axis [0001]. In this case (biaxial stress configuration), the Hooke law is simplified as in **Equation 2.4**, with the coefficients given in **Equations 2.5** and **2.6** shown below:

$$\begin{pmatrix} \sigma \\ \sigma \\ 0 \end{pmatrix} = \begin{pmatrix} c_{11} & c_{12} & c_{13} \\ c_{12} & c_{11} & c_{13} \\ c_{13} & c_{13} & c_{33} \end{pmatrix} \times \begin{pmatrix} \varepsilon_1 \\ \varepsilon_2 \\ \varepsilon_3 \end{pmatrix} \quad (2.4)$$

$$\varepsilon_1 = \varepsilon_2 = \varepsilon_{xx} = \frac{a_s - a}{a} \quad (2.5)$$

$$\varepsilon_3 = \varepsilon_{zz} = -2 \frac{c_{13}}{c_{33}} \varepsilon_{xx} = \frac{c_s - c}{c} \quad (2.6)$$

where a_s and c_s are the lattice parameters of the substrate and a and c the lattice parameters of the epitaxial layer.

2.3. Spontaneous and piezoelectric polarization

Spontaneous polarization is produced due to the difference of electronegativity between the two species, which causes an electron displacement in the bonds resulting in an electrical dipole. Due to the lack of symmetry of the wurtzite structure, these dipoles are not fully compensated along the [0001] direction, which leads to spontaneous polarization, P_{sp} . The mechanical stress also results in polarization, which is then called piezoelectric polarization P_{pe} . The total polarization of the crystal is the vector sum of the spontaneous and piezoelectric polarizations:

$$\vec{P} = \vec{P}_{sp} + \vec{P}_{pe} \quad (2.7)$$

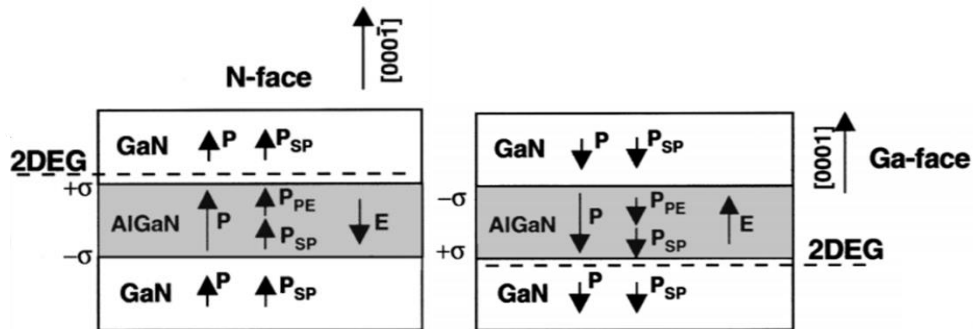


Figure 2.6: Spontaneous, piezoelectric and total polarization of Ga-face and N-face GaN/AlGaIn/GaN heterostructure (2DEG = two dimensional electron gas).⁸⁵

In Figure 2.6 the spontaneous, piezoelectric, and total polarization of an AlGaIn layer embedded in GaN are shown. For the N-face (0001) heterostructure, the sign of the polarization induced sheet charge (σ) is determined to be negative for the lower AlGaIn/GaN and positive for the upper GaN/AlGaIn interface. In the Ga-face (0001) heterostructure, charges have opposite sign.

The values of spontaneous polarization for III-nitride materials are described in **Table 2.4**:

	GaN	AlN	InN
P_{SP}^{86}	-0.029	-0.081	-0.032
P_{SP}^{87}	-0.034	-0.090	-0.042

Table 2.4 : Spontaneous polarization parameters [C/m²].

If stress is applied to the III-nitride lattice, the lattice parameters c and a of the crystal structure will be changed to accommodate the stress. Thus, the polarization strength will be changed. This additional polarization in strained crystals is called piezoelectric polarization. The piezoelectric polarization in planar wurtzite III-nitrides grown along the c -axis can be calculated with the following equation⁸⁸:

$$P_{PE} = e_{33}\epsilon_z + e_{31}(\epsilon_x + \epsilon_y) = 2 \frac{a_s - a}{a} \times \left(e_{31} - e_{33} \frac{c_{13}}{c_{33}} \right) \quad (2.8)$$

where e_{ij} are the piezoelectric coefficient of the material, a_s is the in-plane lattice parameter of the substrate and a is the lattice parameters of the epitaxial layer.

The piezoelectric coefficients for AlN, GaN and InN are indicated in **Table 2.5**.

	AlN	GaN	InN
$e_{33} \text{ (C/m}^2\text{)}^{86}$	1.46	0.73	0.97
$e_{31} \text{ (C/m}^2\text{)}^{86}$	-0.60	-0.49	-0.57

Table 2.5: Piezoelectric coefficients for AlN, GaN and InN.

2.4. Electronic properties

The band structure of a semiconductor emerges as a solution of the Schrödinger equation of non-interacting electrons in the periodic lattice. Visualization of the band gap requires a plot of energy vs. wavevector $k = (k_x, k_y, k_z)$. It is common to plot band structures as curves of $E_n(k)$ for values of k along straight lines connecting symmetry points in the k -space. These points of symmetry occur in the first Brillouin zone and are labelled as Γ , Δ , Λ , Σ . The band gap is described as the energy difference between the bottom of the conduction band and the top of the valence band. If the bottom of the conduction band and top of the valence band occur at the same symmetry point, then the material is said to have a direct band gap. In the case of wurtzite III-nitrides, the band gap is direct, with the conduction band minimum and the valence band maximum located at the Γ point. Because of the lack of symmetry along c -axis, there is a degeneracy splitting of the valence band between the heavy hole (Γ_9 symmetry), light hole (Γ_7 symmetry) and spin-orbit (Γ_7 symmetry) subbands.

The typical tool that is currently used to measure band structures of solid materials is angle-resolved photoemission spectroscopy (ARPES). From the measured energy and momentum

information, the structure of the band, from which the electrons were emitted, can be revealed. The calculated full band structures for GaN, InN and AlN are shown in **Figure 2.7**. It can be observed in zoomed images (**Figure 2.8**) that the heavy hole (HH), light hole (LH), crystal field splitting (CH) subbands are separated.

For GaN, the top of HH and LH subbands are higher than CH subband in energy. So the CH energy has a positive value of 22 meV⁸⁹, the topmost valence band (VB) is the HH band, which is composed of atomic p orbitals perpendicular to c -axis $\langle 0001 \rangle$ direction. Therefore, the transition between the conduction band (CB) and HH band is allowed for electric field perpendicular to the c -axis ($E \perp c$), and the emission intensity is therefore strong along the c -axis direction (from the c -plane) but weak normal to it. However, in the case of AlN the top of the CH subband is at higher energy than the HH or LH subbands. As a result, the CH energy has a *negative* value of -165 meV⁹⁰ and the topmost VB is the CH band, which is composed of atomic p orbitals parallel to the c -axis. Therefore, the transition between the CB and CH band is allowed for electric field parallel to the c -axis ($E \parallel c$), and the emission intensity is, therefore, weak along the c -axis direction (from c -plane) but strong, normal to it^{91,92}.

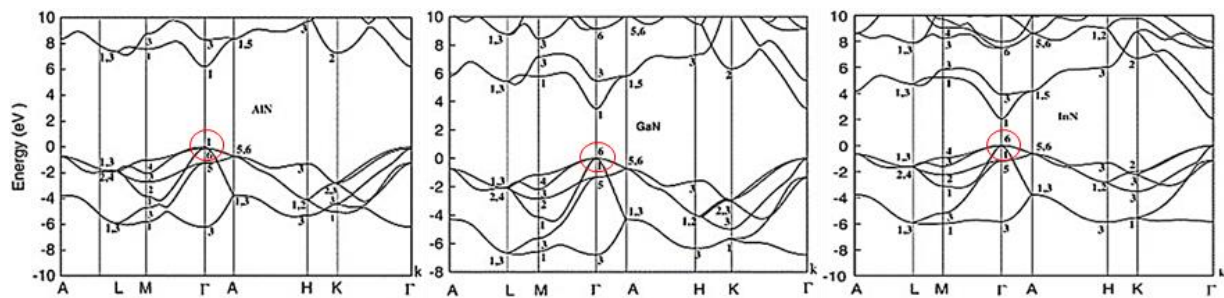


Figure 2.7: Band structure of wurtzite AlN, GaN and InN.⁹³

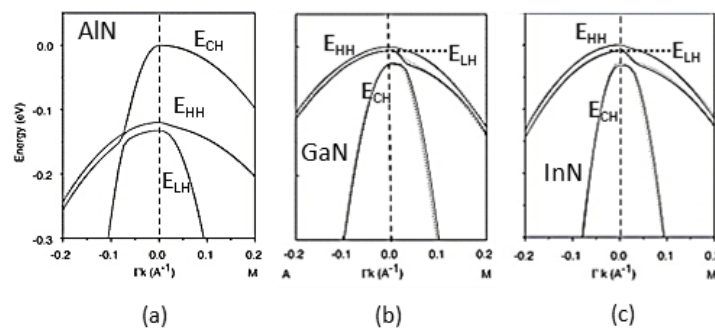


Figure 2.8: Schematic band structures near the Γ point of (a) AlN, (b) GaN and (c) InN.

An effective mass approximation can describe the band structure at $k=0$ by assuming a parabolic band structure at this point. This means that the electron and hole behavior can be modelled as a free particle with an effective mass m^* experiencing a fixed potential. The typical values of the effective masses for electrons and heavy holes in III-nitrides at around $T = 300$ K are recorded in **Table 2.6** below:

	AlN	GaN	InN
m_e^*	0.27 ⁴³	0.20 ⁴⁵	0.11 ⁴⁷
m_h^*	1.44 ⁴⁴	1.25 ⁴⁶	1.63 ⁴⁸

Table 2.6: Effective masses for electrons (e) and heavy-holes (hh) in units of the free electron mass m_0 .

For ternary compounds like AlGaIn or InGaIn the bandgap is approximated by a quadratic equation:

$$E_{G(AB)} = xE_{G(A)} + (1 - x)E_{G(B)} - x(1 - x)b \quad (2.9)$$

where b is the bowing parameter which accounts for the deviation from a linear interpolation between the two binaries A and B having an A alloy mole fraction x . The bowing parameter has a value of 0.8-1.3 eV in the case of AlGaIn⁹⁶ and 1.21 ± 0.03 eV for InGaIn⁹⁷.

The effect of temperature on band gap energy has been quantified through several empirical or semi-empirical relations. Among the empirical relationships, the Varshni relationship⁹⁸ is often used to assess nonlinear temperature dependent band gap shift:

$$E_{G(T)} = E_{G(T=0\text{ K})} - \frac{\alpha T^2}{\beta + T} \quad (2.10)$$

where α and β are fitting parameters, which are the Varshni and Debye coefficients respectively, whose values are listed in Table 2.6, and $E_{G(T=0\text{ K})}$ is the band gap of the semiconductor at 0 K.⁹⁹

The values of the band gap of AlN, InN and GaN and the Varshni parameters are summarized in Table 2.6.

	AlN ⁷³	GaN ⁷³	InN ¹⁰⁰
$E_{G(T=0\text{ K})}$ (eV)	6.23	3.507	0.69
α (meV·K ⁻¹)	1.999	0.909	0.414
β (K)	1429	830	454

Table 2.7: Band parameters of AlN, GaN, and InN: band gap energy at $T = 0$ K and Varshni parameters.

2.5. Hydrostatic and uniaxial stress

Strain may have an important role for the optical and electrical phenomena taken place on nanoscale systems. Strain can be induced by the lattice mismatch or it can be in applied by an external action causing hydrostatic or uniaxial stress in a strongly controlled way.

The application of hydrostatic pressure can cause a shift of the conduction-band edge relative to

the valence-band edge due to the change in volume. The hydrostatic potential is anisotropic due to the reduced symmetry in wurtzite structure.

Strain affects the device properties in several ways:

- It changes the absolute positions of the valence-band maximum (VBM) and the conduction-band minimum (CBM), and hence modifies the QW depth and the confinement of electrons and holes in the active region.
- It induces piezoelectric polarization in InGaN or AlGaIn QWs^{84,101,102}, thus lowering the electron-hole overlap and hence the radiative recombination rate.
- It may also modify the effective masses of carriers and the density of states^{103,104}.
- In polar (c-plane) QWs, the in-plane strain is isotropic^{105–107}. In nonpolar and semipolar QWs, on the other hand, the biaxial stress induces anisotropic strain, which drastically modifies the subband structures and wave-function character^{108,109,109} and induces polarized light emission^{110,111,102}.

Six valence and conduction band deformation potentials, in addition to the strain tensor and the overall hydrostatic deformation potential, are necessary to describe the band structure of GaN under strain as shown in **Table 3.1** in **Chapter 3**. So far, most of the experimental data on deformation potentials of GaN and InN have been obtained by a combination of x-ray and optical measurements from the change of optical transition energies under the biaxial stress induced by the c-plane substrate. However, the accurate determination of deformation potentials by this experimental approach is difficult. One of the main problems is that the uniaxial and biaxial strain components cannot be applied separately, and the measurement only provides results for a combination of several deformation potentials.

For an unstrained wurtzite system, the top three valence bands correspond to the heavy hole (HH), light hole (LH) and crystal-field split-off band (CH). The transition energies from the CBM to these three bands are denoted E_A , E_B , and E_C , respectively.

We first focus on those strain components that do not break the wurtzite symmetry, including biaxial strain in the c-plane ($\varepsilon_{xx} = \varepsilon_{yy}$) and uniaxial strain along the c-axis (ε_{zz}). Such strain perturbations to the 6×6 $\mathbf{k} \cdot \mathbf{p}$ Hamiltonian do not split HH and LH bands, although they induce an energy shift of the conduction and the three valence bands at the Γ point¹¹²:

$$\begin{aligned}\Delta E_{CB} &= a_{cz}\varepsilon_{zz} + a_{ct}\varepsilon_{\perp}, \\ \Delta E_{HH/LH} &= (D_1 + D_3)\varepsilon_{zz} + (D_2 + D_4)\varepsilon_{\perp}, \\ \Delta E_{CH} &= D_1\varepsilon_{zz} + D_2\varepsilon_{\perp}\end{aligned}\tag{2.11}$$

yielding the following transition energies:

$$E_{A/B} = E_{A/B}(0) + (a_{cz} - D_1)\varepsilon_{zz} + (a_{ct} - D_2)\varepsilon_{\perp} - (D_3\varepsilon_{zz} + D_4\varepsilon_{\perp})\tag{2.12}$$

and

$$E_C = E_C(0) + (a_{cz} - D_1)\varepsilon_{zz} + (a_{ct} - D_2)\varepsilon_{\perp} \quad (2.13)$$

When the heavy hole is on the top of the VB, the band gap is given by E_A (e.g. for GaN or InN). When CH is on the top of the VB (e.g. for AlN) then the band gap is calculated using the equation of E_C .

Here ε_{\perp} (defined as $\varepsilon_{xx} + \varepsilon_{yy}$) and ε_{zz} are the strain components in and out of the c-plane. $E_{A/B}(0)$ and E_C are the corresponding transition energies at equilibrium lattice constants. From the slopes of the transition energies under biaxial strain in the c-plane ($\varepsilon_{xx} = \varepsilon_{yy} \neq 0, \varepsilon_{zz} = 0$), we obtain the deformation potentials $a_{ct} - D_2$ and D_4 , while $a_{cz} - D_1$ and D_3 can be obtained from the slope of transition energies under uniaxial strain along the c-axis ($\varepsilon_{xx} = \varepsilon_{yy} = 0, \varepsilon_{zz} \neq 0$).

2.6. Introduction to semiconductor heterostructures

Heterostructures are made by joining different materials at the atomic level. When two semiconductors are joined, it is not clear in advance how the different bands in the two materials will line up in energy with another one, and there is no accurate predictive theory in practice. Hence, an important experimental quantity is the "band offset ratio"; this is the ratio of the difference in conduction band energies to the difference in valence band energies. **Figure 2.9** shows the three possibilities of alignment of band gap minima along the growth direction depending on the band offsets, known as type I, II and III.

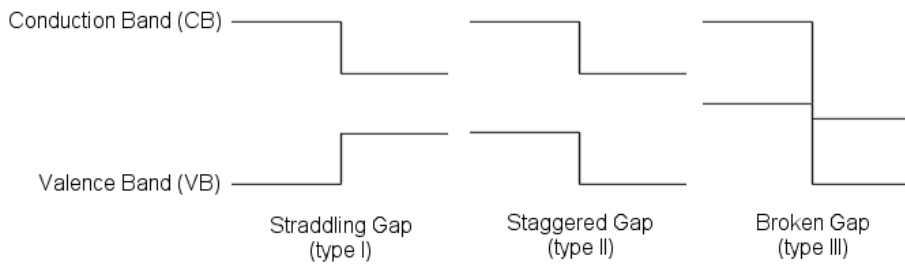


Figure 2.9: Description of the band edge profile at heterojunctions.

In III-nitrides, heterostructures are always type I, which allows the fabrication of QWs, where quantified electron levels appear as a result of the quantum confinement. The conduction band offset in the GaN/AlN system is around 1.8 eV^{113} . The polarization discontinuity at the interface between the two materials results in a fixed charge sheet. In nanostructures, this fixed charge sheet generates an internal electric field, which is maximum for growth along the $\langle 0001 \rangle$ axis, where it can reach several MV/cm. In (0001)-oriented QWs, the internal electric field generates a band bending as seen in **Figure 2.10**. This leads to a spatial separation of electron and hole wave functions along the growth axis, which results in the so-called quantum confined Stark effect (QCSE). This means that the band-to-band transition is shifted to lower energy and the radiative lifetime increases due to the reduced electron-hole wave function overlap.

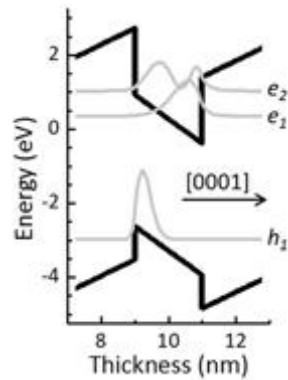


Figure 2.10: Band diagram of a GaN QW in an infinity GaN/AlN (2.1 nm/3 nm) MQW system. In gray lines, squared wavefunctions associated to the first and second confined levels of electrons (e_1 , e_2) and the first confined level of holes (h_1).¹¹⁴

In the case of heterostructures grown on the m-plane or on the a-plane, the polarization dipoles are perpendicular to the direction of growth. Therefore, there is no polarization discontinuity at the heterostructure interfaces along the growth direction.¹¹⁵ Hence, these are called non-polar orientations or non-polar directions. In contrast to polar directions, the nonpolar have no internal electric field, there is no noticeable charge transfer between the layers, the band profiles are flat along this direction, and consequently the band gaps are “direct in real space” and significantly larger than in the polar case.¹¹⁶ A scheme presenting this difference is described in Figure 2.11.

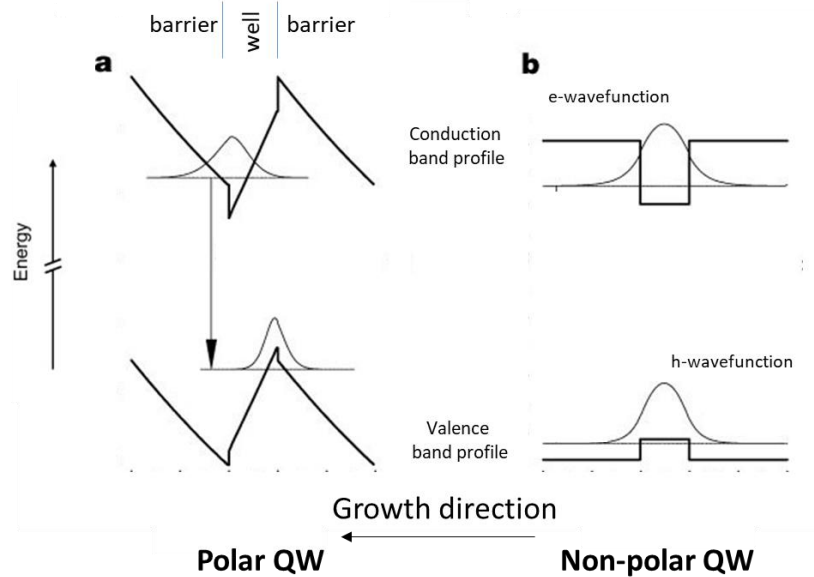


Figure 2.11: Schematic representation of band profiles and electron and hole wavefunctions in (a) polar and (b) non-polar QWs. (modified from ¹¹⁷)

Several different nanostructures are differentiated based on the number of dimensions in the volume of the object with nanoscale size: QWs (quantum confinement along 1 direction), quantum

wires (2 directions), or QDs (three directions).

The energy of free carriers (holes or electrons) is obtained by solving the Schrodinger equation:

$$\left[\frac{-\hbar^2}{2m} \left(\frac{\partial^2}{\partial x^2} + \frac{\partial^2}{\partial y^2} + \frac{\partial^2}{\partial z^2} \right) + V(x, y, z) \right] \Psi(x, y, z) = E\Psi(x, y, z) \quad (2.14)$$

For a square QW perpendicular to the x direction, the potential is $V(x,y,z) = V(x)$. The total energy of an electron with effective mass m^* and with an in plane momentum $k_{x,y,z}$ is given by:

$$E = E_x + E_{z,y} \Rightarrow E = \frac{\hbar^2 k_x^2}{2m^*} + \frac{\hbar^2 (k_z^2 + k_y^2)}{2m^*} \Rightarrow E = E_{nx} + \frac{p_z^2 + p_y^2}{2m^*} \quad (2.15)$$

where

$$k_x = \frac{n\pi}{d_x} \quad (2.16)$$

and d_x is the thickness of the well and n denotes the integer quantum number.

The 3D density of the states for a free electron is:

$$g(E) = \frac{1}{2\pi} \left(\frac{2m^*}{\hbar^2} \right)^{3/2} E^{1/2} \quad (2.17)$$

When the electron is confined in the semiconductor the 3D density of states can be written as:

$$g(E) = \frac{8\pi\sqrt{2}}{h^3} m^{*3/2} \sqrt{E - E_{min}}, \text{ when } E \geq E_{min} \quad (2.18)$$

For a 2D semiconductor such as a QW, where the electrons are confined to a 2D plane, the 2D density of states can be described as:

$$g(E) = \frac{4\pi m^*}{h^2}, \text{ when } E \geq E_{min} \quad (2.19)$$

For quantum wires (typically $\approx 5-20$ nm), we restrict the motion of carriers in 2 dimensions, thus giving rise to one dimensional states. Now if we solve the Schrodinger **Equation** (2.12) for a NW with axis along x, the time potential is $V = V(y,z)$. The equation for the energy levels becomes:

$$E_{n_x n_z} = \frac{\hbar^2 \pi^2}{2m^*} \left(\frac{n_y^2}{L_y^2} + \frac{n_z^2}{L_z^2} \right) + \frac{\hbar^2 k_x^2}{2m^*} \Rightarrow E = E_{n_x, n_y} + \frac{p_z^2}{2m^*} \quad (2.20)$$

where L_y and L_z are the dimensions of the wire along y and z and n_y and n_z are the respective quantum numbers. The density of states is given by:

$$g(E) = \frac{1}{2\pi} \left(\frac{2m^*}{\hbar^2} \right)^{1/2} (E - E_{min})^{-1/2} \quad (2.21)$$

Finally, for QDs, electrons should occupy discrete energy levels. If we once again begin with the Schrodinger **Equation** (2.12), we can write the potential V as the sum of 3D confinement $V(x,y,z) = V(x)+V(y)+V(z)$. The confinement energy within this confinement box follows as:

$$E_{n_x n_z} = \frac{\hbar^2 \pi^2}{2m^*} \left(\frac{n_x^2}{L_x^2} + \frac{n_y^2}{L_y^2} + \frac{n_z^2}{L_z^2} \right) \Rightarrow E = E_{n_x, n_y, n_z} \quad (2.22)$$

Here we need three quantum numbers, n_x , n_y and n_z to label each energy state. The situation regarding the density of states in QDs is quite different. As the particles are confined in all directions, the density of states is dependent on the number of confined levels. One single isolated dot would therefore alter just two states of the energy of each confined level and a plot of the density of states versus energy would be a series of Delta functions:

$$g(E) = 2\delta(E - E_{min}) \quad (2.23)$$

The density of states function for all 3 nanostructures (QWs, quantum wire and QD) is shown below **Figure 2.12**, including the bulk semiconductor.

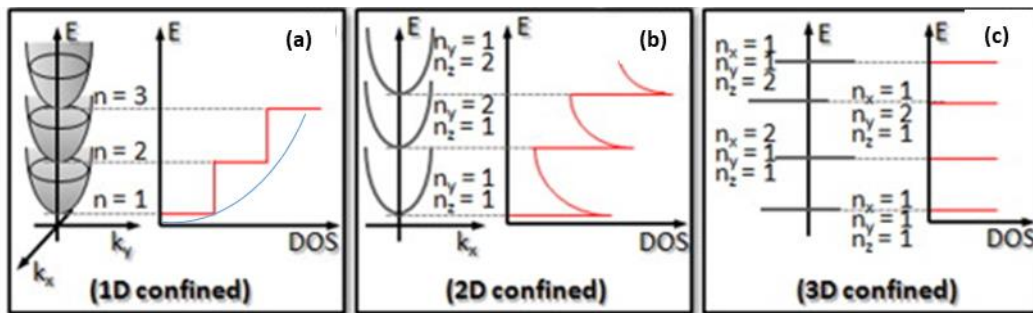


Figure 2.12: Electronic density of states and corresponding energy levels for the QWs, QWRs and QDs, respectively. Blue line represents the density of states in bulk 3D semiconductor. ¹¹⁸

Chapter 3: Experimental methods

In this chapter, we present the experimental techniques and simulation methodology used in this work. We start with the epitaxial growth process using plasma-assisted MBE, including reflection high-energy electron diffraction as real-time in-situ characterization technique. Then, we introduce the various characterization techniques used in this work. In particular, we studied the morphology and structure of our samples using x-ray diffraction and atomic force microscopy, and the optical properties were assessed by photoluminescence and cathodoluminescence techniques. We also describe the preparation of the samples using dual scanning electron microscopy (SEM) / focused ion beam (FIB), and the chemical characterization by La-APT. Particular attention is paid to the APT system that incorporates in-situ micro-photoluminescence spectroscopy. Finally, this chapter provides information about the simulation methods used to model our samples.

3.1. Epitaxial growth

Epitaxy is the word defining the deposition or growth of a crystalline overlayer (called epitaxial film/layer) on a crystalline substrate, when the orientation of the epitaxial layer is determined by the substrate. We speak about *homoepitaxy* if the substrate and the epitaxial layer are essentially the same material, and we call it *heteroepitaxy* if they are different. In this subchapter, we describe the epitaxial growth process using PAMBE, including an introduction to the different growth modes and the operation properties of the MBE machine. We also present a real-time *in-situ* characterization technique, namely reflection high-energy electron diffraction (RHEED). Last but not least, we explain the growth process of the various heterostructures studied in this work. At the end of the subchapter, there is a short description of the substrates used for the growth of the grown nanostructures.

3.1.1. Plasma-assisted molecular beam epitaxy

MBE is a technique used to grow thin crystalline films on a heated crystalline substrate under ultra-high vacuum (UHV) conditions (pressure $\leq 10^{-9}$ Torr). Precursor elements are provided by atomic or molecular beams, impinging on the substrate at extremely low velocities (≤ 0.1 Å/s), under conditions that are far from the thermodynamic equilibrium. The process depends on surface migration phenomena and surface reactions with the substrate. Therefore, it is necessary to control the vacuum in the growth chamber, the substrate temperature and the amount of reagent by adjusting the temperature of the solid sources, or the gas flux and radio frequency power in the case of using a plasma source. If the proper conditions are met, the growth ends up in films with extremely smooth surface.

The surface processes that contribute to nucleation, epitaxial deposition and development of the structure on the surface of the substrate, shown in **Figure 3.1**, are:

1. Multi-layer growth: When the adatom diffusion length is short, it results in the nucleation of multi-layer-thick clusters, ultimately forming a rough surface.
2. Layer-by-layer growth: When the diffusion length is longer, the increased diffusion length results in the nucleation of monolayer (ML) clusters, with the atomic layers completed one by one.
3. Step-flow growth: When diffusion length is even longer, the longer diffusion length gives the adatoms enough mobility to reach the step edges, which are often energetically favorable incorporation sites.

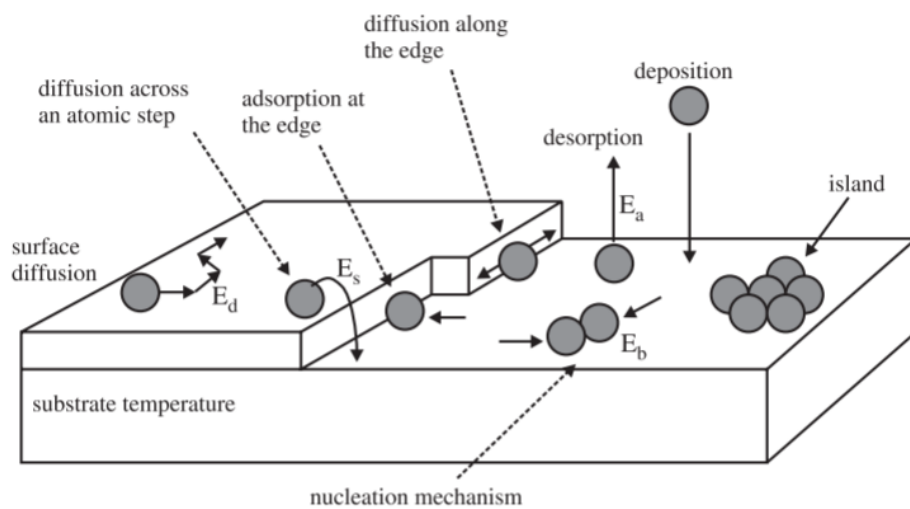


Figure 3.1: Behavior of adatoms during the surface deposition process (diffusion until nucleation with other adatoms; deposition on edges).¹¹⁹

In general, depending on the growth parameters, one can distinguish between three different growth modes¹²⁰ (see **Figure 3.2**):

1. Layer or Franck-Van der Merwe growth mode: A new layer starts to grow only after the preceding one is finished (**Figure 3.2 a**).
2. Island or Vollmer-Weber growth mode: The deposited atoms cannot diffuse past the island boundaries. Already after a light coverage, multiple monolayers can be formed as high islands (**Figure 3.2 b**).
3. Layer plus island or Stranski-Krastanov growth mode: This type is a combination of layer and island growth mode (**Figure 3.2 c**).¹¹⁹

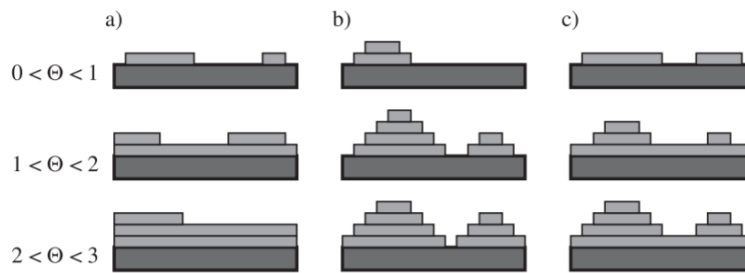


Figure 3.2: Growth modes for layer development by MBE.

The advantages of using MBE are many. First, the MBE growth is carried out under low temperature compared to hydride vapour phase epitaxy (HVPE) or metal organic vapour phase epitaxy (MOVPE), and under relatively low growth rate (generally less than 1 ML/s). This results in a good control over layer thickness and reduced inter-diffusion effects. Then, the UHV environment in the MBE offers the possibility to have in-situ control of the growth, with techniques like reflection high-energy electron diffraction (RHEED) or quadrupole mass spectrometry. This facilitates the study of the structure in various stages of the growth process. Finally, another reason that has made the MBE technique essential for the development of thin films is the growth in out-of-equilibrium conditions, which means that it is possible to stabilize materials that do not exist spontaneously in nature. This enables endless experimentation and testing in order to achieve structures characterized by new desirable physical properties. All these possibilities make MBE a very interesting growth technique, providing a very important tool for researchers involved in the synthesis of materials. Moreover, the reproducibility of the process makes MBE compatible with mass production, which is particularly interesting for devices with critical demands in terms of dimensions or chemical composition (requirement of extreme purity, extreme dopant concentrations, growth of alloys with miscibility issues or low decomposition temperature).

The basic schematics of the MBE used in this study is displayed in **Figure 3.3**. All samples in this work were grown using this technique. Active nitrogen free radicals are obtained by cracking high-purity molecular nitrogen (6N5) with a radio frequency plasma source. This technique is known as plasma-assisted MBE (PAMBE) to differentiate between other sources of nitrogen like ammonia-based sources. Our MBE system was equipped with an automatic N plasma source HD25 supplied by Oxford Applied Research. The output power was varied to modify the flux of active nitrogen.

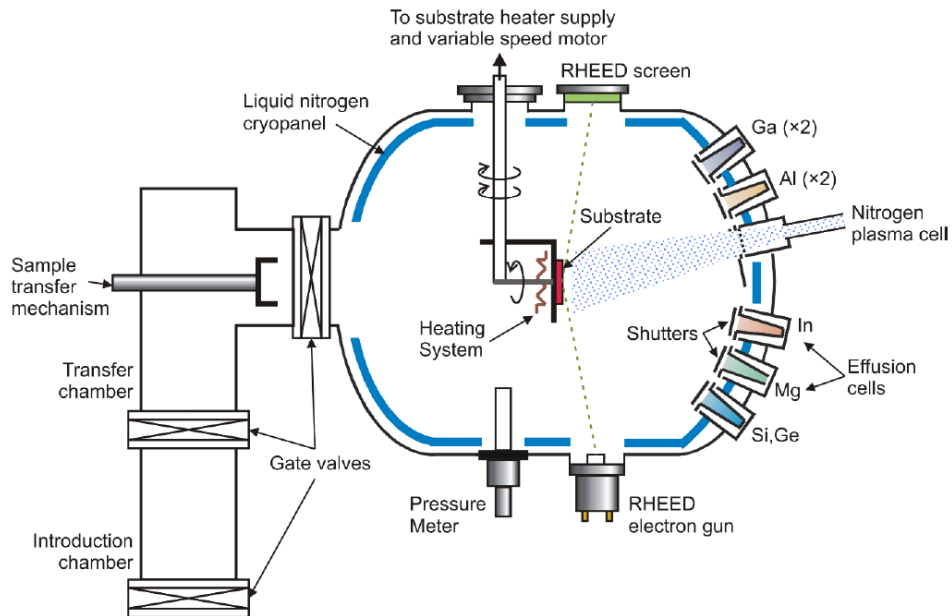


Figure 3.3: Schematics of the PAMBE used in this study (modified from ¹²¹).

From the figure above, we can see that there are various effusion cells, including Ga, Al, In, Si, Mg and Ge. Accurate regulation of the cell temperatures is achieved through proportional-integral-derivative controllers. A mechanical shutter in front of each cell is used to interrupt the atom beam, as illustrated in **Figure 3.4**. The Knudsen-type crucibles are made of pyrolytic boron nitride.



Figure 3.4: Image of the MBE growth chamber of the lab, showing the cells and their effusion cell shutters.

We glue the substrate on a molybdenum sample holder (molyblock) with indium, or we fix it mechanically with molybdenum clamps (indium-free growth). The molyblock is then fixed on a 4-axis manipulator, which allows the automatically rotation and heating of the substrate. The entire section with cells and substrate, where the growth happens is called the growth chamber, which is cooled down with liquid nitrogen to get a base pressure in the 10^{-11} mbar range. The molyblock is loaded into the growth chamber through a load-lock system consisting of an introduction chamber (base pressure in the 10^{-9} mbar range) and transfer chamber (base pressure in the 10^{-10} mbar range). The introduction

chamber is opened under nitrogen flux to exchange the molyblock.

The MBE system is equipped with an in-situ and real-time characterization tool in order to study the morphology and crystal structure of the growing surface. This characterization technique is called RHEED. Electrons are emitted from a hot filament, which is excited by a 1.5 A current, and accelerated under high-voltage of 32 kV (values from our setup). The electron beam strikes the sample at a grazing angle, and the diffracted beam then impinges on a fluorescent phosphor screen mounted in the direction opposite to the electron gun.

A scheme of the RHEED measurement principle is shown in **Figure 3.5**. The obtained image displayed on the screen is the Fourier transform of the lattice interacting with the beam. It corresponds to the intersection of the reciprocal lattice with the Ewald Sphere of radius $k_i = \frac{2\pi}{\lambda}$ where λ is the wavelength of the electron. In an atomically smooth and single crystalline sample the crystal lattice would actually correspond to perpendicular rods as shown. By analysing the pattern one can obtain the 2D (e.g. planar layers) or 3D (e.g. NWs) nature of the growth front and a qualitative estimation of the crystal quality.

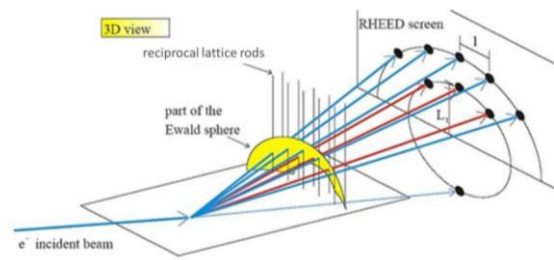


Figure 3.5: Working principle of RHEED used in this study.

The RHEED intensity can give us information about the growth rate. The time-dependent change in the density of atoms at the growth front during the growth process can result in an oscillatory variation of the RHEED intensity with time. If we consider a flat surface, the coverage of atoms on the surface is defined as θ . When the layer is complete, the coverage can be minimum (n^{th} layer, θ is 0) or maximum ($(n+1)^{\text{th}}$ layer, θ is 1) leading to a smooth surface. In both cases the RHEED intensity is maximum. Starting with a minimum coverage of $\theta = 0$, we can describe the procedure to determine the growth rate, as illustrated in **Figure 3.6**. For intermediate coverage, the intensity decreases with increase in coverage up to $\theta = 0.5$. Here the roughness is maximum and the intensity is at its lowest. Further growth would increase the coverage but decrease the roughness as shown in **Figure 3.6**. At $\theta = 0.75$, the intensity recovers as the roughness is reduced as the growth front picks up more adatoms. The surface flattens at $\theta = 1$, reaching again a maximum RHEED intensity and the process continues in a cyclic manner as the growth continues. A single RHEED intensity oscillation period corresponds to the growth of a single layer. During the operation of our PAMBE system, the calibration of the growth rate and the control of the alloy composition and thickness of the 2D layers were done observing such RHEED oscillatory behavior.

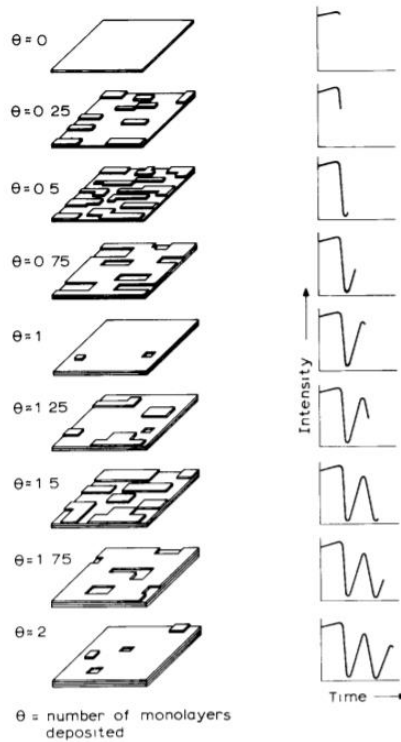


Figure 3.6: Schematic illustration of the origin of RHEED oscillations: The intensity of the specularly reflected electron beam depends on the step density of the sample surface, which changes with the surface coverage θ of the growing layer.¹²²

3.1.2. Growth of III-nitrides

Here, we present extensive information on the mechanisms of MBE growth in III-nitride compounds using the MBE machine available at CEA-IRIG, Grenoble. This subchapter discusses the growth of planar layers, NWs and QDs. Each of them has a specific way of growth (different kind of substrate and temperature of substrate and cell) and different RHEED images showing the planar or 3D deposition.

For the experiments described in this thesis, we used various substrates, which we classify here as GaN-on-sapphire templates and silicon substrates. For GaN-on-sapphire templates, we used GaN(0001)-on-sapphire templates supplied by LUMILOG, consisting of 4- μm -thick GaN on c-sapphire grown by MOCVD with a dislocation density of $\approx 10^8 \text{ cm}^{-2}$. In this work, we used these substrates for growing the InGaN QDs samples. For the growth of NWs, we used n-type Si(111) substrates with a thickness of $500 \pm 25 \mu\text{m}$. The substrates were provided by BT Electronics.

3.1.2.1. Planar layers

The growth of GaN (0001) by PAMBE presents different morphological properties depending on the III/V flux ratio. The GaN layers display a faceted surface when the growth is performed under N-rich conditions^{123–125}. On the contrary, under Ga excess we achieve atomically flat GaN layers. Therefore, in

order to grow planar GaN, it is important to have an adsorbed layer of Ga atoms that covers the growing surface. In the **Figure 3.7**, we present the four regimes of Ga coverage as a function of impinging Ga flux measured at a substrate temperature $T = 740^\circ\text{C}$ and under N flux = 0.28 ML/s:

- A. N-rich growth: for $\Phi_{\text{Ga}} < 0.3$ ML/s, the Ga coverage on the surface is negligible.
- B. Ga excess ≤ 1 ML of Ga: For 0.3 ML/s $< \Phi_{\text{Ga}} < 0.5$ ML/s, there is < 1 ML of Ga presented on the surface.
- C. Ga excess = 2 ML of Ga: For 0.5 ML/s $< \Phi_{\text{Ga}} < 1$ ML/s, there are 2 ML of Ga presented on the surface.
- D. Accumulation of Ga: for $\Phi_{\text{Ga}} > 1$ ML/s, the system reaches the Ga accumulation regime, forming Ga droplets on the surface.

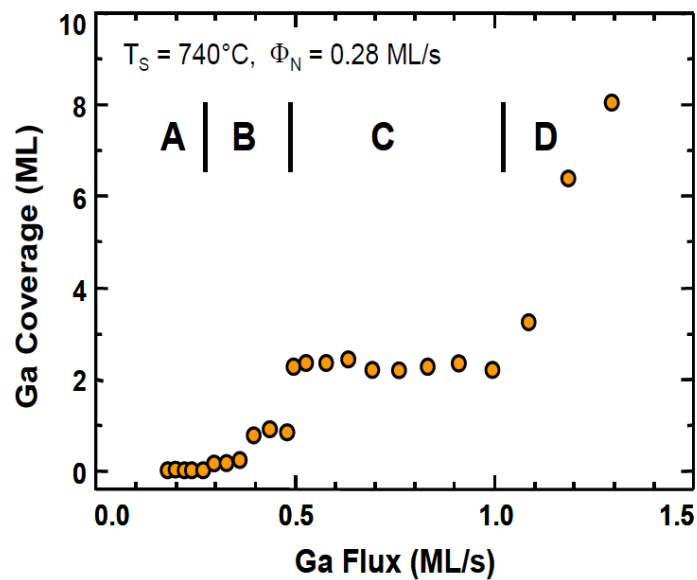


Figure 3.7: Ga coverage on top of the GaN (0001) surface as a function of the Ga flux (modified from ¹²⁶).

The Ga coverage as a function of Ga flux was studied at various substrate temperatures and gives the growth diagram presented in **Figure 3.8**. The AFM images shown in **Figure 3.8** illustrate the benefit of the Ga excess. They demonstrate that, if GaN is grown with a Ga coverage below 2 ML, it presents a rough surface, whereas atomic steps can be seen when GaN is grown under Ga excess.

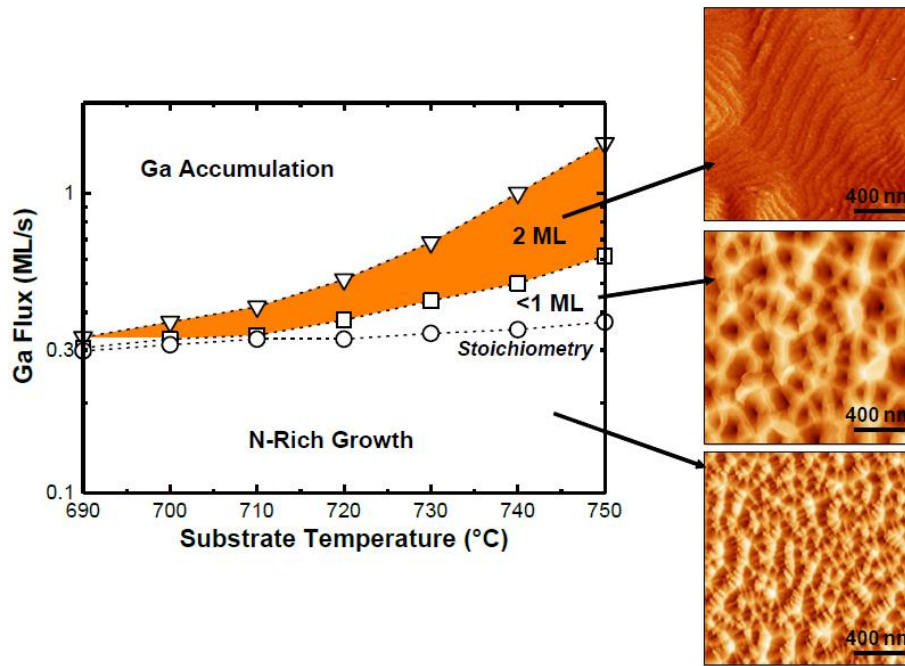


Figure 3.8: Ga coverage regimes as a function of both substrate temperature and impinging Ga flux. Insets show AFM images obtained in the different growth regimes. z-scales are 5 nm, 150 nm and 100 nm (top to bottom) (modified from ¹²⁷).

The presence of a Ga bilayer on the growth front reduces the (0001) surface energy thus favoring 2D growth. In this “2 ML” regime, two Ga layers are floating on top of the Ga-terminated GaN (0001) surface ^{125,125}, following the laterally-contracted Ga bilayer model¹²⁸, as shown in **Figure 3.9**.

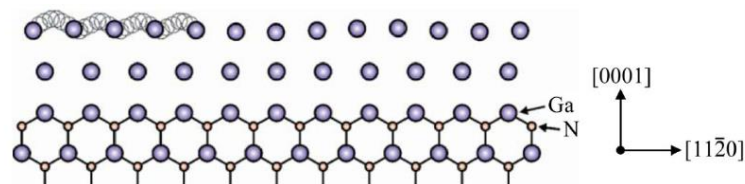


Figure 3.9: Schematic view of the laterally contracted Ga bilayer model. ¹²⁸

Although a large stability window for the Ga bilayer on the GaN surface can be obtained, the 2D growth of heterostructures requires identifying Φ_{Ga} at the transition between 2 ML of Ga coverage and Ga accumulation conditions, to prevent the formation of pits associated to threading dislocations^{129,130}.

3.1.2.2. Nanowires

In addition to the synthesis of planar layers, during my PhD I have also grown III-nitride NWs. In general, all the growth or fabrication approaches can be classified as “bottom-up” or “top-down”. As the name suggests, a top-down approach focuses on simply carving out a structure from a larger piece of material by means of lithographic techniques and etching methods. On the contrary, the bottom-up approaches construct NWs by simply combining constituent adatoms.

In this thesis, GaN NWs are grown by PAMBE without catalyst, under N-rich conditions on Si(111) substrates. Before introducing Si(111) into the PAMBE system, it was degreased using organic chemicals (dichloromethane or trichloromethane, acetone and methanol). In the growth chamber, the Si(111) substrate was heated to $\approx 880^\circ\text{C}$ for 5 min to thermally clean the surface.¹³¹ The cleaned surface was proved by the observation of a (7 \times 7) reconstruction, as illustrated in **Figure 3.10**, which appears at 600-850 $^\circ\text{C}$.

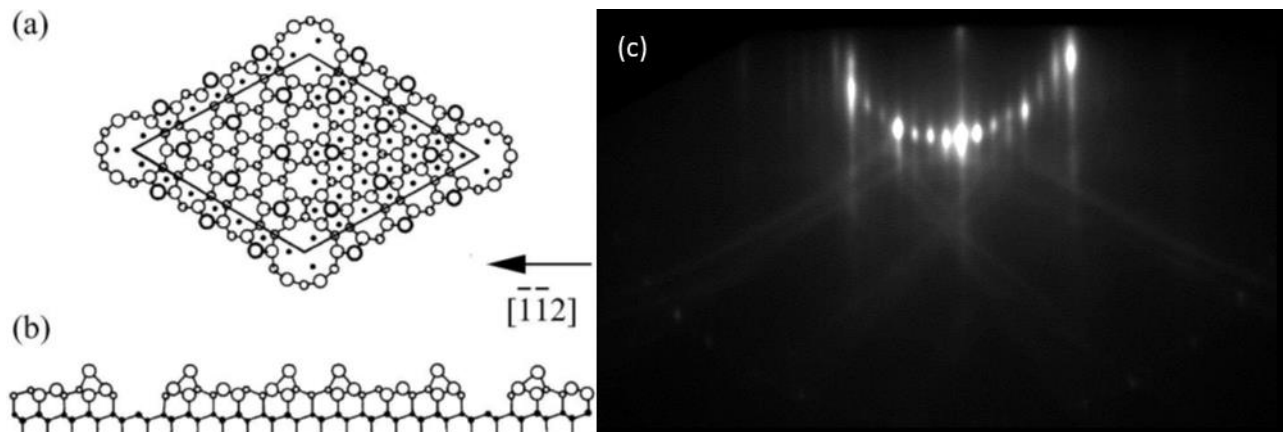


Figure 3.10: a) top view and (b) side view of the Si (111) (7 \times 7) reconstruction¹³¹. (c) 7 \times 7 surface reconstruction observed by RHEED along [-1-12] azimuth.

In order to obtain GaN NWs with improved verticality (avoiding the tilt as reported in previous studies^{132,133}) and without GaN undergrowth (parasitic 2D growth of GaN between the NWs^{134,135}), we used a two-step growth procedure for AlN^{136,137}. After baking the substrate, it was cooled down to 200 $^\circ\text{C}$, and we deposit 1.2 nm of AlN at stoichiometric conditions at this low temperature. At this point, the RHEED pattern evolves from the 7 \times 7 reconstruction to the pattern in **Figure 3.11(a)**. An 8-nm-thick AlN buffer layer was then grown at stoichiometric conditions at 670 $^\circ\text{C}$. This resulted in the characteristic 1 \times 1 RHEED pattern of stoichiometric AlN, in **Figure 3.11(b)**. GaN NWs were then grown at a substrate temperature around 780 $^\circ\text{C}$, for the Ga/N flux ratio = 0.25. The RHEED pattern during the growth was the spotty wurtzite pattern shown in **Figure 3.11(c)**.

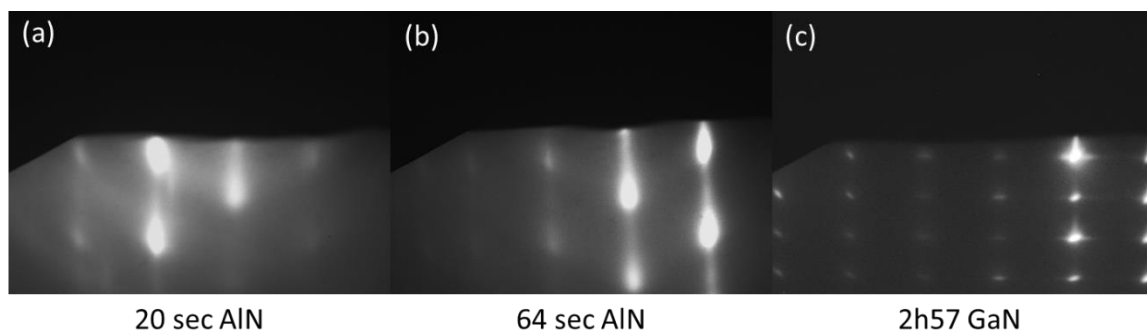


Figure 3.11: RHEED pattern in different steps of generation of GaN NWs grown on thin AlN layer on Si(111) substrate.

Within the NWs, $\text{Al}_x\text{Ga}_{1-x}\text{N}$ dots were grown using the same N-rich conditions as for the GaN base (Ga/N flux ratio = 0.25), and adding a flux of aluminium $\Phi_{\text{Al}} = x/v_G$, where x is the targeted Al mole fraction. The Al mole fraction in the dots was intentionally kept low, $x \leq 0.1$, in order to prevent deformations of the NW morphology and reduce the effects of alloy inhomogeneity, observed for $x \geq 0.3$ ¹³⁸. The AlN sections were grown at stoichiometry ($\Phi_{\text{Al}}/\Phi_{\text{N}} = 1$, with a growth rate $v_G = 450$ nm/h).

Figure 3.12 illustrates a growth diagram for different Ga impinging fluxes and substrate temperatures. The dotted line indicates the N flux, which is kept constant. The “no growth” regime is dominated by thermal decomposition and desorption of Ga from the surface. The regime (b) is where NW nucleation and growth occurs, which is indeed a narrow window. Within such a narrow window, the growth of NWs has to be optimized in terms of the size of the NW, degree of coalescence, and growth rate to obtain NWs according to the design requirements. At lower temperature and higher Ga fluxes (regime (a)), the growth becomes highly planar with heavily coalesced NWs at the boundary of the two regimes. The SEM images in **Figure 3.12** are representatives of the regimes.¹³⁹

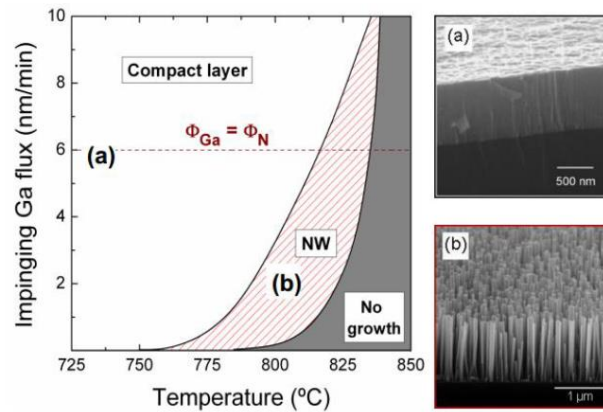


Figure 3.12: NW growth window with substrate temperature and Ga flux.¹⁴⁰

The NWs hence grown with PAMBE on Si (111) have been found to have wurtzite crystal structure with N polarity.¹⁴¹ Knowing the polarity of NWs is important, just like in the case of planar layers, since it influences various physicochemical properties, like incorporation of dopants, polarization fields and formation of defects.^{23, 58}

3.1.2.3. InGaN quantum dots

One of the specific features of group-III nitrides is that various binary compounds have crystalline lattice constants differing significantly from each other. For example, the lattice constant mismatch between GaN and AlN is 2.5% and 4.1% for a and c constants respectively, the mismatch between GaN and InN is much greater – 10.7% and 15.0%. The latter values are even comparable to the mismatch between the lattice constants of GaN and sapphire commonly used as the substrate for growth of group-III nitride epilayers. Such a large difference in the lattice constants results in a considerable strain in ternary nitrides. Even small additions of some group-III elements into a ternary compound changes its lattice constant remarkably.

On the other hand, InGaN exhibits an evident tendency to phase separation. **Figure 3.13** depicts a typical phase diagram in order to study the phase stability of $\text{In}_x\text{Ga}_{1-x}\text{N}$. More in detail it shows the spinodal and binodal curves. Spinodal decomposition occurs when one thermodynamic phase spontaneously separates into two phases. The spinodal curve (dashed line in **Figure 3.13**) in the phase diagram marks the equilibrium solubility limit. Below this curve, solid solution is unstable against decomposition into alloys with different compositions. For example, the diagram says that at 800 °C, a large decomposition tendency is seen for In content between 20% to 80%. The boundary of the unstable region, referred to as the binodal or coexistence curve is presented with a solid line in **Figure 3.13**. Inside the binodal curve is a region called the spinodal. The binodal and spinodal curves meet at the critical point. Above a certain critical temperature the alloy is stable for any composition, this happens when the temperature is critical ($T_{\text{crit}} = 1250$ °C). This is impossible to be achieved as it is found to exceed the melting point of InN. Therefore, as shown in the **Figure 3.13**, we find that unstable two-phase region exists for a wide range of In content. The predicted temperature and composition region for phase separation are consistent with the experimentally observed difficulties in achieving high In content ($x > 0.25$) InGaN.^{143–149} We must mention here that this diagram can show that an equilibrium model is useful for predicting the growth rate and composition compounds grown by MOCVD but for MBE growth we are always working out of equilibrium as the growth takes place in high vacuum conditions.

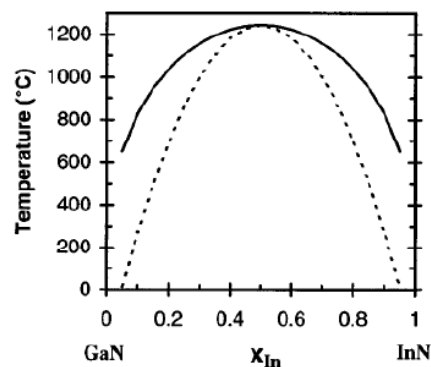


Figure 3.13: Binodal (solid) and spinodal (dashed) curves for the $\text{Ga}_{1-x}\text{In}_x\text{N}$ system, calculated assuming a constant average value for the solid phase interaction parameter.¹⁴³

In PAMBE, as the growth takes place out of thermodynamic equilibrium, the whole range of indium compositions is attainable. For this purpose, low growth temperatures are needed. For the growth of GaN, the substrate temperature in the range of 700-750 °C is calibrated by the Ga desorption time measured by RHEED.¹²⁹ However, for the incorporation of In, the substrate temperature should be reduced below 670 °C, i.e., below the temperature where the Ga desorption rate is significant. In this case, a temperature reference can be provided by the In desorption time from the GaN(0001) surface.¹⁵⁰

The incorporation of indium in InGaN nanostructures depends critically on the deposition temperature. It is hence a priority to establish the reference parameters that guarantee the reproducibility of the substrate temperature. With this purpose, we have analyzed the effect of In

desorption on the RHEED intensity. In this experiment, we expose the GaN surface to In during a certain time—long enough to attain a steady-state situation and the nitrogen cell was off throughout this process. When we close the In shutter, we observe a transient variation of the RHEED intensity with a characteristic shape.¹⁵¹

As an example, we are able to assess the gallium excess during the growth of GaN, and the indium excess on the surface of an InGaN layer, as the **Figure 3.14** presents.

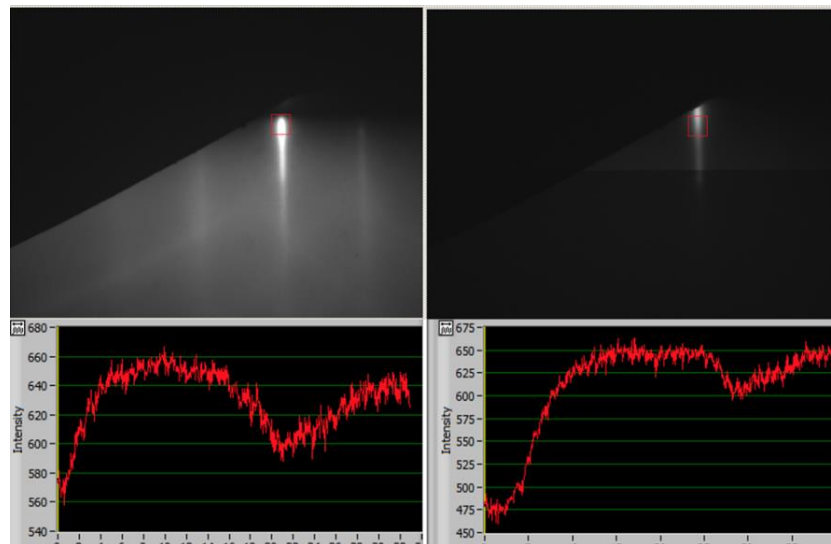


Figure 3.14: RHEED images during the growth of GaN (top left) and InGaN (top right). Measurement of the transient RHEED intensities during the metal desorption, after stopping the growth at $t = 0$ (bottom). The variation is due to the desorption of Ga (bottom left) or In (bottom right).

For the generation of InGaN QDs, we take advantage of the high lattice mismatch between GaN and InN. QDs are considered as the result of strain relaxation during the epitaxy of InGaN. For the Stranski-Krastanov mode, two-dimensional growth converts to three-dimensional growth to form QDs when the InGaN layer reaches a critical thickness, due to the strain accumulation originating from the lattice mismatch.

In our experiments, the active nitrogen flux was adjusted to provide a growth rate of 0.52 monolayers per second (ML/s) under metal-rich conditions. For the generation of InGaN QDs, the Ga flux was fixed at 30% of the stoichiometric value, and the In flux was tuned to have slightly metal-rich conditions, as described in refs.^{151,152}. The growth proceeds as schematically described in **Figure 3.15(a)**. The Stranski-Krastanov transition is due to an elastic relaxation process forced by the strong lattice mismatch [see **Figure 3.15(b)**], in spite of the slightly metal-rich atmosphere and the well-known surfactant effect of In, which promotes planar growth.¹²⁵ The InGaN growth time was 45 s, followed by a growth interruption of 15 s, during which roughening was observed in the RHEED pattern. For the deposition of the GaN barriers, the In shutter was closed and the Ga flux was fixed slightly above the stoichiometric value. Before the growth of the following QD layer, the Ga excess accumulated at the growth front is consumed with active nitrogen during 15 s. The substrate was rapidly cooled down

after the deposition of the last QD layer, to enable characterization of the QD shape and density by AFM.

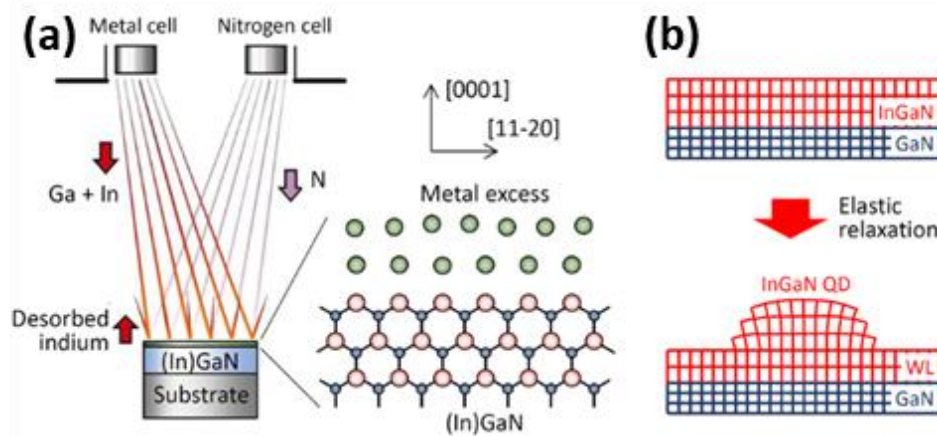


Figure 3.15: (a) Schematic description of the PAMBE growth process. Atomic flows of Ga, In and N imping the substrate surface. At the QD growth temperature, only indium is desorbed. The crystal grows in a metal rich environment, as described in the right side of the image. (b) Formation of InGaN QDs on GaN. The strong lattice mismatch leads to an elastic relaxation when the InGaN layer reaches a certain critical thickness. The resulting structure consists of InGaN islands (QDs) that are linked by a wetting layer (WL).

Figures 3.16 (a) and (b) compare AFM images of InGaN/GaN QDs and the 2D surface GaN surface, respectively.

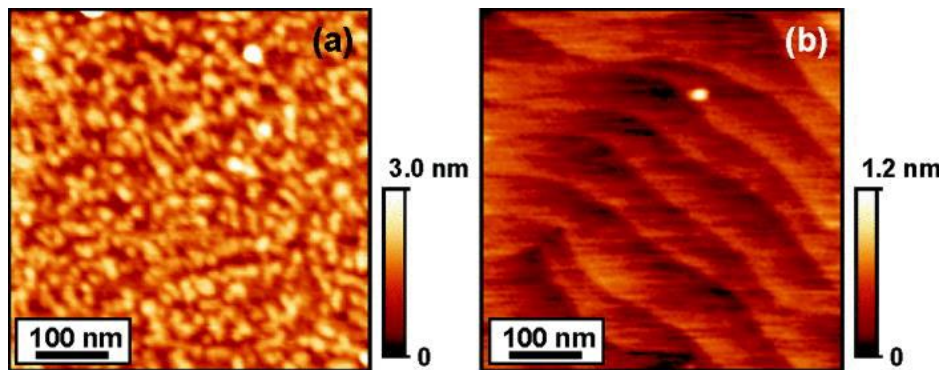


Figure 3.16: AFM images of (a) InGaN/GaN QDs as compared to (b) the planar GaN surface.¹⁵²

3.2. Photoluminescence

Photoluminescence (PL) spectroscopy is a method to measure the light emission induced by excitation and recombination of electron-hole pairs, as depicted in Figure 3.17.

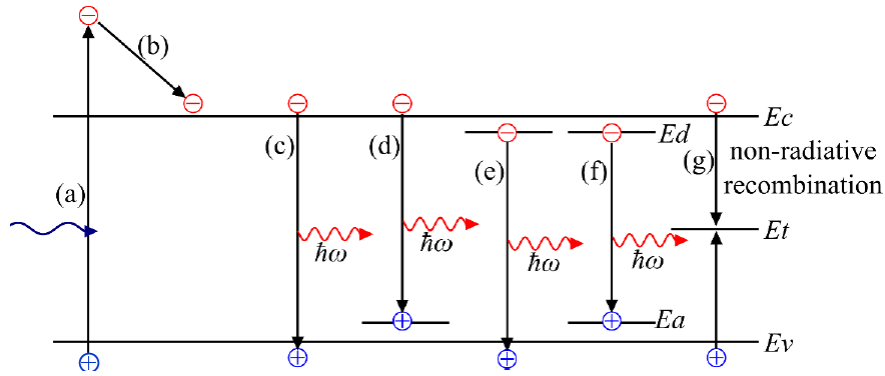


Figure 3.17: Schematic of carrier generation and different radiative and non-radiative recombination paths in semiconductors.

- I. Process-(a): The energy of the incoming photon must exceed the band gap energy (E_G) of semiconductor to allow material to absorb and create an electron-hole pair.
- II. Process-(b): The holes and electrons having excess excitation energy will thermally relax to the edges of conduction and valence band, respectively, by releasing the energy in the form of phonons, i.e. vibration modes of the crystal.
- III. Process-(c): The direct recombination occurs as the electron recombines to the hole in the valence band, giving a photon with specific energy (approximately equal to the E_G). In the case of III-nitrides, the electron and hole generally form an exciton, i.e. a particle resulting from their Coulombic attraction. The recombination energy of the exciton is slightly smaller than the semiconductor band gap, as it is reduced by the exciton binding energy $\approx 25 \text{ meV}$ ^{153,154}.
- IV. In addition to the band-to-band recombination, there are other processes, e.g. donor-to-band (process-(d), band-to-acceptor (process-(e)), and donor-acceptor pair recombination (process-(f)). These processes can emit photons, resulting from additional donor (E_d) and acceptor (E_a) bands, as illustrated in the band diagram. The E_d and E_a can either unintentionally appear because of impurities or lattice defects, or they can be intentionally generated by doping. Also, excitons can be attracted by these impurities, reducing their recombination energy (donor-bound exciton, acceptor-bound exciton)
- V. Process-(g): Non-radiative recombination to mid-gap levels (E_t) is another relaxation path that generally involves phonons. The origin of a mid-gap level might be generated by vacancies, dislocations, impurities, or surface dangling bonds.

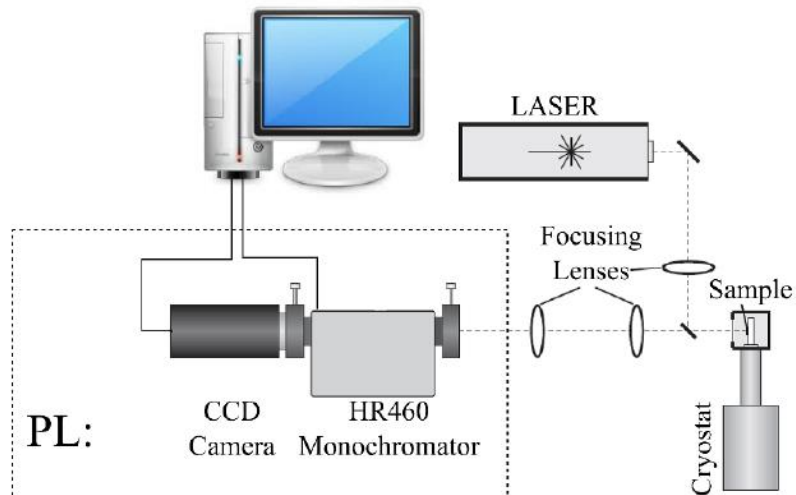


Figure 3.18: (Time-resolved) photoluminescence setup.

Figure 3.18 shows the setup available at CEA-IRIG, Grenoble used to study PL. PL measurements under continuous-wave excitation were obtained by pumping with a frequency-doubled solid-state laser ($\lambda = 488/2 = 244$ nm) focused on a spot with a diameter of ≈ 100 μm . The excitons at low temperatures and low excitation power densities occupy mostly the lowest localized states in the tail of the density of localized states and no significant thermal redistribution takes place¹⁵⁵. To explore the behavior of the heterostructures under operating conditions, we have measured PL under high injection using pulsed laser. PL measurements under pulsed excitation were obtained using a Nd-YAG laser (266 nm, 0.5 ns pulses, repetition rate of 8 kHz). For the NWs under study, an excitation power of 10 μW was used, unless mentioned otherwise. Typically, the planar samples were studied at higher power of 100 μW . In both cases, samples were mounted on a cold-finger of a He cryostat, and the PL emission was collected by a Jobin Yvon HR460 monochromator equipped with a UV-enhanced charge-coupled device (CCD) camera. Low temperature (5K) was employed to minimize thermally activated non-radiative recombination processes and thermal line broadening.

3.3. Cathodoluminescence

Cathodoluminescence refers to the emission of photons from a material excited with electron beam. The injected electrons generate electron-hole pairs via impact ionization. It is a technique for characterizing the optical and electronic properties of semiconductors at the nanoscale.¹⁵⁶ The CL equipment used in this work consists of a SEM coupled to an optical spectrometer, so that it is possible to perform SEM imaging while using the electron beam to excite the material and collect the resulting luminescence. The spatial resolution of CL is determined by the volume of the photon emission, which depends on the material and the operating parameters. The **Figure 3.19** presents different electron-matter interaction process. Elastic interactions give rise to backscattered electrons with energy comparable to those of incident electrons. Inelastic interactions give rise to X-ray and visible photon emissions and low energy electrons such as secondary electron and Auger.

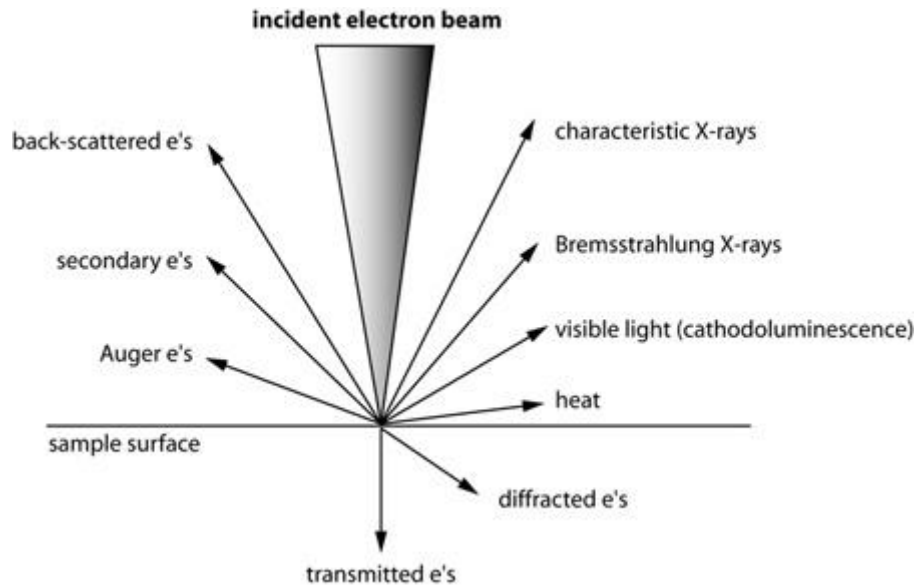


Figure 3.19: Types of interactions between electrons and sample. ¹⁵⁷

Inside the material, the spatial distribution of the electron trajectories is the result of inelastic and elastic interactions in the sample. When the electron beam hits an atom, the electrons give up their energy to an electron in the valence band producing an electron-hole pair, which can recombine emitting a photon. The spatial extent of the interaction depends on the energy of the incident beam and the material density. In our studies, it was calculated by Monte Carlo simulations using the Casino software that will be presented later in the manuscript.

In our CL setup, it is possible to obtain panchromatic or hyperspectral maps. CL panchromatic images are grey scale images [see **Figure 3.20(a)**] where the contrast corresponds to the intensity of light emitted for each pixel and collected by the detector (integrated intensity). In CL hyperspectral images [see **Figure 3.20(b)**], the electron beam scans across sample for small mapping (around hundreds of micrometer scale) and at each point acquire a complete spectrum. A spectrometer equipped with CCD detector is used to collect the light. The color-contrast image shows the energy (or wavelength) that corresponds to the higher emission intensity in each point.

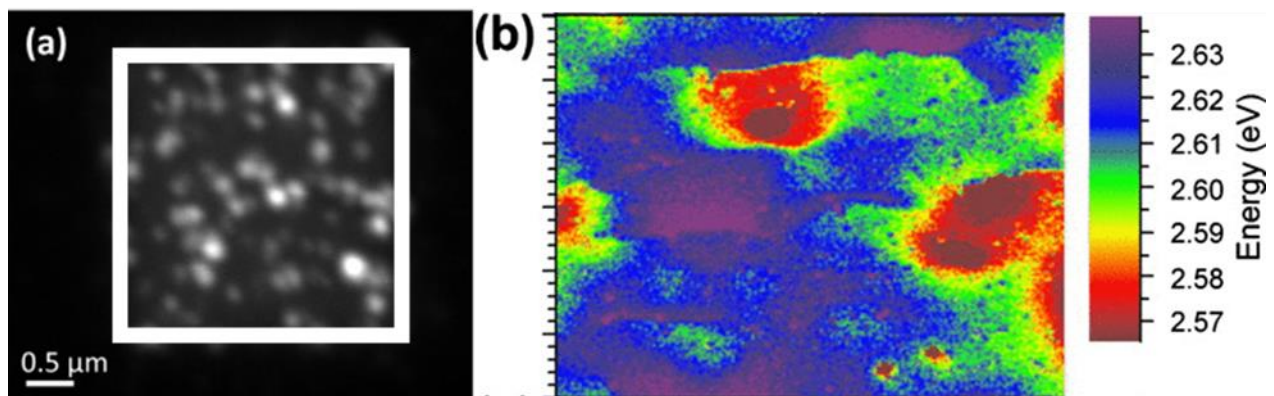


Figure 3.20: (a) Room temperature panchromatic cathodoluminescence image of sample QDisk-InGaN for an aperture of $3 \times 3 \mu\text{m}^2$. ¹⁵⁸ (b) CL hyperspectral information for a different sample of ten periods InGaN/GaN MQW. ¹⁵⁹

In this study, we used an Attolight CL model Rosa equipment combining an SEM and an optical spectrometer (CEA-Leti, Grenoble). The SEM cathode is a field emission electron gun (FEG). The electron beam voltage can be set between 3 keV and 10 keV for a probe size of less than 3 nm in diameter. The probe current can be modulated between 0.1 and 100 nA thanks to the two electromagnetic lenses and the variable aperture (from 25 to 100 μm) that make up the column of the electron microscope. In our study, CL mapping was performed with a beam current ≈ 5 nA. Attolight's equipment has a spectrometer mounted along the axis of the electron microscope for a collection of photons as shown in **Figure 3.21**. This makes the optical collection more efficient and more stable. The light collection system is composed of a large concave collection mirror and a small convex mirror placed in the axis of the electron column. The field of view of this optical spectrometer is in the order of 300 μm . The optical signal extracted from the SEM is analyzed by a spectrophotometer with a focal length of 320 mm equipped with an array of 150 lines / mm blazed at 500 nm and detected by a CCD camera (charge-coupled device) in the range spectral $300 \text{ nm} < \lambda < 1200 \text{ nm}$. The sample holder is a cryostat that can work at temperatures between 4 K and 350 K.

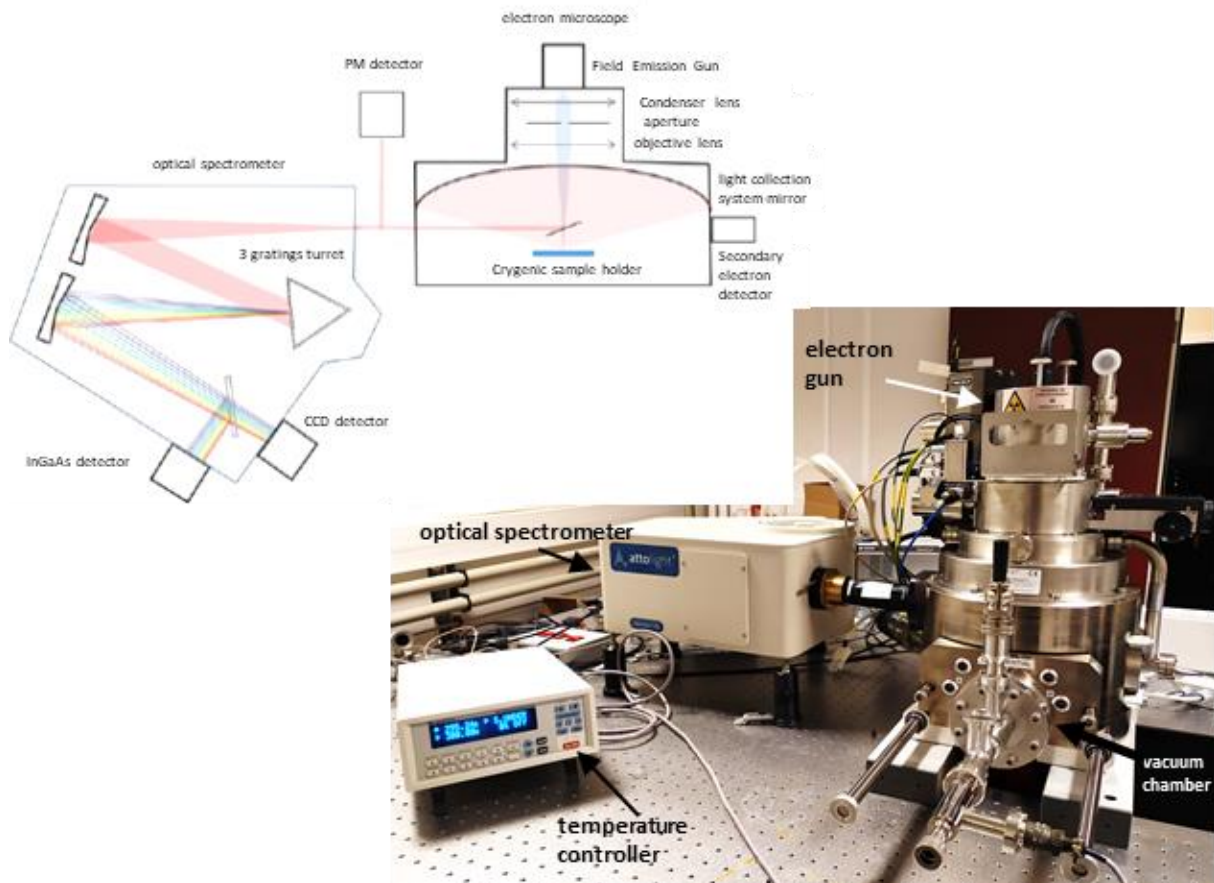


Figure 3.21: Simplified diagram and image of cathodoluminescence by the equipment manufacturer Attolight.¹⁶⁰

3.4. X-ray diffraction

X-ray diffraction analysis (XRD) is a technique used to determine the crystallographic structure of a material. In our study, we characterize the period of our QD superlattices (SLs), to estimate the strain state of the layers, as well as to assess the crystalline quality of our samples from the broadening of the reflections. As x-ray excitation, we used the $k_{\alpha 1}$ emission line of Cu ($\lambda_{XRD} = 0.154056$ nm). In this work, we measured $\theta - 2\theta$ scans and reciprocal space maps.

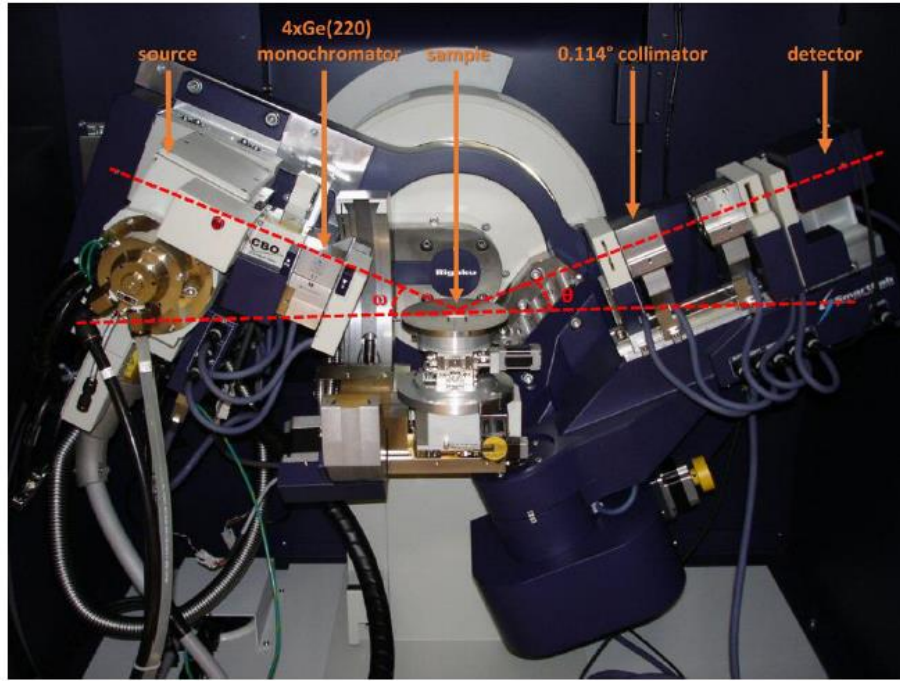


Figure 3.22: The Rigaku Smartlab system in the used configuration.

Primarily we used the XRD system Rigaku Smartlab x-ray diffractometer (CEA-IRIG, Grenoble) presented in **Figure 3.22**. The x-ray source is an evacuated tube in which electrons are emitted from a heated tungsten filament and accelerated by an electric potential (≈ 40 kV) to finally impinge on a Cu target. The x-ray beam coming out from the source is reflected and converted into a parallel beam by a parabolic mirror. A beam of parallel (0.01° divergence) and monochromatic x-rays is incident on a crystal at the angle ω_i , which is the angle between the sample plane and the incident beam. A highly parallel and monochromatic incident x-ray beam is achieved by using one or two monochromators each consisting of two Ge (220) monocrystals. This results in an x-ray beam with a wavelength spread $\Delta\lambda_{XRD}/\lambda_{XRD} = 2.2 \times 10^{-5}$ and divergence, $\Delta\theta = 0.0033^\circ$.

To minimize the background noise, we place the sample on a monocrystalline Si plate. However, the sample surface may not correspond to the epitaxial planes due to the substrate miscue and hence we need to align the epitaxial plane with the optical axis of the setup by using possible angular rotation mechanisms of the sample stage and detectors available in the instrument.

To obtain high-resolution XRD (HR-XRD), a 0.114° collimator or a Ge(220)x2 analyzer is placed

between the sample and the detector. It improves the angular precision of the diffracted beam ($<0.001^\circ$) and is used to measure all the planar samples. In this configuration, the direct beam intensity is higher than 10^6 counts per second (cps) and the noise is about 1 cps. However, NW measurements were made in an open detector configuration; which means that the detectors were directly exposed. This was done because of the scattering induced by the NWs which leads to broadening of the reflections, leaving the high resolution redundant.

The superlattice period P_{SL} can be extracted from the angular separation of two SL satellites in the θ - 2θ scans:

$$P_{SL} = \frac{\pm n \lambda_{XRD}}{2(\sin\theta_{\pm n} - \sin\theta_0)} \quad (3.1)$$

where θ_0 and $\theta_{\pm n}$ are the zero-order and $\pm n$ -order SL satellites, respectively. Information on the mosaicity and crystalline quality of planar structures were extracted from the θ -scans. Finally, evaluation of the strain state of the layers required a combination of θ - 2θ scans of symmetric reflections and reciprocal space maps of asymmetric reflections, to extract the various lattice parameters using Bragg's law.

3.5. Atomic force microscopy

AFM is a characterization technique that allows us to examine the surface morphology of the samples. AFM measurements were performed using a Dimension Icon AFM system operated in the tapping mode using Bruker TESPA-V2 tips and the images were processed using WSxM free software (CEA-IRIG, Grenoble).

AFM can be used to characterize the surface of various types of samples, i.e. conductors, semiconductors, and insulators. The schematics of a typical AFM setup is described in **Figure 3.23**.

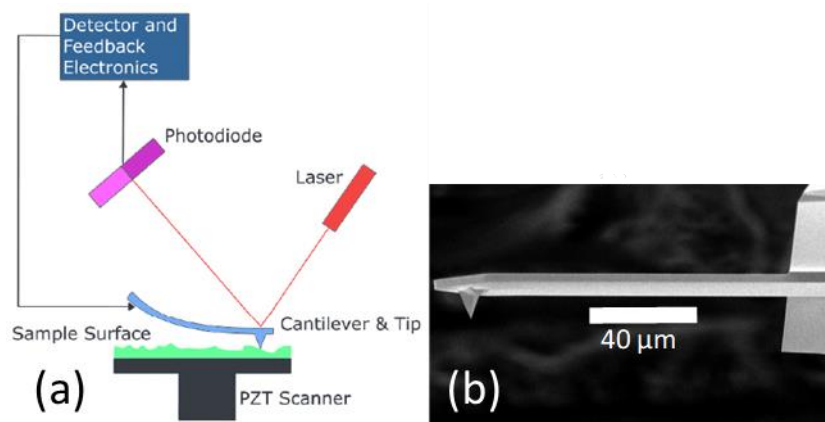


Figure 3.23: (a) Schematics of an AFM system, (b) AFM cantilever.¹⁶¹

The bending of the cantilever, proportional to the force on the cantilever, is measured by the

deviation of a laser beam position on the detector. The applied force is kept constant thanks to feedback circuit by changing the tip-sample distance using piezoelectric actuator driving the lateral movement of the measured sample. The AFM cantilever is illustrated in **Figure 3.23(b)**. At the edge, there is the tip, which is a couple of microns long, less than 100 Å in diameter and 10-15 μm high. The AFM tip and cantilever are fabricated from Si. The type and magnitude of the interaction force between the tip and the sample directly depend on the distance between the tip and the sample.¹⁶² Thus, the variation of the interaction force between the sample and the tip mirrors the variation of the surface height.

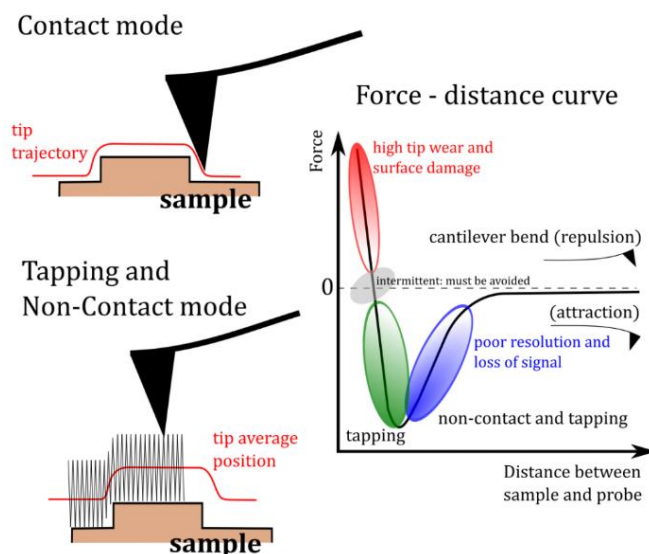


Figure 3.24: Force vs. tip-to-sample distance in AFM operation.¹⁶³

The AFM can be operated in three different modes (**Figure 3.24**), which are contact, non-contact, or tapping mode as described below:

- I. **Contact mode:** In this mode, the cantilever is kept only few ångströms above the surface. The measurement is done by keeping the repulsive force constant throughout the measurement. In this configuration, the presence of frictional and adhesive forces can damage the sample surface or the AFM tip, and distort the measured image.
- II. **Non-contact mode:** In this mode, the cantilever can oscillate with large amplitudes near the tip resonance frequency. The interaction force between the surface and the tip in this mode is attractive Van der Waals force which is a force occurring when the distance between the sample and the tip is in the order of ten to hundreds of ångström. The non-contact mode measurement typically provides low resolution and the measured image can be hampered by the natural oscillations. However, it is very useful for measurements of soft or liquid morphologies.
- III. **Tapping mode:** This mode combines the advantages of the contact and non-contact mode. In this mode, the force between the surface and the tip is kept near zero to avoid the surface and tip damage problems, occurring in the contact-mode and to provide better resolution than that performed by the non-contact mode. This mode is the mode that was used to measure all the samples in this work. In tapping mode, the tip operates near its resonant frequency, ω_0 , typically

in the 100-300 kHz range. The high resonance frequency allows us to decouple the tip oscillating frequency from the low-noise frequency induced by the mechanical vibrations. ω_0 is defined with:

$$\omega_0 = \sqrt{\frac{\kappa}{m}} \quad (3.2)$$

where k and m are the force constant and the mass of the tip respectively.

When the tip is close to the surface less than 100 \AA , it is exposed to Van der Waals interactions. Derivative of the vertical components F of the forces acting on the probe are detected. The orientation of the z -axis (considering the displacement of the tip apex above the contact point to a certain height z) is defined as being perpendicular to the sample surface.¹⁶⁴ The z -gradient of the electrostatic force, $\partial F/\partial z$, affects to the resonance frequency of the tip, which is:

$$\omega = \omega_0 \sqrt{1 - \frac{1}{k} \frac{\partial F}{\partial z}} \quad (3.3)$$

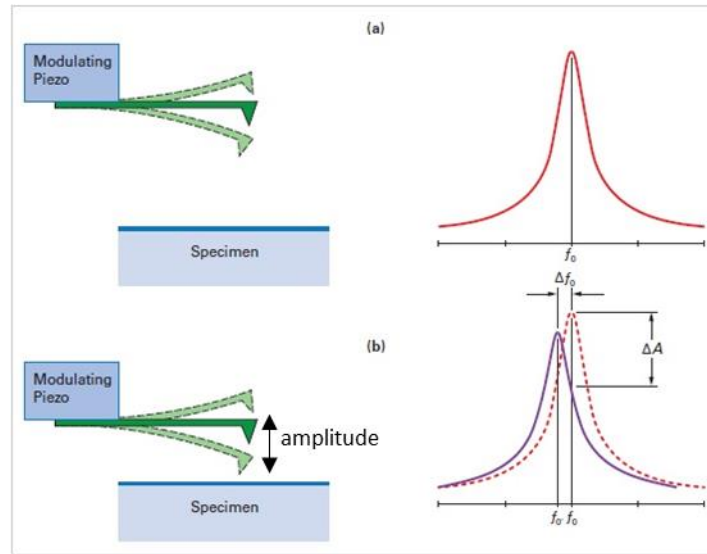


Figure 3.25: Resonance curve of a tapping mode cantilever above and close to the surface. Note that the resonance shifts to lower frequencies and exhibits a drop in amplitude.¹⁶⁵

Working in tapping mode, the tip-sample distance or better the oscillating amplitude is kept constant using a piezo-electronic actuator and a PID regulator to minimize the force gradient, $\frac{\partial F}{\partial z}$. The minimal detectable force gradient is given by¹⁶⁶:

$$\frac{\partial F}{\partial z} = \frac{1}{A} \sqrt{\frac{4 B \kappa k_B T}{Q \omega_0}} \quad (3.4)$$

Here, k_B is Boltzmann constant, A is the root mean square oscillation amplitude (**Figure 3.25**), B is the detection bandwidth, and $Q = \Delta\omega/\omega_0$ is the quality factor of the resonance. Hence, there

are four main parameters to optimize the sensitivity. The force constant (κ) should be small which requires the minimization of the cantilever mass while the quality factor of the resonance (Q) should be high. Measuring at low temperature is usually preferred. In addition, the oscillation amplitude (A) which is limited by the experimental setup should be large.

The spatial resolution of AFM measurement depends on the shape and size of the tip. The actual tip, which is not ideally sharp, might generate the effect called tip-evolution differentiating consequently the measured image and the real topology of the object. The convolution occurred when the radius of the tip is comparable with or larger than the size of measured object.¹⁶⁷

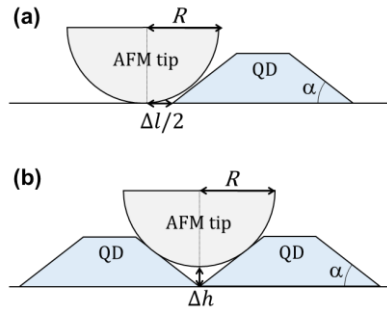


Figure 3.26: (a) Increase of lateral island size with respect to the real island size in the case of a low density of islands. (b) Decrease of the island height when islands are closer to each other than the tip diameter.

In the case of well-separated islands presented in **Figure 3.26(a)**, the measurement of the height is precise, but the measurement of the diameter is larger by Δl , with:

$$\Delta l = 2R \left(\frac{1 - \cos \alpha}{\sin \alpha} \right) \quad (3.5)$$

In the case of close-packed QDs, the measurement of the QD diameter would be correct, but the tip would not be able to reach the WL between two QDs as shown in **Figure 3.26(b)**. The associated error in the measurement of the QD height is:

$$\Delta h = -R \left(\frac{1 - \cos \alpha}{\cos \alpha} \right) \quad (3.6)$$

The accurate convolution of the tip is hard to compensate since it would require a precise knowledge of the tip shape. Furthermore, other factors affecting the resolution are the non-linear response of the piezo-scanner and environmental noise interference.

3.6. Dual scanning electron microscopy / focused ion beam

To be able to analyze the sample in the APT, it is necessary to prepare it in the shape of a needle. This can be done by milling the sample using FIB system. The preparation by FIB is carried out in FIB-SEM type equipment combining an SEM column for observation and an FIB column allowing physical etching

using a gallium beam. The instruments available in the PFNC at CEA-Leti, Grenoble are an FEI Strata DualBeam 400S microscope and an FEI 450 Helios microscope. They are both composed of a source of Ga^+ ions for engraving, inclined at 52° from the SEM column. The electron and ion beams combined allow simultaneous imaging and etching of the targeted area of the sample¹⁶⁸. Ga^+ ions are accelerated in a voltage range between 2 kV and 30 kV and pass through a system of lenses and diaphragms defining the size and the focus of the beam. The FIB-SEM system is presented in **Figure 3.27**.

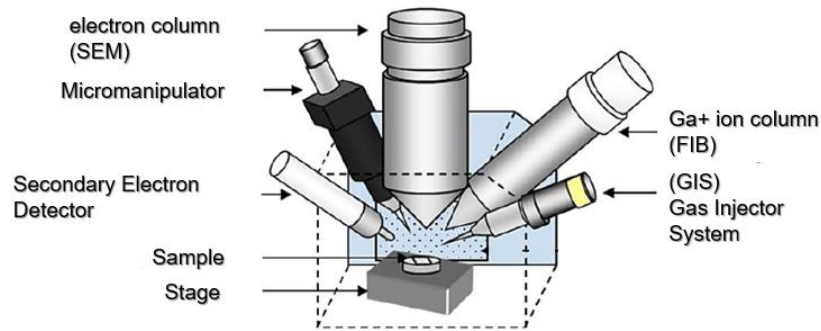


Figure 3.27: Simplified diagram of the FIB-SEM.(modified from¹⁶⁹)

The FIB can be used for^{170,171}:

- I. deposition (protective layers, contacts e.g.: platinum, tungsten, insulator, etc.),
- II. micro(nano)-milling for sample preparation, and
- III. imaging the surface of the sample.

The FIB can operate over a wide range of currents between a few pA and several nA, which can define the beam diameter from 5 nm to $0.5 \mu\text{m}$ and thus determines the ion beam accuracy. Low current allows imaging the surface of the sample. On the contrary, working with high current, the material is etched. The choice of parameters is therefore made as a function of the speed, the engraving precision and the desired quality.

The exposition of a specimen to FIB can produce Ga implantation (low for low current and voltage but the high for high voltage, even if the current is not so high), creating some nm thick amorphous layer. The thickness of the damaged layers strongly depends on both the material properties and the Ga^+ ion energy. The use of a low energy ion beam for the final steps of FIB preparation is recommended because it reduces considerably the thickness of the damaged layer.¹⁷² The presence of amorphous layer enhances the light absorption¹⁷³. FIB damaged surfaces may significantly increase non-radiative recombination processes, and decrease the radiative processes. For these reasons, we paid particular attention to the combination of voltage and current that should be used during FIB specimen preparation.

During my thesis, we have developed a protocol that can preserve the optical and structural properties of our samples. The general steps for tip-shape specimen milling are presented schematically on **Figure 3.28**¹⁷⁴.

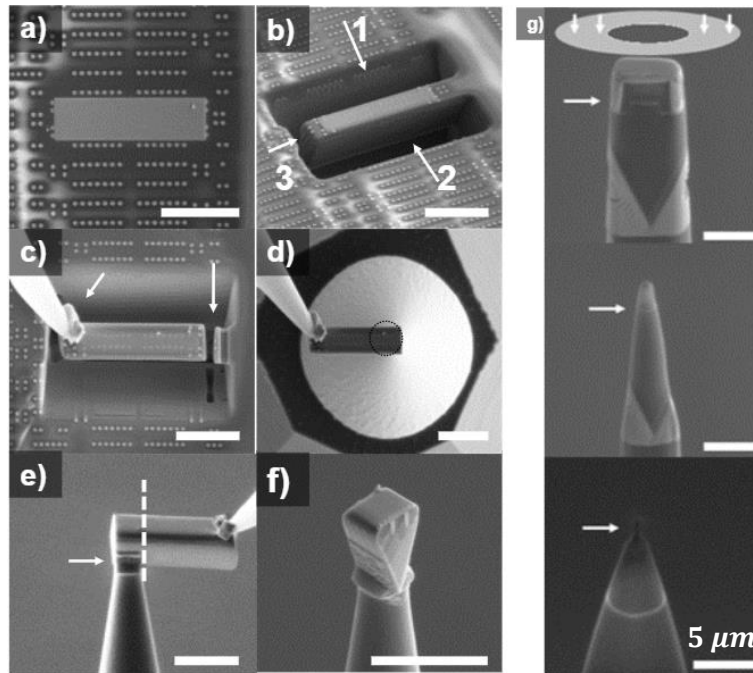


Figure 3.28: Specimen preparation and general FIB Lift-out method described in the text. All scale bars are 5 μm .¹⁷⁴

- a) **Protection of the surface** (Figure 3.28 a): Etching by a Ga^+ ion beam generates a damaged and amorphous layer under the surface, which is due to the formation of defects. In order to avoid the implantation of Ga^+ ions in the area of interest, it is essential to protect the surface by a deposit which is made in two steps :
- A. First deposition of Pt by Precision Etching and Coating System (PECS), getting as a result around 150 nm protective layer.
 - B. Secondary deposition of 300-nm-thick protective layer of Pt in Helios (or W in Strata). FIB (Ga^+ ions) induced deposition of platinum (or Tungsten) from a precursor gas of (methylcyclopentadienyl)trimethyl platinum [$\text{C}_9\text{H}_{17}\text{Pt}$] (or Tungsten hexacarbonyl [$\text{W}(\text{CO})_6$]) using GIS (Gas Injection System) inserted in the SEM/FIB chamber. The nature of the deposited material, Pt or W, depends on which machine we work: in the FEI Strata DualBeam 400S microscope the deposition is W, and in the FEI Helios microscope, it is Pt.
- b) **Cut-out** (Figure 3.28 b): The material is removed around three sides (arrows) of the region of interest (ROI), as well as underneath, to produce a long wedge of material containing the ROI
- c) **Lift-Out** (Figure 3.28 c): The first steps of preparation require the extraction of a prism from the whole sample. This technique is commonly called "Lift-Out". The wedge of 20 μm long is removed by first attaching the micromanipulator to the end of the wedge (left arrow) and then cutting the wedge free from the substrate (right arrow).
- d) **Wedge transfer** (Figure 3.28 d): The wedge is transferred to a carrier microtip (black dashed circle indicates location of flat 2 μm tip for APT analysis) and attached with FIB Pt or W deposition.

- e) The wedge is cut free of the carrier tip (dashed line) containing the active region as indicated by the arrow (**Figure 3.28 e**).
- f) The final mounted wedge-section is shown in **Figure 3.28 f**).
- g) Finally, standard annular milling is performed at 15 kV in the Strata FIB or 16 kV at the Helios FIB, followed by a 2 kV milling-polishing step. This step was done at around 52° to have the FIB column along the axe of the tip as small arrows indicate (evolution described in **Figure 3.28 g**). The horizontal arrow specifies the position of the active region.

To have an idea of combination of voltage and current that we use during all these steps, for imaging by FIB we used 16 kV/11 pA in Helios (15 kV in Strata) and by SEM we use 3 kV/100 pA in Helios (5 kV /0.4 nA in Strata).

An APT analysis requires the preparation of the sample in the form of a needle with a radius of curvature less than 50 nm. Therefore, the final step consists of annular milling by using masks placed in the center of the area of interest. During the process, the internal radius of the mask is reduced and the ion etching current is being decreased as soon as the tip becomes thinner and thinner. The final result is a tip with a radius of curvature <50 nm. It is then polished at a voltage of 2 kV in order to minimize the amorphous layer and implantation due to Ga⁺ ions. It is important to pay attention in the final step because the thinner the tip, the less visible the contrasts between deposit and area of interest. It is essential to fully mill the deposited protective layer before the APT experiment because there is a difference in evaporation fields between these elements (Pt/W) and InGaN alloy that could cause breakage of the tip. On the contrary, milling beyond the metal deposit risks destroying the area of interest, if it is directly below the surface, and induces larger ion implantation.

3.7. Atom probe Tomography

Specimens consisting in needle shaped tips can be investigated by APT, allowing three-dimensional chemical and compositional reconstruction of the elemental distribution. This equipment, available at CEA-Leti in Grenoble, allows precise chemical analysis. With a focus on correlative microscopy of nitrides for visible LEDs and single-photon emitters, we present an advanced version of La-APT made by the group GPM in the University of Rouen. This system offers the possibility to record the variation of the micro-photoluminescence (μ PL) spectrum of the specimen during its evaporation. This innovative approach allows gaining additional insight into the origin of the spectral emission and its association with structural/features. The principle and main advantages of all these techniques are extensively discussed. Finally, an approach for the optimization of the three-dimensional APT reconstruction is proposed.

3.7.1. Laser-assisted APT

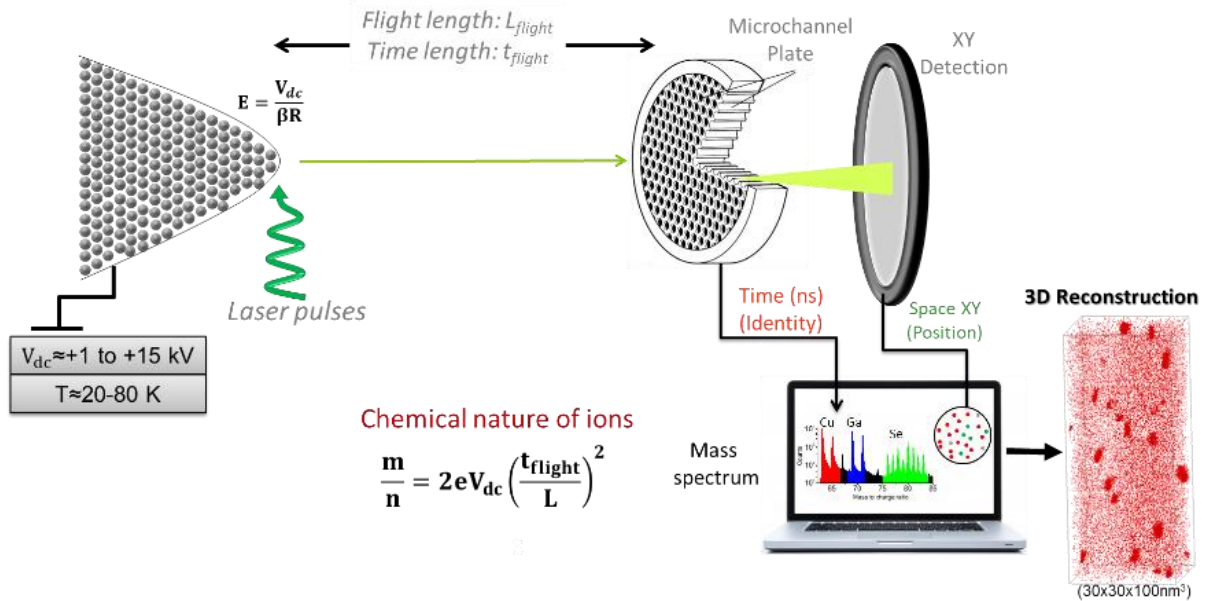


Figure 3.29: Diagram of electron field evaporation in APT.

The APT system is an analytical microscope allowing access to three-dimensional chemical mapping of atoms (around 0.1-0.3nm resolution in depth and 0.3-0.5nm laterally¹⁷⁵). This technique is based on ionization and evaporation by field effect of the atoms located at the end of the sample, prepared in the form of a tip with a radius of curvature $R < 50$ nm. The tip is placed in an ultra-vacuum chamber (10^{-11} Bar) and is cooled down between 20 K and 80 K, as shown in **Figure 3.29**. It is biased at a high DC electric voltage, V_{DC} , in the range of 1 to 15 kV. The very small radius of the tip and the high voltage induce a very high electrostatic field (tens of V/nm) at the tip surface, expressed by:

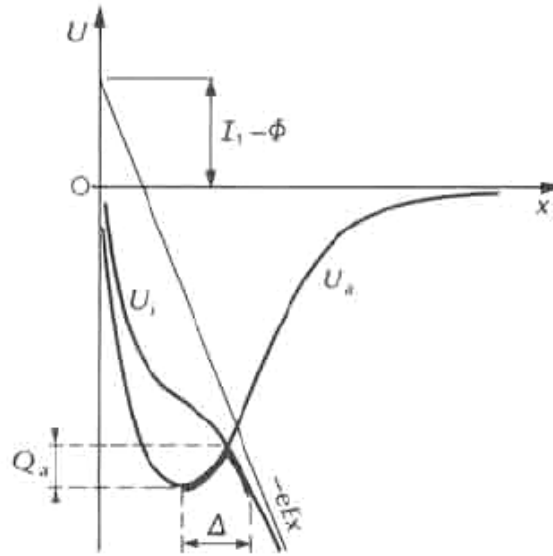
$$E = \frac{V_{DC}}{\beta R} \quad (3.7)$$

where β is a factor taking into account the shape of the tip which is between 2 and 8.

The evaporation rate is expressed by Arrhenius law:

$$v(E, T) = v_0 \exp(-Q_a/k_B T) \quad (3.8)$$

where Q_a is the activation energy, v_0 vibration frequency of the atoms of the surface, k_B is the Boltzmann constant, T is the absolute temperature and E the electric field. **Figure 3.30** presents the diagram of the potential energy of a neutral atom (U_a) and an ion (U_i) in the presence of an electric field E .



I_1 : Energy of the first ionization.

ϕ : Work function.

Q_a, Δ : height and width of the activation energy shown in bold.

Figure 3.30: Potential energy curve of a neutral atom (U_a) and an ion (U_i) under electric field E .¹⁷⁶

In the case of a semiconductor material, the evaporation of the ions is triggered by a femtosecond laser pulse. The electric field is maintained below the field evaporation. Atoms can then cross their potential barrier and be evaporated in the form of ions thanks to the thermal input of the laser pulses.

The laser pulses also trigger the chronometer for the measurement of the ion's time of flight. During the laser-assisted field evaporation of a tip, positive charged ions are generated and accelerated towards the detector. The Position Sensitive Detector (PSD) consists of a stack of two MCPs (MicroChannel Plates) and an advanced Delay Line Detector (aDL) that improves the detection of multiple ion events^{53,177}. The design of this aDL has improved the multihit detection performances of the APT system. With the help of fast digitizers, the aDL has the ability to decompose output signals, potentially overlapped during multihit events, into individual signals. This is possible thanks to the electronic system used to extract the timing information from the analog signals. The idea behind the aDL process is to use a signal shape recognition algorithm in order to decompose step by step output signals potentially made of overlapped signals as illustrated in **Figure 3.31**. This applies a filtering method to increase the signal-to-noise ratio and then a deconvolution method allows extracting the individual analog signals which composed the filtered signal. The timing information of each signal is then extracted and the positions (x,y) of ion impacts are calculated. This approach decreases the error bar of the initial position up to 0.1 nm on the tip surface. As a consequence, the detection of multiple ion events is strongly improved.

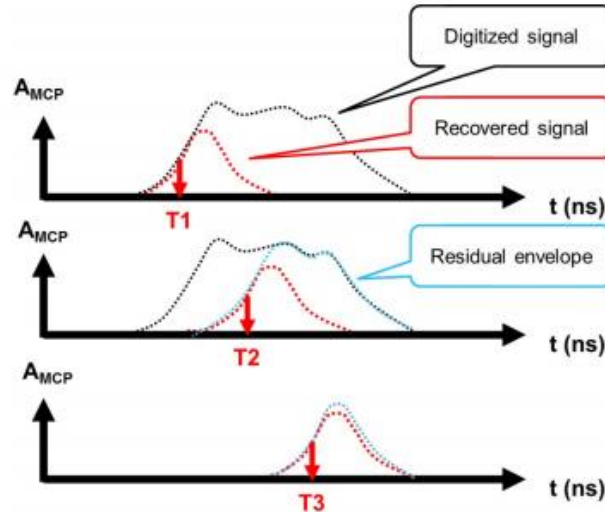


Figure 3.31: aDLD operating process. With the help of a reference signal, the envelope of an acquired signal made of overlapped signals can be decomposed into individual signals.¹⁷⁸

The DLD is composed of two delay lines oriented at 90°, labeled X and Y as it is shown in the **Figure 3.32**. The X and Y coordinates of the ion impacts on the PSD give the initial position of the ions at the surface of the tip. The depth is calculated thanks to the total number of collected ions. The chemical nature of the ions is determined by the time of flight between laser pulses and the PSD giving the m/n (mass over charge) ratio.

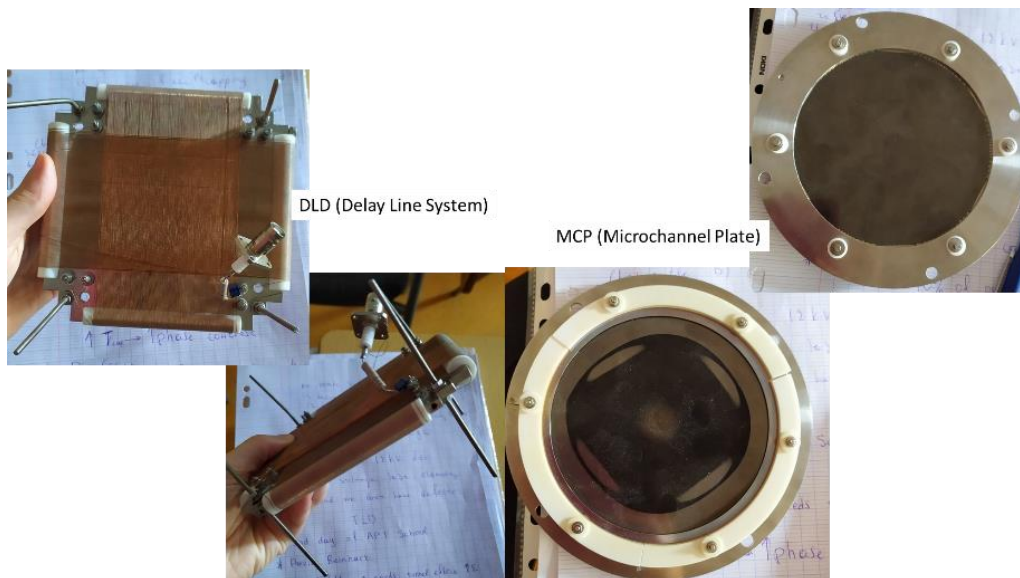


Figure 3.32: Images of the detection system used in APT system.

The initial energy of an ion emitted from the tip surface is equal to the electric potential energy neV_{DC} , where ne is the ion electric charge and V_{DC} is the DC voltage applied to the tip. As an ion reaches the detector, its final energy corresponds to the kinetic energy $\frac{1}{2}mv^2$, where m is the ion mass and $v = \frac{L}{t}$ is the velocity. L represents the flight path, which as a first approximation corresponds to the distance between the tip and the PSD, and t is the Time Of Flight (TOF) interval of the ion ($t = L/v$).

The mass-to-charge ratio m/n of ions is derived from the conservation energy $\frac{1}{2}mv^2 = neV_{DC}$:

$$\frac{m}{n} = 2eV_{DC} \left(\frac{t_{flight}}{L} \right)^2 \quad (3.9)$$

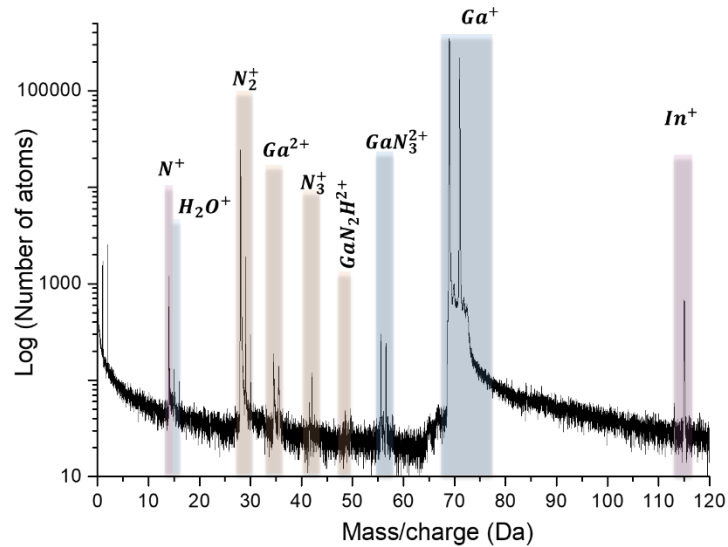


Figure 3.33: Mass spectrum of InGaN QDs sample.

Figure 3.33 shows the mass spectrum obtained for a sample containing InGaN/GaN QDs, where different elements and their isotopes are identified, as well as the molecular ions in different state-of-charge. It gives the number of detected ions as a function of each measured mass to charge ratio. An element or one of its isotopes can be associated to each peak. The identification of the chemical nature of the elements detected is obtained by the time-of-flight mass spectrometry. Thanks to the equation (3.9) we can obtain the mass spectra.



Figure 3.34: CAMECA FlexTAP APT system available in the NanoCharacterisation PlatForm (PFNC).

The **Figure 3.34** presents the CAMECA FlexTAP system (Flexible tomographic atom probe), equipped with an advanced delay-line-detector (aDL) available in the NanoCharacterisation PlatForm (PFNC) at CEA-Leti in Grenoble. FlexTAP allows analysis with three laser wavelengths (IR, Green and

UV) as a function of materials and is equipped with diaphragms combined to electrostatic lenses responsible for a non-linear variable flight path. According to the transfer function of FlexTAP, best mass resolution are obtained for small collection angles. The minimal and maximal field of view configuration of FlexTAP are 8° and 30° , respectively.

The APT analysis was performed at 50 K with a UV femtosecond laser emitting at 343 nm having a pulse energy of 0.2 nJ, laser spot size $\approx 10 \mu\text{m}$, and repetition rate of 50 kHz. The field of view was set to 15° . In this field of view we can only detect a small part of the evaporated specimen but we have better mass resolution in comparison with higher field of view.

3.7.2. Photonic atom probe

Laser enhanced field evaporation of surface atoms in La-APT can simultaneously excite photoluminescence in semiconductor or insulating specimens. At the University of Rouen, an atom probe equipped with appropriate focalization and collection optics has been coupled with an in-situ μPL bench that can be operated during APT analysis. This so-called “Photonic Atom Probe” instrument can carry out La-APT and μPL simultaneously, allowing us to correlate the variation of the photoluminescence signal with the nanometric scale volumes of the tip evaporated during APT. In principle, the emission of single quantum light emitters such as single QWs or QDs can be revealed.

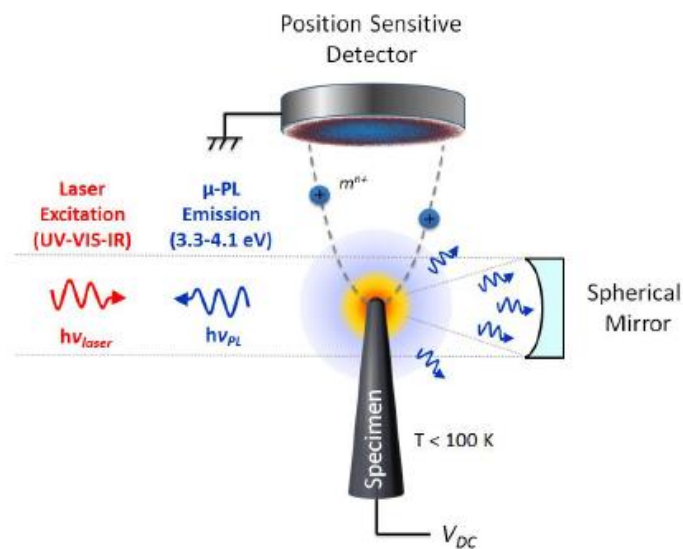


Figure 3.35: Schematic representation of the La-APT/ μPL coupled in-situ.¹⁷⁹

Figure 3.35 shows a schematic representation of the system combining μPL and La-APT. A spherical mirror was introduced inside the analysis chamber to collect the optical emission.⁶⁰ The tip is located inside the APT chamber at the focal point of the mirror. The configuration described in **Figure 3.36** allows focusing the laser on the tip, and collecting the μPL emission using a spectrometer in connection with either a CCD or a streak camera.

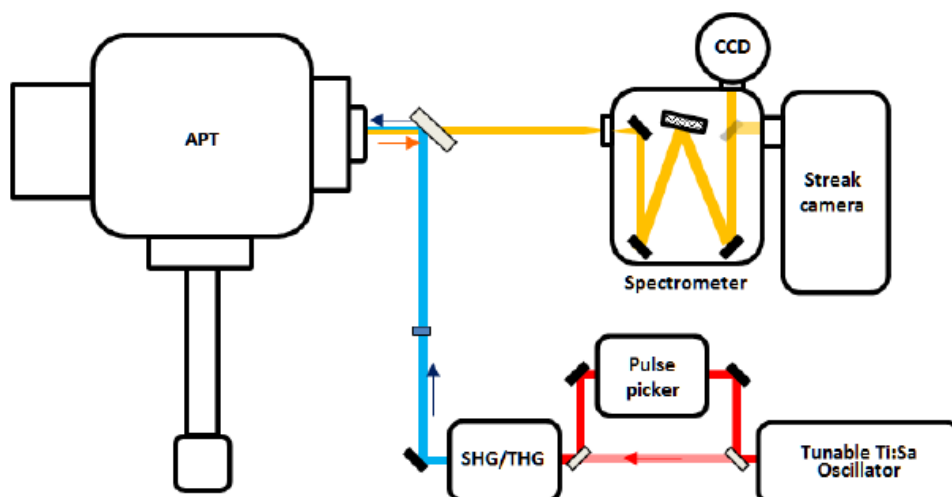


Figure 3.36: Schematic representation of the Photonic Atom Probe setup.

The Photonic Atom Probe instrument operates at frequencies up to 500 kHz with 150 fs laser pulses that are tunable in energy in a large spectral range (spanning from deep UV to near IR). For our experiments, we used a UV laser line at 260 nm focused on a spot with a diameter around 1.5 μm . The system is equipped with an 8-cm-diameter multichannel plate/delay line detector (MCP/DLD). The flight length is around 10 cm, corresponding to a field of view of 22° on the detector and of 35° on the tip. Such detection system is able to perform analysis using laser repetition frequency up to 1.7 MHz with a detection rate of 1 ion/pulse without any loss of information caused by memory management.

The detection rate used for our measurements is 0.0005-0.0025 event/pulse. Unluckily, the detection system currently in use does not support the detection of multiple-ion events due to difficulties related to the high acquisition frequencies. The exclusion of multiple-ion events has a major impact on the compositional measurements. For this reason, the composition as provided by this prototype is not quantitative. Micro-PL spectroscopy is performed using a 320 mm focal length spectrometer equipped with a CCD camera for time-integrated and with a streak camera for time-resolved acquisitions. The spectral resolution is approximately 0.3 nm. Excitation is provided by the same pulsed laser emitting at 260 nm, but increasing the repetition frequency to 4 MHz, to increase the number of counts in the detector. For the μPL studies of our samples, the incident laser power can be tuned in the 15-2000 μW range.

3.7.3. 3D reconstruction of the volume evaporated

Data were processed using the TAP3D software by CAMECA, GPM 3D data software and homemade MATLAB codes. Keeping in mind that the APT is a projection microscope, from the position of the impact of the ions on the detector **X** and **Y** as shown in the **Figure 3.37**, it is possible to determine the initial position of the atoms on the tip surface before their evaporation using an inverse projection.

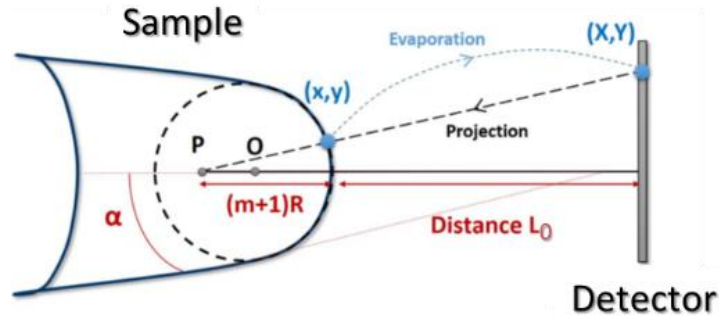


Figure 3.37: Diagram of the projection principle for the 3D reconstruction of the sample at a distance L_0 from the position sensitive detector (x, y) . (modified from ⁶⁵)

The 'radial projection' of the ion flight paths from the specimen tip magnifies spatial differences between the evaporated atoms as they move along the flight path, resulting in a highly magnified and, ideally, uniform 'mapping' of the tip surface to the position-sensitive detector. The magnification G of the tip image depends on curvature radius R and it can be written:

$$G = \frac{L_0}{(m+1)R} \quad (3.10)$$

where L_0 is the flight path of the ions and $(m + 1)$ is image compression factor, parameter related to the projection point P and the fact that ion trajectories are not completely perpendicular to the tip surface. The compression factor varies between 1.2 and 2.

From the **Figure** 3.37, the initial x, y position of the atoms on the tip are given by:

$$x = X/G ; y = Y/G \quad (3.11)$$

The third dimensions z or the depth is determined using the total number of detected ions. So, the atomic volume of each detected ion has to be taken into account :

$$\Delta z = \frac{V_{at}}{Qs} \quad (3.12)$$

where s is the analyzed surface, Q is the detection efficiency and V_{at} is the atomic volume of the charges. The analysis surface s depends on detector surface S and magnification G as follows:

$$s = \frac{S}{G^2} \quad (3.13)$$

Replacing s to the **Equation** (3.12) using the **Equation** 3.13, we can have the depth Δz as follows:

$$\Delta z = \frac{V_{at}G^2}{QS} \quad (3.14)$$

where the depth Δz depends on the magnification G . From the **Equations** (3.10) and (3.14), we can conclude that the value of radius R is needed in order to make the 3D reconstruction.

Several methodologies can be used to determined R . For homogeneous samples, the estimation of R can be done as a function of the applied voltage. Second, knowing the original shape of the tip,

the R, which increases with the depth of the volume analyzed, can be determined by defining initial radius and shank angle. The necessary parameters for this methodology are the cone angle, α , and the radius of curvature, R, which evolve during the evaporation and are in generally estimated initially from an SEM image or TEM images. Third, the estimation of the variation of radius as a function of depth can be done using “Tip Image” mode uploading SEM or TEM image. In this manuscript, the 3D reconstruction was performed using a cone-angle algorithm^{180,181}. The reconstruction parameters were extracted from STEM images of the specimen before performing La-APT. The values measured initially are on average $R = 30 - 50 \text{ nm}$ and $\alpha = 5^\circ - 10^\circ$ over all the samples analyzed.

For the optimization of the mass spectra, it is also important to take into account that the L representing the flight path and presented in the **Equation (3.9)** is not constant but it depends on the variation of straight-flight-path and the ion impact location on the detector. We can write the L as $L(x,y)$ that is dependent of x y coordinates:

$$L(x,y)^2 = L_0^2 + r(x,y)^2 \quad (3.15)$$

In order to have a first approximation of the parabolic trajectory of the ion we can apply the Pythagorean theorem in the **Figure 3.38**.

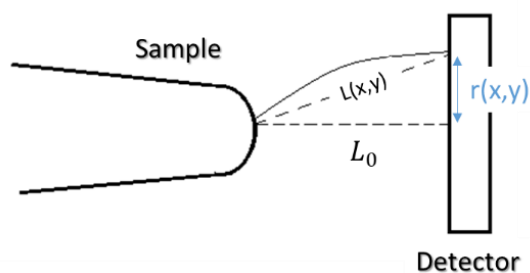


Figure 3.38: Diagram of the projection and the first approximation for the optimization of the spectra.

Figure 3.39 presents the atom probe tomographic study. **Figure 3.39(a)** illustrates the 3D reconstructed map where with blue we see the Ga atoms. The underlined region in the **Figure 3.39(a)** is presented in the **Figure 3.39(b)** with higher magnification. **Figure 3.39(c)** shows 10 nm sliced Ga site fraction map extracted from (b).

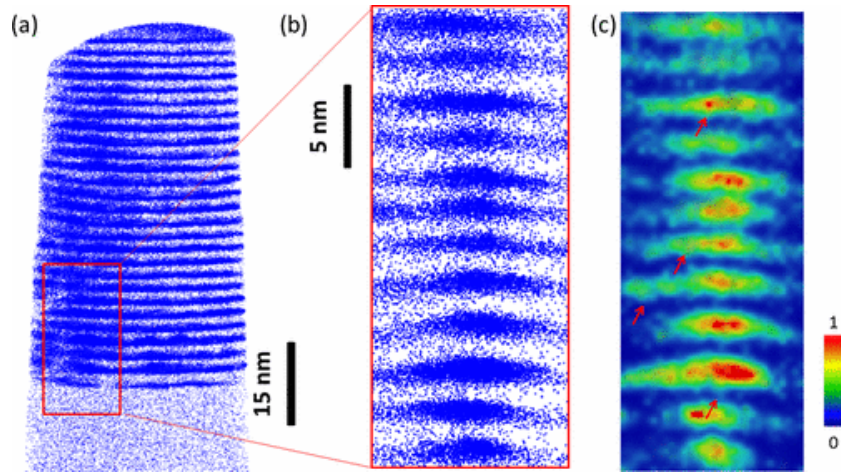


Figure 3.39: Atom probe tomographic study of a tip containing a set of AlGaIn/GaN QDs. (a) Reconstructed positions of the Ga atoms within the whole probed volume. (b) Reconstructed positions of the Ga atoms within a 0.5 nm thick slice corresponding to a cross section of a selected stack of QDs. (c) Ga site fraction map within the volume displayed in (b). The red arrows point to interface monolayer fluctuations at the bottom of several QDs.⁶⁸

3.8. NextNano simulations

Simulations of the strain distribution and electronic structure of the samples were carried out with the nextnano³ software which is a commercial self-consistent Schrödinger-Poisson equation solver. We used a model based on the $\mathbf{k}\cdot\mathbf{p}$ perturbation theory for calculating the quantum levels.¹⁸² For the work presented in this manuscript, the strain distribution, electronic band structure, quantum levels and recombination probabilities of given nanostructures are simulated in one and three dimensions. We used the material parameters given in **Table 3.1**.¹²⁹

For the simulation of $\text{Al}_x\text{Ga}_{1-x}\text{N}$ alloys, all the bowing parameters were set to zero. In the case of $\text{In}_x\text{Ga}_{1-x}\text{N}$ alloys, bowing parameters were only used for the calculation of the band gap energy ($b = 2.1 \text{ eV}^2$,¹⁸³ applied to the conduction band) and the spontaneous polarization ($b = -0.038 \text{ C/m}^2$ ⁷³).¹⁸⁴

Parameters	Units	Symbol	GaN	InN	AlN
Lattice constants ⁷³	nm	a	0.3189	0.3545	0.3112
		c	0.5185	0.5703	0.4982
Spontaneous polarization ¹⁸³	C/m ²	P _{SP}	-0.034	-0.042	-0.090
Piezoelectric constants ⁸⁶	C/m ²	e ₃₁	-0.49	-0.57	-0.60
		e ₃₃	0.73	0.97	1.46
Elastic constants ^{79,81}	GPa	c ₁₁	390	223	396
		c ₁₂	145	115	137
		c ₁₃	106	92	108
		c ₃₃	398	224	373
		c ₄₄	105	48	116
Band gap ^{2,73}	eV	E _G	3.51	0.69	6.2
Conduction-band offset with GaN ^{2,73}	eV	ΔE_{CB}	0	2.44	0
Electron effective mas ^{73,185}	m _{e0}	m _e [*]	0.2	0.07	0.3
Hole effective mass ^{73,185}	m _{h0}	m _h [*]	1.6	1.63	1.44
Luttinger parameters ¹⁸⁶		A ₁	-5.947	-15.803	-3.991
		A ₂	-0.528	-0.497	-0.311
		A ₃	5.414	15.251	3.671
		A ₄	-2.512	-7.151	-1.147
		A ₅	-2.510	-7.060	-1.329
		A ₆	-3.202	-10.078	-1.952
		A ₇	0	0.175	0
Conduction band deformation potentials ¹¹²		a _{c1} -D ₁	-5.81	-3.62	-4.3
		a _{c2} -D ₂	-8.92	-12.1	-4.6
Uniaxial valance band deformation potentials ¹¹²		D ₃	5.47	9.12	2.68
		D ₄	-2.98	-3.79	-1.74
		D ₅	-2.82	-3.23	-2.07
Varshni parameters ^{73,187}	meV/K	α	0.858	0.245	-
	K	β	700	624	-

Table 3.1: Input parameters used for the calculations with the nextnano3 software.

Chapter 4: AlGaN/AlN nanowires for electron-pumped ultraviolet sources

There is a particular demand for solid-state devices emitting in the UV range around 254 nm for application in disinfection and water purification ^{22,188–190}. A promising alternative for the fabrication of highly efficient, eco-friendly UV lamps is based on the injection of electrons into AlGaN/AlN nanostructures using a miniaturized electron gun. In this chapter, we present the design and characterization of nitrogen-polar Al_xGa_{1-x}N/AlN (0 ≤ x ≤ 0.1) QD superlattices integrated along GaN NWs for application in electron-pumped UV sources. We first describe the growth conditions to obtain a high density of non-coalesced NWs, and to improve the uniformity of the height along the substrate. We estimate the NW superlattice is long enough to collect the electron-hole pairs generated by an electron beam with an acceleration voltage of 5 kV, typical value to prevent x-ray emission. We systematically assess the optical performance of GaN/AlN SLs on NWs for various dot/barrier thickness and the effect of incorporating Al in the dots. These studies are complemented by comparing their emission with planar GaN/AlN SLs with the same periodicity. Internal quantum efficiencies are measured under low injection conditions and for higher excitation power densities. Finally, we study the external quantum efficiency of these structures under optical pumping.

In this work, high-angle annular dark-field - scanning transmission electron microscopy (HAADF-STEM) analyses were performed by Dr. M. I. den Hertog (NWs) and Dr. C. Bougerol (lamellas of planar samples prepared by FIB by Dr. N. Mollard). CL measurements have been made by A. Harikumar, Dr. F. Donatini and Dr. J. Lahnemann. I was assisted by Dr. E. Bellet-Amalric and Dr. E. Monroy with XRD and SEM measurements, respectively. The complete study was accepted for publication as “**Assessment of AlGaN/AlN superlattices on GaN nanowires as active region of electron-pumped ultraviolet sources**”, *I. Dimkou, et al., Nanotechnology 31, 204001 (2020)*¹⁹¹.

4.1. Introduction to UV emitters: motivation

Exposure to UV radiation is effective for inactivating a large range of pathogens ^{190,192–194}. It is receiving renewed attention due to the global pandemics as an immediately deployable and cost effective option ^{195–199}. However, the common sources used for disinfection are low-pressure arc lamps, emitting at 254 nm, which contain toxic mercury that Europe is trying to phase out. Different replacements for mercury lamps are recently proposed ^{22,23}. Most attention is now focused on UV light emitting diodes (LEDs) based on semiconductors, with numerous advantages compared with mercury lamps (fast on/off switching, longer lifetime, reduced ozone generation, wider wavelength selection) ^{190,200,201}. AlGaN semiconducting alloys offer an interesting choice for the fabrication of UV emitters because of their direct energy band gap and wide doping capabilities. Even so, the efficiency of AlGaN-based LEDs is still relatively low ¹³¹.

The LED performance is characterized by its external quantum efficiency (EQE) or wall-plug efficiency (WPE). The EQE is the ratio of the number of photons emitted from the LED to the number of electrons passing through the device. The EQE in turn is dependent on the radiative recombination

efficiency η_{rad} , the carrier injection efficiency η_{inj} , and the light extraction efficiency η_{ext} :

$$EQE = \eta_{rad} \cdot \eta_{inj} \cdot \eta_{ext} = \eta_{IQE} \cdot \eta_{ext} \quad (4.1)$$

where the product of the radiative recombination efficiency η_{rad} and the carrier injection efficiency η_{inj} is typically referred to as the internal quantum efficiency η_{IQE} .

The external quantum efficiency (EQE) and wall-plug efficiency (WPE) are related through the following equation²⁰²:

$$WPE = \frac{P_{out}}{I \cdot V} = EQE \frac{\hbar\omega}{e \cdot V} = EQE \cdot \eta_{el} \quad (4.2)$$

where P_{out} , I , and V represent the output power, operating current, and operating voltage of the UV-LED, respectively, $\hbar\omega$ the emitted photon energy, and η_{el} the electrical efficiency²⁰³.

Figure 4.1 (a) presents the schematic of a nitride-based UV LED and **Figure 4.1 (b)** presents the plot of reported EQE values as a function of the emission wavelength. In spite of intense research efforts during the last decade^{200,204}, the WPE of commercial LEDs at ≈ 260 nm is $< 1\%$, far below that of mercury lamps ($\approx 15\%$ at 254 nm). Current world laboratory record of WPE for a UV-C LED is 5.7% at 275 nm²⁴, and there was no improvement in the last 3 years. Furthermore, the LED efficiency drastically decreases at shorter wavelengths²⁰², as illustrated in **Figure 4.1(b)**.

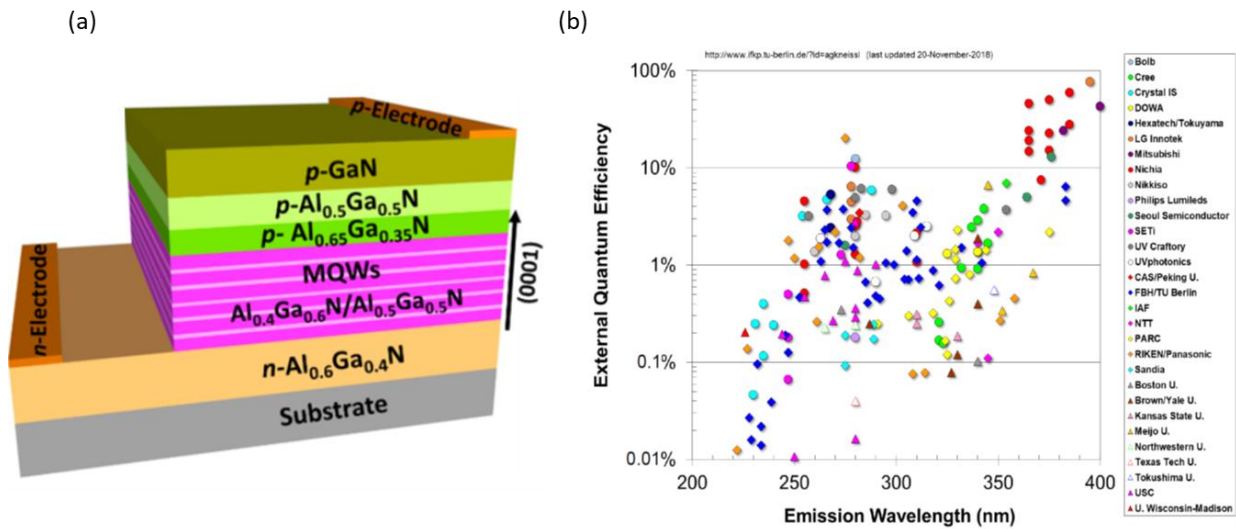


Figure 4.1: (a) Schematic diagram of a UV light-emitting diode (LED)²⁰⁵. (b) EQE of UV LEDs developed over nearly two decades. Noticeable is the big drop in EQE for wavelengths shorter than 365 nm, which marks the transition from InGaN- to AlGaIn-based LED technologies¹⁹⁰.

Several parameters can affect the efficiency of these devices. First, the shortage and the high price of high-quality native AlN substrates leads most of the researchers to use non-native substrates, which present high lattice mismatch, and difference in thermal conductivity and coefficient of thermal expansion with respect to the epitaxial layer. All these factors reduce the IQE in QWs. Second, in spite of the technological progress in doping and contacting of semiconductors, the high activation energy of both donors and acceptors and the asymmetric carrier mobility of electrons and holes in AlGaIn

cause problems on electrical injection^{206–208}. Attaining reasonable hole concentrations and ohmic contacts to the p-type region requires that the structure is terminated with p-GaN, which absorbs the deep-UV LED emission. Subsequently, the increase of the Al content contributes to the low light extraction efficiency due to the optical polarization of the emission. Specifically, for GaN transverse-electric (TE)-polarized photons with the electric field perpendicular to the c-axis ($E \perp c$) can be efficiently out-coupled from the surface of a LED, contrary to the case of AlN where the emission is dominated by transverse-magnetic (TM)-polarized photons with the electric field parallel to the c-axis ($E // c$)²⁰⁹. This different behavior between GaN and AlN is due to the difference of their band structure, as described in **subchapter 2.5**.

4.2. Description of the electron-pumped UV lamp

A promising alternative for the fabrication of highly-efficient, eco-friendly UV lamps consists in mounting the active AlGaIn chip in a vacuum tube, and to inject carriers using a cold cathode^{210–212}. Such a device, which can be miniaturized to the millimetre size, would avoid the problems associated with electrical injection, since both electrons and holes are generated equally in the active region by impact ionization.

A schematic of an electron-pumped UV (EPUV) device is shown in **Figure 4.2**. The device containing the AlGaIn/AlN QD layers is attached to a copper block, to help dissipating the generated heat. The electron source is connected to high voltage whereas the copper block is grounded. Thus electrons are accelerated towards the active medium. The device must operate under vacuum.

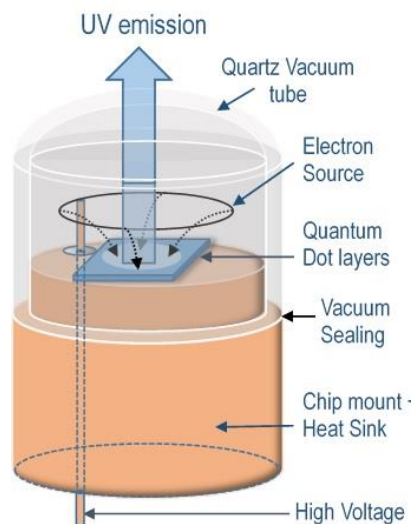


Figure 4.2: Schematic of an electron beam pumped UV emitter.

At the beginning of this PhD work, several reports on electron-pumped emission from GaN-based QWs already existed^{211,213–217}, but the performance was mostly limited by the light extraction efficiency. There were also some demonstration of electron-pumped lasers emitting around 360 nm^{218,219}. E-beam pumped sources compare favorably with state-of-the art efficiencies from

conventional UV-LEDs, and can deliver high optical output powers as the **Figure 4.3** illustrates. We can outline that NIMS (Tsukuba) refers to an output power of 0.2 mW at 225 nm, WPE \approx 0.6% and Kyoto university to an output power of 100 mW at 240 nm. Moreover, output power \approx 2 W at 260 nm, WPE \approx 0.3% were reported by Moscow Tech University and Peking University. All these studies were performed with QW nanostructures.

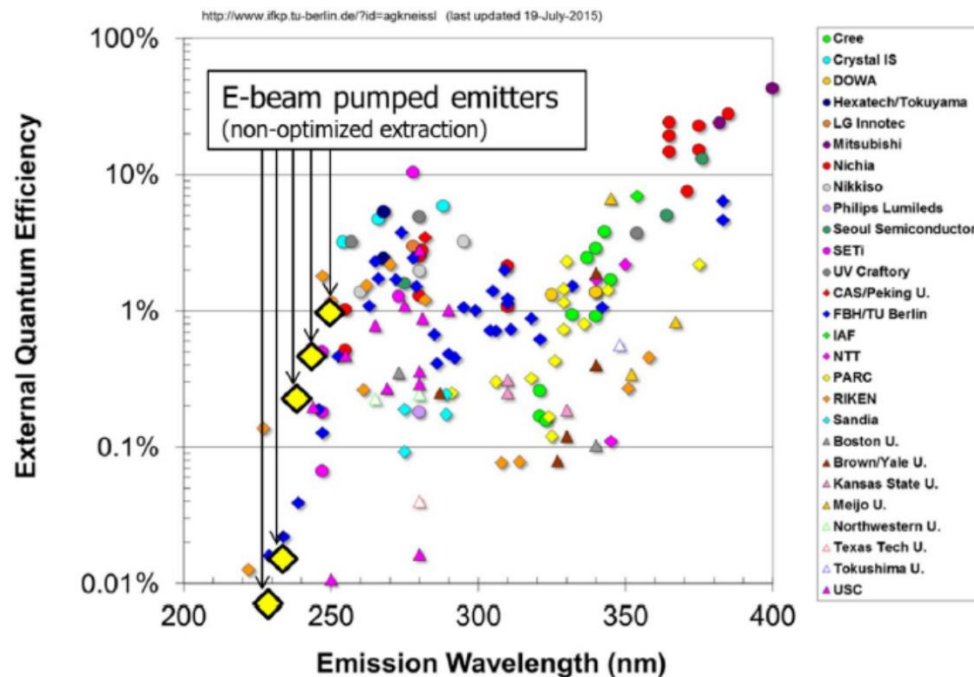


Figure 4.3: Comparison of e-beam pumped spontaneous emission device efficiencies with state-of-the-art conventional LED performance.²⁰²

4.3. Why nanowires?

In this chapter, we demonstrate the importance of NW arrays as active media that opens interesting perspectives for electron-pumped UV emitters. Semiconductor NWs represent an innovative material approach with potential applications in the domains of electronics, optoelectronics, sensors and energy conversion^{12,114,220–225}. The advantages of GaN-NW-based structures can be divided into number of areas. First, the GaN NWs can be grown on Si(111) with high crystalline quality, as individual NWs are almost dislocation-free. Second, they can incorporate axial and radial heterostructures. In axial heterostructures, the elastic relaxation of strain at the NW sidewalls allows combining materials beyond the limits imposed by the critical thickness in planar heterostructures. Radial heterostructures, on the other hand, open the opportunity to increase the device active area, but the critical thickness limitation applies in this latter case.

Additional advantages stem from the light-NW coupling. Using the waveguiding modes of the individual NWs may enhance light emission leading to stimulated emission or even lasing. In addition, the manipulation of growth geometry of NW arrays will allow realization of photonic structures formed

by NW arrays to improve light extraction. Last but not least, controlling the crystallography and composition of NW surfaces, it is possible to design NW optical cavities for advanced photon management and efficient harnessing of inter- and intra-wire energy transfer processes.

For our particular application of the NWs as active region of EPUV emitters, we will take advantage of the relatively easy implementation of nano-objects displaying three-dimensional (3D) quantum confinement (quantum-dot-like) ^{226–229} within a NW, which results in high IQE at room temperature ^{138,230}. From the structural point of view, these objects are often referred to as “nanodisks” as they look more like wells than like dots. However, previous works studied exhaustively the single GaN/AlN dots in a NW ²²⁶ showing correlation measurements indicating antibunching ²³¹, which is a signature of QD behaviour. In addition to this, the strong reduction of non-radiative recombination, which results in photoluminescence lifetimes that remain constant in the 5-300 K temperature range ²³², confirms the presence of 3D confinement of carriers. This is why the NW having diameter around 50 nm presents “quantum dot” behavior, thanks to the radial confinement. For this reason we make the choice of referring to these structures as “quantum dots” based on their optical nature.

4.4. Target structure

The aim of this study is to explore the possibility of using Al_xGa_{1-x}N/AlN QD SLs integrated along GaN NWs as active media for electron-pumped UV emitters. The implementation of a SL of QDs in a wire seems a good strategy, since 3D carrier confinement grants a certain insensitivity to non-radiative processes ²³¹, which results in high internal quantum efficiency at room temperature. However, the semiconductor geometry must be adapted to maximize the energy conversion under electron pumping.

A first specification is that the total length of the active region should be larger than the penetration depth of the electron beam, R_e . A commonly used empirical expression for R_e is ²³³:

$$R_e = \frac{4.28 \times 10^{-6}}{\rho} V_A^{1.75} \quad (4.3)$$

where ρ is the material density in g/cm^3 and V_A is the acceleration voltage in kV. Applied to GaN ($\rho = 6.10 \text{ g/cm}^{-3}$) and AlN ($\rho = 3.26 \text{ g/cm}^{-3}$) assuming $V_A = 5 \text{ kV}$, we obtain $R_e = 115 \text{ nm}$ and $R_e = 215 \text{ nm}$, respectively. For a more precise estimation of R_e , Monte Carlo simulations of the electron beam interaction with GaN, Al_{0.67}Ga_{0.33}N and AlN were performed as a function of V_A , using the CASINO software ²³⁴, with the results depicted in **Figure 4.4**.

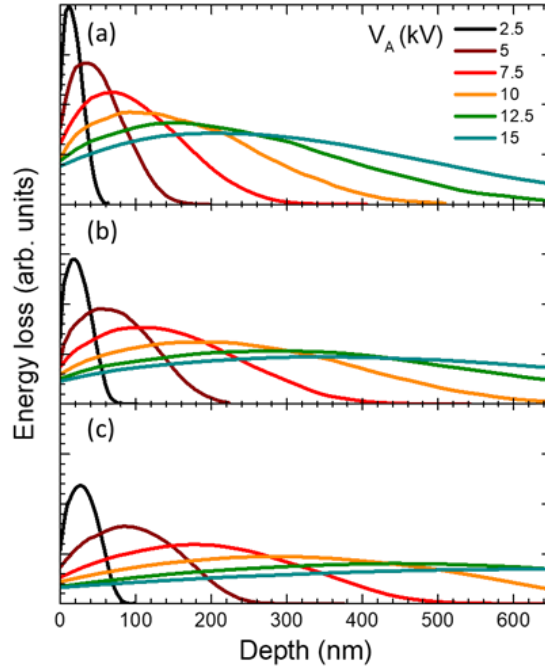


Figure 4.4: Energy loss as a function of depth by an electron beam penetrating in (a) GaN, (b) $\text{Al}_{0.67}\text{Ga}_{0.33}\text{N}$, and (c) AlN for various accelerating voltages, V_A . The curves were obtained by performing Monte Carlo simulations using the CASINO software.

For $V_A = 5$ kV, the calculations predict values of R_e around 175 nm, 224 nm, and 260 nm for GaN, $\text{Al}_{0.67}\text{Ga}_{0.33}\text{N}$ and AlN, respectively [see **Figures 4.4(a), (b) and (c)**, respectively]. The penetration depth in $\text{Al}_{0.67}\text{Ga}_{0.33}\text{N}$ is presented here because it reflects the average Al content in the active region of some of the heterostructures under study, as it will be explained later in this chapter.

In view of these results, and accounting for a reduction of the effective material density in the NW ensemble with respect to bulk material, the length of our QD SLs was chosen to be 400 nm. To maximize the number of emitting centres, the nominal SL period was fixed at 4.5 nm, which means that the active region consists of 88 QD periods. To adjust the spectral response, we varied the Al content in the dots and the dot/barrier thickness ratio, i.e. the total number of dots and the active region length remained constant.

With the purpose of favouring the charge evacuation during the electron pumping process the NWs were grown on n-type Si(111) with a resistivity in the range of 0.001-0.005 Ωcm . The NW base and the dots were doped n-type with $[\text{Si}] = 5 \times 10^{18} \text{ cm}^{-3}$ (value estimated from Hall effect measurements using the Van der Pauw method on planar Si-doped GaN layers).

A schematic presentation of the as grown sample is illustrated in the **Figure 4.5**.

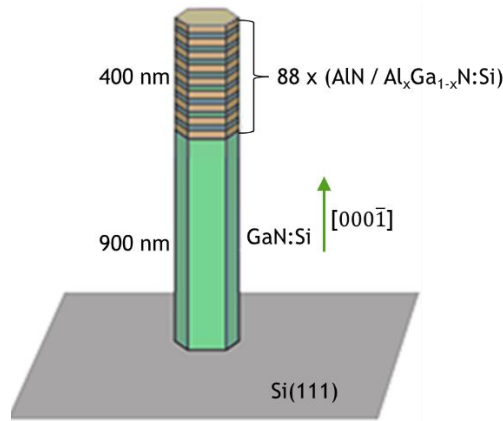


Figure 4.5: Simplified shema of the grown structure.

4.5. Growth conditions

As described in **Chapter 3**, self-assembled N-polar NWs were synthesized using PAMBE on n-type Si(111) substrates on top of a low-temperature two-step AlN nucleation layer^{137,235,236}. To improve the uniformity of the height across the substrate surface²³⁷, the growth starts with a long (≈ 900 nm) GaN NW base grown under N-rich conditions ($\text{Ga/N flux ratio } \Phi_{\text{Ga}}/\Phi_{\text{N}} = 0.25$), at a substrate temperature $T_s = 810$ °C. This leads to a density of GaN NWs around $6\text{-}8 \times 10^9 \text{ cm}^{-2}$, with a NW diameter of 30-50 nm. The choice of growth conditions is based on the study described in **Figure 4.6**. From these bird's eye and top-view SEM images, we observe that increasing the substrate temperature from 770°C to 810°C results in a reduction of the NW density, at the price of a slight decrease of the growth rate due to the enhancement of GaN decomposition. However, at 825°C the decomposition rate is too high, and the NW height becomes highly inhomogeneous.

In this work, one of our main challenges for the growth of NWs for electron-pumped devices is the control and the reproducibility of the QD geometry and composition in a SL that is hundreds-of-nanometres long (exceeding the penetration depth of the electrons). In general, the luminescence from GaN/AlGaN and AlGaN/AlN SLs on GaN NWs presents strong spectral dispersion, with broad and sometimes multi-line spectral profiles^{45,138}. This is due to the variation of the dot height and diameter along the growth axis²³⁸⁻²⁴⁰, the different strain relaxation in the dots along the growth axis^{238,239,241}, the presence of monolayer thickness fluctuations in the dots²³⁸, and the alloy inhomogeneities and inter-diffusion phenomena at the hetero-interfaces, which depend on the strain state of the structure¹³⁸. Additionally, structural perturbations can be introduced by coalesced areas and lateral GaN inclusions²⁴². From all of these, we can conclude that the most critical is to develop precisely controlled growth processes aiming to the synthesis of homogeneous AlGaN/AlN QD SLs in a NW geometry.

The bottom-up approach itself has many subtypes: catalyst-assisted growth, self-catalyzed growth, catalyst free growth, oxide-assisted growth, selective area growth and template-assisted growth. The catalyst-free growth technique utilized here has the advantage of not having to use any

foreign material or impurity, hence producing high quality defect-free NWs. Moreover, compared with selective area growth (SAG), such catalyst free, self-assembled NWs of GaN have already been demonstrated in PAMBE, and when grown, they generally occur as a forest of highly dense NWs^{243–247}. This can be an advantage for electron-pumped lamps compared to SAG of well separated NWs, as the highly dense self-assembled NWs favours the high carrier-injection.

For the synthesis of the active region, we completed the growth of the NWs with the deposition of the $\text{Al}_x\text{Ga}_{1-x}\text{N}/\text{AlN}$ ($x = 0, 0.05, 0.10$) SL, which was 400 nm long (88 periods of QDs). The $\text{Al}_x\text{Ga}_{1-x}\text{N}$ dots were grown using the same N-rich conditions as for the GaN base (Ga/N flux ratio = 0.25) as described with more detail in **subchapter** 3.1.2.1.. The complete heterostructure was synthesized at $T_s = 810^\circ\text{C}$ without any growth interruption. A summary of the samples under study is presented in **Table** 4.1. Some of the samples were repeated to assess the reproducibility of their growth.

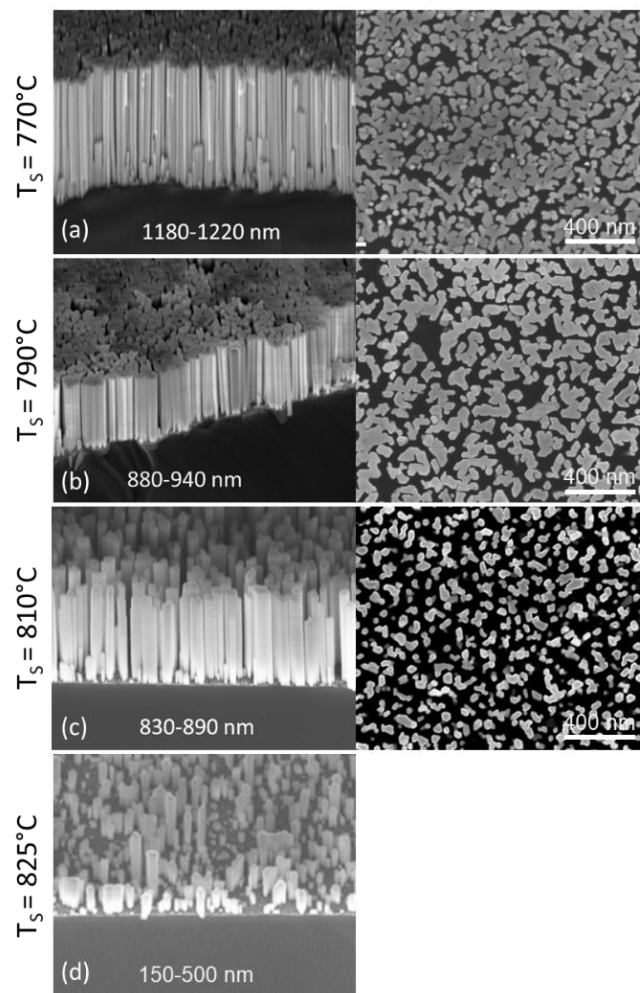


Figure 4.6: SEM images (bird's eye on the left and top view on the right side) of GaN NW samples grown at various substrates temperatures: (a) 770°C, (b) 790°C, (c) 810°C, and 825 °C. The NW height is indicated as a legend in the bird's eye figure. All the samples grew for 3 hours with a flux ratio $\Phi_{\text{Ga}}/\Phi_{\text{N}} = 0.25$ at a growth rate $v_G = 290 \text{ nm/h}$.¹³⁹

Sample	t_w (nm)	t_b (nm)	alloy fraction x	XRD Period (nm)	Peak emission (nm)	IQE (%)	FWHM (nm)	average diameter (nm)
E3857	1.5	3.0	0	4.4±0.1	340	63	31	54.5±11.6
E3898					336	60	30	91.6±19.9
E3858	1.5	3.0	0.05	4.4±0.1	331	34	27	
E3859	1.5	3.0	0.1	4.6±0.1	335	42	29	65.6±14.0
E3861	1.0	4.0	0	5.0±0.1	324	55	25	64.0±28.7
E3862	0.75	3.75	0	4.4±0.1	296	48	22	90.7±29.5
E3863	0.75	3.75	0.1	4.3±0.1	286	44	16	88.8±13.5
E3918	0.65	3.85	0	4.1±0.1	277	29	23	81.3±16.7
E3864					265	31	36	87.5±19.6
E3865	0.65	3.85	0.1	4.1±0.1	258	22	34	91.2±24.4
E3889G	1.5	3.0	0	4.4±0.1	329, 343	<0.05	9, 11	
E3889N	1.5	3.0	0	4.1±0.1	329, 342, 367	<0.4	9, 13, 24	

Table 4.1: Structural and optical characteristics of the samples under study: Nominal thickness of the AlN barriers (t_b) and of the $Al_xGa_{1-x}N$ wells (t_w), Al concentration in the wells (x), MQW period measured by XRD, peak emission wavelength at room temperature (in the case of multiple peaks, the dominant peak appears in bold fonts), internal quantum efficiency (IQE) at room temperature (measurement under low-injection conditions), and full width at half maximum (FWHM) of the emission at room temperature.

In order to compare the performance of the NWs with standard QWs, one of the samples (E3857) has been reproduced as a planar structure with similar thicknesses of well/dot, barrier and total active region. The sample was grown simultaneously on the Ga-face (E3889G in Table 4.1) and on the N-face (E3889N in Table 4.1) of free-standing n-type GaN substrates (resistivity at room temperature < 0.05 Ωcm , dislocation density < $5 \times 10^6 \text{ cm}^{-2}$). Growth was performed at 720 °C, under Ga-rich conditions (nitrogen-limited growth rate $v_{\text{GN}} = 450 \text{ nm/h}$) and without growth interruptions¹²⁹.

4.6. GaN/AlN NWs

Our description of the results will focus first on GaN/AlN QD superlattices on GaN NWs (samples E3857, E3898, E3861, E3862, E3918, E3864 in Table 4.1). In order to compare the performance of NWs with standard QWs, we have also studied planar structures with the same layer sequence grown along the [0001] (Ga-polar) or [000-1] (N-polar) crystallographic axis of GaN, starting from free-standing GaN substrates (samples E3889G and E3889N in Table 4.1, respectively). The structural properties of GaN/AlN heterostructures have been analyzed using a combination of XRD, SEM and high resolution TEM experiments. The optical studies have been performed using PL and CL measurements. Moreover, we compare the optical characterization with theoretical simulations of the electronic structure.

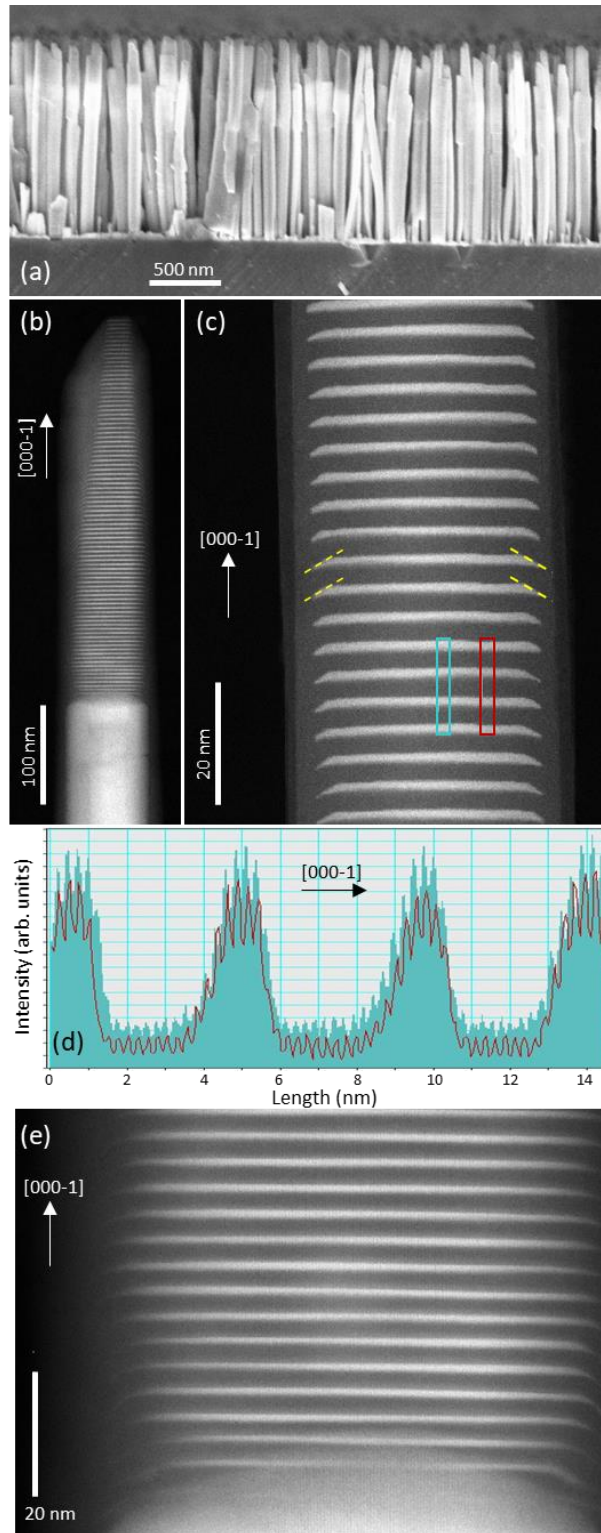


Figure 4.7: (a) SEM image of as-grown sample E3857. (b-c) HAADF-STEM views of a NW, where bright contrast corresponds to GaN and dark contrast corresponds to AlN: (b) general view of the heterostructure, and (c) zoomed image in the centre of the heterostructure. Dashed yellow lines outline the $\{1-102\}$ facets in one of the GaN dots. (d) Integrated intensity of the HAADF-STEM image analysed along the turquoise and red rectangles outlined in (c). (e) HAADF-STEM image of the first periods of the heterostructure. Dark/bright contrast corresponds to Al-rich/Ga-rich areas.

4.6.1. Structural properties

In a first experiment, we have studied the structural properties of GaN/AlN QD superlattices on GaN NWs (samples E3857 and E3898 in **Table 4.1**). An SEM image of E3857 is displayed in **Figure 4.7(a)**, illustrating the high density of NWs in the ensemble. **Figures 4.7(b-c)** present HAADF-STEM images of the GaN/AlN heterostructure (88 periods) in E3857, where the bright contrast is GaN and the darker contrast corresponds to AlN. Along the NW, the heterostructure exhibits a regular thickness of 1.5 ± 0.2 nm for GaN and 2.8 ± 0.2 nm of AlN, with the whole GaN/AlN QD superlattice enveloped by an AlN shell. Along the SL, the thickness of the GaN section increases by a maximum of 0.5 nm from the base to the end. It can be observed in zoomed images [**Figure 4.7(c)**] that the thickness of the AlN shell decreases along the NW growth axis, being negligible at the top of the NWs and having a maximum thickness of around 5 nm at the interface with the GaN base. The vertical cross section of the GaN dots is not rectangular but trapezoidal, with $\{1-102\}$ facets towards the NW sidewalls [see dashed yellow lines in **Figure 4.7(c)**].

Figure 4.7(d) depicts the integrated intensity of the HAADF-STEM image in (c) analysed along the turquoise and red rectangles outlined in the figure. From these profiles, the interface resulting from the deposition of AlN on GaN is systematically sharp at the scale of one atomic layer. On the contrary the GaN-on-AlN interface is widened by interdiffusion, extending 2-3 atomic layers. Note that the results are similar in the centre of the NW (data in turquoise) as closer to the sidewalls (data in red). If we focus on the initial stage of the growth of the heterostructure, illustrated in **Figure 4.7(e)**, there is a diffusion of Ga from the stem into the first two periods of the SL. Such Al-Ga intermixed regions have previously been reported at the beginning of the growth of GaN/AlN SLs¹³⁸, and are explained by the strain-driven out-diffusion of Ga induced by the lattice mismatch between GaN and AlN.

As a comparison, we have studied the structural properties of planar structures with the same layer sequence grown along the $[0001]$ (Ga-polar) or $[000-1]$ (N-polar) crystallographic axis of GaN, starting from free-standing GaN substrates (samples E3889G and E3889N in **Table 4.1**, respectively). **Figure 4.8(a)** displays a HAADF-STEM image of a Ga-polar planar sample containing 88 periods of GaN/AlN (E3889G), and **Figure 4.8(b)** is a bright-field (BF) TEM off-axis (10° tilt from the $[11-20]$ zone axis) image showing five periods in the centre of the SL.

The structure presents sharp and symmetric hetero-interfaces at the atomic level, only disturbed by clearly identified atomic steps [marked by white arrows in **Figure 4.8(b)**], characteristic of the step-flow layer-by-layer growth mode. The equivalent N-polar planar structure is shown in **Figures 4.8(c-d)**. The heterointerfaces are still relatively sharp and symmetric, but they extend to about two atomic layers.

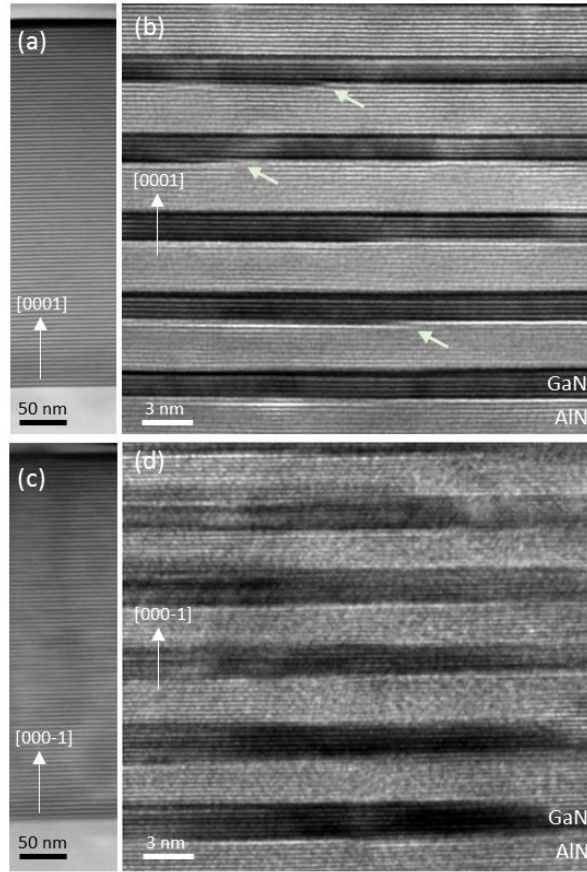


Figure 4.8: (a) HAADF-STEM image of planar sample E3889G showing the 88 periods of GaN/AlN. Dark/bright contrast corresponds to Al-rich/Ga-rich areas. (b) BF TEM off-axis (10° tilt from the $[11\bar{2}0]$ zone axis) image of E3889G showing five periods in the centre of the superlattice, tilted viewed along $\langle 1\bar{1}00 \rangle$. Bright/dark contrast corresponds to Al-rich/Ga-rich areas. The arrows mark atomic steps at the heterointerfaces. (c) HAADF-STEM image of sample E3889N showing the 88 periods of GaN/AlN. Dark/bright contrast corresponds to Al-rich/Ga-rich areas. (d) BF TEM off-axis (10° tilt from the $[11\bar{2}0]$ zone axis) image of E3889N showing five periods in the centre of the superlattice, viewed along $\langle 1\bar{1}00 \rangle$. Bright/dark contrast corresponds to Al-rich/Ga-rich areas. The arrows mark atomic steps at the heterointerfaces.

The structural characteristics of the GaN/AlN superlattice were also investigated by high-resolution XRD. **Figure 4.9** shows θ - 2θ scans around the GaN (0002) reflection for samples E3857, E3889G and E3889N. In the NW sample, the angular location of the reflection from the GaN stem is shifted to higher angles with respect to relaxed GaN, which confirms that it is compressively strained by the AlN shell. From the inter-satellite distance, we extract the MQW periods listed in **Table 4.1**, which are in good agreement with the nominal values. Using the Ga-polar sample as a reference, the N-polar structure presents broader reflections due to the larger inhomogeneity in thickness observed in the TEM images. In the case of NWs, thickness fluctuations from wire to wire within the ensemble introduce an additional broadening factor. Nevertheless, the satellites of the MQW reflection are still well resolved, and their linewidth is comparable to the N-polar structure.

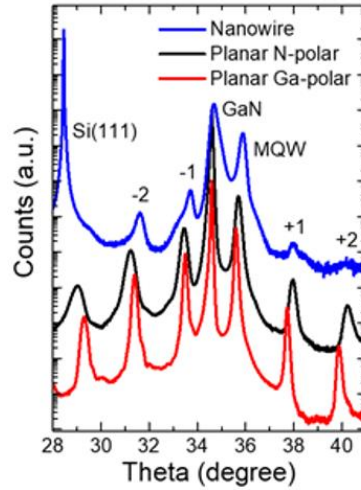


Figure 4.9: XRD θ - 2θ scans of samples E3857, E3889G and E3889N, recorded around the (0002) reflection of GaN. The scans are vertically shifted for clarity. Labels indicate the (111) reflection of the Si substrate, the (0002) reflection of GaN, and the (0002) reflection of the MQW, with several satellites

4.6.2. Optical properties

To get an idea of the impact of the structural properties on the optical characteristics we studied the PL emission of the three heterostructures E3857, E3889G and E3889N. Normalized spectra recorded at low temperature ($T = 5$ K) are displayed in **Figure 4.10**. The peak emission wavelength of the three samples is relatively close, in the 336-340 nm range. The spectra from planar samples present a multi-peak structure due to the monolayer thickness fluctuations in the QWs²⁴⁸, with the Ga polar sample presenting narrower lines. In contrast the emission for the NW sample consists of a single spectral line, centred at 337 nm, with a large linewidth due to the geometry fluctuations in the NW ensemble.

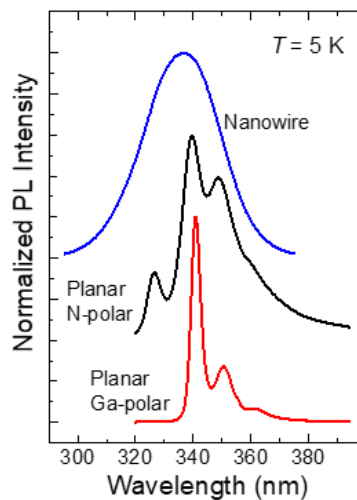


Figure 4.10: Low-temperature PL spectra of samples E3857, E3889G and E3889N. Spectra are normalised to their maximum value and vertically shifted for clarity.

Then, we have assessed the IQE of the samples by analyzing the variation of their emission, either PL or CL, as a function of temperature. As an example, **Figure 4.11(a)** displays the evolution of the PL spectrum as a function of temperature of the sample E3857. The variation of the PL intensity as a function of temperature is presented in **Figure 4.11(b)**. The luminescence from the planar structures drops by more than two orders of magnitude when increasing the temperature from 5 K to 300 K. In contrast the emission intensity from the NWs remains constant up to 100 K and remains at 63% of its maximum (low temperature) value at 300 K. This result confirms the relevance of carrier confinement in hindering non-radiative recombination.

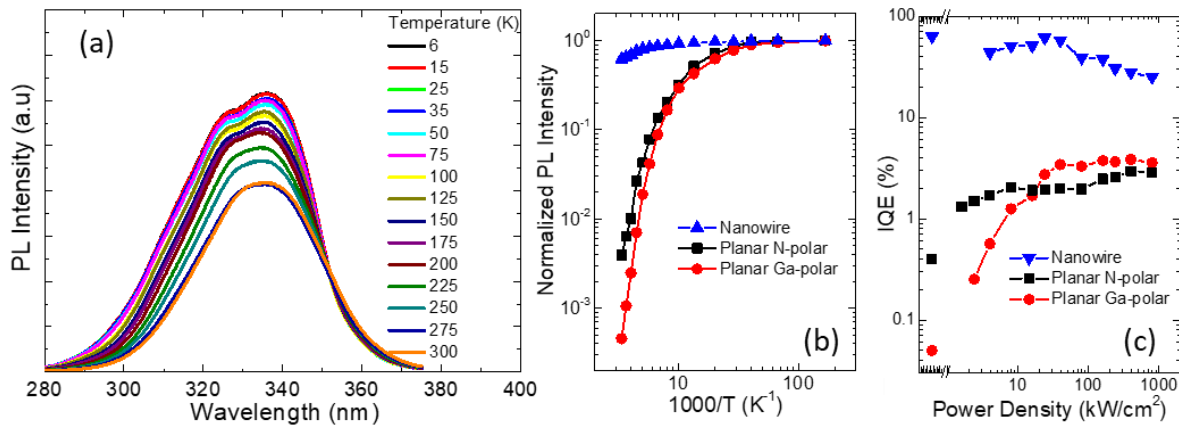


Figure 4.11: (a) Variation of the PL spectra as a function of the temperature of the sample E3857. (b) Variation of the integrated PL intensity as a function of temperature for samples E3857, E3889G and E3889N. Measurements are taken under continuous-wave, low-injection (power density = 0.00013 kW/cm²) excitation. (c) Variation of the IQE at room temperature as a function of the excitation power density measured with a pulsed Nd-YAG laser.

The room-temperature internal quantum efficiency (IQE) of the nanostructures is often estimated as the ratio of the room-temperature and low-temperature integrated PL intensities:

$$IQE(300K) = \frac{I(300K)}{I(0K)} \quad (4.4)$$

This estimation is based on the hypothesis that the PL intensity saturates at low temperature as a result of the carrier freeze out which prevents carriers from reaching defect-related non-radiative recombination centres. There is hence a risk of overestimation of the IQE if non-radiative recombination is active at low temperature, but also if the pumping intensity is high enough to saturate non-radiative recombination paths at high temperature.

To get an estimation of the IQE associated with the material properties, we tried to introduce as few extraneous perturbations as possible to straightforward linear response. Thus the measurements presented here were performed using a continuous-wave laser, and very low power density excitation (10 μ W laser power, focused on a spot with a diameter of 100 μ m). The results in **Figure 4.11(b)** show

that the luminescence from planar samples E3889G and E3889N clearly does not attain saturation at low temperature, so that the IQE calculated from these curves should be taken as an upper limit. On the contrary, all the NW samples in the study present a clear saturation of their PL for temperatures lower than 100 K, as shown for E3857 in **Figure 4.11(b)**. Therefore, the ratio of their room-temperature and low-temperature PL intensities can be considered as a good estimation of their IQE. The obtained IQE values are summarized in **Table 4.1**, together with the peak emission wavelength and linewidth at room temperature. In the case of E3857 and E3898, the IQE at room temperature is 60-63%, orders of magnitude higher than the IQE of planar structures with the same layer sequence (E3889G and E3889N). The higher value of IQE in E3889N in comparison to E3889G is explained by the localization of carriers in the thickness fluctuations observed in the N-polar structure.

When the perturbation introduced by the excitation source is very small (low injection regime), the IQE values describe the material properties in terms of radiative and non-radiative processes. However, it is difficult to compare these data with the literature since most reported values are measured under pulsed excitation^{155,217,249–257}, using power densities in the range of 5-1000 kW/cm²^{155,249–251,253,254}, to emulate the carrier injection at LED operating conditions. In this pumping regime, the photogenerated carrier densities are higher than the doping level of the original structure (high injection) and nonradiative recombination paths are partially saturated. Therefore the obtained IQE is significantly higher than the low-injection value and depends on the excitation power density^{155,249–251,254,258}. Maximum values of IQE are obtained for an excitation power density around 10-100 kW/cm²^{251,254}. Note that in an electron-pumped UV lamp using an acceleration voltage of 5 kV and an injection current of 1 mA to irradiate a spot with a diameter of 1 mm, the excitation density would be below 1 kW/cm².

To explore the behavior of the NW heterostructures under operating conditions, and compare with previous literature, we have measured PL as a function of the excitation power using a pulsed Nd-YAG laser. Measurements were performed at 6 K and at 300 K. Under high injection, the calculation of the IQE at room temperature must take into account the drop of the PL efficiency at low temperature due to the many-body effects induced by high-power excitation²⁵⁴ so that:

$$IQE(300K, P) = \frac{I(300K, P)}{I(0K, P)} \times \frac{I(0K, P)/P}{I(0K, P_{li})/P_{li}} \quad (4.5)$$

where $I(T, P)$ is the integrated PL intensity as a function of temperature and excitation power (P), and P_{li} is an excitation power at low injection conditions. The results for samples E3857, E3889G and E3889N are presented in **Figure 4.11(c)**. In the case of planar samples, the IQE increases with pulsed excitation. A maximum IQE around 3-4% is obtained for excitation in the range of 100-500 kW/cm². The values are lower than the IQE = 15-50% that can be found in the literature for this spectral range (measured by the same method)^{251,254,258}. This difference can be explained by the choice of AlN/GaN as materials for barriers/wells, to be used as a reference for the NW heterostructures. In this case, the lattice mismatch is maximum in comparison with generally-used Al_xGa_{1-x}N/Al_yGa_{1-y}N heterostructures. This leads to enhanced plastic relaxation of the misfit strain²⁵⁹, which has an important effect on the maximum IQE²⁴⁹. Looking back to **Figure 4.11(c)**, in the case of QDs contained in NWs, the IQE is stable

under pulsed excitation up to around 50 kW/cm^2 , and then decreases slightly.

4.6.3. Band profile simulations

We have compared the optical characterization results with theoretical calculations of the electronic structure. A schematic description of the simulated structure is presented in **Figure 4.12(a)**, where the GaN dots are modelled as regular hexagonal prisms. To assess the effect of the sidewall facets observed in **Figure 4.7(c)**, the structure was also modelled considering a reduction of the prism radius along the growth axis, as illustrated in **Figure 4.12(b)**.

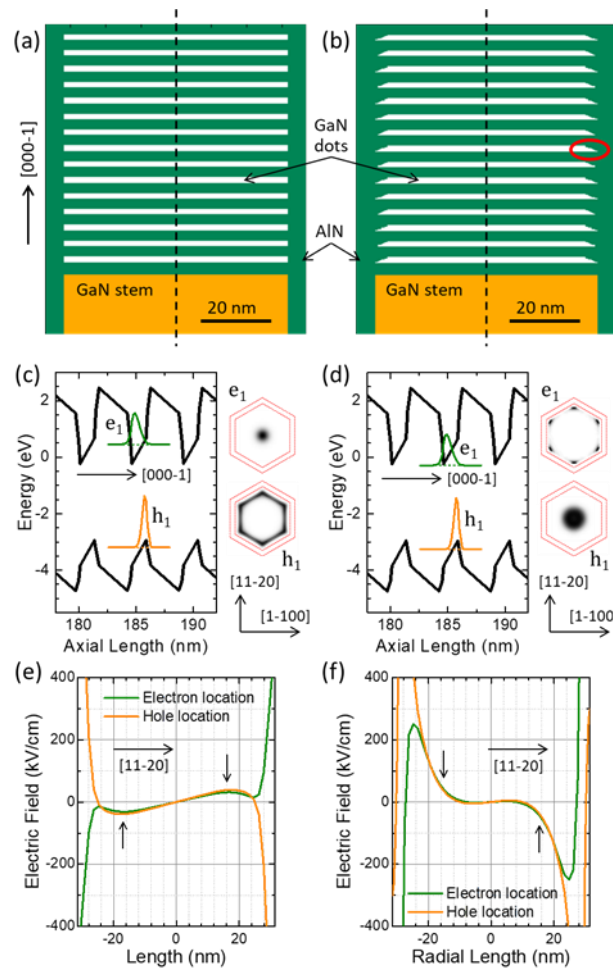


Figure 4.12: (a,b) Schematic description of the simulated structures (a) without taking into account the top facets of the QDs, and (b) including the facets (outlined with a red ellipse). (c, d) Left: Band diagram along the $[000-1]$ NW growth axis showing three QDs in the centre of the superlattice, including a projection of the squared wavefunctions of the first electron (e_1) and hole (h_1) levels in the central dot. Right: In-plane view of the squared wavefunctions of e_1 and h_1 . Dark contrast indicates higher probability to find the electron/hole. The red hexagons represent the GaN core and the AlN shell. Results in (c) and (d) correspond to the simulated structures described in (a) and (b), respectively. (e,f) Component of the electric field along the $[11-20]$ axis represented along the NW diameter. Green/orange curves are obtained at the location of the maximum of the electron/hole wavefunction. The arrows highlight the areas with a change of sign of the electric field if we compare figures (e) and (f). Results in (e) and (f)

correspond to the simulated structures described in (a) and (b), respectively.

The band profile of 3 QDs in the centre of the superlattice, taken at the radial centre of the NW [dashed lines in **Figures** 4.12(a) and (b)], is displayed in **Figures** 4.12(c) and (d), for calculations with and without sidewall facets, respectively. The squared wavefunctions of the ground electron and hole levels depicted in the figure represent in-plane integrated values. The effect of the polarization in the bands, rendering the characteristic saw-tooth profile of GaN, is clearly visible. The internal electric field in the dots shifts the electron wavefunction towards the NW stem and the hole wavefunction towards the cap. However, the separation of electron and hole along the growth axis remains relatively small due to the small QD height. The electron-hole transition at room temperature is predicted to occur at 340 nm and 349 nm, as a result of the calculations in **Figures** 4.12(a,c) and 4.12(b,d), respectively. These results are very close to the experimental value of 340 nm (room temperature, 31 nm linewidth) in sample E3857 (i.e. the sample analysed by HAADF-STEM in **Figure** 4.7).

Simulation	ε_a^{QD} (%)	ε_c^{QD} (%)	ε_a^B (%)	ε_c^B (%)	λ_{RT} (nm)
Without facets	-1.70	0.61	0.78	-0.80	340
With facets	-1.68	0.56	0.78	-0.80	349

Table 4.2: Some results of the theoretical calculations described in Figure 4.12: in-plane and out-of-plane strain at the centre of GaN dots (ε_a^{QD} and ε_c^{QD} , respectively) and at the centre of the barrier (ε_a^B and ε_c^B , respectively), and emission wavelength at room temperature (λ_{RT}).

If we compare the results of the calculations for the structures in **Figures** 4.12(a) and (b), the presence of the facets in the dots does not have a major effect on the strain in the centre of the NW (see values in **Table** 4.2). However, it has a drastic effect on the in-plane distribution of the electron and hole wavefunctions, depicted on the right side of **Figures** 4.12(c) and (d). In the structure without facets [**Figure** 4.12(c)] the maximum of the electron wavefunction is located in the centre of the NW, whereas the hole is shifted towards the sidewalls. In the structure with facets the radial distribution of carriers is opposite, with the hole wavefunction in the centre of the NW and the electron close to the sidewalls. The radial separation of the electron and hole wavefunctions is known to exist in GaN NWs and its effects on the carrier lifetime have been measured by time-resolved PL²³². In homogeneous NWs (without heterostructure) the separation occurs due to the Fermi level pinning at the NW sidewalls²⁶⁰. However in heterostructured NWs the separation is enhanced due to a radial electric field that appears because of the radial gradient of strain and the sheer component of the strain associated to elastic relaxation at the surface²³². **Figures** 4.12(e) and (f) represent the in-plane electric field along the [11–20] axis, measured at the point along the growth axis where the electron and hole wavefunctions reach their maxima. In the structure without facets [**Figure** 4.12(e)] the field points towards the sidewalls, with a maximum value of 37 kV/cm. Even if this value is much smaller than the electric field along the growth axis (7.3 MV/cm in the dots), it is enough to force a radial separation of

electron and hole. However it should be noted that the calculations do not take into account the Coulomb attraction, so that the radial separation should be smaller than the calculated result. The presence of the facets in the QDs changes the strain distribution, which leads to an inversion of the radial electric field, now more intense (maximum of 250 kV/cm) and pointing towards the centre of the wire [see **Figure 4.12(f)**], which results in a different radial distribution of charges. In spite of these radial changes the emission wavelength does not vary significantly since it is dominated by the axial electric field, which is one order of magnitude more intense.

4.6.4. Cathodoluminescence measurements

To better understand the origin of the spectral broadening in the NW samples, and the presence of multiple peaks in the planar layers, we investigated E3889G and E3857 using CL spectral line-scans on the cross-section of the samples, recorded at 7 K. The results are depicted in **Figures 4.13(a)** and **(b)**. In the case of the planar structure [**Figure 4.13(a)**], analysing from bottom to top, the narrow emission from the GaN substrate is observed around 356 nm. The line remains visible when the excitation shifts into the superlattice (position = 0-0.4 μm in the graph), which points to a good vertical diffusion of carriers, facilitated by the orientation of the polarization-induced internal electric field for this Ga-polar sample. The emission from the superlattice presents two distinct peaks, which is consistent with the PL measurements in **Figure 4.10**. The spectral separation of the two peaks corresponds to a change in QW thickness of 1 monolayer, which is in line with the atomic steps at the top interface of the QWs identified in HAADF-STEM [see **Figure 4.8(b)**]. Towards the surface these peaks are slightly shifted to shorter wavelengths as outlined by the white dashed lines in the figure. The small value of the total shift, around 1 nm along the superlattice thickness, points to strain relaxation.

If we turn to the behaviour of the NW structure [**Figure 4.13(b)**], the emission from the GaN stem around 350 nm is visible in the 0.4-0.5 μm position range. The fact that the emission is no longer observed when exciting the superlattice (position = 0-0.4 μm) is explained by the N-polarity of the NWs. In this crystallographic orientation the internal electric field pushes the electrons away from the interface between the stem and the SL. The emission from the superlattice shifts from 320 to 344 nm, following the dashed white line in the figure, when the excitation moves from the stem to the top of the NW. Note that in individual spectra at a specific position, the emission linewidth is comparable to that of the planar SP. Therefore the spectral broadening of the luminescence in **Figure 4.10** is mostly due to the shift of the emission along the growth axis. Looking at theoretical calculations for GaN/AlN SLs in NWs ²⁶¹ this shift can be explained by a difference in the QD height of 1-2 atomic layers (\approx 0.3-0.5 nm) along the growth axis, consistent with STEM observations.

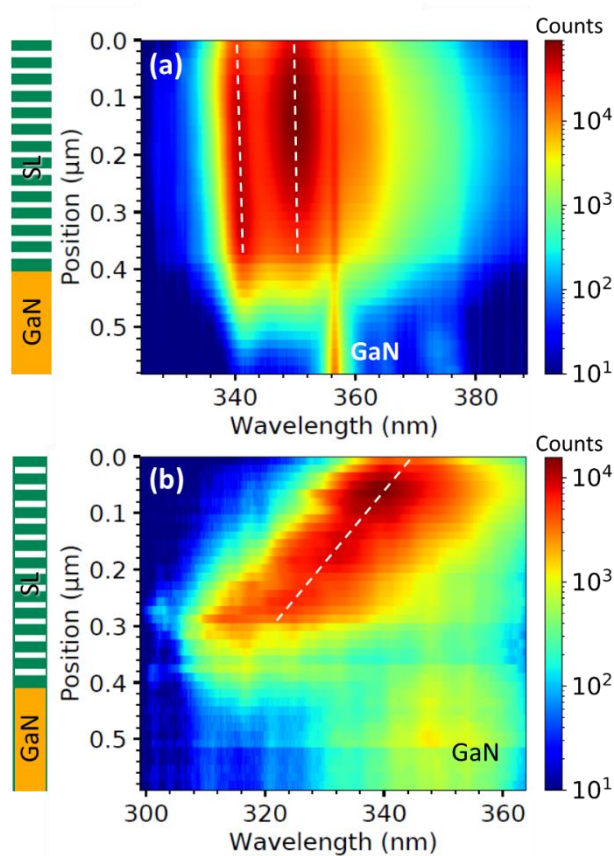


Figure 4.13: CL spectral line-scan on the cross-section of samples (a) E3889G and (b) E3857 measured at 7 K. The intensity is colour-coded on a logarithmic scale. The sketches on the left side of the images show the schematics of the samples. White dashed lines highlight the evolution of the peak emission wavelength of the SLs along the growth axis.

To study the penetration depth of the electron beam under operating conditions, samples E3889G and E3857 were characterized by CL (excitation normal to the surface in the SEM) as a function of the acceleration voltage, with the results described in **Figure 4.14**. **Figure 4.14(a)** shows that the superlattice presents a multi-peak emission as described by the PL studies [**Figure 4.10**]. Luminescence from the GaN substrate (at 357 nm) is only visible for acceleration voltages higher than 10 kV. This result is consistent with the calculations in **Figure 4.4(b)**, which show that acceleration voltages higher than 7.5 kV are required for electrons to generate electron hole pairs in the substrate. Note that the $\text{Al}_x\text{Ga}_{1-x}\text{N}$ layer modelled in **Figure 4.4(b)** presents the same average aluminium mole fraction as the active region of samples E3889G and E3857. In the case of the NW sample [**Figure 4.14(b)**] the emission spectra are dominated by a line around 340 nm, assigned to carrier recombination in the QD superlattice. The emission from the stem becomes visible for acceleration voltages above 5.5 kV, which points to a higher penetration depth in comparison with planar layers, which is justified by the reduced average material density in the NW ensemble.

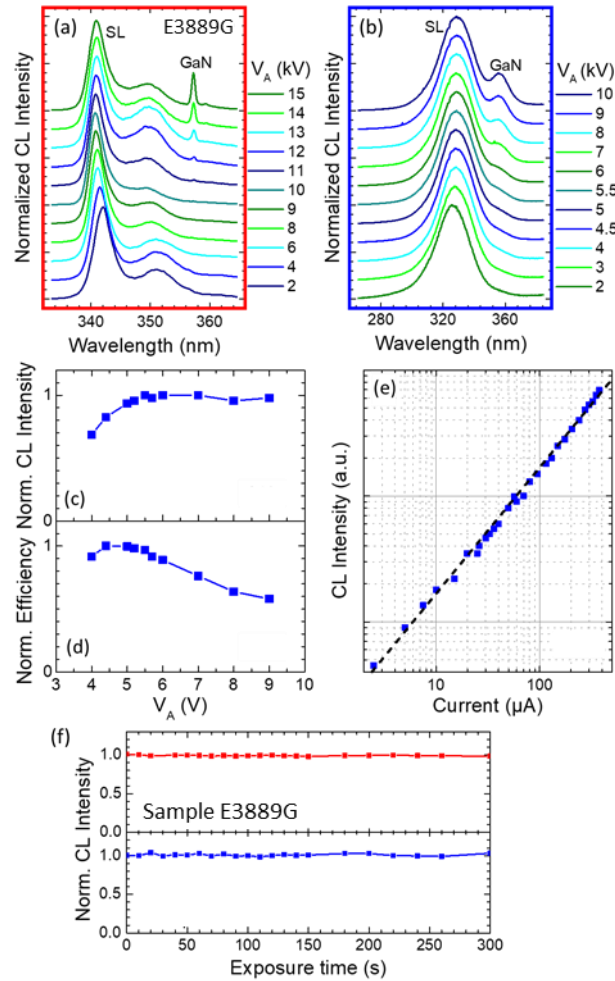


Figure 4.14: CL measurements of samples (a) E3889G and (b) E3898 as a function of the acceleration voltage, V_A . Spectra are normalized at the peak value and vertically shifted for clarity. The emissions from the QD/well SL and from GaN are identified. (c) Normalized CL intensity and (d) emission efficiency as a function of V_A for sample E3857. Measurements were performed using an electron gun operated in direct current mode, under normal incidence, with a beam spot diameter of 4 ± 1 mm. (e) Variation of the CL intensity from sample E3857 as a function of the current injected in the sample. Measurements were performed using an electron gun operated in direct current mode, under normal incidence, with a beam spot diameter of 4 ± 1 mm, and keeping $V_A = 5$ kV. (f) Variation of the CL intensity as a function of time, measured with $V_A = 5$ kV and an injection current of 25 pA concentrated in a 20 nm spot.

The evolution of the CL intensity as a function of the acceleration voltage, V_A , was studied using an electron gun operated in direct current mode, under normal incidence, with a beam spot diameter of 4 ± 1 mm. Measurements were performed with an injection current of 100 μA . **Figure 4.14(c)** depicts the result for the NW sample E3857, showing that the maximum CL intensity is attained for $V_A \approx 5.5$ kV, which is consistent with the penetration depth estimated from **Figure 4.14(b)**. Accordingly, a decrease of the emission efficiency is observed for $V_A > 5.5$ kV [see **Figure 4.14(d)**].

To validate the results in **Figures 4.14(c)** and (d), it is necessary to assess the influence of the electron beam current on the CL emission. With this purpose, sample E3857 was pumped with an

electron gun operated in direct current mode, under normal incidence, with a beam spot diameter of 4 ± 1 mm, keeping $V_A = 5$ kV and varying the injected current. As shown in **Figure 4.14(e)**, the integrated emission of the sample scales linearly with the current, without any indication of saturation up to 400 μ A.

Finally, CL studies of GaN NWs have been previously reported^{44,45,262,263} with some groups observing a reversible degradation of the emission during the experiments^{262,263} which they attributed to charge accumulation and trapping at the NW surface. The CL quenching was reduced in the case of NWs with an AlN shell²⁶². The stability of our samples under electron irradiation was studied by measuring the evolution of the CL intensity with time. The experiment was performed at room temperature with an acceleration voltage $V_A = 5$ kV, the injected current was 25 pA and the beam was concentrated in a 20 nm spot (i.e. excitation power density around 8 kW/cm² at the impact point). **Figure 4.14(f)** shows the evolution of the emission from E3889G and E3857 over a period of 300 seconds. In contrast to refs.^{262,263}, we did not observe any degradation of the CL emission. The stability of the samples is probably due to the relatively thick AlN shell that embeds the QDs and renders them insensitive to recombination at the NW surface.

4.7. Towards shorter wavelengths: Al_xGa_{1-x}N/AlN

In order to shift the peak emission wavelength towards the spectral region efficient for disinfection (around 260-270 nm), we have first explored the effect of reducing the size of the GaN dots in the heterostructure from 1.5 nm to 0.65 nm, while keeping the same number of periods and total thickness of the heterostructure. Note that 0.65 nm is approximately 2.5 monolayers.

4.7.1. Structural properties

We have performed an analysis of the structural properties at the nanometre scale with the results illustrated in **Figure 4.15**. A typical top-view SEM image of an as-grown sample of GaN NWs containing an Al_xGa_{1-x}N/AlN SL where the image corresponds to a sample with 88 periods of Al_{0.1}Ga_{0.9}N / AlN (sample E3863) displayed in **Figure 4.15(a)**. The NWs are detached from each other, but highly packed. Top view images point to a NW density of $6-8\times 10^9$ cm⁻³. The NW diameter is in the range of 30-50 nm at the base, increasing to 50-70 nm in the top region due to the enhancement of lateral growth when depositing AlN^{246,264}. An SEM image of E3865 displayed in **Figure 4.15(b)**, does not show significant differences in shape or density with respect to the GaN/AlN samples [see **Figure 4.7(a)**]. **Figures 4.15(c-e)** present HAADF-STEM images of the complete heterostructure and zoomed images of the last and first AlGa_xN/AlN periods, respectively. Bright contrast corresponds to Ga-rich areas and darker contrast represents Al-rich areas. If we focus on the initial stage of the growth of the heterostructure, illustrated in **Figure 4.15(e)**, the strain-driven diffusion of Ga from the stem into the superlattice is also visible in this case and it extends around 1.5 periods. The thickness of the dots and barriers is homogeneous along the NW (0.7-1 nm dots and 3.5-3.7 nm barriers). The image contrast points to a slight increase

of the Ga content in the dots along the growth axis but this might be partially due to the increasing thickness of the AlN shell when moving from the top of the wire to the GaN stem, or to a slight bending of the NW crystal resulting in the heterostructure being better oriented with respect to the electron beam in the top part of the wire.

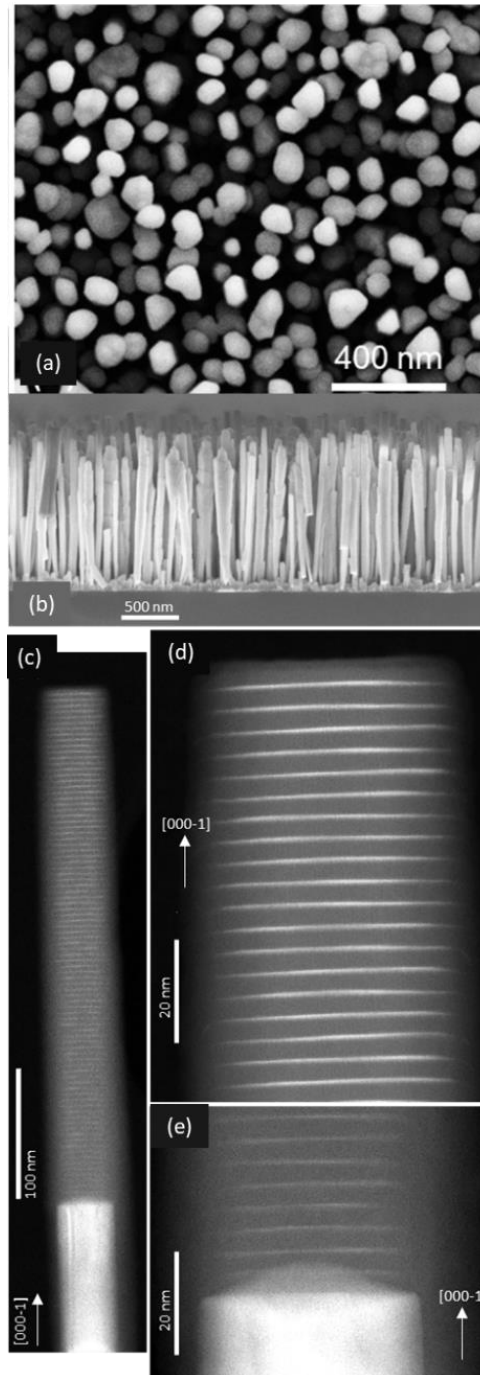


Figure 4.15: (a) Top-view SEM image of a sample containing GaN NWs with a SL consisting of 88 periods of $Al_{0.1}Ga_{0.9}N$ / AlN (sample E3863). (b) SEM image of as-grown sample E3865. (c-e) HAADF-STEM views of a NW, where dark/bright contrast corresponds to Al-rich/Ga-rich areas: (c) general view of the heterostructure, (d) zoomed image of the topmost periods of the heterostructure, and (e) the lowermost periods of the heterostructure.

The as-grown $\text{Al}_{0.1}\text{Ga}_{0.9}\text{N}/\text{AlN}$ QD SL ensemble was characterized using XRD in order to validate the periodicity of the structure, with the results illustrated in **Figure 4.16**. These measurements provide average information over a surface of several millimeters squared, and are hence sensitive to the dispersion of tilts and twists in the NW ensemble. Several satellites of the (0002) reflection of the SL are resolved, which confirms the thickness uniformity along the growth axis and the reproducibility of the period length from sample to sample (period = 4.3 ± 0.2 nm). The period measured by XRD for all the samples under study is listed in Table 4.1. It should be noticed that the (0002) reflection of GaN originated by the NW base is not located at the angular position of relaxed GaN ($2\theta = 34.57^\circ$), but at slightly larger angles, due to the uniaxial compressive strain induced by the AlN shell.

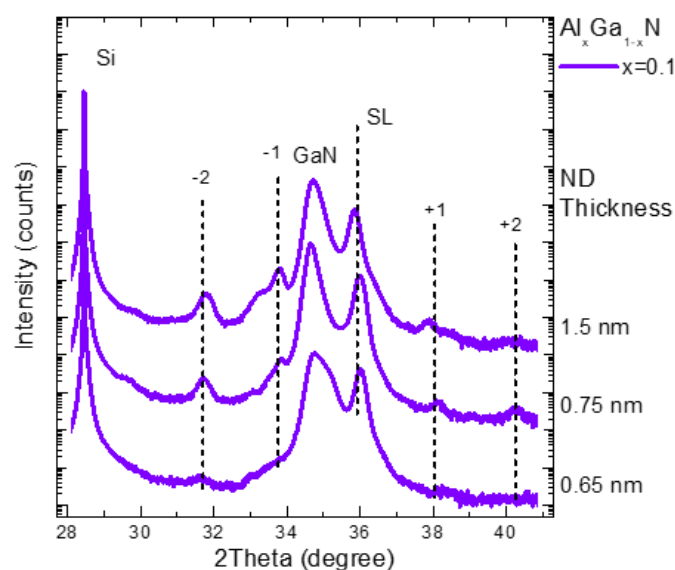


Figure 4.16: XRD ϑ - 2ϑ scans of the (0002) reflection of GaN NWs containing an 88-period $\text{Al}_{0.1}\text{Ga}_{0.9}\text{N}/\text{AlN}$ QD SL. The diffractograms are vertically shifted for clarity.

4.7.2. Optical properties

The normalized room-temperature PL emission from the GaN/AlN NW samples (E3898, E3861, E3862 and E3918) is displayed in **Figure 4.17** (green spectra), and the peak emission wavelength is summarized in **Table 4.1**. The emission shifts from 340-336 nm (samples E3857-E3898) to 265-277 nm (samples E3918-E3864). However, the blue shift comes with a monotonous decrease of the IQE at room temperature measured in the low-injection regime, which evolves from 63% to $\approx 30\%$, as illustrated in the inset of **Figure 4.17**.

The incorporation of aluminium in the dots allows for an additional blue shift of the emission, as depicted in **Figure 4.17** (pink spectra). For 10% of Al in the dots, the room temperature emission is still dominated by a single spectral line that can be tuned from 331 nm (E3858, 1.5 nm well thickness) to 258 nm (E3865, 0.65 nm well thickness). Like in the case of GaN dots a decrease of the IQE and an increase of the relative linewidth is observed as the emission shifts to shorter wavelengths (see **Table**

4.1). However, if we compare samples with GaN and $\text{Al}_{0.1}\text{Ga}_{0.9}\text{N}$ dots emitting at the same wavelength, the IQE is roughly the same (see inset of **Figure 4.17**). Therefore, we conclude that the presence of Al in the dots does not introduce any additional degradation of the optical properties.

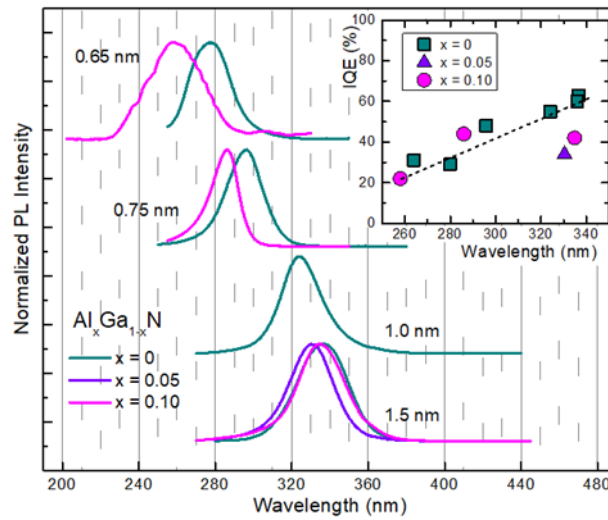


Figure 4.17: Room-temperature emission from the samples under study normalized to their maxima. The thickness of the AlGa_{1-x}N wells is indicated in the figure. The spectra are vertically shifted for clarity. The spectra from samples with 0.65 nm wells were measured by CL. The rest of the spectra were obtained from PL measurements. Inset: Variation of the IQE as a function of the peak emission wavelength. Different colours represent different content of Al in the wells. The dashed line is a guide for the eye.

As we have done for AlN/ GaN NWs, we have studied the variation of the CL spectra as a function of V_A , as shown in **Figure 4.18**. If the emission spectra are normalized to their maximum, the emission from the GaN base becomes visible only for $V_A > 5$ kV. This implies that the NW ensemble is compact enough to prevent important deviations of their behavior with respect to planar structures.

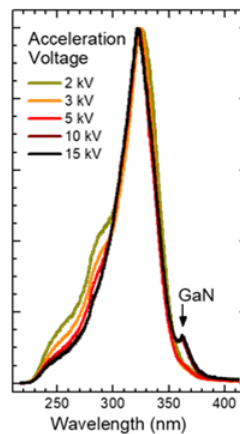


Figure 4.18: Normalized CL spectra of the E3863 structure as a function of the accelerating voltage. The emission from the GaN stem of the NWs is only resolved for $V_A > 5$ kV.

Finally, we have assessed the IQE of the samples by analyzing the variation of their emission, either photoluminescence (PL) or CL, as a function of temperature. As an example, **Figure 4.19(a)** displays the evolution of the PL spectrum as a function of temperature for a sample containing an $\text{Al}_{0.1}\text{Ga}_{0.9}\text{N}/\text{AlN}$ (0.75 nm / 3.75 nm) SL (sample E3863). **Figure 4.19(b)** depicts the integrated luminescence intensity from E3863 as a function of the inverse temperature measured both by PL and CL, showing that there is no significant difference between the two measuring techniques. From **Figure 4.19(b)** we can extract an IQE $\approx 44\%$ for sample E3863, emitting at 286 nm. This value decreases to $\approx 22\%$ for E3865, emitting at 258 nm. The results for sample E3859, presented in the inset of **Figure 4.19(b)**, show that the NW samples are stable enough to stand pulsed operation at high power densities up to around $50 \text{ kW}/\text{cm}^2$ without degradation of the IQE.

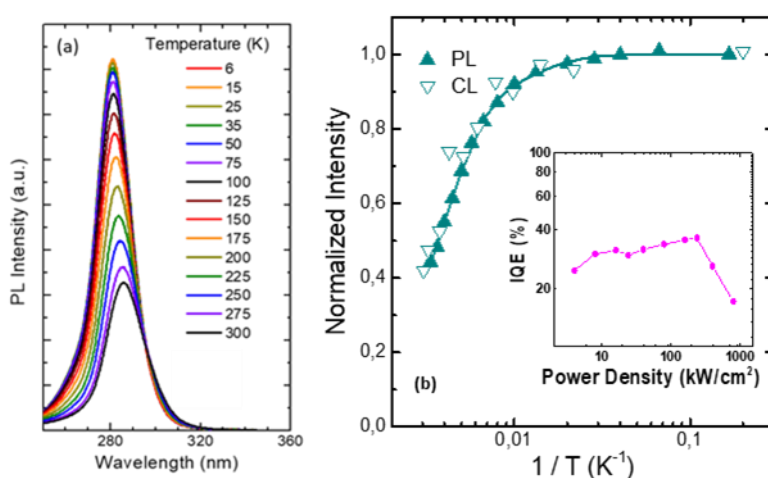


Figure 4.19: (a) Variation of the PL spectra as a function of temperature (sample E3863: 0.75 nm $\text{Al}_{0.1}\text{Ga}_{0.9}\text{N}$ / 3.75 nm AlN). (b) Variation of the integrated PL intensity of E3863, and the integrated CL intensity of E3863 as a function of the inverse temperature, normalized to their value at low temperature. The solid lines are fits to $1/[1 + A \exp(-E_a/(kT))]$, where E_a is a thermal activation energy, kT is the thermal energy, and A is a fitting constant ($E_a = 48 \pm 4 \text{ meV}$ and $A = 7 \pm 2$). Inset: Variation of the IQE as a function of the excitation power density, measured with a pulsed laser for sample E3859.

4.8. External quantum efficiency

In a further study, the efficiency of some of the NW samples in **Table 4.1** was evaluated in terms of EQE. For this purpose, we used a pulsed Nd-YAG laser ($\lambda = 266 \text{ nm}$, 2 ns pulses, repetition rate of 8 kHz) with two different values of pumping power, namely $100 \mu\text{W}$ and $50 \mu\text{W}$. The optically pumped sample was placed in an IE385836A-4 Thorlabs 2" integrating sphere, as described in **Figure 4.20**. The emitted light is collected by an SM05P Thorlabs UV photodetector. The signal obtained by exciting the sample was compared to the measurement of the obtained by replacing the sample with a reflector.

Measurements were performed on samples E3857, E3859, E3858, E3862, E3863, E3881ⁱ, E3899ⁱⁱ, E3901ⁱⁱⁱ, and E3911^{iv}, obtaining an average EQE = $3.42 \pm 0.55\%$, independent of the pumping power.

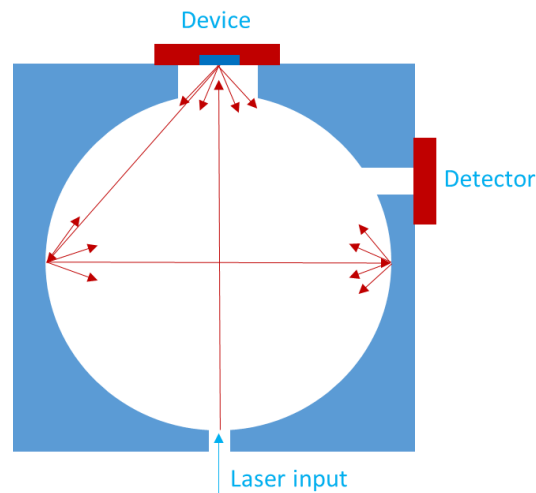


Figure 4.20: External Quantum efficiency measurement System.

4.9. Conclusion

In summary, we have presented a feasibility study of NW arrays as active media for electron-pumped UV emitters. The nanostructures under study consist of 400-nm-long $\text{Al}_x\text{Ga}_{1-x}\text{N}/\text{AlN}$ ($0 \leq x \leq 0.1$) QD superlattices grown on self-assembled GaN NWs by PAMBE on n-type Si(111) wafers. By growing the $\text{Al}_x\text{Ga}_{1-x}\text{N}$ sections under N-rich conditions and the AlN sections under stoichiometric conditions, we obtain QDs with highly homogeneous dimensions along the whole superlattice. When compared with the emission of planar samples with the same periodicity and thickness, GaN/AlN NW structures are less sensitive to nonradiative recombination, attaining IQE higher than 60% at room temperature, even under low injection conditions. Using pulsed optical excitation we demonstrate that the IQE remains stable for excitation power densities up to 50 kW/cm^2 . Experiments under electron pumping show that the NW superlattice is long enough to collect the electron-hole pairs generated by an electron beam with an acceleration voltage $V_A = 5 \text{ kV}$. By varying the dot/barrier thickness ratio and the Al content in the dots, we demonstrate the adjustment of the NW peak emission in the range from 340 to 258 nm.

This work describes the first assessment of NWs for application in electron-pumped UV sources and our results confirm the feasibility of the approach. Electron channelling effects can be compensated by an increase of the active region length by $\approx 60\%$ in comparison to planar layers. Using QD superlattices as active media, it is possible to keep the homogeneity of the dot geometry all along

ⁱ Repetition of E3857, undoped

ⁱⁱ Repetition of E3857, undoped

ⁱⁱⁱ Repetition of E3857, slightly Mg doped

^{iv} Repetition of E3861

the active region in order to obtain NW ensembles providing a single emission line in the deep UV range. Furthermore, we have demonstrated the stability of the NWs under electron pumping. Next validation steps should include an evaluation of the external quantum efficiency under electron pumping, lifetime in operation conditions, and x-ray emission. The results reported here are very promising for the fabrication of electron-pumped UV lamps which could find application in the domains of disinfection and water purification. An electron-pumped device can be scaled down to millimetre size, so that it can compete with LEDs in domains where efficiency and total output power are relevant. The implantation of such a technology would depend mostly on the cost per milliwatt of optical power, which could become competitive with LEDs thanks to the simpler material growth and processing. Keeping the acceleration voltage at 5 kV, the x-ray emission should be low enough for domestic use. In industrial applications where x-ray irradiation is not a problem, V_A could be increased and, in such a case, the feasibility of longer active regions should be further assessed.

Chapter 5: Correlative-microscopy investigation of InGaN/GaN QDs

InGaN/GaN nanostructures form the active region of III-nitride emitters (light emitting diodes, laser diodes, single photon emitters) in the visible spectral range. In order to understand the optical performance of these nanostructures it is necessary to obtain a direct correlation of alloy distribution and optical features. With this purpose in mind, La-APT is a unique tool to visualize the three-dimensional distribution of chemical species at the nanometer scale. Recent advances in this technique also offer the possibility of recording simultaneously the photoluminescence spectrum of the specimen under investigation. Here, we report the results of a correlative study of a stack of InGaN/GaN QDs, combining high-resolution chemical and optical characterization by La-APT and in-situ micro-photoluminescence, compared to ex-situ cathodoluminescence. We demonstrate that the structural information extracted from these techniques allows the precise modelling of these nanostructures, obtaining excellent agreement with the optical measurements. During the La-APT experiment, it was possible to resolve the emission of single QDs located in the 9 QD layers closer to the substrate. Single QD lines display a spectral shift during the experiment which is assigned to the relaxation of elastic strain due to material evaporation. Our study conveys an image of the Stranski-Krastanov InGaN/GaN QDs that is very different from the GaN/AlN systems. The thickness of the InGaN wetting layer is thicker than the part of the dots that protrudes above the layer, and the indium mole fraction in the wetting layer is lower than that in the dots. This perturbed Stranski-Krastanov growth is explained by the surfactant effect of indium, which favors planar growth.

For this study, HAADF- and BF-STEM analysis was performed by Dr. E. Di Russo, Dr. D. Cooper and Dr. A. Grenier. I was assisted by Dr. E. Bellet-Amalric with XRD. The complete study was accepted for publication as **“InGaN Quantum Dots Studied by Correlative Microscopy Techniques for Enhanced Light-Emitting Diodes”**, *Dimkou I. et al., ACS Appl. Nano Mater.* 2020, 3, 10, 10133–10143²⁶⁵.

5.1. Motivation

III-nitride semiconductors (AlN, GaN and InN) with wurtzite crystalline structure are the keystone of blue and green optoelectronics. In particular, few-nanometer-thick InGaN/GaN QWs and QDs form the active region of III-nitride emitters (light emitting diodes, laser diodes, single photon emitters).^{266–269} The localization of carriers in intentional grown (QDs) or unintentional formed [alloy fluctuations at the scale of the exciton Bohr radius (≈ 2.8 nm in GaN)] quantum confined systems may play a crucial role in their optical properties, having an impact on emission energies, oscillator strengths, and eventually on the recombination efficiency of the system.^{270,271} Even in the case of QWs, structural factors like alloy fluctuations, extended defects or strain inhomogeneities can induce a weak 3D confinement of carriers at the nanometer scale,⁶⁷ which reduces the radiative lifetime, but also broadens the emission spectra and possibly enhances Auger recombination,^{272,273} contributing to the efficiency droop in light emitting diodes.²⁷⁴ Although the effect of indium fluctuations on the luminescence properties has been extensively discussed, a key challenge has been to correlate optical and structural properties to reach

a full understanding of these 3D phenomena.

A similar situation occurs in the case of intentionally created QD structures,³⁵ whose optical signature can only be predicted by getting access to the 3D structure and chemical distribution with a resolution close to the atomic scale.^{36,37} In the case of QDs synthesized following the Stranski–Krastanov growth method, most studies correlate typical optical properties with typical structural properties, since the dispersion of size, shape and composition in the QD ensemble sets a limit to precise modeling. The analysis is easier in the case of the GaN/AlN system⁶⁸ since interdiffusion is negligible and the QD facets and wetting layer thickness are well defined.²⁷⁵ In contrast, the study of Stranski–Krastanov InGaN/GaN QDs^{35,151,276–278} presents a major challenge, since little is known about their shape, the thickness of their wetting layer and the distribution of indium in the QD+wetting layer ensemble.

For the study of InGaN nanostructures, TEM based techniques were called into question since the exposure to the imaging electron beam can induce alloy clustering and this is the case mostly for strong e⁻beams in high doses.²⁷⁹ In this direction, La-APT is a valuable alternative providing 3D chemical information.^{48,49} Furthermore, the possibility of analyzing the luminescence in situ during the La-APT measurement (the so-called photonic atom probe⁶⁰ or PAP technique) allows linking the emission lines to the atomic layers that are evaporated.⁶¹ However, quantitative La-APT of III-nitrides faces some particular challenges since the result depends on experimental parameters such as the electric field at the sample surface, the laser pulse energy and the sample temperature.⁶²

Here, we investigate the correlation of the spectral emission properties of Stranski-Krastanov InGaN/GaN QDs with their structural and chemical features, even at the level of a single QD. The structure of the QDs is defined in detail by combining the chemical information extracted by La-APT, the distribution of QD size and shape measured by TEM and AFM, and the superlattice period extracted from XRD measurements. The model of the QD structure is validated by the measured optical lines and those predicted by theoretical calculations. The study also reveals that the emission linewidth of the QD ensemble is mostly due to in-plane fluctuations of the indium content in the QDs and the dispersion of the QD diameter.

5.2. Characterization of the as-grown specimen

Self-assembled InGaN islands were grown by molecular-beam epitaxy on GaN-on-sapphire, following a Stranski–Krastanov growth mode. AFM, XRD and TEM studies were performed in order to provide structural information on the bulk sample. Strong blue photoluminescence of the dots is observed by CL measurements and the temperature dependence of the luminescence is exhaustively analyzed.

5.2.1. Growth procedure

We have grown three samples (E3868, E3869 and E3870) consisting of 40 periods of InGaN/GaN QDs deposited on commercial 3.5- μm -thick GaN-on-sapphire templates by PAMBE. The nominal QD height was 2.0 ± 0.2 nm and the nominal barrier thickness was ≈ 10 nm. The growth process was monitored by Reflection high-energy electron diffraction (RHEED). With the aim of incorporating different indium content in the InGaN QDs, the substrate temperatures were fixed at 409°C, 597°C and 587°C for the samples E3868, E3869 and E3870 respectively (calibrated by measuring the In desorption time, as described by S. Valdueza-Felip et al.¹⁵⁰).

The RHEED image of the samples E3868 and E3869 captured at the end of the growth is illustrated in **Figure 5.1** where we can see the (10-10) and (-1010) streaks in the $\langle 11\bar{2}0 \rangle$ azimuth. With the mixture of streak and spot patterns presented more clear in **Figure 5.1(b)**, RHEED seems very sharp indicating that the surface is not flat and contains 3D islands confirming the formation of quantum dots.

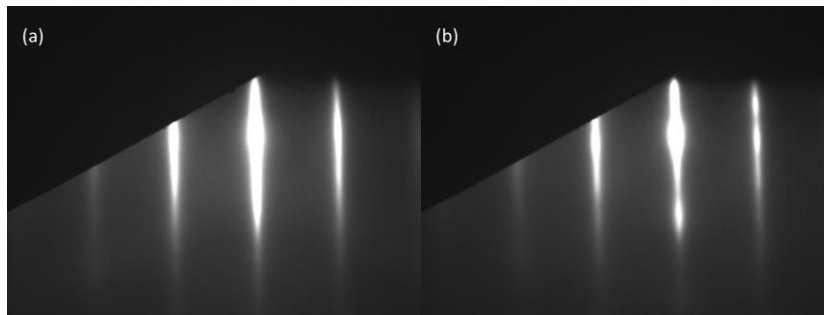


Figure 5.1: RHEED pattern of the samples (a) E3868 and (b) E3869.

5.2.2. Structural characterization

Figure 5.2 (a), (b) and (c) presents a 0.7×0.7 μm^2 AFM scan of the topmost uncapped InGaN QDs (QDs) layer of the samples E3868, E3869 and E3870 respectively. It shows a high density (mid- 10^{11} cm^{-2}) of QDs with a height = 1.5 ± 0.2 nm, = 0.9 ± 0.2 nm, for the samples E3868, E3869 respectively. Note that this value corresponds to the QD height above the wetting layer. For the sample E3870, the substrate was cooled down some minutes after the deposition of the last QD layer, so it is not comparable to the others, since QDs had the time to evolve in vacuum (ripening effect²⁸⁰). We also observed that the sample E3869 is the only sample with lower density of V-pits (defect which appears at the dislocation surface termination during the growth of InGaN/GaN superlattices), so we decided to study extensively this sample.

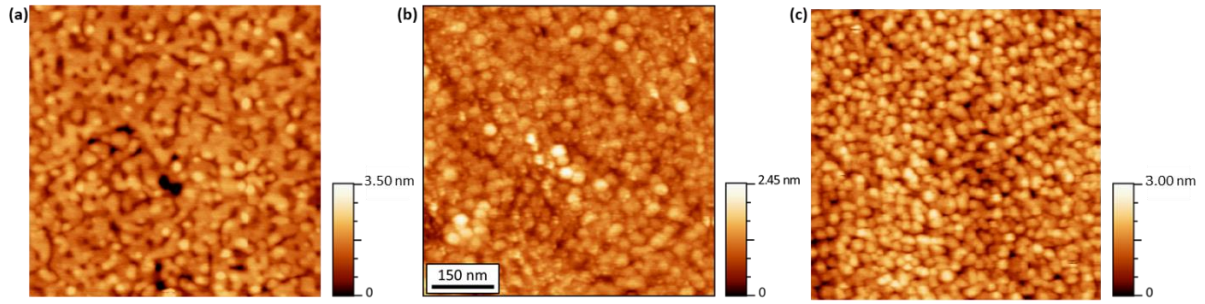


Figure 5.2: AFM scan of the InGaN/GaN QD sample under study. All scale bars are 150 nm.

From AFM measurements, it is difficult to extract reliable measurements of the QD base diameter since the expected value (10-20 nm^{152,281}) is comparable to the dimension of the AFM tip (see **Figure 3.26** and associated discussion in the **subchapter 3.5**). Using **Equation (3.5)** for the sample E3869 with the typical radius of TESPA-V2 tips (7 nm) and knowing that the commonly observed faceting of III-nitride QDs is {10-13}, forming an angle $\alpha \approx 30^\circ$ with the growing surface, the expected error would be $\Delta l = 3.8$ nm. Also, using **Equation (3.6)** with a tip radius $R = 7$ nm and QDs with $\alpha \approx 30^\circ$, the expected error in the measurements of QD height is $\Delta h = -1.1$ nm.

Looking back at **Figure 5.2**, the QD ensemble is dense, which makes it difficult to identify if the configuration is closer to **Figure 3.26(a)** or **3.26(b)** without supporting information from another characterization technique. Analyzing height profiles of **Figure 5.2**, the distance between QDs is in the range of 20-40 nm. However, TEM images of the sample (shown below) suggest a QD diameter in the range of 12-17 nm, and a typical in-plane diameter of 15.4 ± 1.4 nm is extracted from APT measurements, as described later in this chapter. Therefore, comparing these results, we conclude that the QDs are far enough to obtain a reliable measurement of the height by AFM, with an overestimation of the QD base diameter.

The BF-STEM image of the E3869 heterostructure in **Figure 5.3(a)** shows the 40 periods of InGaN/GaN QDs. HAADF- and high-resolution BF-STEM images of the specimen observed along [11–20] zone axis with higher magnification are presented in **Figure 5.3(b)-(d)**. The wetting layer is not well defined due to the high density of dots with a diameter smaller than the thickness of the lamella specimen, 70 ± 10 nm, which results in more than one dot being projected in the images. It is nevertheless possible to measure with atomic precision the height of the QD layer (including WL), which is 8 ± 1 ML, i.e. 2.0 ± 0.3 nm. The diameter of the QDs, estimated from the variations of contrast in the images, would be in the range of 12-17 nm.

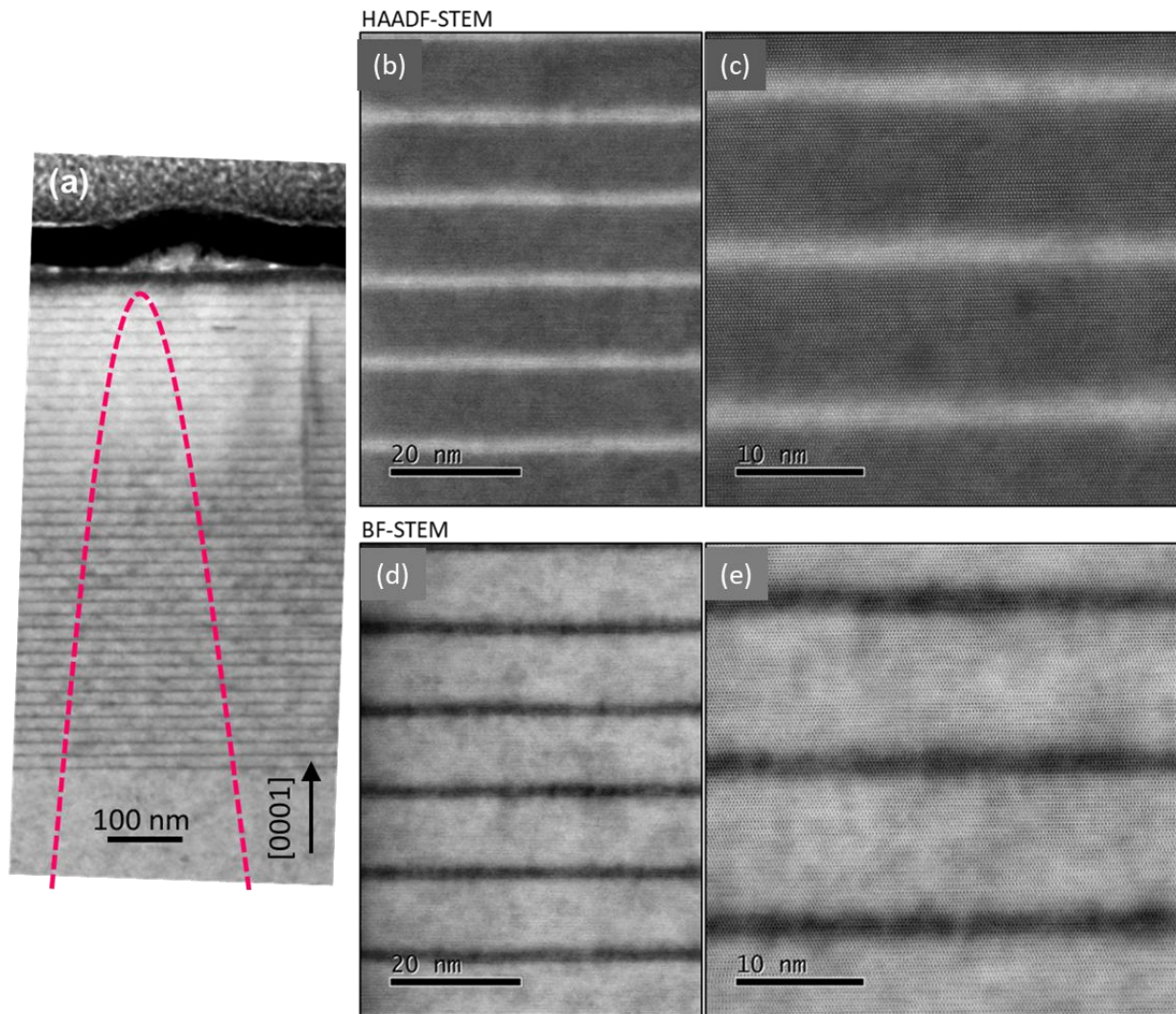


Figure 5.3: (a) BF-STEM image of the E3869 heterostructure showing the 40 periods of InGaN QDs. Cross-section (b,c) HAADF and (d,e) BF-STEM images of the InGaN/GaN QD superlattice viewed along the $\langle 11-20 \rangle$ zone axis.

Comparing the results of AFM and TEM, we can extract an estimation of the thickness of the WL (≈ 1.1 nm). This value should be taken cautiously, since the AFM analysis is performed in an uncapped QD layer, and the capping process can lead to morphological changes in the QD structures. In the case of GaN/AlN QDs grown by MBE, the geometry remains undisturbed during capping for growth temperatures below 730°C . At higher temperatures, we observed a reduction of thickness that was more severe in the case of plastic relaxation during the growth of the QD layer, i.e. QDs containing misfit dislocations.²⁸² In the case of InGaN/GaN grown by MBE, Figge et al. reported the complete dissolution of their InGaN QD structures when overgrown at 510°C .²⁸³ However, their uncapped QDs contained around 80% of In and there was evidence of plastic relaxation. Other groups have reported stable QD luminescence for InGaN QDs grown by MBE and capped at significantly higher temperatures ($550\text{-}640^\circ\text{C}$),^{152,284,285} and no effect of capping was observed in the case of InGaN/GaN QDs grown by metalorganic vapor phase epitaxy when the GaN barriers are grown at the same temperature as the QDs.²⁸⁶ In our case, TEM images show that the relaxation process is purely elastic and the GaN barriers

were grown at the same temperature as the InGaN QDs. Therefore, in a first approximation, we have considered that the QD height measured by AFM is also valid for capped QDs. The validity of this statement will be further discussed later.

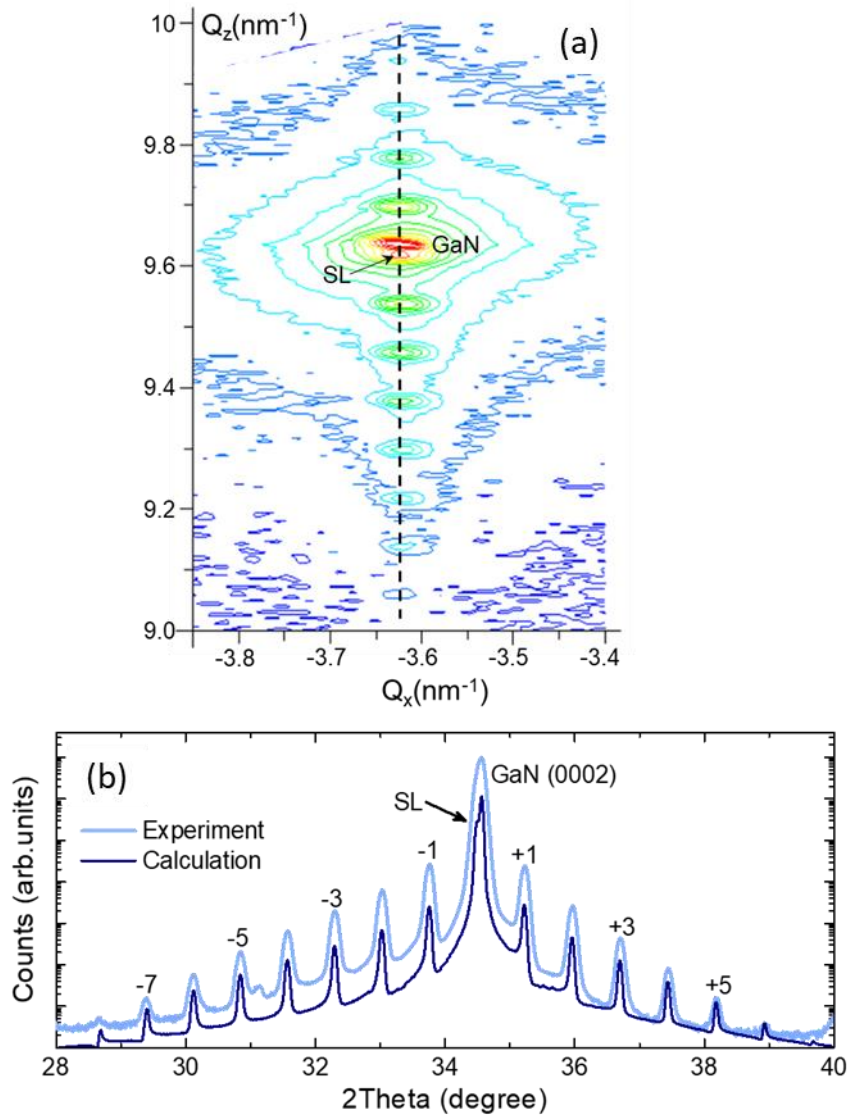


Figure 5.4: (a) Reciprocal space map around the (10–15) x-ray reflection of the GaN/InGaN QD SL grown on GaN. The dashed line outlines the shape of the tip specimen that is analyzed APT. (b) XRD ϑ -2 ϑ scan (light blue) recorded around the (0002) reflection of GaN. Labels indicate the (0002) reflection of GaN, and the (0002) reflection of the QD superlattice, with several satellites. The experimental result is compared with a theoretical calculation (dark blue).

To get access to the average superlattice period and strain state, we performed an XRD study. The reciprocal space map around the (10–15) x-ray reflection of the GaN/InGaN QD superlattice is reported in **Figure 5.4(a)**. The peak corresponding to the GaN substrate is located at the reciprocal lattice point $Q_x = -2/(a\sqrt{3}) = -3.625 \text{ nm}^{-1}$ and $Q_z = 1/(5c) = 9.625 \text{ nm}^{-1}$, where a and c are the in-plane and out-of-plane lattice parameters. The multiple peaks corresponding to the periodic heterostructure are aligned along $Q_x = -3.625 \text{ nm}^{-1}$, which demonstrates a pseudomorphic structure on GaN. Precise values

of the superlattice period and lattice parameters were extracted from the θ - 2θ x-ray diffractogram recorded around the (0002) reflection of GaN, depicted in **Figure 5.4(b)**. The experimental result is compared with a theoretical calculation using the Rigaku GobaFit software. The best fit is obtained assuming an average period of 12.6 ± 0.1 nm, and modeling the QDs as an InGaN layer with a thickness of 1.6 nm and an average indium composition around 10%. However, the values of InGaN layer thickness and alloy composition must be taken cautiously. The model assumes a pseudomorphic structure on GaN, with biaxial strain in the InGaN layers. In this situation, the out-of-plane strain is given by the expression $\varepsilon_{zz} = -(2c_{13}/c_{33})\varepsilon_{xx}$, where ε_{xx} is the in-plane strain and c_{13} and c_{33} are elastic constants (we use here $c_{13} = 106$ GPa and $c_{33} = 398$ GPa for GaN,⁸¹ and $c_{13} = 92$ GPa and $c_{33} = 224$ GPa for InN,⁷⁹ with a linear interpolation for the ternary alloy). This approximation is not valid in the case of QDs.^{287–289} Therefore, the fit in **Figure 5.4(b)** tells us only that the QDs can be approximated by layers with a thickness of 1.6 nm and an average out-of-plane lattice parameter equivalent to that of $\text{In}_{0.1}\text{Ga}_{0.9}\text{N}$ fully strained on GaN, without any conclusion about the indium mole fraction in the QDs.

5.2.3. Optical spectroscopy

The three as-grown samples were characterized by PL measurements at room temperature, as illustrated in **Figure 5.5**. The peak emission wavelength is around 408 nm for the E3868, and shifts to 430 nm and 440 nm for E3869 and E3870 respectively, i.e. lower growth temperature results in higher indium incorporation and red shifted luminescence. This means that the samples were grown in a regime where the indium incorporation is controlled by the substrate temperature.

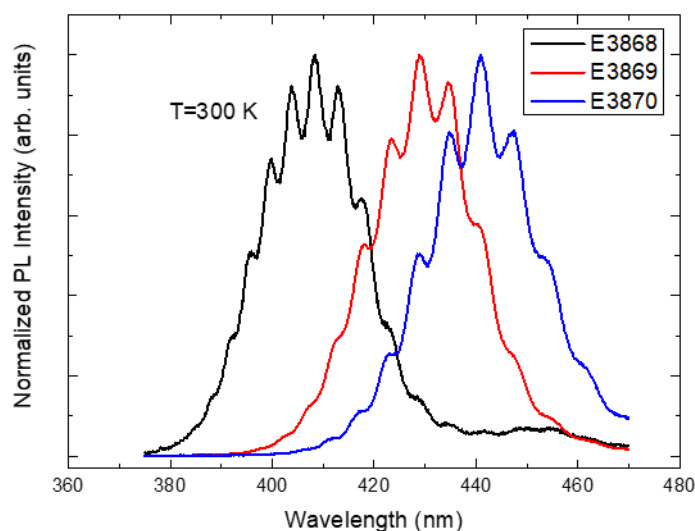


Figure 5.5: PL measurements for the three samples.

The E3869 sample was characterized by temperature-dependent CL, as illustrated in **Figure 5.6(a)**. The peak emission wavelength is around 413 nm at 5 K, and shifts to 422 nm at 300 K. The evolution of the CL integrated intensity normalized to its low temperature value as a function of the inverse temperature is displayed in **Figure 5.6(b)**.

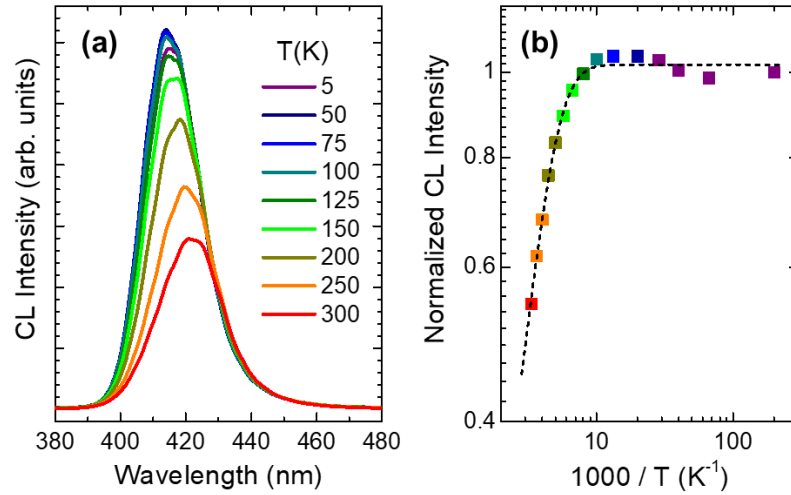


Figure 5.6: (a) CL spectra of the as-grown sample recorded at different temperatures. (b) Normalized CL intensity as a function of the inverse temperature. The dashed line is a fit that assumes dominance of a monoexponential nonradiative process.

The slight increase of the luminescence from 5 K to 50 K can be explained by the improved transfer of carriers from the barriers to the dots when increasing the temperature. The integrated intensity remains constant in the range of 50 to 100 K and drops sharply for higher temperature due to the activation of nonradiative recombination paths.²⁹⁰ The dashed line is a fit that assumes dominance of a monoexponential nonradiative process, so that the variation of the normalized intensity is described by

$$\frac{I(T)}{I_0} = \frac{1}{1 + A \exp(-E_a/kT)} \quad (5.1)$$

where I_0 is the integrated intensity at low temperature, A is a fitting parameter, E_a is the activation energy of the nonradiative process, and kT is the thermal energy. In the figure, $A = 11 \pm 3$ and $E_a = 67 \pm 5$ meV, which is comparable to the values reported in the literature.^{151,152} The ratio of the room-temperature and low-temperature CL integrated intensities, which is generally considered as an estimation of the internal quantum efficiency, is 52%. The stability of the luminescence with temperature supports our assumption that the QDs were not dissolved during the QD process (see comparison of InGaN/GaN QD and QW luminescence in Gačević, *et al.*¹⁵²).

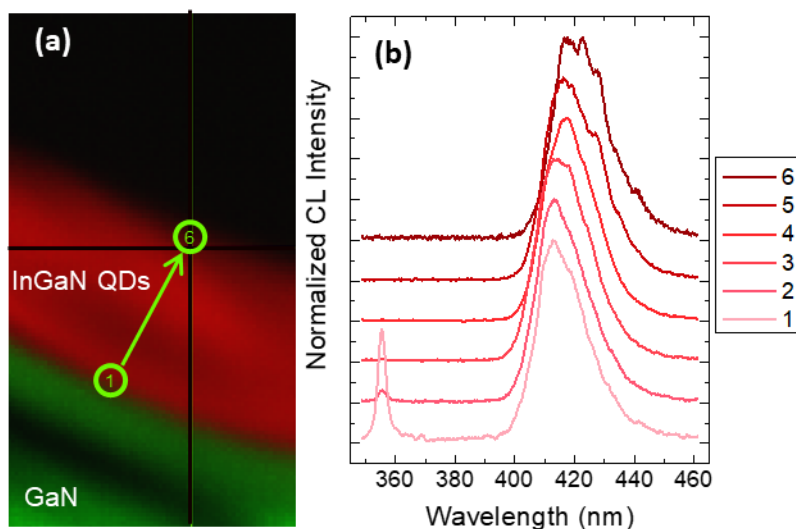


Figure 5.7: (a) Cross-section CL mapping of the as-grown structure, measured at 8 K. The area where the GaN emission (line at 355 nm) is dominant appears in green, and the area where the InGaN QD emission is dominant (417-419 nm) appears in red. (b) CL spectra measured at extracted at points of (a), moving from the GaN/InGaN interface (1) to the surface (6).

To gain further insight on the origin of the CL linewidth, we have performed cross-section CL mapping of a cleaved edge of the sample, with the result displayed in **Figure 5.7** which presents (a) a hyperspectral cross-section CL image of a cleaved edge of the as-grown sample, and (b) CL spectra extracted at various points of (a), moving from the interface between the GaN and the InGaN QD superlattice (1) to the surface of the sample (6). The spectra recorded close to the interface presents a narrow emission line at 355 nm, characteristic of GaN, and a broad emission that peaks at 317-319 nm, which is assigned to the QDs. In (a), the area where the GaN line is dominant is colored green and the area dominated by the QD emission is colored red. Analyzing the CL spectra at different points along the growth axis and focusing on the emission from the InGaN QDs, we observe that the linewidth is rather constant along the structure (with full width at half-maximum FWHM ≈ 20 nm), and comparable to that obtained in the top-view configuration. There is a slight shift of the peak emission along the growth axis, but its value (≈ 2 nm) is of the order of the spectral resolution of the spectrometer (± 0.8 nm) and significantly smaller than the linewidth. Therefore, the spectral broadness of emission is due to in-plane QD inhomogeneties, rather than to a drift of the growth conditions.

At this point, we face some limitations hampering a proper correlation of optical and structural properties, and thus the achievement of a complete understanding of these 3D objects. AFM and TEM provide information on the QD height and density. In addition, XRD gives precise information on the periodicity of the structure. However, we only have a rough estimate of the lateral dimensions of the dots, and no reliable information on the indium distribution in the structure.

5.3. Characterization of the APT specimen

In order to analyze the InGaN/GaN QDs using La-APT, field emission tip specimens were fabricated by dual SEM/FIB. It is hence important to be rigorous in the characterization of the specimens before their introduction in the APT system, if results are to be extrapolated to the as-grown material. Several APT tips were analyzed using in-situ μ PL measurements performed during the La-APT evaporation under different analysis conditions. FlexTAP APT system has been also used to extract precise chemical analysis.

5.3.1. Structural and ex-situ optical characterization

Aiming to analyze the InGaN/GaN QDs using La-APT, field emission tip specimens were fabricated by standard FIB based lift out followed by annular milling procedures. Further details on the specimen preparation are described in the **Chapter 3**. The FIB process can cause several kinds of damage:²⁹¹ amorphization of the surface due to Ga implantation¹⁷² and redeposition of milled material, and formation of voids and bubbles at the surface, which further agglomerate into metallic nano-blitters.²⁹² In the case of InGaN, indium redistribution and evaporation is also possible.²⁹³

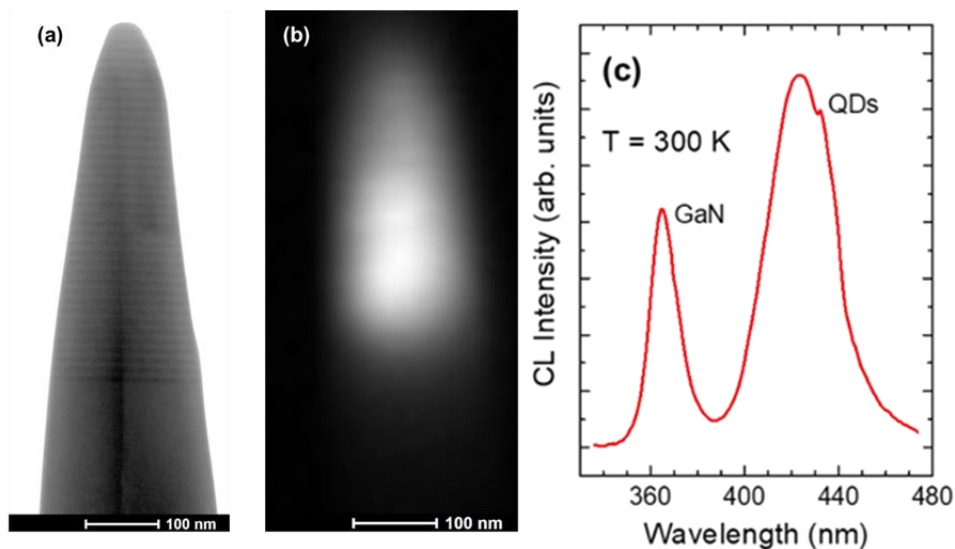


Figure 5.8: (a) TEM image of the tip after FIB preparation. (b) Panchromatic CL map of the needle-shaped specimen in (a). (c) CL spectrum at room temperature, where labels indicate the emission bands associated to the GaN substrate and to the QD superlattice.

FIB prepared tips were first observed in TEM, as illustrated in **Figure 5.8(a)**. The optical activity of the needle-like samples was then measured in the CL system. **Figure 5.8(b)** is a panchromatic CL map of the tip in (a), suggesting that the entire superlattice is optically active. **Figure 5.8(c)** displays the integrated CL spectrum at room temperature, which presents an emission line at 364 nm that originates from the GaN substrate, and a large band peaked at 422 nm that is assigned to

recombination in the QDs.

Figure 5.9 displays a hyperspectral CL map of an APT specimen at 5 K. The regions where the GaN and InGaN QD emission are dominant appear in red in **Figure 5.9(a)** and **Figure 5.9(b)**, respectively. **Figure 5.9(c)** presents the CL spectrum of the whole tip and red is the selected area that originates from the GaN substrate and corresponds to the red region presented in **Figure 5.9(a)**. **Figure 5.9(d)** presents the CL spectrum of the whole tip and red is the selected area that is assigned to recombination in the QDs, corresponding to the red region presented in **Figure 5.9(b)**.

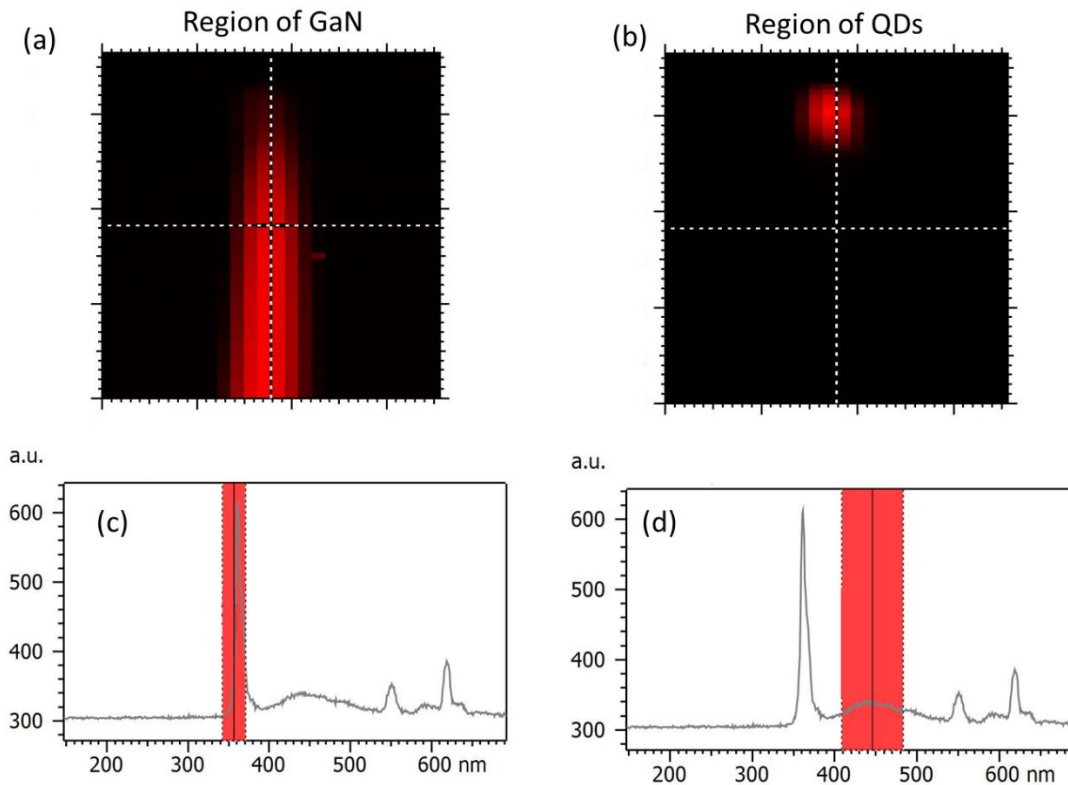


Figure 5.9: CL mapping of the APT specimen, measured at 5 K. (a) Area where the GaN emission originates; resulting from selecting the spectral region marked in red in the CL spectra in (c). (b) Area where the InGaN QD emission originates; resulting from selecting the spectral region marked in red in the CL spectra in (d).

The evolution of the emission spectrum along the tip is shown in **Figure 5.10** where (a) is a hyperspectral CL mapping showing the emission from GaN and from the QD region, and (b) presents CL spectra extracted by integrating slices of (a) moving from the interface between the GaN and the InGaN QD superlattice (7) to the specimen apex (1). In **Figure 5.10(a)**, the area where the GaN line is dominant is colored green and the area dominated by the QD emission is colored red. Looking at (b), the spectra recorded close to the interface present a narrow emission line at 355 nm, characteristic of GaN, and a broad emission that peaks at 417-419 nm, which is assigned to the QDs. The peak wavelength and linewidth remain approximately constant along the tip (spectral shift smaller than 2 nm and the emission linewidth \approx 20 nm).

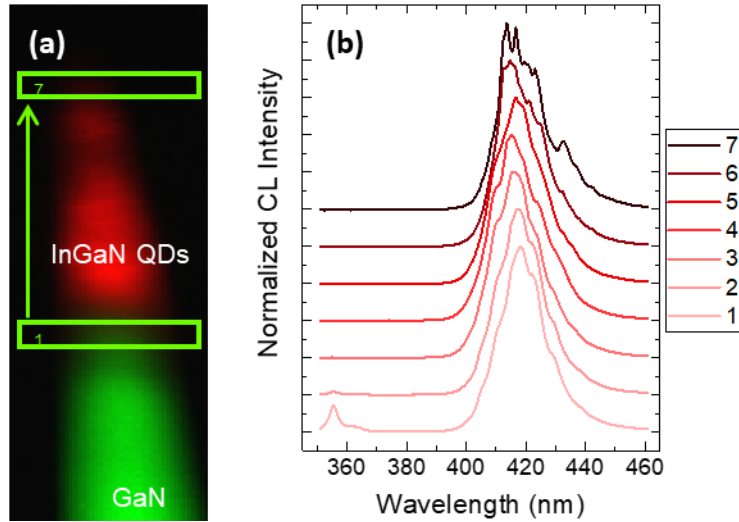


Figure 5.10: (a) CL map of the APT specimen, measured at 8 K. The area where the GaN emission (line at 355 nm) is dominant appears in green, and the area where the InGaN QD emission is dominant (417-419 nm) appears in red. (b) CL spectra measured at extracted from different areas of (a), moving from the GaN/InGaN interface (7) to the apex (1).

The variation of the CL integrated intensity as a function of temperature is described in **Figure 5.11(a)**. The dashed line is a fit to **Equation (5.1)** where $A = 33 \pm 12$ and $E_a = 38 \pm 10$ meV, and the room-temperature to high-temperature integrated intensity rate is around 11%. The energy of the QD emission of the tip shape sample remained the same as the as-grown sample, which confirms that the FIB protocol did not introduce significant loss or rearrangement of indium in the specimen. However, the reduced activation energy and increased prefactor A points to a moderate enhancement of nonradiative recombination, due to the higher surface-to-volume ratio.

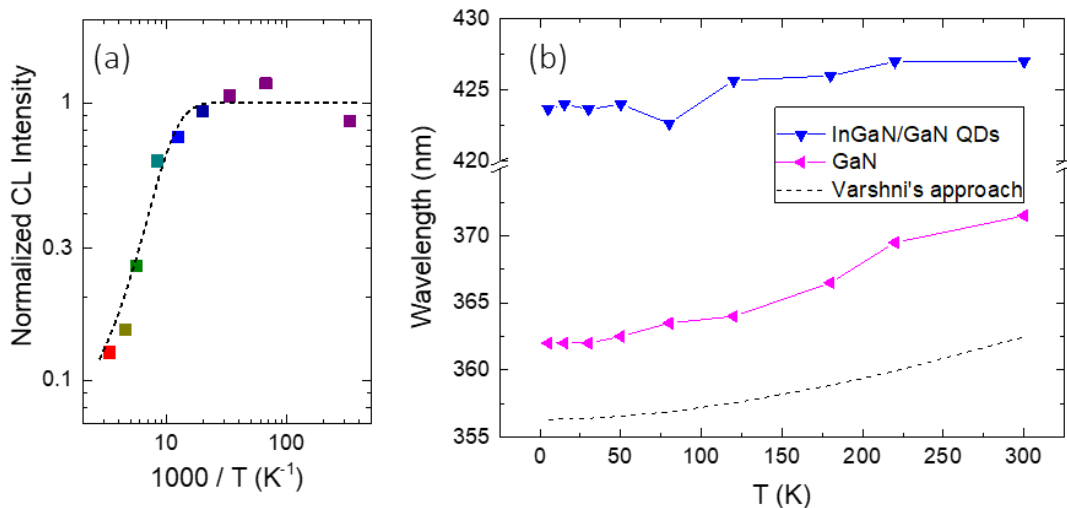


Figure 5.11: (a) Normalized CL intensity of the specimen as a function of temperature. The dashed line is a fit that assumes dominance of a monoexponential nonradiative process. (b) The temperature dependence of the CL peak position for GaN in purple and InGaN/GaN QDs in blue. The evolution of the GaN band gap calculated using Varshni's equation (parameters taken from ^{152,294}) is represented in black dashed line.

Figure 5.11(b) presents the evolution of the CL peak energy as a function of temperature for GaN and InGaN/GaN QDs measured on a tip studied. The evolution of the CL peak energy from GaN follows Varshni's equation: $E_G(T) = E_G(T = 0 \text{ K}) - \alpha T^2 / (T + \beta)$, with $\alpha = 0.59 \text{ meV/K}$ and $\beta = 600 \text{ K}$ for GaN¹⁵² and $E(0) = 3.48 \text{ eV}$ ²⁹⁴. Regarding the emission from the QDs, the trend is similar, but more noisy, due to the broadness of the line, which involves transitions from multiple QDs. A slight deviation from Varshni's equation could be understood as due to the different efficiency of the multiple QDs involved in the transition. On the contrary, intra-dot localization in alloy fluctuations would lead to a major deviation from Varshni's equation, with the emission describing a spectral S-shaped evolution as a function of temperature¹⁵². This is clearly not the case in our experiment.

5.3.2. Photonic atom probe analysis

Here, we present the La-APT experiments. First the tips were introduced in a photonic atom probe (PAP) system that enables *in-situ* μPL spectroscopy measurements during the La-APT process, as described in the **Chapter 3**. *In-situ* μPL measurements were performed during the La-APT evaporation after determining the best conditions carrying out preliminary measurements adjusting the laser pumping power.

In order to determine the best experimental conditions to perform simultaneous μPL and APT characterization, we have first measured *in-situ* μPL as a function of the laser pumping power, as shown in **Figure 5.12(a)**. During these preliminary measurements, we used a repetition rate of 3.8 MHz, adjusting the laser power in the range of 25 to 700 μW . In these spectra, it is possible to identify the narrow emission of the GaN substrate at 358 nm and a broad band peaked around 411 nm, which is assigned to the InGaN QDs. Plotting their intensity as a function of the laser power [**Figure 5.12(b)**], the luminescence from GaN scales linearly. On the contrary, the intensity of the QD emission saturates for laser power higher than 300 μW . **Figure 5.12(c)** shows the evolution of peak wavelength of the luminescence from GaN and InGaN QDs as a function of the laser power. The FWHM of the emission is indicated as an error bar. The GaN line presents a red shift starting at 300 μW , with an increase of the FWHM. The behavior at high pumping power points to a local increase of the tip temperature, whose effect is dominant over a potential band-filling phenomenon. The spectral shift of the QD band is not so obvious due to the broad emission, but the FWHM increases clearly for laser power higher than 300 μW .

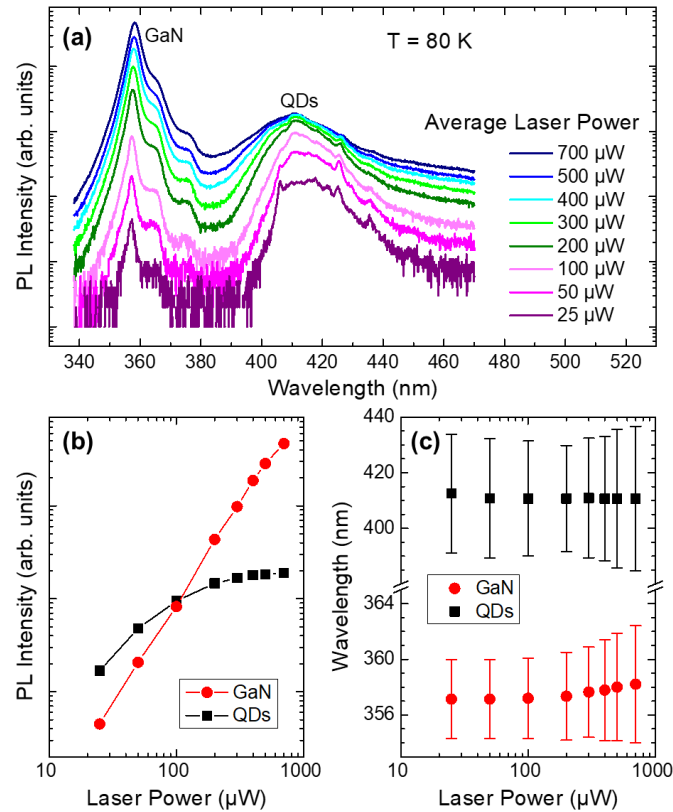


Figure 5.12: μ PL measurements performed before the La-APT evaporation of InGaN/GaN QDs with different laser power. The experiment was performed at 80 K and the frequency and wavelength of laser were 300 kHz and 260 nm, respectively. (b) Intensity of the GaN and QD PL lines as a function of the laser power, extracted from (a). (c) Peak wavelength of the GaN and QD PL lines as a function of the laser power. The FWHM is indicated as an error bar.

In view of the preliminary results described in the previous paragraph, we decided to perform the APT experiment with a laser energy corresponding to the 300 μ W experiment, which is the point where the tip starts warming up due to pumping. However, during the APT experiments coupled with μ PL the laser frequency was reduced to 340 kHz to allow a time delay between pulses longer than the expected time of flight of the ions from the specimen during the APT process.²⁹⁵

The *in-situ* μ PL emission during the PAP analysis of the last 15 InGaN/GaN QD layers is displayed in **Figure 5.13**. **Figure 5.13(a)** shows μ PL spectra recorded *in-situ* during the La-APT characterization of InGaN/GaN QDs at 80 K. Tip contained 15 QDs layers and we selected spectra that were recorded during the evaporation of each GaN barrier. As described for the preliminary experiments in **Figure 5.12**, the peak at 358 nm is related to the carrier recombination in the GaN buffer, whereas the broad band at around 415 nm is assigned to carrier recombination in the InGaN QDs. **Figure 5.13(b)** displays the APT reconstruction of the APT specimen obtained simultaneously with the μ PL measurements.

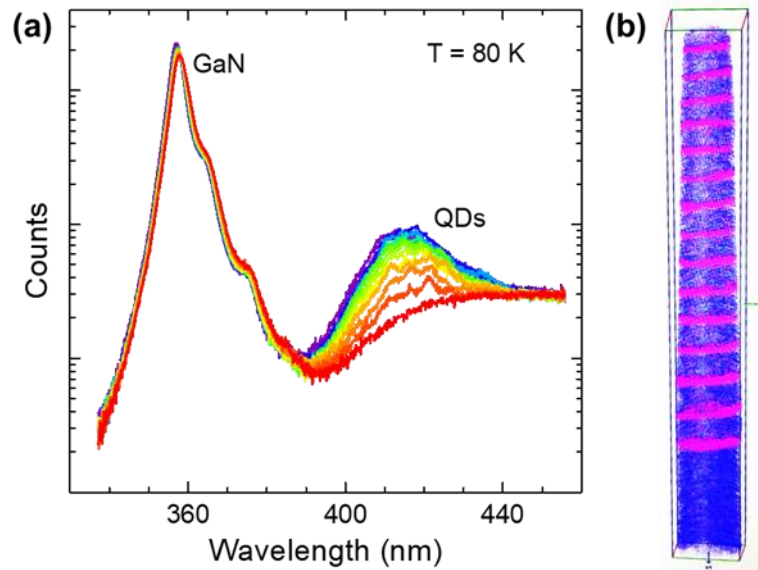


Figure 5.13: (a) Evolution of the μ PL spectrum during the evaporation of the APT specimen. The spectra represented in the figure were recorded during the evaporation of each barrier. (b) 3D reconstruction of the In atom distribution in the analysed sample. The APT experiment was performed simultaneously with the μ PL measurements. Ga atoms are represented in blue and In atoms are represented in magenta.

Figure 5.14(a) shows a zoomed view of the emission of the QDs acquired at different stages of the tip evaporation. The legend indicates the number of QD layers that were left in the tip when the PL spectra were recorded. Figure 5.14(b) shows the 3D APT reconstruction of the indium signal when only 5, 3 and 2 layers remain in the specimen, as an example. In Figure 5.14(a), the initial luminescence peak of the whole tip appears broad, as it results from the overlap of the emission of multiple QDs. The spectra do not display major variations during the evaporation of the 5 topmost QD layers (shown in Figure 5.13). However, during the evaporation of the last 10 layers, the total emission intensity decreases, as expected from the reduction of the tip volume containing multiple QDs. As only a few dots remain in the tip, the spectra present a multi-peak structure due to fluctuations of the size and the indium content of the QDs.³⁷ When only 5-2 layers are left, we can identify the signature of single InGaN QDs. The QD signal disappears when there is still one InGaN layer, which means that most probably that first InGaN layer does not contain any dot. Dashed lines in Figure 5.14(a) are Lorentzian fits that identify the QDs contained in layer 2: a first line (QD1) is located at 422.7 nm with FWHM = 1.2 nm, and a second emission line (QD2) peaks at 417.36 nm with FWHM = 0.87 nm. A third peak (QD3) that disappeared after evaporation of layer 3 was located at 413.2 nm with FWHM = 1.3 nm.

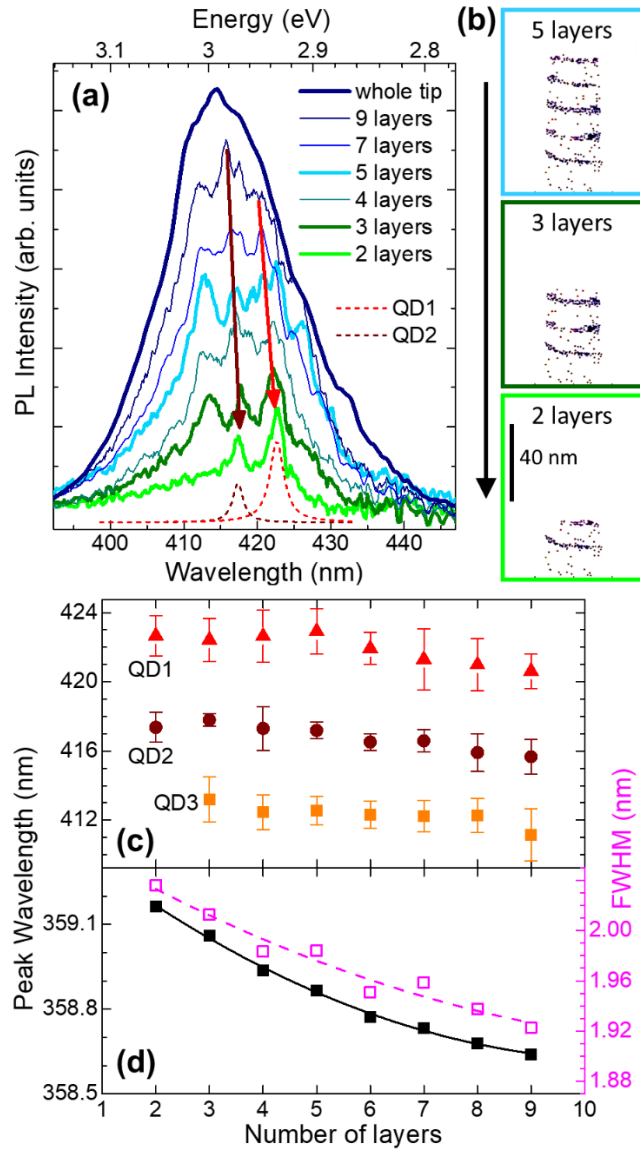


Figure 5.14: (a) In-situ μ PL measurements performed during the La-APT evaporation of InGaN/GaN QDs. The experiment was performed at 80 K. The legend indicates the number of layers that remain in the specimen when recording the PL data. Dashed lines are Lorentzian fits that identify the QDs contained in layer 2. Their evolution of the emission of these two QDs is marked with arrows. (b) Indium 3D APT reconstruction of the last 2, 3 and 5 layers of QDs detected during analysis. (c) μ PL peak wavelength of three QDs (the signals of QD1 and QD2 disappeared after evaporation of layer 2, as shown in (b), and QD3 had disappeared after evaporation of layer 3). The FWHM is indicated as an error bar. (d) μ PL peak wavelength of the GaN emission vs. number of layers remaining on the specimen during evaporation. The evolution of the FWHM is indicated with open symbols (right axis).

The evolution of peak wavelength and FWHM of these QD lines (QD1, QD2, QD3) during the evaporation of the tip is described in the **Figure 5.14(c)**, and **Figure 5.14(d)** shows the evolution of the μ PL line assigned to the GaN buffer (at 358 nm, shown in **Figure 5.13**). The QD emission lines present a red shift of around 2 nm during the APT process of the last 9 QD layers.²⁹⁶ In contrast, the GaN line presents only a slight red shift of around 0.55 nm. The different behavior of QDs and GaN points out

that the shift is not thermally induced but rather strain related. Strain is the result of mechanical stress, and it leads to a change of the semiconductor band gap (which can be estimated using the band deformation potentials) and the generation of piezoelectric polarization. During the experiment, two sources of mechanical stress act on the QDs, namely the stress resulting from the lattice mismatch between GaN and InGaN and the stress induced by the electric field during the APT measurement. It is hence important to assess the magnitude of both sources of stress to know if the spectral shift is associated to the material properties or to the experimental conditions.

Therefore, in order to understand the evolution of the emission of QDs and GaN during the APT experiment, we have calculated the strain distribution in the QDs. The stress associated with the lattice mismatch between GaN and InGaN results in a deformation of the lattice to minimize the elastic energy accumulated during the growth of the sample, as illustrated in **Figure 5.15**.

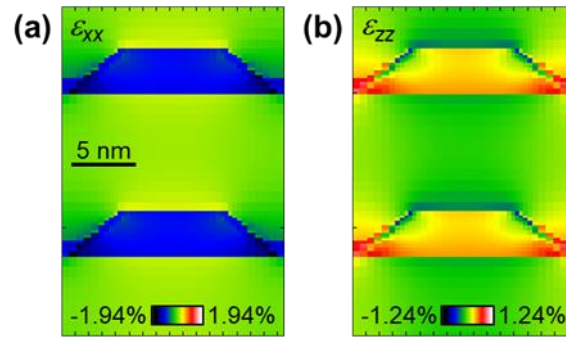


Figure 5.15: Calculation of the strain distribution in the QDs: (a) in-plane strain (ϵ_{xx}) and (b) out of plane strain (ϵ_{zz}).

Figure 5.15 shows the distribution of the (a) in-plane (ϵ_{xx}) and (b) out-of-plane (ϵ_{zz}) strain in two InGaN QDs in the center of the QD stack. The simulation process is described in **Chapter 3**. The geometry and indium distribution in the simulated structure corresponds to the nominal values, illustrated in **Figure 5.15(a)**. The wetting layer is defined separately from the QDs having homogeneous concentration different from the QD whose alloy doesn't present any gradient. The morphology of InGaN QD is defined as a regular hexagonal prism following the form of GaN QDs knowing that the In incorporation in the dot is low and will not drastically affect its form.

As expected, the in-plane lattice is compressed, and the out-of-plane lattice is expanded. However, the out of plane deformation is significantly smaller than expected in the case of biaxial strain. This is clearly visible in the image, where the value of ϵ_{zz} inside the QDs is significantly smaller (yellow-orange) than its value in the wetting layer (red), in spite of the higher indium content in the dots (13%) with respect to the wetting layer (6%). The difference is due to the presence of GaN in contact with the QD side facets, which imposes in a uniaxial compressive stress on the dots.

In the case of the InGaN QDs, there is an in-plane compressive stress due to the growth of InGaN on top of GaN, and a uniaxial compressive stress along the c crystal axis (growth direction) due to the

GaN that is in contact with the QD side facets. The stress along the c axis in the QDs can be calculated as

$$\sigma_{zz} = 2c_{13}\varepsilon_{xx} + c_{33}\varepsilon_{zz} \quad (5.2)$$

where c_{ij} are elastic constants and ε_{xx} and ε_{zz} are the in-plane and out-of-plane strain. With the values of strain in **Figure 5.15** ($\varepsilon_{xx} = -1.15\%$ and $\varepsilon_{zz} = 0.33\%$), the stress is estimated at $\sigma_{zz} = -1,16$ GPa. Note the negative sign, which indicates that the stress is compressive along c . In this strain configuration, using the deformation potentials from Vurgaftman and Meyer,⁷³ the InGaN band gap increases by ≈ 106 meV with respect to the relaxed value. When evaporating the layers on top of a certain QD, the uniaxial stress imposed by the material surrounding the dot decreases, but the in-plane stress due to the GaN underlayer remains. Therefore, evaporation should lead to an expansion of the lattice along c (higher ε_{zz}). Keeping $\varepsilon_{xx} = -1.15\%$ and releasing the uniaxial stress ($\sigma_{zz} = 0$) would lead to $\varepsilon_{zz} = 0.64\%$, resulting in an increase of the band gap by only ≈ 74 meV with respect to the relaxed value. In addition to this modification of the band gap, the increase of ε_{zz} induces an enhancement of the piezoelectric polarization. These two phenomena explain a red shift during the APT process of the order of magnitude observed in **Figure 5.14(c)**.

The GaN PL signal in **Figure 5.14(d)** stems from the GaN layer below the QD superlattice. The topmost nanometers of this layer are strained by the presence of the InGaN QDs on top. Our Nextnano calculations point out strain that can reach $\varepsilon_{xx} = 0.15\%$ and $\varepsilon_{zz} = -0.26\%$ ($\sigma_{zz} = -0.71$ GPa) right below an InGaN QD. Using again the deformation potentials in ref.⁷³, the strain increases the GaN band gap by ≈ 7.6 meV. This strain is fully relaxed when the InGaN material is evaporated, which should lead to a slight red shift of the PL signal, as experimentally observed.

On the other hand, during the APT experiment, a high positive voltage in the range of $V_{DC} = 5-10$ kV is applied to the InGaN/GaN tip, which results in an electric field F at the tip that can be estimated by²⁹⁷

$$F = \frac{V_{DC}}{kR} \quad (5.3)$$

where $k \approx 7$ is a geometrical factor and R is the curvature radius of the tip apex. Free carriers generated by laser illumination drift due to the electric field and holes accumulate at the needle apex screening the electric field inside the semiconductor material. However, the field induces a mechanical stress along the tip, which is given by

$$\sigma_F = \frac{1}{2}\varepsilon_0 F^2 \quad (5.4)$$

where ε_0 is the vacuum permittivity. As we evaporate the sample, V_{DC} increases and the radius of the tip, R , increases. Tracing those values, the average electric field when the apex evolves along the 9 deepest QD layers can be estimated to be in the range 8-10 MV/cm, corresponding to a field-induced stress in the range $\sigma_F \approx 0.25$ GPa to $\sigma_F \approx 0.42$ GPa. As the electric field points towards the detector, the stress is uniaxial, tensile, along the c axis of the semiconductor crystal. The field-related stress σ_F has the opposite direction of σ_{zz} ; however, both σ_F and σ_{zz} increase during the experiment (σ_{zz}

becomes less negative and σ_F becomes more positive). However, it should be kept in mind that σ_F is at least 4 times smaller than σ_{zz} in the QDs, and about half the value of σ_{zz} in the GaN material right below the superlattice. Furthermore, σ_F is expected to increase only by 10% for an increase of the tip curvature radius of 5%. Therefore, we can conclude that it is the variation of the stress induced by the lattice mismatch that dominates the spectral shift of the PL during the APT measurement. This is further supported by the fact that, at the beginning of the experiment, there is no major difference in the PL peak energy with and without electric field.

5.3.3. Chemical analysis by atom probe tomography

Here, it should be mentioned that the PAP requires the use of a fast APT detection system, at the expense of a lower detection efficiency and accuracy in assessing composition. Therefore, in order to quantify the alloy composition within InGaN layers, La-APT measurements were performed using a CAMECA FlexTAP system, equipped with an aDLD.¹⁷⁷ **Figure 5.16(a)** shows the indium site fraction map obtained through the analysis of 18 InGaN QD layers present in a 3D APT reconstruction. The InGaN layers contain In-rich regions with a typical in-plane diameter of 15.4 ± 1.4 nm and typical In-site fraction $\approx 13\%$, connected by the wetting layer, a thinner InGaN layer with an In-site fraction $\approx 6\%$. The shape and size of these In-rich regions correspond to InGaN QDs rather than to random alloy fluctuations.²⁹⁸ This picture is confirmed by the complementary isosurface analysis of one of the QD layers [marked with a square in **Figure 5.16(a)**], which is reported in **Figures 5.16(b)** and **5.16(c)**. **Figure 5.16(b)** displays the isosurface corresponding to an In-site fraction of 14% (in red), representing a single QD. The diameter of the QD is 15.0 ± 0.5 nm, with a height of 2.0 ± 0.1 nm. On the other hand, the isosurface corresponding to an In site fraction of 6% [displayed in **Figure 5.16(c)**] shows a layer connecting neighboring QDs, consistent with the wetting layer. The combination of both isosurfaces provides a consistent representation of composition and morphology of both wetting layer and QD.

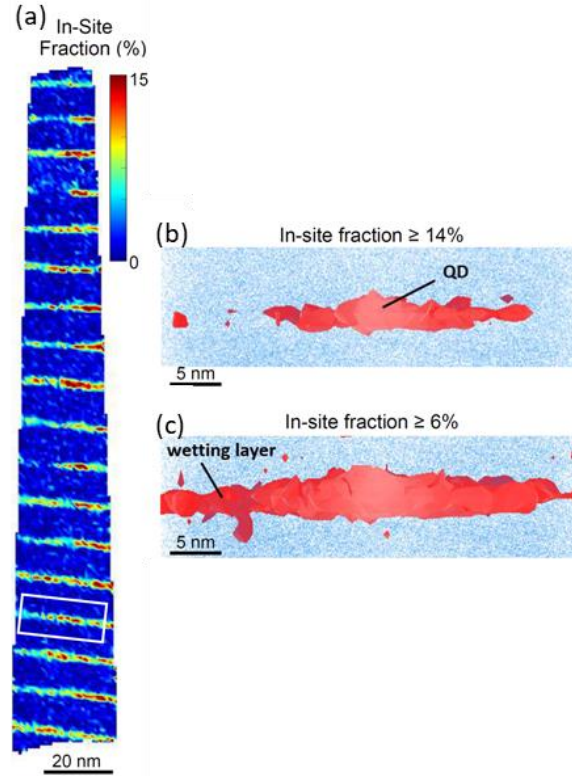


Figure 5.16: (a) Indium site fraction map calculated from an APT 3D reconstructed volume. In this two-dimensional representation, the composition is integrated over 10 nm in the direction perpendicular to the page. (b-c) In red, isosurfaces enclosing (b) the QD region (indium fraction $\geq 14\%$), and (c) the wetting layer (In fraction $\geq 6\%$), extracted for the layer indicated in **Figure 5.16(a)**.

5.3.4. Modeling the quantum dot structure

At this point, combining the result of STEM, XRD, AFM and La-APT, we have a complete description of the QD structure, including the period of the superlattice (12.6 nm, from XRD), the height of the QDs (2.0 nm, from STEM), the QD height above the wetting layer (0.9 nm from AFM), and the In content of the QDs and of the wetting layer (13% and 6%, respectively, from APT). To validate these results, we have compared the optical emission with theoretical calculations of the electronic structure using the geometrical and chemical parameters listed above. A schematic description of the simulated structure is presented in **Figure 5.17(a)**, and a complete description of the modelled cell and conditions are described in the previous paragraphs in this chapter. In a first stage of the 3D simulations, we obtain the strain distribution in the structure. The in-plane and out-of-plane components of the strain are presented in **Figure 5.15**. In the center of the dot, the $\varepsilon_{zz}/\varepsilon_{xx}$ ratio is -0.284 , which confirms a significant deviation from the biaxial strain configuration, where $\varepsilon_{zz}/\varepsilon_{xx} = -(2c_{13}/c_{33}) = -0.556$.

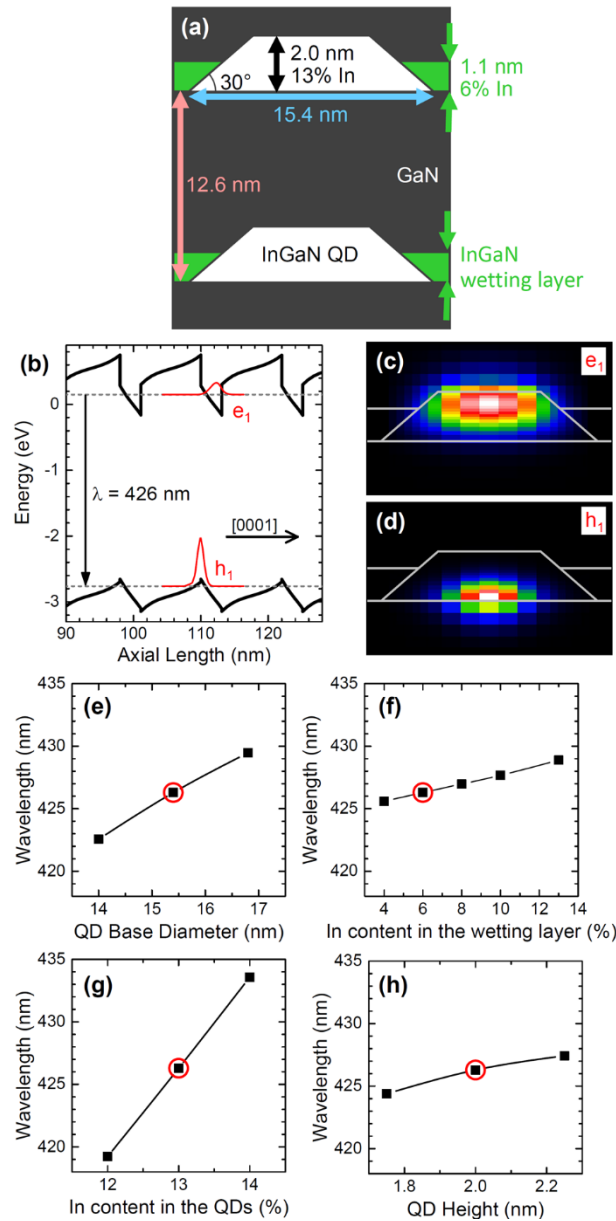


Figure 5.17: (a) Schematic description of the QDs with composition and dimensions extracted by combination of XRD, AFM, TEM and APT measurements. (b) From 3D Schrödinger-Poisson calculations at room temperature, band profile along [0001] crossing the center of the QDs, with the (c) electron and (d) hole probability distribution obtained by projecting their squared wavefunctions. (e-h) Calculation of the emission wavelength at room temperature as a function of the (e) QD base diameter, (f) indium content in the WL, (g) indium content in the QD, and (h) QD height. In (e-h), red circles outline the result of the simulation with the input parameters described in (a).

Taking into account the In content and the calculation of the elastic strain, the results are consistent with XRD measurements: Assuming that the structure is well described by **Figure 5.17(a)** and with an $\text{In}_{0.06}\text{Ga}_{0.94}\text{N}$ wetting layer that is biaxially strained and $\text{In}_{0.13}\text{Ga}_{0.87}\text{N}$ QDs with $\varepsilon_{zz}/\varepsilon_{xx} = -0.284$, the average lattice parameter in a period of the superlattice is approximately the same as in an InGaN/GaN QW superlattice with the same thickness and pseudomorphic, 1.6-nm-thick $\text{In}_{0.1}\text{Ga}_{0.9}\text{N}$ QWs, i.e. the structure used for the XRD calculation presented in **Figure 5.4(b)**. The consistency of the

results with the structural characterization data supports our initial assumption that the fact of capping the QDs with GaN does not introduce a significant perturbation of their morphology.

Taking the strain distribution into account, the band diagram of the 3D structure was calculated. The band profile along [0001] axis crossing the center of the QDs is displayed in **Figure 5.17(b)**. The electron and hole quantum confined levels are calculated in a QD in the center of the stack. The electron–hole transition at room temperature is predicted to occur at 426 nm, in agreement with the experimental CL peak wavelength. **Figure 5.17(c)** and (d) show the electron and hole probability distribution, respectively. The polarization-induced internal electric field in the dots shifts the electron wavefunction towards the QD apex, whereas the hole wavefunction is located deep into the base of the hexagonal truncated pyramid. However, the separation of electron and hole along the growth axis remains relatively small due to the small QD height.

For the purpose of gaining some insight into the variation of the emission wavelength from one dot to another, we performed calculations changing the QD diameter, In content in the wetting layer, In content in the QD, and the QD height [**Figure 5.17(e)**, (f), (g), and (h), respectively] in ranges that reflect the experimentally revealed structural/chemical fluctuations. Red circles in these figures outline the result of the simulation with the nominal input parameters described in **Figure 5.17(a)**. The emission wavelength is particularly sensitive to fluctuations of the indium content in the dot: adjusting the In content from 12% to 14%, the emission shifts from 419 to 434 nm [**Figure 5.17(g)**]. There is also a high sensitivity to the QD base diameter, with the emission shifting from 423 to 430 nm when the base diameter increases from 14.0 to 16.8 nm [**Figure 5.17(e)**]. Note that this shift is larger than that obtained by changing the QD height by ± 1 ML (approximately ± 0.25 nm), in **Figure 5.17(h)**. Keeping in mind that the PL emission of the QDs have a FWHM around 22 nm at room temperature [from **Figure 5.6(a)**], the linewidth seems mostly due to in-plane fluctuations of the In content in the QDs and the QD diameter.

5.3.5. Sample uniformity and reproducibility of the results

The correlation of PAP and of the structural parameters issued by TEM has also been performed at the level of a second tip as described in **Figure 5.18** and confirming the reproducibility of the results and the homogeneity of the sample. PL and CL measurements were performed in several points of the as-grown sample (10×10 mm²) and we did not observe significant variations in terms of intensity or spectral location of the emission. Then, as a whole, we fabricated with FIB preparation 27 tips, coming from different parts of the sample. The TEM images in **Figure 5.3** were taken from a 70-nm-thick lamella specimen processed by FIB. However, it was verified that the results were consistent with TEM images of 11 tips. Eight tips were characterized using *ex-situ* CL. The emission from the dots was systematically observed and its spectral location was consistent with the PL and CL results in the as-grown sample, and with μ PL measurements in 3 other tips. Two tips were examined coupling μ PL in-situ with La-APT, allowing the identification of the signature of single QDs in the first layers of the stack. **Figure 5.14(a)**

displays the results from one of the tips, and those of the second tip are shown in **Figure 5.18**. Precise chemical mapping using La-APT [**Figure 5.16(a)**] was performed on one tip.

The reproducibility of the measurements and the consistency of the various measurements and calculations confirms the reliability of obtained results and the homogeneity of the sample.

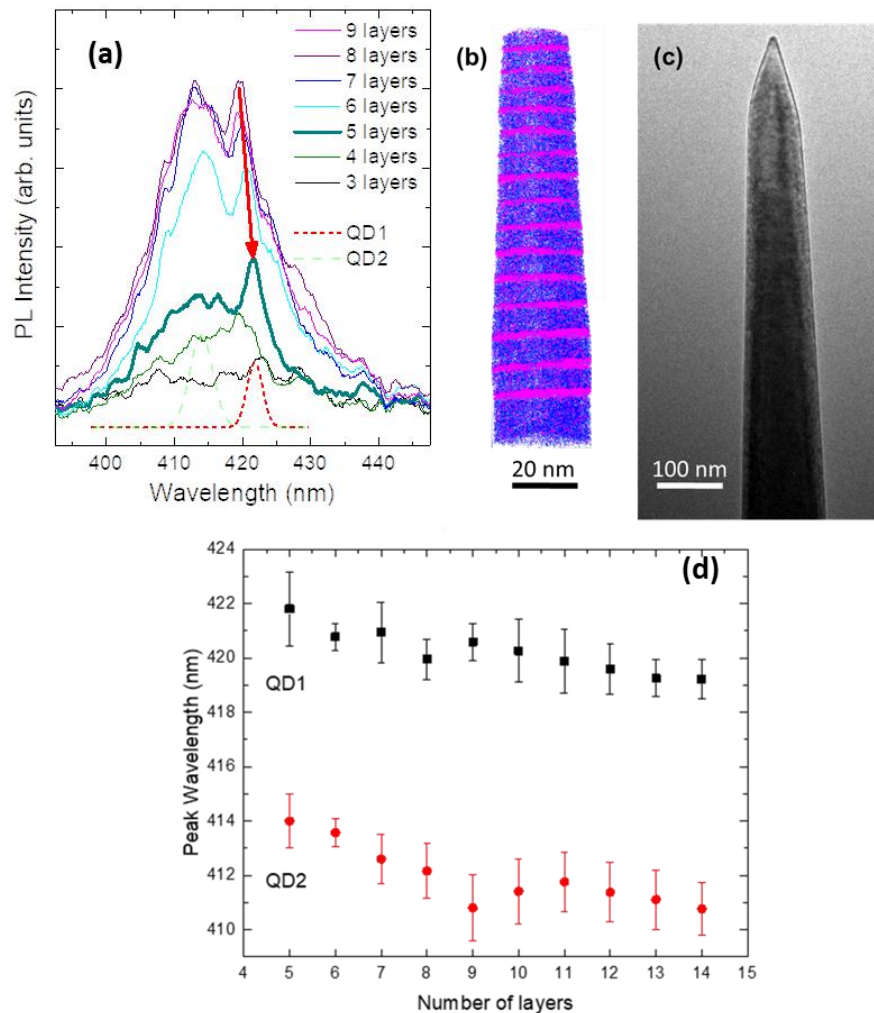


*Figure 5.18: (a) Evolution of the μ PL spectrum during the evaporation of the second APT specimen. The spectra represented in the figure were recorded during the evaporation of each barrier. The legend indicates the number of QD layers that were left in the tip. The dashed-line peaks are a Lorentzian fit of the emission lines that appear in the spectrum labelled “5 layers”. (b) 3D reconstruction of the In atom distribution in the analysed sample. The APT experiment was performed simultaneously with the μ PL measurements. Ga atoms are represented in blue and In atoms are represented in magenta. (c) BF-STEM image of the same tip before being introduced into the APT equipment. (d) μ PL peak wavelength of two QDs (the signals of QD1 and QD2 disappeared after evaporation of layer 5, as shown in (a)). The FWHM is indicated as an error bar. Note that these emissions red shifted during the evaporation of the tip, as observed for the emission lines from the first specimen [see **Figures 5.14(a)** and **5.14(c)**].*

In summary, the excellent agreement between the theoretical calculations and the experimental optical features show that the model extracted from structural and chemical characterization provides

a good description of this InGaN/GaN QD system. This model conveys an image of the InGaN/GaN QDs that is very different from the Stranski-Krastanov growth in the InGaAs/GaAs or GaN/AlN systems, where the dots and wetting layer can be distinctly and separately visualized. On the contrary, in the structure under study, the thickness of the wetting layer is thicker than the part of the QDs that protrudes above the layer. The dots look rather the coexistence of a thickness undulation and a local increase of the In mole fraction. This perturbed Stranski-Krastanov growth is caused by the presence of indium at the growth front, with a surfactant effect that favors planar growth.^{125,299} However, these nanostructures behave optically as QDs, with an enhanced stability of the luminescence at high temperature thanks to their capability to confine free carriers a three-dimensional volume with a size comparable that of the exciton in InGaN.

5.4. Conclusions and prospects

To conclude, we have performed a correlative microscopy study of a stack of self-assembled InGaN/GaN (2 nm / 10 nm) QDs embedded in a needle-shaped atom probe specimen fabricated by FIB. Comparative optical characterization of the as-grown sample and the atom probe specimen shows that there was no loss or rearrangement of indium during the FIB process. This allows the extrapolation of the characterization results to the as-grown sample. We have performed spectroscopic (*in-situ* micro-photoluminescence and *ex-situ* cathodoluminescence) and structural (XRD, AFM, STEM and APT) measurements, to get a full view of the sample at the nanometer scale. During APT measurement of the 9 QD layers closer to the substrate, it was possible to resolve single QD emission lines. The spectral red shift observed in these single QD lines during the APT process was assigned to the relaxation of elastic strain due to the material evaporation. Theoretical modeling of the QDs considering the experimental values of their size and indium distribution predicts room temperature photoluminescence at 426 nm, in excellent agreement with the measured spectra. Furthermore, the spectral linewidth of the as-grown sample is explained as due to in-plane fluctuations of the QD In content and diameter. These results confirm the relevance of PAP studies to provide a complete view of the InGaN QDs, and shows the potential of this technique for the analysis of nanostructured materials.

In terms of nanomaterials, a conclusion of this study is that Stranski-Krastranov InGaN/GaN QDs look like a thickness undulation and a local increase of the In mole fraction. The thickness of the wetting layer is comparable to the QD height, and the indium content in the wetting layer is significantly lower than the indium content in the QDs. The nanostructures behave optically as QDs, but these structural parameters can have an important impact on the design of the active region of a light emitting device, since they affect the band diagram and carrier transport properties.

In particular, we have shown that PAP can be used in samples containing a large set of nanoscale emitters in order to isolate the optical emission of few of them by a controlled reduction of the optically active volume induced by field evaporation. Furthermore, the technique allows the correlation of the

3D image of the chemical composition of a few light emitters contained in a nanoscale object with their spectral signature. This opens perspectives for the application of this technique to super-resolution studies, to discriminate the optical emission of neighboring QDs, or to strictly correlative studies, in which the 3D chemical map of a single QD is correlated with its optical signature.

Chapter 6: Effect of structural and point defects on InGaN/GaN QDs

In order to study the effect of structural defects on the luminescence of InGaN QDs, we have performed a correlative microscopy study of three stacks of InGaN/GaN QDs grown at different substrate temperatures, each stack consisting of 3 layers of QDs. Decreasing the substrate temperature along the growth axis leads to an increased density of structural defects. However, the first QD layers behave as traps for non-radiative point defects, so that the luminescence intensity increases towards the surface, in spite of the higher density of threading dislocations. During APT experiments combined with in-situ micro-photoluminescence, it was possible to isolate the optical emission of a single QD located in the topmost QD stack, closer to the sample surface. The single QD line displayed a spectral shift during the experiment confirming the relaxation of elastic strain due to material evaporation.

In this work, the HAADF-STEM analysis of the as-grown material was performed by Dr. E. Di Russo, Dr. D. Cooper and Dr. A. Grenier. The entire study has been submitted for publication and it is currently available online as as **“A Photonic Atom Probe Analysis of the Effect of Extended and Point Defects on the Luminescence of InGaN/GaN Quantum Dots”**, *Dimkou I. et al.*, arXiv:2106.03649, 2021³⁰⁰.

6.1. Introduction

III-Nitride LEDs have reached their maturity and are now a standard commercial product that finds wide application, for example in lighting and signalling. However, some unsolved problems remain. The efficiency droop that appears associated with Auger phenomena sets a performance limit^{301,302}, which is currently circumvented through electronics and increasing the number of LED chips needed to maintain the high efficiency. The indium distribution in the active QWs plays a relevant role on the Auger recombination rate. The use of self-assembled QDs as active media has been proposed as an approach to attenuate the droop^{303,304}. On the other hand, the wall-plug efficiency is maximum for devices that emit in the blue range, but it decreases markedly for green LEDs, with a higher In content in the active region, therefore higher alloy inhomogeneities and higher density of misfit-related defects. These problems become even more acute in III-nitride based red LEDs, still in development³⁰⁵. It is hence important to perform correlated optical/structural studies at the nanoscale, to understand the role of defects on the performance of light emitters. The correlation of TEM and La-APT provides visualization of chemical inhomogeneities at the nanometer scale, and sheds some light on their correlation with the device optical performance. This method has been first used for InGaN/GaN QWs by Bennet et al.³⁰⁶. The first systematic study by Riley et al.³⁰⁷ compared the correlated scanning transmission microscopy (STEM) and APT data obtained on different sets of InGaN/GaN QWs in NW LEDs with the spatially resolved cathodoluminescence (CL) spectra collected on other wires from the same sample. We have recently demonstrate the application of this technique

to the study of the indium distribution in Stranski-Krastanov InGaN/GaN QD layers ²⁶⁵, attaining excellent correlation between the structural/chemical study, optical measurements and 3D theoretical calculations of the electronic structure of the QDs.

In this work, we analyse the optical performance of 3 stacks of InGaN/GaN QDs grown at different substrate temperature, each stack consisting of 3 layers of InGaN QDs. Lowering the substrate temperature leads to an increased density of structural defects. However, the luminescence efficiency of the sample does not correlate with the structural quality. On the contrary, higher emission intensity is observed in more defective low-temperature layers. This result reveals the predominant role of point defects in the luminescence properties of InGaN nanostructures, and highlights the relevance of inserting InGaN underlayers to bury non-radiative point defects. Thus, in the topmost, more defective layer of QDs, the signature of single QD emission is observed in APT specimens.

6.2. Description of the as-grown sample and properties

The test structure was synthesized by PAMBE, and the growth process was monitored by RHEED. In order to explore the role of the growth temperature and material quality on the optical properties of InGaN QDs, we designed sample containing 3 stacks of 3 layers of self-assembled $\text{In}_x\text{Ga}_{1-x}\text{N}/\text{GaN}$ (2 nm/12 nm) QDs, separated by 70 nm of GaN [see schematic description in **Figure 6.1(a)**]. This structure was deposited on a GaN-on-sapphire template and capped with 500 nm of GaN. At the beginning of each QD stack, we changed the growth temperature and adjusted the indium flow to compensate for the change in the indium desorption rate. The substrate temperature was calibrated by measuring the In desorption time, as described elsewhere ¹⁵⁰. It decreased monotonically during the growth, fixed at 615°C, 580°C and 550°C for the first, second and third QD stack, respectively. The precise regime is described in **Chapter 3**.

Figure 6.1(b) presents a HAADF-STEM image of the heterostructure. STEM studies were performed in an aberration-corrected FEI Titan 80-300 microscope operated at 200 kV, using HAADF and BF detectors. In the **Figure 6.1(b)**, three InGaN/GaN QDs stacks can be identified: InGaN is located in discontinuous horizontal lines with clear contrast, whereas GaN has darker contrast due to the difference in atomic number. **Figure 6.2** displays a HAADF-STEM zoomed image of the three stacks in the centre of the superlattice showed in the **Figure 6.1(b)**. **Figure 6.2(b)** depicts the integrated intensity of the HAADF-STEM image in **Figure 6.2(a)** analysed along the red rectangle outlined in the figure. The contrast fluctuations in the InGaN layers confirm the presence of InGaN QDs. In **Figure 6.1(b)**, threading dislocations (white vertical lines) propagating from the underlying GaN substrate are outlined with yellow arrows. In the proximity of these initial defects, additional threading dislocations appear at the GaN/InGaN interface (see also **Figure 6.2**). This points to the generation of interfacial misfit dislocations, which thread upward ³⁰⁸, a well-known phenomenon in In-rich InGaN/GaN heterostructures. The local strain in In-rich areas may cause the decomposition of (a+c)-type threading dislocations to produce an a-type and a c-type dislocation threading towards to

the surface. The a-type component of the dislocation bends to an interfacial direction giving rise to a misfit dislocation with Burgers vector $b = \frac{1}{3}\langle 11-20 \rangle$ in the $\{0001\}$ slip plane. When the misfit dislocation attains an In-poor area, the local change in strain provides the driving force for the dislocation to climb and to the $[0001]$ direction. The decrease of temperature during the growth is an important factor promoting the generation of misfit dislocations and the general decline of material quality^{309–311}, in agreement with our STEM observations. Moreover, it is known that In can incorporate along the defects, forming In nanoparticle arrays extending along the growth direction³¹².

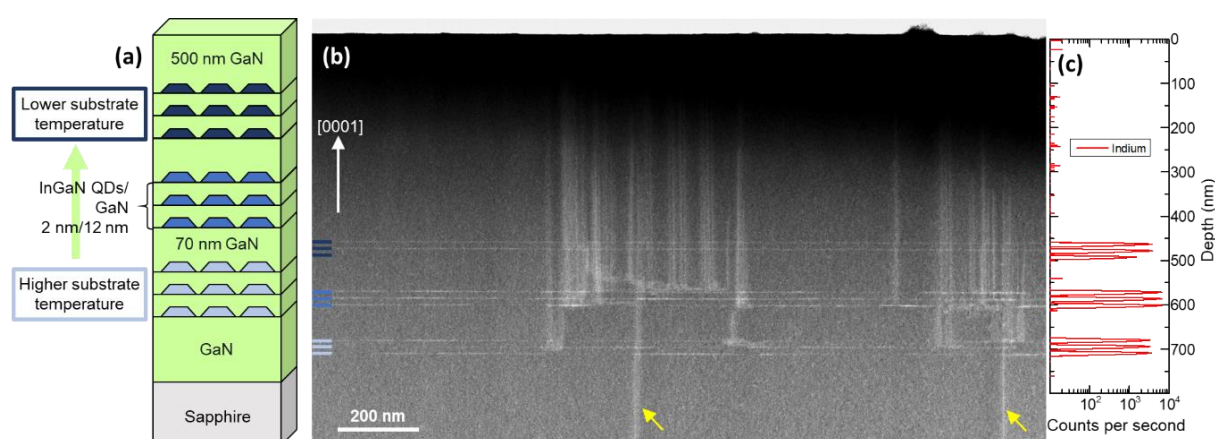


Figure 6.1: (a) Schematic of the InGaN/GaN QD structure. (b) HAADF-STEM image of the sample observed along the $[10-10]$ zone axis (lamella specimen thickness 100–120 nm). Yellow arrows indicate threading dislocations propagating from the substrate. (c) SIMS depth profile for indium.

To confirm the presence of In in the ultrathin InGaN QD layers, and assess the defect-promoted diffusion of In along the growth axis, we have used secondary ion mass spectroscopy (SIMS), as it is shown in **Figure 6.1(c)**. SIMS investigations were performed in a SIMS magnetic selector instrument from CAMECA³¹³, using $^{133}\text{Cs}^+$ as primary beam, accelerated at 2.0 kV, and analysing a $175 \times 175 \mu\text{m}$ spot. All the QD layers are well identified in the profile, and the three bottommost and the three topmost layers seem to have roughly the same amount of In. On the contrary, the 3 layers in the middle present a slightly higher total amount of In. The measurement of the In concentration in the QD layers is only qualitative, since the small size of the nanostructures and their three-dimensional nature does not allow quantitative analysis. In the GaN material within the QD layers, the In concentration goes down below the detection limit of the system ($\approx 4 \times 10^{17} \text{ cm}^{-3}$).

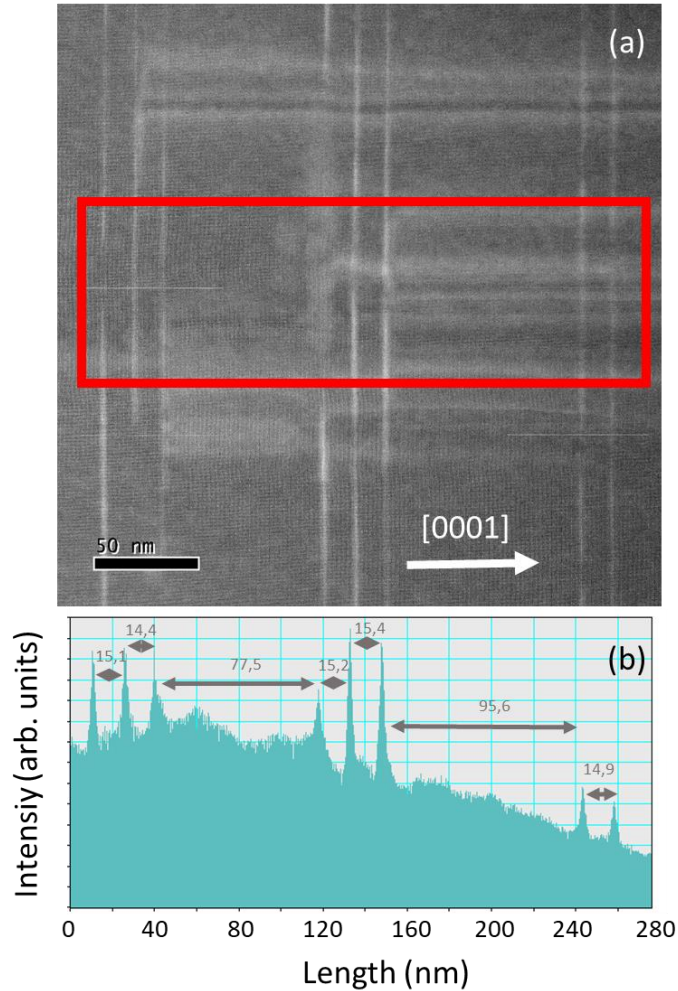


Figure 6.2: (a) HAADF-STEM zoomed image in the centre of the heterostructure showed in **Figure 6.1(b)**. (b) Integrated intensity of the HAADF-STEM image analysed along the red rectangle outlined in (a).

Figure 6.3(a) presents a low-temperature ($T = 5$ K) CL map (wavelength window = 395-420 nm) of the STEM lamella specimen (thickness of 100-120 nm), compared with a section of the HAADF-STEM image, in **Figure 6.3(b)**, to visualize the location of the QD stacks. In **Figure 6.3(a)**, most of the CL intensity originates in the two topmost QD stacks, being significantly higher in the topmost stack, grown at the lowest substrate temperature. This trend was confirmed at several points of the specimen. **Figure 6.3(c)** presents the CL spectra extracted from slices of **Figure 6.3(a)**, moving from the GaN substrate (1), crossing the 3 InGaN/GaN QD stacks (2-6), to the middle of the GaN cap layer (7,8). All the spectra show a narrow emission line at 357 nm, characteristic of GaN. The spectra recorded along the QD region display also a broad emission that peaks at 387-402 nm, which is assigned to recombination in the QDs. Along the growth axis, the peak emission wavelength shifts only by 15 nm, which is smaller than the emission linewidth (spectra 3, 4 and 5 show QD emission linewidths of 29 nm, 33, nm and 17 nm, respectively). If we keep in mind that the CL measurements were performed on a lamella specimen, which means that the electron beam can only excite a few dots, the spectral shift and variation of the emission are explained by the expected dot-to-dot variations of morphology and indium composition.

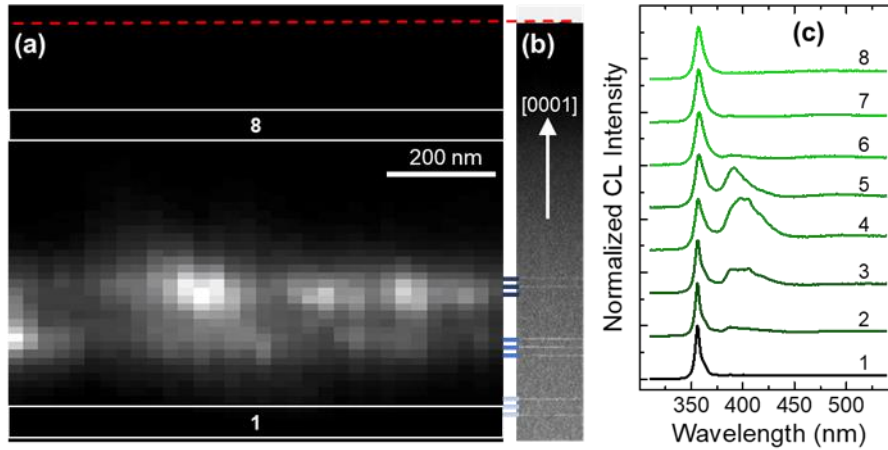


Figure 6.3: (a) Low temperature (5 K) CL mapping (spectral window = 395-420 nm) of the STEM lamella imaged in **Figure 6.1**, containing the 3 stacks of InGaN/GaN QDs, compared with (b) a section of the HAADF-STEM image of the same specimen. (c) CL spectra extracted from different areas of (b), moving from the GaN substrate and through InGaN QDs towards the surface (#1 → #8).

6.3. Characterization of the field emission tip

In order to investigate the luminescence coming from InGaN/GaN QD layers, we used La-APT after having prepared APT tips by using FIB procedure. Several APT tips were analyzed using in-situ μ PL measurements performed before or during the La-APT evaporation under different analysis conditions. Laser-assisted wide-angle tomographic atom probe (LaWaTAP) system has been also used to extract supplementary chemical analysis confirming the accuracy of the extracted indium content values.

6.3.1. Photonic atom probe analysis

With the intention to analyse the indium distribution in the InGaN/GaN QDs and the luminescence at the scale of a single emitter, field-emission tip specimens were fabricated and characterized by La-APT. FIB prepared tips were first observed in TEM, as illustrated in **Figure 6.4(a)**. The tips were then introduced in the PAP system. To determine the best experimental conditions to perform simultaneous μ PL and APT characterization, we first measured *in-situ* μ PL as a function of the laser pumping power at 28 K, as shown in **Figure 6.4(b)**. During these preliminary measurements, we used a repetition rate of 3.8 MHz, adjusting the laser power in the range of 25 to 600 μ W. In these spectra, it is possible to identify the emission of GaN at 356 nm and a narrow line around 390 nm, which is assigned to InGaN QDs. As previously observed ²⁶⁵, the luminescence from GaN increases monotonously with the pumping power, but the QD emission intensity saturates [see **Figure 6.4(c)**]. More importantly, the full width at half maximum (FWHM) of the main QD line shows a drastic increase for excitation power higher than 200 μ W [see **Figure 6.4(d)**], which could point to an increase of the temperature.

Considering this observation, we decided to perform the La-APT experiment with a laser pulse energy corresponding to $140\ \mu\text{W}$, to prevent thermal effects or artefacts associated with many-body phenomena.

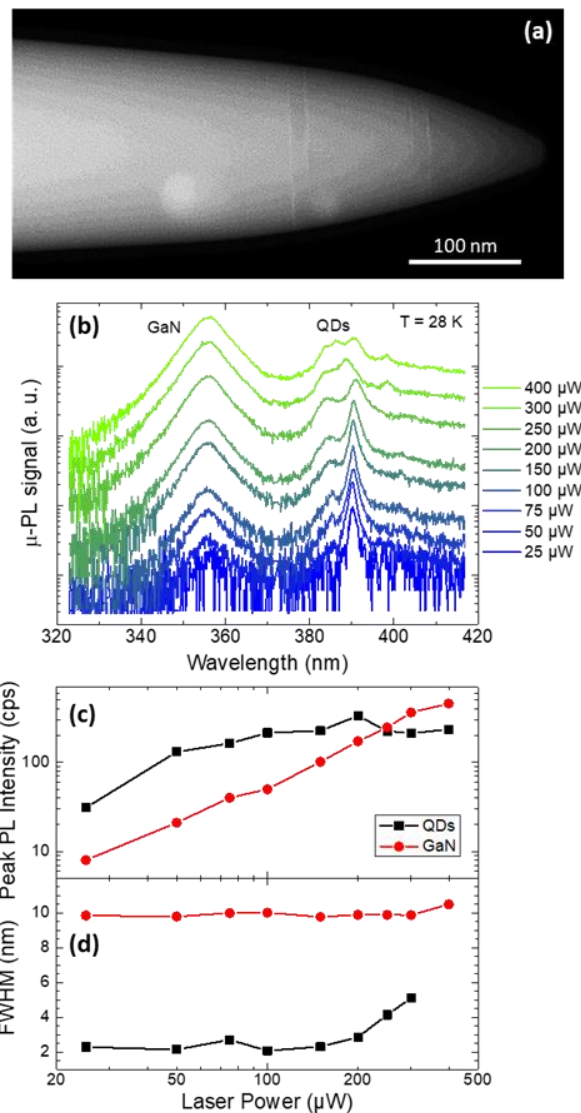


Figure 6.4: (a) TEM image of the tip after FIB preparation. (b) Micro-PL spectra before La-APT evaporation of a tip specimen containing InGaN/GaN QDs. Spectra recorded after excitation with different levels of laser power were normalized to the maximum of the QD emission and vertically shifted for clarity. The experiment was performed at 28 K and the pulse rate and wavelength of laser were 300 kHz and 260 nm, respectively. Variation of (c) the peak PL intensity and (d) FWHM of the lines assigned to the QDs and to GaN, as a function of the laser power.

During the APT measurements coupled with μPL , the laser frequency was reduced to 340 kHz for the reasons that are well explained in ²⁹⁵. The tip was kept at 40 K. In the experiment described in **Figure 6.5**, the tip contained originally the three InGaN/GaN QDs stacks. **Figure 6.5(a)** presents PL spectra recorded at various moments of the evaporation process, and **Figure 6.5(b)** shows 3D APT reconstructions of the indium signal where we can clearly identify the QD layers. The three images in (b) illustrate what was left on the specimen when the spectra #4, #5 and #6 in (a) were recorded. The spectra did not display major variations during the evaporation of the two topmost QD layers of the

first QD stack (spectra #1 → #5). As explained before, the peak at 356 nm is related to the carrier recombination in GaN, and the narrow line at 398 nm is assigned to the carrier recombination in the InGaN QDs. The FWHM, around 1.5 nm confirms that this peak comes from a single dot, comparing to the literature^{314–316}. During the evaporation of the third QD layer (spectrum #6), the QD emission disappeared. This result confirms that the emitting single dot was located in the third top most QD layer. Note that the QD signal disappeared even if there were still InGaN layers, which means that either the other InGaN layers below do not contain any dot or non-radiative recombination processes dominate.

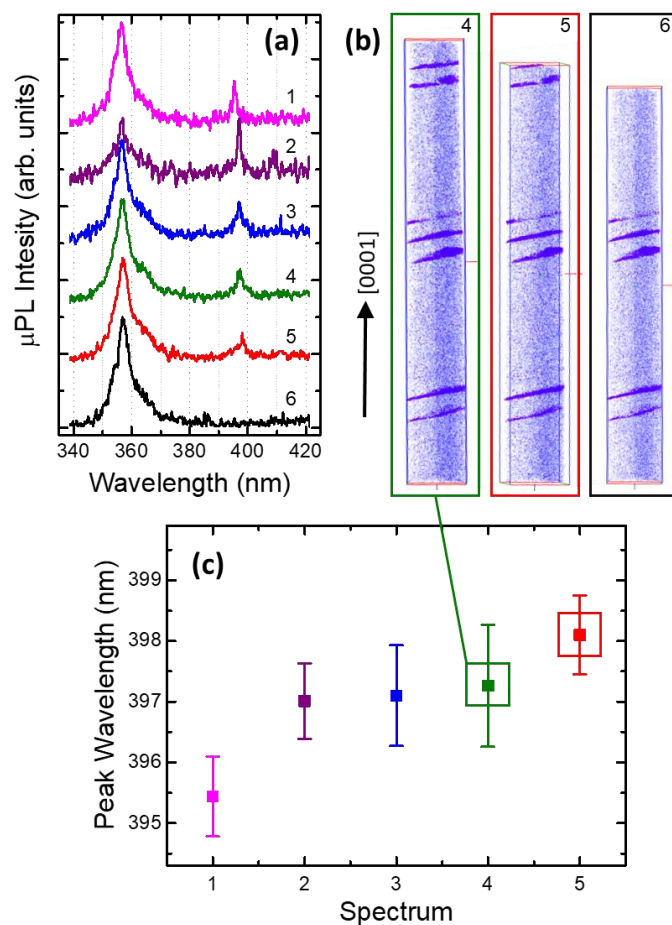


Figure 6.5: (a) In-situ μ PL measurements performed during the La-APT evaporation of InGaN/GaN QDs. Evaporation takes place from 1 to 6. The experiment was performed at 40 K. (b) Quantitative indium-site 3D APT reconstruction of the tip. The images describe what was left of the specimen when recording the spectra 4, 5 and 6 in (a). (c) μ PL peak wavelength of the QD signal in the spectra presented in (a). The FWHM is indicated as error bars.

The evolution of the peak wavelength and FWHM of the QD line during the evaporation of the tip is described in the **Figure 6.5(c)**. The QD emission line presents a red shift of around 2 nm during the APT process of the first 3 topmost QD layers. This shift is mostly explained by the relaxation of the misfit strain during the evaporation²⁶⁵, since the possible contribution of the stress induced by the external electric field when the dot approaches the surface of the tip³¹⁷ is very small in this system²⁶⁵.

Note that the difference of the voltage applied to the InGaN/GaN tip from the beginning to the end of the experiment (spectra #1 → #5) is in the range of $\Delta V_{DC} = 1$ kV ($V_{DC} = 4.5$ - 5.5 kV), which is not enough to justify such spectral shift. The FWHM of the emission, indicated as an error bar, does not present a clear trend.

6.3.2. Chemical analysis by atom probe tomography

Figure 6.6(a) shows the indium site fraction map obtained through the analysis of the whole tip. The InGaN layers contain In-rich regions with a typical in-plane diameter of around 15 nm and typical In-site fraction $\approx 10\%$, on a thin, discontinuous wetting layer, with an In-site fraction $\approx 2.5\%$. The shape and size of these In-rich regions correspond to InGaN QDs rather than to random alloy fluctuations^{265,298}.

The distribution of electric field in the tip can cause artifacts in the measurement of alloy composition. To assess the relevance of these effects, **Figure 6.6(b)** illustrates the spatial distribution of the $\text{Ga}^{2+}/\text{Ga}^+$ charge state ratio. This map allows the correlation between surface electric field and measured composition visualized at a microscopic scale. The effective electric field can be estimated by the ratios of different charge states of given species through Kingham's post-ionization model³¹⁸. The intense electric field is responsible for the evaporation of single charged ions from the tip surface. However, post-ionization³¹⁸ can occur close to the tip surface. When an ion reaches a critical distance from the tip surface (several angstroms), additional electrons can be transferred from the ion to the tip surface by quantum tunnelling effects³¹⁹. Comparing the **Figures 6.6(a)** and **(b)**, we can suggest that there is a certain correlation between the composition and the surface field. The high field region (up to 0.015) is associated with an In III-site fraction about 10%. Comparing our values with those from literature^{62,173,320–322}, the highest field recorded here seems to be sufficiently low to ensure accuracy of the measured composition.

Plane-views of the indium composition of the second topmost (outlined with a blue rectangle in **Figure 6.6(a)**) and the first bottommost InGaN QD layer (outlined with an orange rectangle in **Figure 6.6(a)**) are presented in **Figures 6.6(c-d)** and **(e-f)**, respectively. Note that the scales of **Figures 6.6(c)** and **(e)** are the same, pointing to relatively similar indium distribution and QD diameter, in the range of 10-20 nm. Moreover, the spatial distribution of the $\text{Ga}^{2+}/\text{Ga}^+$ charge state ratio in **Figures 6.6(d)** and **(f)** are also similar. From this chemical analysis, the 3 stacks of QD layers are quite similar in terms of size and composition, which does not justify major changes in the radiative properties.

Note that **Figures 6.6(a)**, **(c)** and **(e)** are slices of the tip reconstruction with a thickness of 10 nm in the direction perpendicular to the page. The indium concentration is calculated by integrating the In and Ga atoms in the depth of the slice. As the base diameter of the QDs is in the range of 10-20 nm and the height is in the range of 2 nm, the In content in the dots in the plane-views (**Figures 6.6(c)** and **(e)**) is strongly underestimated due to the surrounding GaN. This is the reason why the In-site fraction for the in-plane is only $\approx 5\%$, compared to 10% in **Figure 6.6(a)**.

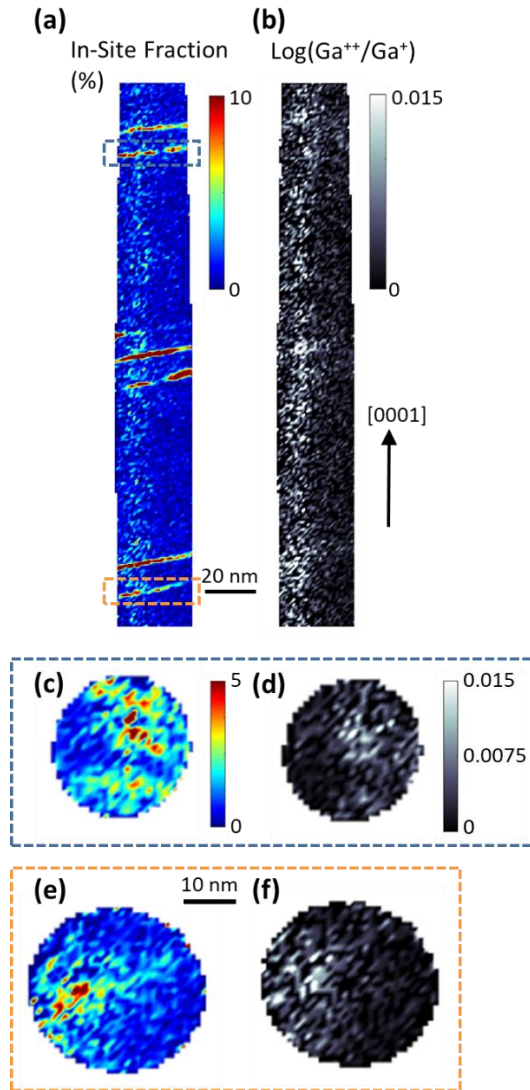


Figure 6.6: (a) Indium-site map calculated from the APT 3D reconstructed volume illustrated in **Figure 6.5(b)**. (b) Ga charge-state ratio (Ga^{++}/Ga^{+}) revealing the field distribution. The results are shown for a side view (perpendicular to the c axis). (c) Top view map (along the c axis) of the indium content and (d) Ga charge-state ratio (Ga^{++}/Ga^{+}) in the second topmost InGaN QD layer, outlined with a blue rectangle in (a). (e) Top view map (along the c axis) of the indium content and (f) Ga charge-state ratio (Ga^{++}/Ga^{+}), outlined with an orange rectangle in (a). Note that the color scales in (c) and (e) are the same, and those in (d) and (f) are also the same. The indium content shown in (a), (c) and (e) are relative to a 10 nm thick slice in the direction perpendicular to the page.

Complementary APT analyses were conducted by a LaWaTAP operated with femtosecond laser pulses (350 fs) at a wavelength of $\lambda = 515$ nm (green). The pulse repetition frequency was 100 kHz. The laser pulse energy E_{las} was 3 nJ. The detection system used was a custom-designed MCP/aDLD with an MCP detection efficiency $\eta_{MCP} \approx 0.6$, with diameter $D = 7.6$ cm. Such a system is improved for the multihit detection. The analysis conditions changed during the experiment, the field became weaker along the experiment, which leads to an increase in the relative quantity of Ga^{+} and greater loss of nitrogen. The La-APT analysis was performed between detection rates 1.10^{-3} to 4.10^{-3} at/pulse. Under

these conditions, the entire tip was evaporated in about 2 days. The specimen base temperature (T_{base}) was maintained at 80 K. **Figure 6.7**(a) shows the 3D reconstruction of the whole tip and (b-c) illustrate its indium site fraction map and the spatial distribution of the $\text{Ga}^{2+}/\text{Ga}^+$ charge state ratio, respectively. The indium site fraction obtained in these measurements confirm the reproducibility of the results and the accuracy of the value of the indium content in the sample.

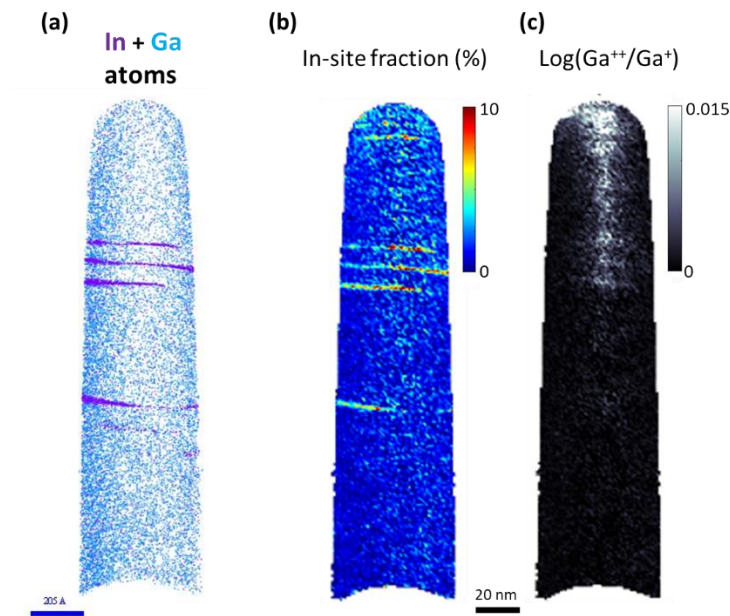


Figure 6.7: (a) 3D reconstruction of the In and Ga atom distribution in the analysed sample using LawaTap. (b) Indium-site fraction map calculated from the APT 3D reconstructed volume showed in (a). (c) Ga charge-state ratio ($\text{Ga}^{2+}/\text{Ga}^+$) revealing the field distribution. In this two-dimensional representation, the composition and the distribution are integrated over 10 nm in the direction perpendicular to the page.

For a tip which presents a multi-peak structure emission, we have studied the spectral lines emitted by QDs with the purpose of checking if they are consistent with the indium content measured by APT. **Figure 6.8** shows *in-situ* μPL spectra recorded as a function of the laser pumping power. In these spectra, it is possible to identify the narrow emission of the GaN substrate at 358 nm and a multi-peak structure where we can identify 3 main lines at 386 nm, 391 nm and 398 nm, which are assigned to the InGaN QDs. In the **Table 6.1** we summarize the result of 1D calculations that were performed changing the In content in the QD layer compared with the experimentally revealed values (APT). We have adjusted the In content from 8% to 11%, the emission shifts from 384 to 400 nm. Good agreement between the theoretical calculations and the experimental optical results show that the values extracted from APT provide a precise description of this InGaN/GaN QD heterostructure.

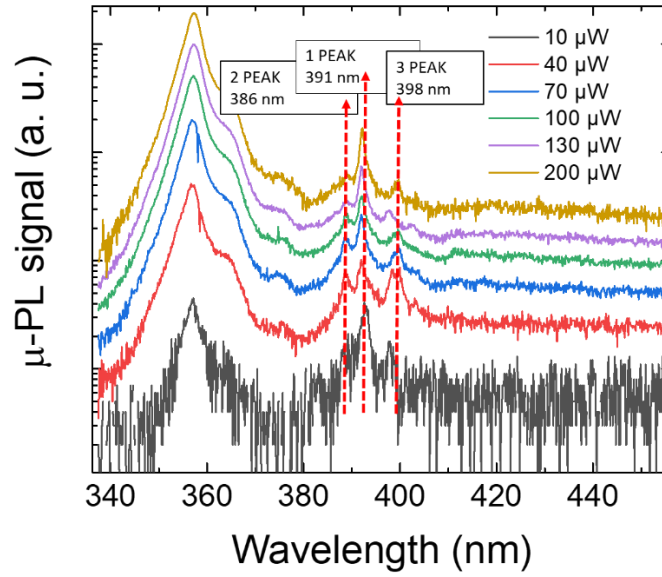


Figure 6.8: μ PL measurements performed before the La-APT evaporation of InGaN/GaN QDs with different laser power. The experiment was performed at 25 K and the frequency and wavelength of laser were 300 kHz and 260 nm, respectively.

In content in the QD layer (calculated transition wavelength)	Experimental peak emission wavelength
8% (384 nm)	386 nm
9% (389 nm)	391 nm
11% (400 nm)	398 nm

Table 6.1: Calculation of the emission wavelength at 25 K as a function of the indium content in the QD layer.

6.4. Discussion: effect of extended and point defects

Coming back to the structural properties of the sample, there is an important degradation of the structural quality along the growth axis due to the progressive reduction of substrate temperature during the growth. These results, illustrated in **Figure 6.1(b)**, seem to be in contradiction with the systematic enhancement of the luminescence intensity along the growth axis. It is known that the potential fluctuations generated by inhomogeneities in the In content can reduce non-radiative recombination in InGaN layers^{270,323}, to the point of suppressing the non-radiative effects associated to dislocations³²⁴. However, the effect of carrier localization in In-rich areas should be visible from the first QD layer. Therefore, enhancement of the luminescence along the growth axis points to the fact that non-radiative processes in the layers close to the substrate are dominated by point defects. This is consistent with recent reports of points defects as a main source of degradation of the luminescence

of InGaN/GaN QW structures^{325–327}. Several groups have demonstrated that such defects can be buried by depositing InGaN layers before the growth of the active region^{325,326,328}. In our case, the first QD layers in the structure play the role of InGaN underlayers trapping non-radiative point defects. The filtering efficiency of such layers is high enough to resolve single QD luminescence in the topmost stack, in spite of the high density of threading dislocations.

6.5. Conclusions

In summary, we have performed a correlative microscopy study of 3 stacks of 3 layers of self-assembled $\text{In}_x\text{Ga}_{1-x}\text{N}/\text{GaN}$ (2 nm/12 nm) QDs, separated by 70 nm of GaN, and each of the three stacks grown at different substrate temperature. Although lowering the substrate temperature leads to an increased density of structural defects, we observed higher emission intensity in the topmost layers, grown at lower temperature. This result highlights the relevance of inserting InGaN underlayers to bury non-radiative point defects. During APT measurement of the topmost QD layers, it was possible to resolve one single QD emission line. The single QD line displayed a spectral shift during the experiment confirming the relaxation of elastic strain due to material evaporation.

Chapter 7: Conclusions and perspectives

This final chapter is divided in two main subchapters. First, I present the conclusions and perspectives of my work on AlGa_xN/AlN QDs inserted in NWs (chapter 4), and then I focused on the results of my studies of InGa_xN QDs (chapters 5 and 6).

7.1. AlGa_xN/AlN quantum dots in nanowires

A feasibility study of NW arrays as active media for electron-pumped UV emitters was presented. The NWs consisted of a GaN stem with a 400-nm-thick Al_xGa_{1-x}N/AlN multi-quantum dot heterostructure. Structural and optical studies demonstrated that the QD dimensions were highly homogeneous along the whole superlattice. Comparing with the emission of planar samples with the same periodicity and thickness, NW structures are less sensitive to non-radiative recombination, attaining IQE higher than 60% at room temperature, even under low injection conditions. Under pulsed optical excitation the IQE remains stable for excitation power densities up to 50 kW/cm². Experiments under electron pumping show that the NW superlattice is long enough to collect the electron-hole pairs generated by an electron beam with an acceleration voltage $V_A = 5$ kV. By varying the dot/barrier thickness ratio and the Al content in the dots the NW peak emission is adjusted in the range from 340 to 258 nm.

This work describes the first assessment of NWs for application in electron-pumped UV sources and our results confirm the feasibility of the approach. Electron channelling effects can be compensated by an increase of the active region length by $\approx 60\%$ in comparison to planar layers. Using QD superlattices in NWs as active media, it is possible to keep the homogeneity of the dot geometry all along the active region in order to obtain NW ensembles providing a single emission line in the deep UV range. Furthermore, we have demonstrated the stability of the NWs under electron pumping. The external quantum efficiency was measured for some samples, with promising results ($3.42 \pm 0.55\%$). Further improvement could be achieved by removing the silicon substrate and transferring the ensemble to a UV reflecting material. Also, growth efforts should be made to reduce the length of the GaN stem, or replace it by AlGa_xN. In the path towards an operating prototype, the cathodoluminescence efficiency should be quantified and the lifetime under electron excitation should be evaluated (we have already confirmed stability in the scale of 5 min, but long term studies should still be performed).

The data reported here are very promising for a lot of applications of NWs in flexible electronics, high efficient optoelectronic devices, implantable devices. The demonstrated study opens prospects for novel miniature ultrasensitive photodetectors or for building blocks in LEDs, as the NWs present high crystalline quality, enhanced light extraction efficiency, and facilitate the film separation and transfer. In the early future is expected to see several novel approaches taking advantage of NW diameter size and doping concentration to be able to determine the operation modes for specific applications including intersubband (ISB) ultrafast devices (electro-optical modulators, power switching devices) and horizontal NW transistors or vertical NW FETs. Going further, advanced

manipulation techniques for single nano-objects can be developed, and this will help in processing and building newer and better devices.

To further understand and improve such devices, it would be very interesting to adapt the correlative microscopy method developed in this work to the characterization of NWs. Studies on doping or alloy distribution would provide essential information for a transition towards the fabrication of nanowire devices. This requires the determination of a reproducible process to isolate and mount single nanowires on the APT holder. Efforts are currently being made in this direction, and results are expected in the next months.

7.2. InGaN/GaN Stranski-Krastanov QDs

We have performed correlative microscopy studies of self-assembled InGaN/GaN QDs. Comparative optical characterization of as-grown samples and atom probe specimens shows that there was no loss or rearrangement of indium during the FIB process. This allows the extrapolation of the characterization results to the as-grown samples. We have performed spectroscopic (in-situ micro-photoluminescence and ex-situ cathodoluminescence) and structural (XRD, AFM, STEM and APT) measurements, to get a full view of these nanostructures.

A conclusion of this study is that Stranski-Krastranov InGaN/GaN QDs look like a thickness undulation and a local increase of the In mole fraction. The thickness of the wetting layer is comparable to the QD height, and the indium content in the wetting layer is significantly lower than the indium content in the QDs. The nanostructures behave optically as QDs, but these structural parameters can have an important impact on the design of the active region of a light emitting device, since they affect the band diagram and carrier transport properties.

It was possible to resolve single QD emission lines in μ PL measurements performed in situ during APT evaporation. The spectral red shift observed in these single QD lines during the APT process was assigned to the relaxation of elastic strain due to the material evaporation. Theoretical modeling of the QDs considering the experimental values of their size and indium distribution predicts room temperature photoluminescence in excellent agreement with the measured spectra. Furthermore, the spectral linewidth is explained as due to in-plane fluctuations of the QD In content and diameter.

We have also studied the effect of extended and point defects on the luminescence of such QD structures. We observed that emission intensity is higher in the upper QD layers (closer to the surface) and it is not correlated with the dislocation density. This result highlights the relevance of inserting InGaN underlayers to bury non-radiative point defects.

Our results confirm the relevance of PAP studies to provide a complete view of the InGaN QDs, and shows the potential of this technique for the analysis of nanostructured materials. The PAP can be used in samples containing a large set of nanoscale emitters in order to isolate the optical emission of few of them by a controlled reduction of the optically active volume induced by field evaporation.

Furthermore, the technique allows the correlation of the 3D image of the chemical composition of a few light emitters contained in a nanoscale object with their spectral signature. This opens perspectives for the application of this technique to super-resolution studies, to discriminate the optical emission of neighboring QDs, or to strictly correlative studies, in which the 3D chemical map of a single QD is correlated with its optical signature.

Bibliography

- (1) Vurgaftman, I.; Meyer, J. R. Band Parameters for Nitrogen-Containing Semiconductors. *J. Appl. Phys.* **2003**, *94* (6), 3675. <https://doi.org/10.1063/1.1600519>.
- (2) Gorczyca, I.; Suski, T.; Christensen, N. E.; Svane, A. Size Effects in Band Gap Bowing in Nitride Semiconducting Alloys. *Phys. Rev. B* **2011**, *83* (15), 153301. <https://doi.org/10.1103/PhysRevB.83.153301>.
- (3) Tchernycheva, M.; Nevou, L.; Doyennette, L.; Julien, F.; Warde, E.; Guillot, F.; Monroy, E.; Bellet-Amalric, E.; Remmele, T.; Albrecht, M. Systematic Experimental and Theoretical Investigation of Intersubband Absorption in GaN/AlN Quantum Wells. *Phys. Rev. B* **2006**, *73* (12), 125347. <https://doi.org/10.1103/PhysRevB.73.125347>.
- (4) King, P. D. C.; Veal, T. D.; Kendrick, C. E.; Bailey, L. R.; Durbin, S. M.; McConville, C. F. InN/GaN Valence Band Offset: High-Resolution x-Ray Photoemission Spectroscopy Measurements. *Phys. Rev. B* **2008**, *78* (3), 033308. <https://doi.org/10.1103/PhysRevB.78.033308>.
- (5) Razeghi, M.; Henini, M. Chapter 1 - Introduction. In *Optoelectronic Devices: III Nitrides*; Razeghi, M., Henini, M., Eds.; Elsevier: Oxford, 2005; pp 1–8. <https://doi.org/10.1016/B978-008044426-0/50001-8>.
- (6) Chemistry and Physics in One Dimension: Synthesis and Properties of Nanowires and Nanotubes | Accounts of Chemical Research <https://pubs.acs.org/doi/10.1021/ar9700365> (accessed 2021 -06 -22).
- (7) Duan, X.; Lieber, C. M. Laser-Assisted Catalytic Growth of Single Crystal GaN Nanowires. *J. Am. Chem. Soc.* **2000**, *122* (1), 188–189. <https://doi.org/10.1021/ja993713u>.
- (8) Cui, Y.; Lieber, C. M. Functional Nanoscale Electronic Devices Assembled Using Silicon Nanowire Building Blocks. *Science* **2001**, *291* (5505), 851–853. <https://doi.org/10.1126/science.291.5505.851>.
- (9) Huang, M. H.; Mao, S.; Feick, H.; Yan, H.; Wu, Y.; Kind, H.; Weber, E.; Russo, R.; Yang, P. Room-Temperature Ultraviolet Nanowire Nanolasers. *Science* **2001**, *292* (5523), 1897–1899. <https://doi.org/10.1126/science.1060367>.
- (10) Johnson, J. C.; Choi, H.-J.; Knutsen, K. P.; Schaller, R. D.; Yang, P.; Saykally, R. J. Single Gallium Nitride Nanowire Lasers. *Nat. Mater.* **2002**, *1* (2), 106–110. <https://doi.org/10.1038/nmat728>.
- (11) Duan, X.; Niu, C.; Sahi, V.; Chen, J.; Parce, J. W.; Empedocles, S.; Goldman, J. L. High-Performance Thin-Film Transistors Using Semiconductor Nanowires and Nanoribbons. *Nature* **2003**, *425* (6955), 274–278. <https://doi.org/10.1038/nature01996>.
- (12) Hochbaum, A. I.; Yang, P. Semiconductor Nanowires for Energy Conversion. *Chem. Rev.* **2010**, *110* (1), 527–546. <https://doi.org/10.1021/cr900075v>.
- (13) Yang, P.; Yan, R.; Fardy, M. Semiconductor Nanowire: What's Next? *Nano Lett.* **2010**, *10* (5), 1529–1536. <https://doi.org/10.1021/nl100665r>.
- (14) Zhao, S.; Nguyen, H. P. T.; Kibria, Md. G.; Mi, Z. III-Nitride Nanowire Optoelectronics. *Prog. Quantum Electron.* **2015**, *44*, 14–68. <https://doi.org/10.1016/j.pquantelec.2015.11.001>.
- (15) Eaton, S. W.; Fu, A.; Wong, A. B.; Ning, C.-Z.; Yang, P. Semiconductor Nanowire Lasers. *Nat. Rev. Mater.* **2016**, *1* (6), 1–11. <https://doi.org/10.1038/natrevmats.2016.28>.
- (16) Nanowires: Building Blocks for Nanoscience and Nanotechnology | SpringerLink <https://link.springer.com/article/10.1557/mrs.2017.157> (accessed 2021 -06 -22).
- (17) Ishikawa, F.; Buyanova, I. A. *Novel Compound Semiconductor Nanowires*; Pan Stanford Publishing, 2017.
- (18) Bi, W. (Wayne); Kuo, H. (Henry); Ku, P.; Shen, B. *Handbook of GaN Semiconductor Materials and Devices*; CRC Press, 2017.
- (19) Zhao, C.; Alfaraj, N.; Chandra Subedi, R.; Liang, J. W.; Alatawi, A. A.; Alhamoud, A. A.; Ebaid, M.; Alias, M. S.; Ng, T. K.; Ooi, B. S. III-Nitride Nanowires on Unconventional Substrates: From Materials to Optoelectronic Device Applications. *Prog. Quantum Electron.* **2018**, *61*, 1–31. <https://doi.org/10.1016/j.pquantelec.2018.07.001>.

- (20) Quan, L. N.; Kang, J.; Ning, C.-Z.; Yang, P. Nanowires for Photonics. *Chem. Rev.* **2019**, *119* (15), 9153–9169. <https://doi.org/10.1021/acs.chemrev.9b00240>.
- (21) Zhao, S.; Wang, R.; Chu, S.; Mi, Z. Molecular Beam Epitaxy of III-Nitride Nanowires: Emerging Applications From Deep-Ultraviolet Light Emitters and Micro-LEDs to Artificial Photosynthesis. *IEEE Nanotechnol. Mag.* **2019**, *13* (2), 6–16. <https://doi.org/10.1109/MNANO.2019.2891370>.
- (22) Chen, J.; Loeb, S.; Kim, J.-H. LED Revolution: Fundamentals and Prospects for UV Disinfection Applications. *Environ. Sci. Water Res. Technol.* **2017**, *3* (2), 188–202. <https://doi.org/10.1039/C6EW00241B>.
- (23) Song, K.; Mohseni, M.; Taghipour, F. Application of Ultraviolet Light-Emitting Diodes (UV-LEDs) for Water Disinfection: A Review. *Water Res.* **2016**, *94*, 341–349. <https://doi.org/10.1016/j.watres.2016.03.003>.
- (24) Takano, T.; Mino, T.; Sakai, J.; Noguchi, N.; Tsubaki, K.; Hirayama, H. Deep-Ultraviolet Light-Emitting Diodes with External Quantum Efficiency Higher than 20% at 275 Nm Achieved by Improving Light-Extraction Efficiency. *Appl. Phys. Express* **2017**, *10* (3), 031002. <https://doi.org/10.7567/APEX.10.031002>.
- (25) Mukai, T.; Yamada, M.; Nakamura, S. Characteristics of InGaN-Based UV/Blue/Green/Amber/Red Light-Emitting Diodes. *Jpn. J. Appl. Phys.* **1999**, *38* (7R), 3976. <https://doi.org/10.1143/JJAP.38.3976>.
- (26) Kim, A. Y.; Götz, W.; Steigerwald, D. A.; Wierer, J. J.; Gardner, N. F.; Sun, J.; Stockman, S. A.; Martin, P. S.; Krames, M. R.; Kern, R. S.; Steranka, F. M. Performance of High-Power AlInGaN Light Emitting Diodes. *Phys. Status Solidi A* **2001**, *188* (1), 15–21. [https://doi.org/10.1002/1521-396X\(200111\)188:1<15::AID-PSSA15>3.0.CO;2-5](https://doi.org/10.1002/1521-396X(200111)188:1<15::AID-PSSA15>3.0.CO;2-5).
- (27) Shen, Y. C.; Mueller, G. O.; Watanabe, S.; Gardner, N. F.; Munkholm, A.; Krames, M. R. Auger Recombination in InGaN Measured by Photoluminescence. *Appl. Phys. Lett.* **2007**, *91* (14), 141101. <https://doi.org/10.1063/1.2785135>.
- (28) Maier, M.; Köhler, K.; Kunzer, M.; Pletschen, W.; Wagner, J. Reduced Nonthermal Rollover of Wide-Well GaInN Light-Emitting Diodes. *Appl. Phys. Lett.* **2009**, *94* (4), 041103. <https://doi.org/10.1063/1.3073860>.
- (29) Delaney, K. T.; Rinke, P.; Van de Walle, C. G. Auger Recombination Rates in Nitrides from First Principles. *Appl. Phys. Lett.* **2009**, *94* (19), 191109. <https://doi.org/10.1063/1.3133359>.
- (30) Taki, T.; Strassburg, M. Review—Visible LEDs: More than Efficient Light. *ECS J. Solid State Sci. Technol.* **2019**, *9* (1), 015017. <https://doi.org/10.1149/2.0402001JSS>.
- (31) Rozhansky, I. V.; Zakheim, D. A. Analysis of Processes Limiting Quantum Efficiency of AlGaInN LEDs at High Pumping. *Phys. Status Solidi A* **2007**, *204* (1), 227–230. <https://doi.org/10.1002/psa.200673567>.
- (32) Kim, M.-H.; Schubert, M. F.; Dai, Q.; Kim, J. K.; Schubert, E. F.; Piprek, J.; Park, Y. Origin of Efficiency Droop in GaN-Based Light-Emitting Diodes. *Appl. Phys. Lett.* **2007**, *91* (18), 183507. <https://doi.org/10.1063/1.2800290>.
- (33) Liu, J. P.; Ryou, J.-H.; Dupuis, R. D.; Han, J.; Shen, G. D.; Wang, H. B. Barrier Effect on Hole Transport and Carrier Distribution in InGaN/GaN Multiple Quantum Well Visible Light-Emitting Diodes. *Appl. Phys. Lett.* **2008**, *93* (2), 021102. <https://doi.org/10.1063/1.2957667>.
- (34) Ni, X.; Fan, Q.; Shimada, R.; Özgür, Ü.; Morkoç, H. Reduction of Efficiency Droop in InGaN Light Emitting Diodes by Coupled Quantum Wells. *Appl. Phys. Lett.* **2008**, *93* (17), 171113. <https://doi.org/10.1063/1.3012388>.
- (35) Moriwaki, O.; Someya, T.; Tachibana, K.; Ishida, S.; Arakawa, Y. Narrow Photoluminescence Peaks from Localized States in InGaN Quantum Dot Structures. *Appl. Phys. Lett.* **2000**, *76* (17), 2361–2363. <https://doi.org/10.1063/1.126346>.
- (36) Park, I.-K.; Kwon, M.-K.; Cho, C.-Y.; Kim, J.-Y.; Cho, C.-H.; Park, S.-J. Effect of InGaN Quantum Dot Size on the Recombination Process in Light-Emitting Diodes. *Appl. Phys. Lett.* **2008**, *92* (25), 253105. <https://doi.org/10.1063/1.2951607>.
- (37) Rigutti, L.; Blum, I.; Shinde, D.; Hernández-Maldonado, D.; Lefebvre, W.; Houard, J.; Vurpillot, F.; Vella, A.; Tchernycheva, M.; Durand, C.; Eymery, J.; Deconihout, B. Correlation of

- Microphotoluminescence Spectroscopy, Scanning Transmission Electron Microscopy, and Atom Probe Tomography on a Single Nano-Object Containing an InGaN/GaN Multiquantum Well System. *Nano Lett.* **2014**, *14* (1), 107–114. <https://doi.org/10.1021/nl4034768>.
- (38) Spirkoska, D.; Arbiol, J.; Gustafsson, A.; Conesa-Boj, S.; Glas, F.; Zardo, I.; Heigoldt, M.; Gass, M. H.; Bleloch, A. L.; Estrade, S.; Kaniber, M.; Rossler, J.; Peiro, F.; Morante, J. R.; Abstreiter, G.; Samuelson, L.; Fontcuberta i Morral, A. Structural and Optical Properties of High Quality Zinc-Blende/Wurtzite GaAs Nanowire Heterostructures. *Phys. Rev. B* **2009**, *80* (24). <https://doi.org/10.1103/PhysRevB.80.245325>.
- (39) Rigutti, L.; Jacopin, G.; Largeau, L.; Galopin, E.; De Luna Bugallo, A.; Julien, F. H.; Harmand, J.-C.; Glas, F.; Tchernycheva, M. Correlation of Optical and Structural Properties of GaN/AlN Core-Shell Nanowires. *Phys. Rev. B* **2011**, *83* (15), 155320. <https://doi.org/10.1103/PhysRevB.83.155320>.
- (40) Zardo, I.; Conesa-Boj, S.; Peiro, F.; Morante, J. R.; Arbiol, J.; Uccelli, E.; Abstreiter, G.; Fontcuberta i Morral, A. Raman Spectroscopy of Wurtzite and Zinc-Blende GaAs Nanowires: Polarization Dependence, Selection Rules, and Strain Effects. *Phys. Rev. B* **2009**, *80* (24), 245324. <https://doi.org/10.1103/PhysRevB.80.245324>.
- (41) Correlation between the Extinction Spectrum of a Single Metal Nanoparticle and Its Electron Microscopy Image | The Journal of Physical Chemistry C <https://pubs.acs.org/doi/abs/10.1021/jp076955m> (accessed 2021 -07 -01).
- (42) Hestroffer, K.; Mata, R.; Camacho, D.; Leclere, C.; Tourbot, G.; Niquet, Y. M.; Cros, A.; Bougerol, C.; Renevier, H.; Daudin, B. The Structural Properties of GaN/AlN Core-Shell Nanocolumn Heterostructures. *Nanotechnology* **2010**, *21* (41), 415702. <https://doi.org/10.1088/0957-4484/21/41/415702>.
- (43) Nanoscale Imaging of InN Segregation and Polymorphism in Single Vertically Aligned InGaN/GaN Multi Quantum Well Nanorods by Tip-Enhanced Raman Scattering | Nano Letters <https://pubs.acs.org/doi/abs/10.1021/nl401277y> (accessed 2021 -07 -01).
- (44) Lim, S. K.; Brewster, M.; Qian, F.; Li, Y.; Lieber, C. M.; Gradečak, S. Direct Correlation between Structural and Optical Properties of III-V Nitride Nanowire Heterostructures with Nanoscale Resolution. *Nano Lett.* **2009**, *9* (11), 3940–3944. <https://doi.org/10.1021/nl9025743>.
- (45) Zagonel, L. F.; Mazzucco, S.; Tencé, M.; March, K.; Bernard, R.; Laslier, B.; Jacopin, G.; Tchernycheva, M.; Rigutti, L.; Julien, F. H.; Songmuang, R.; Kociak, M. Nanometer Scale Spectral Imaging of Quantum Emitters in Nanowires and Its Correlation to Their Atomically Resolved Structure. *Nano Lett.* **2011**, *11* (2), 568–573. <https://doi.org/10.1021/nl103549t>.
- (46) Tourbot, G.; Bougerol, C.; Glas, F.; Zagonel, L. F.; Mahfoud, Z.; Meuret, S.; Gilet, P.; Kociak, M.; Gayral, B.; Daudin, B. Growth Mechanism and Properties of InGaN Insertions in GaN Nanowires. *Nanotechnology* **2012**, *23* (13), 135703. <https://doi.org/10.1088/0957-4484/23/13/135703>.
- (47) Nelayah, J.; Kociak, M.; Stéphan, O.; García de Abajo, F. J.; Tencé, M.; Henrard, L.; Taverna, D.; Pastoriza-Santos, I.; Liz-Marzán, L. M.; Colliex, C. Mapping Surface Plasmons on a Single Metallic Nanoparticle. *Nat. Phys.* **2007**, *3* (5), 348–353. <https://doi.org/10.1038/nphys575>.
- (48) Galtrey, M. J.; Oliver, R. A.; Kappers, M. J.; McAleese, C.; Zhu, D.; Humphreys, C. J.; Clifton, P. H.; Larson, D.; Cerezo, A. Compositional Inhomogeneity of a High-Efficiency In_xGa_{1-x}N Based Multiple Quantum Well Ultraviolet Emitter Studied by Three Dimensional Atom Probe. *Appl. Phys. Lett.* **2008**, *92* (4), 041904. <https://doi.org/10.1063/1.2829592>.
- (49) Cadel, E.; Vurpillot, F.; Lardé, R.; Duguay, S.; Deconihout, B. Depth Resolution Function of the Laser Assisted Tomographic Atom Probe in the Investigation of Semiconductors. *J. Appl. Phys.* **2009**, *106* (4), 044908. <https://doi.org/10.1063/1.3186617>.
- (50) Müller, E. W.; Panitz, J. A.; McLane, S. B. The Atom-Probe Field Ion Microscope. *Rev. Sci. Instrum.* **1968**, *39* (1), 83–86. <https://doi.org/10.1063/1.1683116>.
- (51) Tsong, T. T.; Müller, E. W. THE FIELD ION MICROSCOPICAL IMAGE OF AN ORDERED PLATINUM-COBALT ALLOY. *Appl. Phys. Lett.* **1966**, *9* (1), 7–10. <https://doi.org/10.1063/1.1754605>.
- (52) Blavette, D.; Bostel, A.; Sarrau, J. M.; Deconihout, B.; Menand, A. An Atom Probe for Three-

- Dimensional Tomography. *Nature* **1993**, *363* (6428), 432–435. <https://doi.org/10.1038/363432a0>.
- (53) Da Costa, G.; Vurpillot, F.; Bostel, A.; Bouet, M.; Deconihout, B. Design of a Delay-Line Position-Sensitive Detector with Improved Performance. *Rev. Sci. Instrum.* **2005**, *76* (1), 013304. <https://doi.org/10.1063/1.1829975>.
- (54) Gault, B.; Vurpillot, F.; Vella, A.; Gilbert, M.; Menand, A.; Blavette, D.; Deconihout, B. Design of a Femtosecond Laser Assisted Tomographic Atom Probe. *Rev. Sci. Instrum.* **2006**, *77* (4), 043705. <https://doi.org/10.1063/1.2194089>.
- (55) Kelly, T. F.; Larson, D. J.; Thompson, K.; Alvis, R. L.; Bunton, J. H.; Olson, J. D.; Gorman, B. P. Atom Probe Tomography of Electronic Materials. *Annu. Rev. Mater. Res.* **2007**, *37* (1), 681–727. <https://doi.org/10.1146/annurev.matsci.37.052506.084239>.
- (56) Chen, Y. M.; Ohkubo, T.; Kodzuka, M.; Morita, K.; Hono, K. Laser-Assisted Atom Probe Analysis of Zirconia/Spinel Nanocomposite Ceramics. *Scr. Mater.* **2009**, *61* (7), 693–696. <https://doi.org/10.1016/j.scriptamat.2009.05.043>.
- (57) Marquis, E. A.; Yahya, N. A.; Larson, D. J.; Miller, M. K.; Todd, R. I. Probing the Improbable: Imaging C Atoms in Alumina. *Mater. Today* **2010**, *13* (10), 34–36. [https://doi.org/10.1016/S1369-7021\(10\)70184-X](https://doi.org/10.1016/S1369-7021(10)70184-X).
- (58) Chen, Y. M.; Ohkubo, T.; Hono, K. Laser Assisted Field Evaporation of Oxides in Atom Probe Analysis. *Ultramicroscopy* **2011**, *111* (6), 562–566. <https://doi.org/10.1016/j.ultramic.2010.12.013>.
- (59) Panciera, F.; Hoummada, K.; Gregoire, M.; Juhel, M.; Bicais, N.; Mangelinck, D. Three Dimensional Distributions of Arsenic and Platinum within NiSi Contact and Gate of an N-Type Transistor. *Appl. Phys. Lett.* **2011**, *99*, 051911-. <https://doi.org/10.1063/1.3616150>.
- (60) Houard, J.; Normand, A.; Di Russo, E.; Bacchi, C.; Dalapati, P.; Beainy, G.; Moldovan, S.; Da Costa, G.; Delaroche, F.; Vaudolon, C.; Chauveau, J. M.; Hugues, M.; Blavette, D.; Deconihout, B.; Vella, A.; Vurpillot, F.; Rigutti, L. A Photonic Atom Probe Coupling 3D Atomic Scale Analysis with in Situ Photoluminescence Spectroscopy. *Rev. Sci. Instrum.* **2020**, *91* (8), 083704. <https://doi.org/10.1063/5.0012359>.
- (61) Mancini, L.; Moyon, F.; Houard, J.; Blum, I.; Lefebvre, W.; Vurpillot, F.; Das, A.; Monroy, E.; Rigutti, L. Multi-Excitonic Emission from Stranski-Krastanov GaN/AlN Quantum Dots inside a Nanoscale Tip. *Appl. Phys. Lett.* **2017**, *111* (24), 243102. <https://doi.org/10.1063/1.5004417>.
- (62) Di Russo, E.; Cherkashin, N.; Korytov, M. N.; Nikolaev, A. E.; Sakharov, A. V.; Tsatsulnikov, A. F.; Bonaf, B.; Blum, I.; Houard, J.; da Costa, G.; Blavette, D.; Rigutti, L. Compositional Accuracy in Atom Probe Tomography Analyses Performed on III-N Light Emitting Diodes. *J. Appl. Phys.* **2019**, *126* (12), 124307. <https://doi.org/10.1063/1.5113799>.
- (63) Galtrey, M. J.; Oliver, R. A.; Kappers, M. J.; Humphreys, C. J.; Stokes, D. J.; Clifton, P. H.; Cerezo, A. Three-Dimensional Atom Probe Studies of an In_xGa_{1-x}N/GaN Multiple Quantum Well Structure: Assessment of Possible Indium Clustering. *Appl. Phys. Lett.* **2007**, *90* (6), 061903. <https://doi.org/10.1063/1.2431573>.
- (64) Tang, F.; Zhu, T.; Oehler, F.; Fu, W. Y.; Griffiths, J. T.; Massabuau, F. C.-P.; Kappers, M. J.; Martin, T. L.; Bagot, P. A. J.; Moody, M. P.; Oliver, R. A. Indium Clustering in A-Plane InGa_N Quantum Wells as Evidenced by Atom Probe Tomography. *Appl. Phys. Lett.* **2015**, *106* (7), 072104. <https://doi.org/10.1063/1.4909514>.
- (65) Amichi, L. Etude Du Dopage de Type p Dans Des Nanostructures de GaN Par Corrélation Entre Sonde Atomique Tomographique et Holographie Électronique Hors Axe Optique. These de doctorat, Université Grenoble Alpes (ComUE), 2018.
- (66) Amichi, L.; Mouton, I.; Di Russo, E.; Boureau, V.; Barbier, F.; Dussaigne, A.; Grenier, A.; Jouneau, P.-H.; Bougerol, C.; Cooper, D. Three-Dimensional Measurement of Mg Dopant Distribution and Electrical Activity in GaN by Correlative Atom Probe Tomography and off-Axis Electron Holography. *J. Appl. Phys.* **2020**, *127* (6), 065702. <https://doi.org/10.1063/1.5125188>.
- (67) Mancini, L.; Hernández-Maldonado, D.; Lefebvre, W.; Houard, J.; Blum, I.; Vurpillot, F.; Eymery, J.; Durand, C.; Tchernycheva, M.; Rigutti, L. Multi-Microscopy Study of the Influence of Stacking

- Faults and Three-Dimensional In Distribution on the Optical Properties of m-Plane InGaN Quantum Wells Grown on Microwire Sidewalls. *Appl. Phys. Lett.* **2016**, *108*, 04102. <https://doi.org/10.1063/1.4940748>.
- (68) Mancini, L.; Moyon, F.; Hernández-Maldonado, D.; Blum, I.; Houard, J.; Lefebvre, W.; Vurpillot, F.; Das, A.; Monroy, E.; Rigutti, L. Carrier Localization in GaN/AlN Quantum Dots As Revealed by Three-Dimensional Multimicroscopy. *Nano Lett.* **2017**, *17* (7), 4261–4269. <https://doi.org/10.1021/acs.nanolett.7b01189>.
- (69) Daudin, B.; Feuillet, G.; Hübner, J.; Samson, Y.; Widmann, F.; Philippe, A.; Bru-Chevallier, C.; Guillot, G.; Bustarret, E.; Bentoumi, G.; Deneuve, A. How to Grow Cubic GaN with Low Hexagonal Phase Content on (001) SiC by Molecular Beam Epitaxy. *J. Appl. Phys.* **1998**, *84* (4), 2295–2300. <https://doi.org/10.1063/1.368296>.
- (70) As, D.; Schmilgus, F.; Wang, C.; Schöttker, B.; Schikora, D.; Lischka, K. The near Band Edge Photoluminescence of Cubic GaN Epilayers. *Appl. Phys. Lett. - APPL PHYS LETT* **1997**, *70*, 1311–1313. <https://doi.org/10.1063/1.118521>.
- (71) Frentrup, M.; Lee, L. Y.; Sahonta, S.-L.; Kappers, M.; Massabuau, F.; Gupta, P.; Oliver, R.; Humphreys, C.; Wallis, D. X-Ray Diffraction Analysis of Cubic Zincblende III-Nitrides. *J. Phys. Appl. Phys.* **2017**, *50*, 433002. <https://doi.org/10.1088/1361-6463/aa865e>.
- (72) Morkoç, H.; Strite, S.; Gao, G. B.; Lin, M. E.; Sverdlov, B.; Burns, M. Large-band-gap SiC, III-V Nitride, and II-VI ZnSe-based Semiconductor Device Technologies. *J. Appl. Phys.* **1994**, *76* (3), 1363–1398. <https://doi.org/10.1063/1.358463>.
- (73) Vurgaftman, I.; Meyer, J. R. Band Parameters for Nitrogen-Containing Semiconductors. *J. Appl. Phys.* **2003**, *94* (6), 3675. <https://doi.org/10.1063/1.1600519>.
- (74) Roul, B.; Chandan, G.; Mukundan, S.; Krupanidhi, S. B. Heterostructures of III-Nitride Semiconductors for Optical and Electronic Applications. *Epitaxy* **2017**. <https://doi.org/10.5772/intechopen.70219>.
- (75) curtis.suplee@nist.gov. GaN Nanowires: Knowing Which End Is Up <https://www.nist.gov/news-events/news/2015/09/gan-nanowires-knowing-which-end> (accessed 2020 -11 -22).
- (76) Monroy, E.; Sarigiannidou, E.; Fossard, F.; Gogneau, N.; Bellet-Amalric, E.; Rouvière, J.-L.; Monnoye, S.; Mank, H.; Daudin, B. Growth Kinetics of N-Face Polarity GaN by Plasma-Assisted Molecular-Beam Epitaxy. *Appl. Phys. Lett.* **2004**, *84* (18), 3684–3686. <https://doi.org/10.1063/1.1739511>.
- (77) Huang, D.; Visconti, P.; Jones, K. M.; Reshchikov, M. A.; Yun, F.; Baski, A. A.; King, T.; Morkoç, H. Dependence of GaN Polarity on the Parameters of the Buffer Layer Grown by Molecular Beam Epitaxy. *Appl. Phys. Lett.* **2001**, *78* (26), 4145–4147. <https://doi.org/10.1063/1.1380399>.
- (78) Kim, K.; Lambrecht, W. R. L.; Segall, B. Elastic Constants and Related Properties of Tetrahedrally Bonded BN, AlN, GaN, and InN. *Phys. Rev. B* **1996**, *53* (24), 16310–16326. <https://doi.org/10.1103/PhysRevB.53.16310>.
- (79) Wright, A. F. Elastic Properties of Zinc-Blende and Wurtzite AlN, GaN, and InN. *J. Appl. Phys.* **1997**, *82* (6), 2833–2839. <https://doi.org/10.1063/1.366114>.
- (80) Takagi, Y.; Ahart, M.; Azuhata, T.; Sota, T.; Suzuki, K.; Nakamura, S. Brillouin Scattering Study in the GaN Epitaxial Layer. *Phys. B Condens. Matter* **1996**, *219–220*, 547–549. [https://doi.org/10.1016/0921-4526\(95\)00807-1](https://doi.org/10.1016/0921-4526(95)00807-1).
- (81) Polian, A.; Grimsditch, M.; Grzegory, I. Elastic Constants of Gallium Nitride. *J. Appl. Phys.* **1996**, *79* (6), 3343–3344. <https://doi.org/10.1063/1.361236>.
- (82) McNeil, L. E.; Grimsditch, M.; French, R. H. Vibrational Spectroscopy of Aluminum Nitride. *J. Am. Ceram. Soc.* **1993**, *76* (5), 1132–1136. <https://doi.org/10.1111/j.1151-2916.1993.tb03730.x>.
- (83) Deger, C.; Born, E.; Angerer, H.; Ambacher, O.; Stutzmann, M.; Hornsteiner, J.; Riha, E.; Fischerauer, G. Sound Velocity of Al_xGa_{1-x}N Thin Films Obtained by Surface Acoustic-Wave Measurements. *Appl. Phys. Lett.* **1998**, *72* (19), 2400–2402. <https://doi.org/10.1063/1.121368>.
- (84) Romanov, A. E.; Baker, T. J.; Nakamura, S.; Speck, J. S.; ERATO/JST UCSB Group. Strain-Induced

- Polarization in Wurtzite III-Nitride Semipolar Layers. *J. Appl. Phys.* **2006**, *100* (2), 023522. <https://doi.org/10.1063/1.2218385>.
- (85) Ambacher et al. - 1999 - Two-Dimensional Electron Gases Induced by Spontane.Pdf.
- (86) Bernardini, F.; Fiorentini, V.; Vanderbilt, D. Spontaneous Polarization and Piezoelectric Constants of III-V Nitrides. *Phys. Rev. B* **1997**, *56* (16), R10024–R10027. <https://doi.org/10.1103/PhysRevB.56.R10024>.
- (87) Bernardini, F.; Fiorentini, V.; Vanderbilt, D. Accurate Calculation of Polarization-Related Quantities in Semiconductors. *Phys. Rev. B* **2001**, *63* (19), 193201. <https://doi.org/10.1103/PhysRevB.63.193201>.
- (88) Ambacher, O.; Foutz, B.; Smart, J.; Shealy, J. R.; Weimann, N.; Chu, K.; Murphy, M.; Sierakowski, A.; Schaff, W.; Eastman, L.; Dimitrov, R.; Mitchell, A.; Stutzmann, M. Two Dimensional Electron Gases Induced by Spontaneous and Piezoelectric Polarization Undoped and Doped AlGa_N/Ga_N Heterostructures. *J. Appl. Phys.* **2000**, *87*, 334–344. <https://doi.org/10.1063/1.371866>.
- (89) Dingle, R.; Sell, D. D.; Stokowski, S. E.; Ilegems, M. Absorption, Reflectance, and Luminescence of Ga_N Epitaxial Layers. *Phys. Rev. B* **1971**, *4* (4), 1211–1218. <https://doi.org/10.1103/PhysRevB.4.1211>.
- (90) Taniyasu, Y.; Kasu, M. Origin of Exciton Emissions from an AlN P-n Junction Light-Emitting Diode. *Appl. Phys. Lett.* **2011**, *98* (13), 131910. <https://doi.org/10.1063/1.3574025>.
- (91) Taniyasu, Y.; Kasu, M.; Makimoto, T. Radiation and Polarization Properties of Free-Exciton Emission from AlN (0001) Surface. *Appl. Phys. Lett.* **2007**, *90* (26), 261911. <https://doi.org/10.1063/1.2752727>.
- (92) Prinz, G. i M.; Ladenburger, A.; Schirra, M.; Feneberg, M.; Thonke, K.; Sauer, R.; Taniyasu, Y.; Kasu, M.; Makimoto, T. Cathodoluminescence, Photoluminescence, and Reflectance of an Aluminum Nitride Layer Grown on Silicon Carbide Substrate. *J. Appl. Phys.* **2007**, *101* (2), 023511. <https://doi.org/10.1063/1.2423141>.
- (93) Rezaei, B.; Asgari, A.; Kalafi, M. Electronic Band Structure Pseudopotential Calculation of Wurtzite III-Nitride Materials. *Phys. B Condens. Matter* **2006**, *371* (1), 107–111. <https://doi.org/10.1016/j.physb.2005.10.003>.
- (94) Lambrecht, W. R. L.; Segall, B. Anomalous Band-Gap Behavior and Phase Stability of c-BN--Diamond Alloys. *Phys. Rev. B* **1993**, *47* (15), 9289–9296. <https://doi.org/10.1103/PhysRevB.47.9289>.
- (95) Pugh, S. K.; Dugdale, D. J.; Brand, S.; Abram, R. A. Electronic Structure Calculations on Nitride Semiconductors. *Semicond. Sci. Technol.* **1999**, *14* (1), 23. <https://doi.org/10.1088/0268-1242/14/1/003>.
- (96) Dridi, Z.; Bouhafs, B.; Ruterana, P. First-Principles Investigation of Lattice Constants and Bowing Parameters in Wurtzite Al_xGa_{1-x}N, In_xGa_{1-x}N and In_xAl_{1-x}N Alloys. *Semicond. Sci. Technol.* **2003**, *18* (9), 850–856. <https://doi.org/10.1088/0268-1242/18/9/307>.
- (97) Kuo, Y.-K. K. Y.-K.; Lin, W.-W. L. W.-W.; Lin, J. L. J. Band-Gap Bowing Parameter of the In_xGa_{1-x}N Derived From Theoretical Simulation. *Jpn. J. Appl. Phys.* **2001**, *40* (5R), 3157. <https://doi.org/10.1143/JJAP.40.3157>.
- (98) Varshni, Y. P. Temperature Dependence of the Energy Gap in Semiconductors. *Physica* **1967**, *34* (1), 149–154. [https://doi.org/10.1016/0031-8914\(67\)90062-6](https://doi.org/10.1016/0031-8914(67)90062-6).
- (99) Sarswat, P. K.; Free, M. L. A Study of Energy Band Gap versus Temperature for Cu₂ZnSnS₄ Thin Films. *Phys. B Condens. Matter* **2012**, *407* (1), 108–111. <https://doi.org/10.1016/j.physb.2011.09.134>.
- (100) Walukiewicz, W.; Li, S. X.; Wu, J.; Yu, K. M.; Ager, J. W.; Haller, E. E.; Lu, H.; Schaff, W. J. Optical Properties and Electronic Structure of InN and In-Rich Group III-Nitride Alloys. *J. Cryst. Growth* **2004**, *269* (1), 119–127. <https://doi.org/10.1016/j.jcrysro.2004.05.041>.
- (101) Park, S.-H.; Chuang, S.-L. Crystal-Orientation Effects on the Piezoelectric Field and Electronic Properties of Strained Wurtzite Semiconductors. *Phys. Rev. B* **1999**, *59* (7), 4725–4737. <https://doi.org/10.1103/PhysRevB.59.4725>.
- (102) Masui, H.; Yamada, H.; Iso, K.; Nakamura, S.; DenBaars, S. P. Optical Polarization Characteristics

- of M-Oriented InGaN/GaN Light-Emitting Diodes with Various Indium Compositions in Single-Quantum-Well Structure. *Appl Phys* **2008**, *8*.
- (103) Azize, M.; Palacios, T. Effect of Substrate-Induced Strain in the Transport Properties of AlGaIn/GaN Heterostructures. *J. Appl. Phys.* **2010**, *108* (2), 023707. <https://doi.org/10.1063/1.3463150>.
- (104) Dreyer, C. E.; Janotti, A.; Van de Walle, C. G. Effects of Strain on the Electron Effective Mass in GaN and AlN. *Appl. Phys. Lett.* **2013**, *102* (14), 142105. <https://doi.org/10.1063/1.4801520>.
- (105) McCluskey, M. D.; Van de Walle, C. G.; Romano, L. T.; Krusor, B. S.; Johnson, N. M. Effect of Composition on the Band Gap of Strained In_xGa_{1-x}N Alloys. *J. Appl. Phys.* **2003**, *93* (7), 4340–4342. <https://doi.org/10.1063/1.1560563>.
- (106) O'Donnell, K. P.; Martin, R. W.; Trager-Cowan, C.; White, M. E.; Esona, K.; Deatcher, C.; Middleton, P. G.; Jacobs, K.; Van der Stricht, W.; Merlet, C.; Gil, B.; Vantomme, A.; Mosselmanns, J. F. W. The Dependence of the Optical Energies on InGaIn Composition. *Mater. Sci. Eng. B* **2001**, *82* (1), 194–196. [https://doi.org/10.1016/S0921-5107\(00\)00706-6](https://doi.org/10.1016/S0921-5107(00)00706-6).
- (107) Parker, C. A.; Roberts, J. C.; Bedair, S. M.; Reed, M. J.; Liu, S. X.; El-Masry, N. A.; Robins, L. H. Optical Band Gap Dependence on Composition and Thickness of In_xGa_{1-x}N (0. *Appl. Phys. Lett.* **1999**, *75* (17), 2566–2568. <https://doi.org/10.1063/1.125079>.
- (108) Kojima, K.; Kamon, H.; Funato, M.; Kawakami, Y. Theoretical Investigations on Anisotropic Optical Properties in Semipolar and Nonpolar InGaIn Quantum Wells. *Phys. Status Solidi C* **2008**, *5* (9), 3038–3041. <https://doi.org/10.1002/pssc.200779277>.
- (109) Yan, Q.; Rinke, P.; Scheffler, M.; Van de Walle, C. G. Role of Strain in Polarization Switching in Semipolar InGaIn/GaN Quantum Wells. *Appl. Phys. Lett.* **2010**, *97* (18), 181102. <https://doi.org/10.1063/1.3507289>.
- (110) Zhao, Y.; Tanaka, S.; Yan, Q.; Huang, C.-Y.; Chung, R. B.; Pan, C.-C.; Fujito, K.; Feezell, D.; Van de Walle, C. G.; Speck, J. S.; DenBaars, S. P.; Nakamura, S. High Optical Polarization Ratio from Semipolar (202°) Blue-Green InGaIn/GaN Light-Emitting Diodes. *Appl. Phys. Lett.* **2011**, *99* (5), 051109. <https://doi.org/10.1063/1.3619826>.
- (111) Zhao, Y.; Yan, Q.; Feezell, D.; Fujito, K.; Walle, C. G. V. de; Speck, J. S.; DenBaars, S. P.; Nakamura, S. Optical Polarization Characteristics of Semipolar (303°) and (303°) InGaIn/GaN Light-Emitting Diodes. *Opt. Express* **2013**, *21* (101), A53–A59. <https://doi.org/10.1364/OE.21.000A53>.
- (112) Yan, Q.; Rinke, P.; Janotti, A.; Scheffler, M.; Van de Walle, C. G. Effects of Strain on the Band Structure of Group-III Nitrides. *Phys. Rev. B* **2014**, *90* (12), 125118. <https://doi.org/10.1103/PhysRevB.90.125118>.
- (113) Tchernycheva, M.; Nevou, L.; Doyennette, L.; Julien, F. H.; Warde, E.; Guillot, F.; Monroy, E.; Bellet-Amalric, E.; Remmele, T.; Albrecht, M. Systematic Experimental and Theoretical Investigation of Intersubband Absorption in GaN/AlN Quantum Wells. *Phys. Rev. B* **2006**, *73* (12), 125347. <https://doi.org/10.1103/PhysRevB.73.125347>.
- (114) Spies, M.; Monroy, E. Nanowire Photodetectors Based on Wurtzite Semiconductor Heterostructures. *Semicond. Sci. Technol.* **2019**, *34* (5), 053002. <https://doi.org/10.1088/1361-6641/ab0cb8>.
- (115) Farrell, R. M.; Young, E. C.; Wu, F.; DenBaars, S. P.; Speck, J. S. Materials and Growth Issues for High-Performance Nonpolar and Semipolar Light-Emitting Devices. *Semicond. Sci. Technol.* **2012**, *27* (2), 024001. <https://doi.org/10.1088/0268-1242/27/2/024001>.
- (116) Band gaps in InN/GaN superlattices: Nonpolar and polar growth directions: Journal of Applied Physics: Vol 114, No 22 <https://aip.scitation.org/doi/10.1063/1.4843015> (accessed 2021 -02 -24).
- (117) Waltereit, P.; Brandt, O.; Trampert, A.; Grahn, H. T.; Menniger, J.; Ramsteiner, M.; Reiche, M.; Ploog, K. H. Nitride Semiconductors Free of Electrostatic Fields for Efficient White Light-Emitting Diodes. *Nature* **2000**, *406* (6798), 865–868. <https://doi.org/10.1038/35022529>.
- (118) Arbiol, J.; de la Mata, M.; Eickhoff, M.; Morral, A. F. i. Bandgap Engineering in a Nanowire: Self-Assembled 0, 1 and 2D Quantum Structures. *Mater. Today* **2013**, *16* (6), 213–219.

- <https://doi.org/10.1016/j.mattod.2013.06.006>.
- (119) AR2010.Pdf.
- (120) Venables, J. A. Atomic Processes in Crystal Growth. *Surf. Sci.* **1994**, 299–300, 798–817. [https://doi.org/10.1016/0039-6028\(94\)90698-X](https://doi.org/10.1016/0039-6028(94)90698-X).
- (121) Lim, C. B. Hétérostructures GaN/Al(Ga)N Pour l'optoélectronique Infrarouge : Orientations Polaires et Non-Polaires. PhD Thesis, Université Grenoble Alpes, Grenoble, 2017.
- (122) Joyce, B. A.; Dobson, P. J.; Neave, J. H.; Woodbridge, K.; Zhang, J.; Larsen, P. K.; Bølger, B. RHEED Studies of Heterojunction and Quantum Well Formation during MBE Growth — from Multiple Scattering to Band Offsets. *Surf. Sci.* **1986**, 168 (1), 423–438. [https://doi.org/10.1016/0039-6028\(86\)90873-3](https://doi.org/10.1016/0039-6028(86)90873-3).
- (123) Adelman, C.; Brault, J.; Mula, G.; Daudin, B.; Lymperakis, L.; Neugebauer, J. Gallium Adsorption on (0001) GaN Surfaces. *Phys. Rev. B* **2003**, 67 (16), 165419. <https://doi.org/10.1103/PhysRevB.67.165419>.
- (124) Mula, G.; Adelman, C.; Moehl, S.; Oullier, J.; Daudin, B. Surfactant Effect of Gallium during Molecular-Beam Epitaxy of GaN on AlN (0001). *Phys. Rev. B* **2001**, 64 (19), 195406. <https://doi.org/10.1103/PhysRevB.64.195406>.
- (125) Neugebauer, J.; Zywiets, T.; Scheffler, M.; Northrup, J.; Chen, H.; Feenstra, R. Adatom Kinetics On and Below the Surface: The Existence of a New Diffusion Channel. *Phys. Rev. Lett.* **2003**, 90 (5), 056101. <https://doi.org/10.1103/PhysRevLett.90.056101>.
- (126) Kotsar, Y. Puits Quantiques GaN/Al(Ga)N Pour l'optoélectronique Inter-Sous-Bande Dans l'infrarouge Proche, Moyen et Lointain. PhD Thesis, Université de Grenoble, Grenoble, 2012.
- (127) Adelman, H. C. Growth and Strain Relaxation Mechanisms of Group III Nitride Heterostructures. PhD Thesis, Université Joseph Fourier, Grenoble, 2002.
- (128) Northrup, J.; Neugebauer, J.; Feenstra, R.; Smith, A. Structure of GaN(0001) : The Laterally Contracted Ga Bilayer Model. *Phys. Rev. B* **2000**, 61 (15), 9932–9935. <https://doi.org/10.1103/PhysRevB.61.9932>.
- (129) Kandaswamy, P. K.; Guillot, F.; Bellet-Amalric, E.; Monroy, E.; Nevou, L.; Tchernycheva, M.; Michon, A.; Julien, F. H.; Baumann, E.; Giorgetta, F. R.; Hofstetter, D.; Remmele, T.; Albrecht, M.; Birner, S.; Dang, L. S. GaN/AlN Short-Period Superlattices for Intersubband Optoelectronics: A Systematic Study of Their Epitaxial Growth, Design, and Performance. *J. Appl. Phys.* **2008**, 104 (9), 093501. <https://doi.org/10.1063/1.3003507>.
- (130) Hermann, M.; Monroy, E.; Helman, A.; Baur, B.; Albrecht, M.; Daudin, B.; Ambacher, O.; Stutzmann, M.; Eickhoff, M. Vertical Transport in Group III-Nitride Heterostructures and Application in AlN/GaN Resonant Tunneling Diodes. *Phys. Status Solidi C* **2004**, 1 (8), 2210–2227. <https://doi.org/10.1002/pssc.200404771>.
- (131) Takayanagi, K.; Tanishiro, Y.; Takahashi, M.; Takahashi, S. Structural Analysis of Si(111)-7×7 by UHV-transmission Electron Diffraction and Microscopy. *J. Vac. Sci. Technol. A* **1985**, 3 (3), 1502–1506. <https://doi.org/10.1116/1.573160>.
- (132) Shtrichman, I.; Metzner, C.; Ehrenfreund, E.; Gershoni, D.; Maranowski, K. D.; Gossard, A. C. Depolarization Shift of the Intersubband Resonance in a Quantum Well with an Electron-Hole Plasma. *Phys. Rev. B* **2001**, 65 (3), 035310. <https://doi.org/10.1103/PhysRevB.65.035310>.
- (133) Songmuang, R.; Landré, O.; Daudin, B. From Nucleation to Growth of Catalyst-Free GaN Nanowires on Thin AlN Buffer Layer. *Appl. Phys. Lett.* **2007**, 91 (25), 251902. <https://doi.org/10.1063/1.2817941>.
- (134) Cherns, D.; Meshi, L.; Griffiths, I.; Khongphetsak, S.; Novikov, S. V.; Farley, N.; Campion, R. P.; Foxon, C. T. Defect Reduction in GaN/(0001)Sapphire Films Grown by Molecular Beam Epitaxy Using Nanocolumn Intermediate Layers. *Appl. Phys. Lett.* **2008**, 92 (12), 121902. <https://doi.org/10.1063/1.2899944>.
- (135) Brubaker, M. D.; Levin, I.; Davydov, A. V.; Rourke, D. M.; Sanford, N. A.; Bright, V. M.; Bertness, K. A. Effect of AlN Buffer Layer Properties on the Morphology and Polarity of GaN Nanowires Grown by Molecular Beam Epitaxy. *J. Appl. Phys.* **2011**, 110 (5), 053506. <https://doi.org/10.1063/1.3633522>.

- (136) Schenk, H. P. D.; Kipshidze, G. D.; Kaiser, U.; Fissel, A.; Kräußlich, J.; Schulze, J.; Richter, W. Investigation of Two-Dimensional Growth of AlN(0001) on Si(111) by Plasma-Assisted Molecular Beam Epitaxy. *J. Cryst. Growth* **1999**, *200* (1–2), 45–54. [https://doi.org/10.1016/S0022-0248\(98\)01245-7](https://doi.org/10.1016/S0022-0248(98)01245-7).
- (137) Musolino, M.; Tahraoui, A.; Fernández-Garrido, S.; Brandt, O.; Trampert, A.; Geelhaar, L.; Riechert, H. Compatibility of the Selective Area Growth of GaN Nanowires on AlN-Buffered Si Substrates with the Operation of Light Emitting Diodes. *Nanotechnology* **2015**, *26* (8), 085605. <https://doi.org/10.1088/0957-4484/26/8/085605>.
- (138) Himwas, C.; Hertog, M. den; Dang, L. S.; Monroy, E.; Songmuang, R. Alloy Inhomogeneity and Carrier Localization in AlGaIn Sections and AlGaIn/AlN Nanodisks in Nanowires with 240–350 Nm Emission. *Appl. Phys. Lett.* **2014**, *105* (24), 241908. <https://doi.org/10.1063/1.4904989>.
- (139) Ajay, A. GaN/AlGaIn Nanowires for Quantum Devices.
- (140) Fernández-Garrido, S.; Grandal, J.; Calleja, E.; Sánchez-García, M. A.; López-Romero, D. A Growth Diagram for Plasma-Assisted Molecular Beam Epitaxy of GaN Nanocolumns on Si(111). *J. Appl. Phys.* **2009**, *106* (12), 126102. <https://doi.org/10.1063/1.3267151>.
- (141) Hestroffer, K.; Leclere, C.; Bougerol, C.; Renevier, H.; Daudin, B. Polarity of GaN Nanowires Grown by Plasma-Assisted Molecular Beam Epitaxy on Si(111). *Phys. Rev. B* **2011**, *84* (24), 245302. <https://doi.org/10.1103/PhysRevB.84.245302>.
- (142) Chichibu, S. F.; Setoguchi, A.; Uedono, A.; Yoshimura, K.; Sumiya, M. Impact of Growth Polar Direction on the Optical Properties of GaN Grown by Metalorganic Vapor Phase Epitaxy. *Appl. Phys. Lett.* **2000**, *78* (1), 28–30. <https://doi.org/10.1063/1.1337641>.
- (143) Ho, I. H.; Stringfellow, G. B. Incomplete Solubility in Nitride Alloys. *MRS Online Proc. Libr. OPL* **1996**, *449*. <https://doi.org/10.1557/PROC-449-871>.
- (144) Koukitsu, A.; Taki, T.; Takahashi, N.; Seki, H. Thermodynamic Study on the Role of Hydrogen during the MOVPE Growth of Group III Nitrides. *J. Cryst. Growth* **1999**, *197* (1), 99–105. [https://doi.org/10.1016/S0022-0248\(98\)00894-X](https://doi.org/10.1016/S0022-0248(98)00894-X).
- (145) Takayama, T.; Yuri, M.; Itoh, K.; Baba, T.; Harris, J. S. Theoretical Analysis of Unstable Two-Phase Region and Microscopic Structure in Wurtzite and Zinc-Blende InGaIn Using Modified Valence Force Field Model. *J. Appl. Phys.* **2000**, *88* (2), 1104–1110. <https://doi.org/10.1063/1.373783>.
- (146) Mohamad, R.; Béré, A.; Chen, J.; Ruterana, P. Investigation of Strain Effects on Phase Diagrams in the Ternary Nitride Alloys (InAlN, AlGaIn, InGaIn). *Phys. Status Solidi A* **2017**, *214* (9), 1600752. <https://doi.org/10.1002/pssa.201600752>.
- (147) Stringfellow, G. B. Microstructures Produced during the Epitaxial Growth of InGaIn Alloys. *J. Cryst. Growth* **2010**, *312* (6), 735–749. <https://doi.org/10.1016/j.jcrysgro.2009.12.018>.
- (148) Caetano, C.; Teles, L. K.; Marques, M.; Dal Pino, A.; Ferreira, L. G. Phase Stability, Chemical Bonds, and Gap Bowing of $\text{In}_x\text{N}_{1-x}\text{Ga}_{1-x}\text{N}_x$ Alloys: Comparison between Cubic and Wurtzite Structures. *Phys. Rev. B* **2006**, *74* (4), 045215. <https://doi.org/10.1103/PhysRevB.74.045215>.
- (149) Karpov, S. Yu. Suppression of Phase Separation in InGaIn Due to Elastic Strain. *MRS Internet J. Nitride Semicond. Res.* **1998**, *3*, e16. <https://doi.org/10.1557/S1092578300000880>.
- (150) Valdueza-Felip, S.; Bellet-Amalric, E.; Núñez-Cascajero, A.; Wang, Y.; Chauvat, M.-P.; Ruterana, P.; Pouget, S.; Lorenz, K.; Alves, E.; Monroy, E. High In-Content InGaIn Layers Synthesized by Plasma-Assisted Molecular-Beam Epitaxy: Growth Conditions, Strain Relaxation, and In Incorporation Kinetics. *J. Appl. Phys.* **2014**, *116* (23), 233504. <https://doi.org/10.1063/1.4903944>.
- (151) Das, A.; Sinha, P.; Kotsar, Y.; Kandaswamy, P. K.; Dimitrakopoulos, G. P.; Kehagias, Th.; Komninou, Ph.; Nataf, G.; De Mierry, P.; Monroy, E. Growth and Characterization of Polar (0001) and Semipolar (11–22) InGaIn/GaN Quantum Dots. *J. Cryst. Growth* **2011**, *323* (1), 161–163. <https://doi.org/10.1016/j.jcrysgro.2010.10.130>.
- (152) Gačević, Ž.; Das, A.; Teubert, J.; Kotsar, Y.; Kandaswamy, P. K.; Kehagias, Th.; Koukoulou, T.; Komninou, Ph.; Monroy, E. Internal Quantum Efficiency of III-Nitride Quantum Dot

- Superlattices Grown by Plasma-Assisted Molecular-Beam Epitaxy. *J. Appl. Phys.* **2011**, *109* (10), 103501. <https://doi.org/10.1063/1.3590151>.
- (153) Calle, F.; Sánchez, F. J.; Tijero, J. M. G.; Sánchez-García, M. A.; Calleja, E.; Beresford, R. Exciton and Donor - Acceptor Recombination in Undoped GaN on Si(111). *Semicond. Sci. Technol.* **1997**, *12* (11), 1396–1403. <https://doi.org/10.1088/0268-1242/12/11/011>.
- (154) Shan, W.; Little, B. D.; Fischer, A. J.; Song, J. J.; Goldenberg, B.; Perry, W. G.; Bremser, M. D.; Davis, R. F. Binding Energy for the Intrinsic Excitons in Wurtzite GaN. *Phys. Rev. B* **1996**, *54* (23), 16369–16372. <https://doi.org/10.1103/PhysRevB.54.16369>.
- (155) Shatalov, M.; Yang, J.; Sun, W.; Kennedy, R.; Gaska, R.; Liu, K.; Shur, M.; Tamulaitis, G. Efficiency of Light Emission in High Aluminum Content AlGaIn Quantum Wells. *J. Appl. Phys.* **2009**, *105* (7), 073103. <https://doi.org/10.1063/1.3103321>.
- (156) SIEBER, B. Cathodoluminescence - Principes physiques et systèmes de détection <https://www.techniques-ingenieur.fr/base-documentaire/mesures-analyses-th1/analyses-de-surface-et-de-materiaux-42383210/cathodoluminescence-p3792/> (accessed 2021 -01 -28).
- (157) Electron Interactions https://serc.carleton.edu/research_education/geochemsheets/electroninteractions.html (accessed 2021 -01 -28).
- (158) Damilano, B.; Vézian, S.; Portail, M.; Alloing, B.; Brault, J.; Courville, A.; Brändli, V.; Leroux, M.; Massies, J. Optical Properties of In_xGa_{1-x}N/GaN Quantum-Disks Obtained by Selective Area Sublimation. *J. Cryst. Growth* **2017**, *477*, 262–266. <https://doi.org/10.1016/j.jcrysgro.2017.01.010>.
- (159) Bruckbauer, J.; Edwards, P. R.; Wang, T.; Martin, R. W. High Resolution Cathodoluminescence Hyperspectral Imaging of Surface Features in InGaN/GaN Multiple Quantum Well Structures. *Appl. Phys. Lett.* **2011**, *98* (14), 141908. <https://doi.org/10.1063/1.3575573>.
- (160) Roque, J. Corrélation Luminescence/Défauts Étendus Dans Les Structures à Puits Quantique InGaAs Épitaxiées Sélectivement Sur Substrats Si. These de doctorat, Université Grenoble Alpes (ComUE), 2018.
- (161) Bruker AFM Probes - TESPA-V2 <https://www.brukerafmprobes.com/p-3844-tespa-v2.aspx> (accessed 2021 -02 -02).
- (162) Binnig, G.; Quate, C. F.; Gerber, Ch. Atomic Force Microscope. *Phys. Rev. Lett.* **1986**, *56* (9), 930–933. <https://doi.org/10.1103/PhysRevLett.56.930>.
- (163) AFM scanning modes – MAX IV <https://www.maxiv.lu.se/accelerators-beamlines/support-labs-microscopy/atomic-force-microscopy/afm-scanning-modes/> (accessed 2021 -02 -02).
- (164) Dunaevskiy, M.; Alekseev, P.; Girard, P.; Lashkul, A.; Lahderanta, E.; Titkov, A. Analysis of the Lateral Resolution of Electrostatic Force Gradient Microscopy. *J. Appl. Phys.* **2012**, *112* (6), 064112. <https://doi.org/10.1063/1.4752430>.
- (165) Fundamentals of Contact Mode and TappingMode Atomic Force Microscopy <https://www.azonano.com/article.aspx?ArticleID=3010> (accessed 2021 -02 -02).
- (166) Wiesendanger, R.; Roland, W. *Scanning Probe Microscopy and Spectroscopy: Methods and Applications*; Cambridge University Press, 1994.
- (167) Tegenfeldt, J. O.; Montelius, L. Image Widening Not Only a Question of Tip Sample Convolution. *Appl. Phys. Lett.* **1995**, *66* (9), 1068–1070. <https://doi.org/10.1063/1.113575>.
- (168) Giannuzzi, L. A.; University, N. C. S. *Introduction to Focused Ion Beams: Instrumentation, Theory, Techniques and Practice*; Springer Science & Business Media, 2004.
- (169) Denneulin, T. Holographie électronique en champ sombre : une technique fiable pour mesurer des déformations dans les dispositifs de la microélectronique. phdthesis, Université de Grenoble, 2012.
- (170) Giannuzzi, L. A.; Stevie, F. A. A Review of Focused Ion Beam Milling Techniques for TEM Specimen Preparation. *Micron* **1999**, *30* (3), 197–204. [https://doi.org/10.1016/S0968-4328\(99\)00005-0](https://doi.org/10.1016/S0968-4328(99)00005-0).
- (171) Langford, R. M.; Petford-Long, A. K. Preparation of Transmission Electron Microscopy Cross-

- Section Specimens Using Focused Ion Beam Milling. *J. Vac. Sci. Technol. A* **2001**, *19* (5), 2186–2193. <https://doi.org/10.1116/1.1378072>.
- (172) Bogdanowicz, J.; Kumar, A.; Fleischmann, C.; Gilbert, M.; Houard, J.; Vella, A.; Vandervorst, W. Laser-Assisted Atom Probe Tomography of Semiconductors: The Impact of the Focused-Ion Beam Specimen Preparation. *Ultramicroscopy* **2018**, *188*, 19–23. <https://doi.org/10.1016/j.ultramic.2018.03.001>.
- (173) Mancini, L.; Amirifar, N.; Shinde, D.; Blum, I.; Gilbert, M.; Vella, A.; Vurpillot, F.; Lefebvre, W.; Lardé, R.; Talbot, E.; Pareige, P.; Portier, X.; Ziani, A.; Davesne, C.; Durand, C.; Eymery, J.; Butté, R.; Carlin, J.-F.; Grandjean, N.; Rigutti, L. Composition of Wide Bandgap Semiconductor Materials and Nanostructures Measured by Atom Probe Tomography and Its Dependence on the Surface Electric Field. *J. Phys. Chem. C* **2014**, *118* (41), 24136–24151. <https://doi.org/10.1021/jp5071264>.
- (174) *Springer Handbook of Electronic and Photonic Materials*; Kasap, S. O., Capper, P., Eds.; Springer: New York, 2006.
- (175) Atom Probe Tomography - Introduction to the technique <https://www.cameca.com/products/apt/technique> (accessed 2021 -07 -02).
- (176) BLAVETTE, D.; MENAND, A. Microscopie Ionique à Effet de Champ et Sonde Atomique. *Microsc. Ion. À Eff. Champ Sonde At.* **1989**, *P1* (P900), P900.1-P900.14.
- (177) Costa, G. D.; Wang, H.; Duguay, S.; Bostel, A.; Blavette, D.; Deconihout, B. Advance in Multi-Hit Detection and Quantization in Atom Probe Tomography. *Rev. Sci. Instrum.* **2012**, *83* (12), 123709. <https://doi.org/10.1063/1.4770120>.
- (178) Bacchi, C. Nouvelle génération de détecteurs d'ions sensible en position et en temps pour le développement de la sonde atomique tomographique. 221.
- (179) Russo, E. D. Study of the Physical Mechanisms Leading to Compositional Biases in Atom Probe Tomography of Semiconductors. phdthesis, Normandie Université, 2018.
- (180) Lefebvre, W.; Vurpillot, F.; Sauvage, X. *Atom Probe Tomography: Put Theory Into Practice*; Academic Press, 2016.
- (181) Gault, B.; Moody, M. P.; Cairney, J. M.; Ringer, S. P. *Atom Probe Microscopy*; Springer Science & Business Media, 2012.
- (182) Birner, S. Modeling of Semiconductor Nanostructures and Semiconductor–Electrolyte Interfaces. PhD Thesis, Technische Universität München, Garching b. München, 2011.
- (183) Fiorentini, V.; Bernardini, F.; Ambacher, O. Evidence for Nonlinear Macroscopic Polarization in III–V Nitride Alloy Heterostructures. *Appl. Phys. Lett.* **2002**, *80* (7), 1204–1206. <https://doi.org/10.1063/1.1448668>.
- (184) Suski, T.; Staszczak, G.; Korona, K. P.; Lefebvre, P.; Monroy, E.; Drozd, P. A.; Muzioł, G.; Skierbiszewski, C.; Kulczykowski, M.; Matuszewski, M.; Grzanka, E.; Grzanka, S.; Pieniak, K.; Gibasiewicz, K.; Khachapuridze, A.; Smalc-Koziorowska, J.; Marona, L.; Perlin, P. Switching of Exciton Character in Double InGaN/GaN Quantum Wells. *Phys. Rev. B* **2018**, *98* (16), 165302. <https://doi.org/10.1103/PhysRevB.98.165302>.
- (185) Morkoç, H. *Nitride Semiconductor Devices: Fundamentals and Applications*; John Wiley & Sons, 2013.
- (186) Rinke, P.; Winkelkemper, M.; Qteish, A.; Bimberg, D.; Neugebauer, J.; Scheffler, M. Consistent Set of Band Parameters for the Group-III Nitrides AlN, GaN, and InN. *Phys. Rev. B* **2008**, *77* (7), 075202. <https://doi.org/10.1103/PhysRevB.77.075202>.
- (187) Salvador, A.; Liu, G.; Kim, W.; Aktas, Ö.; Botchkarev, A.; Morkoç, H. Properties of a Si Doped GaN/AlGaIn Single Quantum Well. *Appl. Phys. Lett.* **1995**, *67* (22), 3322–3324. <https://doi.org/10.1063/1.115234>.
- (188) Würtele, M. A.; Kolbe, T.; Lipsz, M.; Külberg, A.; Weyers, M.; Kneissl, M.; Jekel, M. Application of GaN-Based Ultraviolet-C Light Emitting Diodes – UV LEDs – for Water Disinfection. *Water Res.* **2011**, *45* (3), 1481–1489. <https://doi.org/10.1016/j.watres.2010.11.015>.
- (189) Beck, S. E.; Ryu, H.; Boczek, L. A.; Cashdollar, J. L.; Jeanis, K. M.; Rosenblum, J. S.; Lawal, O. R.; Linden, K. G. Evaluating UV-C LED Disinfection Performance and Investigating Potential Dual-

- Wavelength Synergy. *Water Res.* **2017**, *109*, 207–216. <https://doi.org/10.1016/j.watres.2016.11.024>.
- (190) Kneissl, M.; Seong, T.-Y.; Han, J.; Amano, H. The Emergence and Prospects of Deep-Ultraviolet Light-Emitting Diode Technologies. *Nat. Photonics* **2019**, *13* (4), 233–244. <https://doi.org/10.1038/s41566-019-0359-9>.
- (191) Dimkou, I.; Harikumar, A.; Donatini, F.; Lähnemann, J.; den Hertog, M. I.; Bougerol, C.; Bellet-Amalric, E.; Mollard, N.; Ajay, A.; Ledoux, G.; Purcell, S. T.; Monroy, E. Assessment of AlGaN/AlN Superlattices on GaN Nanowires as Active Region of Electron-Pumped Ultraviolet Sources. *Nanotechnology* **2020**, *31* (20), 204001. <https://doi.org/10.1088/1361-6528/ab704d>.
- (192) Buonanno, M.; Welch, D.; Shuryak, I.; Brenner, D. J. Far-UVC Light (222 Nm) Efficiently and Safely Inactivates Airborne Human Coronaviruses. *Sci. Rep.* **2020**, *10* (1), 10285. <https://doi.org/10.1038/s41598-020-67211-2>.
- (193) Buonanno, M.; Ponnaiya, B.; Welch, D.; Stanislauskas, M.; Randers-Pehrson, G.; Smilenov, L.; Lowy, F. D.; Owens, D. M.; Brenner, D. J. Germicidal Efficacy and Mammalian Skin Safety of 222-Nm UV Light. *Radiat. Res.* **2017**, *187* (4), 493–501. <https://doi.org/10.1667/RR0010CC.1>.
- (194) Ultraviolet C light with wavelength of 222 nm inactivates a wide spectrum of microbial pathogens | Elsevier Enhanced Reader <https://reader.elsevier.com/reader/sd/pii/S0195670120301298?token=644276D07778B73B42E5039E549E7E6136592B04E625DBCC5B8A3987CCB56141D8E2030912DEA358935C26F38B7F2571&originRegion=eu-west-1&originCreation=20210410140722> (accessed 2021 -04 -10). <https://doi.org/10.1016/j.jhin.2020.03.030>.
- (195) Report: UV-C LED Market Set to Surge https://www.osa-opn.org/home/industry/2020/october/report_uv-c_led_market_set_to_surge/ (accessed 2021 -04 -09).
- (196) UV LEDs – Market and Technology Trends 2020 <https://www.i-micronews.com/products/uv-leds-market-and-technology-trends-2020/> (accessed 2021 -04 -09).
- (197) COVID-19: Putting UV-C to Work https://www.osa-opn.org/home/newsroom/2020/june/covid-19_putting_uv-c_to_work/ (accessed 2021 -04 -09).
- (198) Buonanno, M.; Randers-Pehrson, G.; Bigelow, A. W.; Trivedi, S.; Lowy, F. D.; Spotnitz, H. M.; Hammer, S. M.; Brenner, D. J. 207-Nm UV Light - A Promising Tool for Safe Low-Cost Reduction of Surgical Site Infections. I: In Vitro Studies. *PLOS ONE* **2013**, *8* (10), e76968. <https://doi.org/10.1371/journal.pone.0076968>.
- (199) Buonanno, M.; Stanislauskas, M.; Ponnaiya, B.; Bigelow, A. W.; Randers-Pehrson, G.; Xu, Y.; Shuryak, I.; Smilenov, L.; Owens, D. M.; Brenner, D. J. 207-Nm UV Light—A Promising Tool for Safe Low-Cost Reduction of Surgical Site Infections. II: In-Vivo Safety Studies. *PLOS ONE* **2016**, *11* (6), e0138418. <https://doi.org/10.1371/journal.pone.0138418>.
- (200) Nagasawa, Y.; Hirano, A. A Review of AlGaN-Based Deep-Ultraviolet Light-Emitting Diodes on Sapphire. *Appl. Sci.* **2018**, *8* (8), 1264. <https://doi.org/10.3390/app8081264>.
- (201) Moustakas, T. D.; Paiella, R. Optoelectronic Device Physics and Technology of Nitride Semiconductors from the UV to the Terahertz. *Rep. Prog. Phys.* **2017**, *80* (10), 106501. <https://doi.org/10.1088/1361-6633/aa7bb2>.
- (202) Amano, H.; Collazo, R.; Santi, C. D.; Einfeldt, S.; Funato, M.; Glaab, J.; Hagedorn, S.; Hirano, A.; Hirayama, H.; Ishii, R.; Kashima, Y.; Kawakami, Y.; Kirste, R.; Kneissl, M.; Martin, R.; Mehnke, F.; Meneghini, M.; Ougazzaden, A.; Parbrook, P. J.; Rajan, S.; Reddy, P.; Römer, F.; Ruschel, J.; Sarkar, B.; Scholz, F.; Schowalter, L. J.; Shields, P.; Sitar, Z.; Sulmoni, L.; Wang, T.; Wernicke, T.; Weyers, M.; Witzigmann, B.; Wu, Y.-R.; Wunderer, T.; Zhang, Y. The 2020 UV Emitter Roadmap. *J. Phys. Appl. Phys.* **2020**, *53* (50), 503001. <https://doi.org/10.1088/1361-6463/aba64c>.
- (203) *III-Nitride Ultraviolet Emitters: Technology and Applications*; Kneissl, M., Rass, J., Eds.; Springer series in materials science; Springer: Cham Heidelberg New York Dordrecht London, 2016.
- (204) Kneissl, M. A Brief Review of III-Nitride UV Emitter Technologies and Their Applications. In *III-Nitride Ultraviolet Emitters*; Kneissl, M., Rass, J., Eds.; Springer International Publishing: Cham,

- 2016; Vol. 227, pp 1–25. https://doi.org/10.1007/978-3-319-24100-5_1.
- (205) Jain, B.; Velpula, R. T.; Patel, M.; Sadaf, S. M.; Nguyen, H. P. T. Improved Performance of Electron Blocking Layer Free AlGaIn Deep Ultraviolet Light-Emitting Diodes Using Graded Staircase Barriers. *Micromachines* **2021**, *12* (3), 334. <https://doi.org/10.3390/mi12030334>.
- (206) Pampili, P.; Parbrook, P. J. Doping of III-Nitride Materials. *Mater. Sci. Semicond. Process.* **2017**, *62*, 180–191. <https://doi.org/10.1016/j.mssp.2016.11.006>.
- (207) Blasco, R.; Ajay, A.; Robin, E.; Bougerol, C.; Lorentz, K.; Alves, L. C.; Mouton, I.; Amichi, L.; Grenier, A.; Monroy, E. Electrical and Optical Properties of Heavily Ge-Doped AlGaIn. *J. Phys. Appl. Phys.* **2019**, *52* (12), 125101. <https://doi.org/10.1088/1361-6463/aafec2>.
- (208) Mori, T.; Nagamatsu, K.; Nonaka, K.; Takeda, K.; Iwaya, M.; Kamiyama, S.; Amano, H.; Akasaki, I. Crystal Growth and P-Type Conductivity Control of AlGaIn for High-Efficiency Nitride-Based UV Emitters. *Phys. Status Solidi C* **2009**, *6* (12), 2621–2625. <https://doi.org/10.1002/pssc.200982547>.
- (209) Northrup, J. E.; Chua, C. L.; Yang, Z.; Wunderer, T.; Kneissl, M.; Johnson, N. M.; Kolbe, T. Effect of Strain and Barrier Composition on the Polarization of Light Emission from AlGaIn/AlN Quantum Wells. *Appl. Phys. Lett.* **2012**, *100* (2), 021101. <https://doi.org/10.1063/1.3675451>.
- (210) Saito, Y.; Hamaguchi, K.; Mizushima, R.; Uemura, S.; Nagasako, T.; Yotani, J.; Shimojo, T. Field Emission from Carbon Nanotubes and Its Application to Cathode Ray Tube Lighting Elements. *Appl. Surf. Sci.* **1999**, *146* (1–4), 305–311. [https://doi.org/10.1016/S0169-4332\(99\)00059-8](https://doi.org/10.1016/S0169-4332(99)00059-8).
- (211) Oto, T.; Banal, R. G.; Kataoka, K.; Funato, M.; Kawakami, Y. 100 MW Deep-Ultraviolet Emission from Aluminium-Nitride-Based Quantum Wells Pumped by an Electron Beam. *Nat. Photonics* **2010**, *4* (11), 767–770. <https://doi.org/10.1038/nphoton.2010.220>.
- (212) Herbert J. Reich. *Principles of Electron Tubes*; Literary Licensing, LLC, 2013.
- (213) Matsumoto, T.; Iwayama, S.; Saito, T.; Kawakami, Y.; Kubo, F.; Amano, H. Handheld Deep Ultraviolet Emission Device Based on Aluminum Nitride Quantum Wells and Graphene Nanoneedle Field Emitters. *Opt. Express* **2012**, *20* (22), 24320. <https://doi.org/10.1364/OE.20.024320>.
- (214) Shimahara, Y.; Miyake, H.; Hiramatsu, K.; Fukuyo, F.; Okada, T.; Takaoka, H.; Yoshida, H. Fabrication of Deep-Ultraviolet-Light-Source Tube Using Si-Doped AlGaIn. *Appl. Phys. Express* **2011**, *4* (4), 042103. <https://doi.org/10.1143/APEX.4.042103>.
- (215) Ivanov, S. V.; Jmerik, V. N.; Nechaev, D. V.; Kozlovsky, V. I.; Tiberi, M. D. E-Beam Pumped Mid-UV Sources Based on MBE-Grown AlGaIn MQW: Mid-UV Sources Based on MBE-Grown AlGaIn MQW. *Phys. Status Solidi A* **2015**, *212* (5), 1011–1016. <https://doi.org/10.1002/pssa.201431756>.
- (216) Tabataba-Vakili, F.; Wunderer, T.; Kneissl, M.; Yang, Z.; Teepe, M.; Batres, M.; Feneberg, M.; Vancil, B.; Johnson, N. M. Dominance of Radiative Recombination from Electron-Beam-Pumped Deep-UV AlGaIn Multi-Quantum-Well Heterostructures. *Appl. Phys. Lett.* **2016**, *109* (18), 181105. <https://doi.org/10.1063/1.4967220>.
- (217) Wang, Y.; Rong, X.; Ivanov, S.; Jmerik, V.; Chen, Z.; Wang, H.; Wang, T.; Wang, P.; Jin, P.; Chen, Y.; Kozlovsky, V.; Sviridov, D.; Zverev, M.; Zhdanova, E.; Gamov, N.; Studenov, V.; Miyake, H.; Li, H.; Guo, S.; Yang, X.; Xu, F.; Yu, T.; Qin, Z.; Ge, W.; Shen, B.; Wang, X. Deep Ultraviolet Light Source from Ultrathin GaN/AlN MQW Structures with Output Power Over 2 Watt. *Adv. Opt. Mater.* **2019**, *7* (10), 1801763. <https://doi.org/10.1002/adom.201801763>.
- (218) Hayashi, T.; Kawase, Y.; Nagata, N.; Senga, T.; Iwayama, S.; Iwaya, M.; Takeuchi, T.; Kamiyama, S.; Akasaki, I.; Matsumoto, T. Demonstration of Electron Beam Laser Excitation in the UV Range Using a GaN/AlGaIn Multiquantum Well Active Layer. *Sci. Rep.* **2017**, *7* (1), 2944. <https://doi.org/10.1038/s41598-017-03151-8>.
- (219) Wunderer, T.; Jeschke, J.; Yang, Z.; Teepe, M.; Batres, M.; Vancil, B.; Johnson, N. Resonator-Length Dependence of Electron-Beam-Pumped UV-A GaN-Based Lasers. *IEEE Photonics Technol. Lett.* **2017**, *29* (16), 1344–1347. <https://doi.org/10.1109/LPT.2017.2722359>.
- (220) Gudiksen, M. S.; Lauhon, L. J.; Wang, J.; Smith, D. C.; Lieber, C. M. Growth of Nanowire Superlattice Structures for Nanoscale Photonics and Electronics. *Nature* **2002**, *415* (6872),

- 617–620. <https://doi.org/10.1038/415617a>.
- (221) Lu, W.; Xie, P.; Lieber, C. M. Nanowire Transistor Performance Limits and Applications. *IEEE Trans. Electron Devices* **2008**, *55* (11), 2859–2876. <https://doi.org/10.1109/TED.2008.2005158>.
- (222) Krogstrup, P.; Jørgensen, H. I.; Heiss, M.; Demichel, O.; Holm, J. V.; Aagesen, M.; Nygard, J.; Fontcuberta i Morral, A. Single-Nanowire Solar Cells beyond the Shockley–Queisser Limit. *Nat. Photonics* **2013**, *7* (4), 306–310. <https://doi.org/10.1038/nphoton.2013.32>.
- (223) Xu, Y.; Gong, T.; Munday, J. N. The Generalized Shockley–Queisser Limit for Nanostructured Solar Cells. *Sci. Rep.* **2015**, *5*, 13536.
- (224) Cui, Y. Nanowire Nanosensors for Highly Sensitive and Selective Detection of Biological and Chemical Species. *Science* **2001**, *293* (5533), 1289–1292. <https://doi.org/10.1126/science.1062711>.
- (225) Barrigón, E.; Heurlin, M.; Bi, Z.; Monemar, B.; Samuelson, L. Synthesis and Applications of III–V Nanowires. *Chem. Rev.* **2019**, *119* (15), 9170–9220. <https://doi.org/10.1021/acs.chemrev.9b00075>.
- (226) Renard, J.; Songmuang, R.; Bougerol, C.; Daudin, B.; Gayral, B. Exciton and Biexciton Luminescence from Single GaN/AlN Quantum Dots in Nanowires. *Nano Lett.* **2008**, *8* (7), 2092–2096. <https://doi.org/10.1021/nl0800873>.
- (227) Nguyen, H. P. T.; Cui, K.; Zhang, S.; Fatholouloumi, S.; Mi, Z. Full-Color InGaN/GaN Dot-in-a-Wire Light Emitting Diodes on Silicon. *Nanotechnology* **2011**, *22* (44), 445202. <https://doi.org/10.1088/0957-4484/22/44/445202>.
- (228) Holmes, M. J.; Choi, K.; Kako, S.; Arita, M.; Arakawa, Y. Room-Temperature Triggered Single Photon Emission from a III-Nitride Site-Controlled Nanowire Quantum Dot. *Nano Lett.* **2014**, *14* (2), 982–986. <https://doi.org/10.1021/nl404400d>.
- (229) Gačević, Ž.; Vukmirović, N.; García-Lepetit, N.; Torres-Pardo, A.; Müller, M.; Metzner, S.; Albert, S.; Bengoechea-Encabo, A.; Bertram, F.; Veit, P.; Christen, J.; González-Calbet, J. M.; Calleja, E. Influence of Composition, Strain, and Electric Field Anisotropy on Different Emission Colors and Recombination Dynamics from InGaN Nanodisks in Pencil-like GaN Nanowires. *Phys. Rev. B* **2016**, *93* (12), 125436. <https://doi.org/10.1103/PhysRevB.93.125436>.
- (230) Jahangir, S.; Mandl, M.; Strassburg, M.; Bhattacharya, P. Molecular Beam Epitaxial Growth and Optical Properties of Red-Emitting ($\lambda = 650$ nm) InGaN/GaN Disks-in-Nanowires on Silicon. *Appl. Phys. Lett.* **2013**, *102* (7), 071101. <https://doi.org/10.1063/1.4793300>.
- (231) Renard, J.; Kandaswamy, P. K.; Monroy, E.; Gayral, B. Suppression of Nonradiative Processes in Long-Lived Polar GaN/AlN Quantum Dots. *Appl. Phys. Lett.* **2009**, *95* (13), 131903. <https://doi.org/10.1063/1.3238311>.
- (232) Beeler, M.; Lim, C. B.; Hille, P.; Bleuse, J.; Schörmann, J.; de la Mata, M.; Arbiol, J.; Eickhoff, M.; Monroy, E. Long-Lived Excitons in GaN/AlN Nanowire Heterostructures. *Phys. Rev. B* **2015**, *91* (20), 205440. <https://doi.org/10.1103/PhysRevB.91.205440>.
- (233) Leamy, H. J. Charge Collection Scanning Electron Microscopy. *J. Appl. Phys.* **1982**, *53* (6), R51–R80. <https://doi.org/10.1063/1.331667>.
- (234) Hovington, P.; Drouin, D.; Gauvin, R. CASINO: A New Monte Carlo Code in C Language for Electron Beam Interaction -Part I: Description of the Program. *Scanning* **2006**, *19* (1), 1–14. <https://doi.org/10.1002/sca.4950190101>.
- (235) Ajay, A.; Lim, C. B.; Browne, D. A.; Polaczynski, J.; Bellet-Amalric, E.; den Hertog, M. I.; Monroy, E. Intersubband Absorption in Si- and Ge-Doped GaN/AlN Heterostructures in Self-Assembled Nanowire and 2D Layers. *Phys. Status Solidi B* **2017**, *254* (8), 1600734. <https://doi.org/10.1002/pssb.201600734>.
- (236) Dimkou, I.; Harikumar, A.; Ajay, A.; Donatini, F.; Bellet-Amalric, E.; Grenier, A.; den Hertog, M. I.; Purcell, S. T.; Monroy, E. Design of AlGaIn/AlN Dot-in-a-wire Heterostructures for Electron-Pumped UV Emitters. *Phys. Status Solidi A* **2019**, pssa.201900714. <https://doi.org/10.1002/pssa.201900714>.
- (237) Sabelfeld, K. K.; Kaganer, V. M.; Limbach, F.; Dogan, P.; Brandt, O.; Geelhaar, L.; Riechert, H.

- Height Self-Equilibration during the Growth of Dense Nanowire Ensembles: Order Emerging from Disorder. *Appl. Phys. Lett.* **2013**, *103* (13), 133105. <https://doi.org/10.1063/1.4822110>.
- (238) Rigutti, L.; Teubert, J.; Jacopin, G.; Fortuna, F.; Tchernycheva, M.; De Luna Bugallo, A.; Julien, F. H.; Furtmayr, F.; Stutzmann, M.; Eickhoff, M. Origin of Energy Dispersion in Al(x)Ga(1-x)N/GaN Nanowire Quantum Disks with Low Al Content. *Phys. Rev. B* **2010**, *82* (23), 235308. <https://doi.org/10.1103/PhysRevB.82.235308>.
- (239) Furtmayr, F.; Teubert, J.; Becker, P.; Conesa-Boj, S.; Morante, J. R.; Chernikov, A.; Schäfer, S.; Chatterjee, S.; Arbiol, J.; Eickhoff, M. Carrier Confinement in GaN/Al_xGa_{1-x}N Nanowire Heterostructures (0 < x ≤ 1). *Phys. Rev. B* **2011**, *84* (20), 205303. <https://doi.org/10.1103/PhysRevB.84.205303>.
- (240) Carnevale, S. D.; Yang, J.; Phillips, P. J.; Mills, M. J.; Myers, R. C. Three-Dimensional GaN/AlN Nanowire Heterostructures by Separating Nucleation and Growth Processes. *Nano Lett.* **2011**, *11* (2), 866–871. <https://doi.org/10.1021/nl104265u>.
- (241) Rivera, C.; Jahn, U.; Flissikowski, T.; Pau, J.; Muñoz, E.; Grahn, H. T. Strain-Confinement Mechanism in Mesoscopic Quantum Disks Based on Piezoelectric Materials. *Phys. Rev. B* **2007**, *75* (4), 045316. <https://doi.org/10.1103/PhysRevB.75.045316>.
- (242) Zagonel, L. F.; Rigutti, L.; Tchernycheva, M.; Jacopin, G.; Songmuang, R.; Kociak, M. Visualizing Highly Localized Luminescence in GaN/AlN Heterostructures in Nanowires. *Nanotechnology* **2012**, *23* (45), 455205. <https://doi.org/10.1088/0957-4484/23/45/455205>.
- (243) Calleja, E.; Ristić, J.; Fernández-Garrido, S.; Cerutti, L.; Sánchez-García, M. A.; Grandal, J.; Trampert, A.; Jahn, U.; Sánchez, G.; Griol, A.; Sánchez, B. Growth, Morphology, and Structural Properties of Group-III-Nitride Nanocolumns and Nanodisks. *Phys. Status Solidi B* **2007**, *244* (8), 2816–2837. <https://doi.org/10.1002/pssb.200675628>.
- (244) Yoshizawa, M.; Kikuchi, A.; Mori, M.; Fujita, N. F. N.; Kishino, K. K. Growth of Self-Organized GaN Nanostructures on Al₂O₃(0001) by RF-Radical Source Molecular Beam Epitaxy. *Jpn. J. Appl. Phys.* **1997**, *36* (4B), L459. <https://doi.org/10.1143/JJAP.36.L459>.
- (245) Sanchez-Garcia, M. A.; Calleja, E.; Monroy, E.; Sanchez, F. J.; Calle, F.; Muñoz, E.; Beresford, R. The Effect of the III/V Ratio and Substrate Temperature on the Morphology and Properties of GaN- and AlN-Layers Grown by Molecular Beam Epitaxy on Si(1 1 1). *J. Cryst. Growth* **1998**, *183* (1–2), 23–30. [https://doi.org/10.1016/S0022-0248\(97\)00386-2](https://doi.org/10.1016/S0022-0248(97)00386-2).
- (246) Calarco, R.; Meijers, R. J.; Debnath, R. K.; Stoica, T.; Sutter, E.; Lüth, Hans. Nucleation and Growth of GaN Nanowires on Si(111) Performed by Molecular Beam Epitaxy. *Nano Lett.* **2007**, *7* (8), 2248–2251. <https://doi.org/10.1021/nl0707398>.
- (247) Fernández-Garrido, S.; Kong, X.; Gotschke, T.; Calarco, R.; Geelhaar, L.; Trampert, A.; Brandt, O. Spontaneous Nucleation and Growth of GaN Nanowires: The Fundamental Role of Crystal Polarity. *Nano Lett.* **2012**, *12* (12), 6119–6125. <https://doi.org/10.1021/nl302664q>.
- (248) Tchernycheva, M.; Nevou, L.; Doyennette, L.; Julien, F. H.; Guillot, F.; Monroy, E.; Remmele, T.; Albrecht, M. Electron Confinement in Strongly Coupled GaN/AlN Quantum Wells. *Appl. Phys. Lett.* **2006**, *88* (15), 153113. <https://doi.org/10.1063/1.2193057>.
- (249) Ban, K.; Yamamoto, J.; Takeda, K.; Ide, K.; Iwaya, M.; Takeuchi, T.; Kamiyama, S.; Akasaki, I.; Amano, H. Internal Quantum Efficiency of Whole-Composition-Range AlGa_N Multi-quantum Wells. *Appl. Phys. Express* **2011**, *4* (5), 052101. <https://doi.org/10.1143/APEX.4.052101>.
- (250) Bryan, Z.; Bryan, I.; Xie, J.; Mita, S.; Sitar, Z.; Collazo, R. High Internal Quantum Efficiency in AlGa_N Multiple Quantum Wells Grown on Bulk AlN Substrates. *Appl. Phys. Lett.* **2015**, *106* (14), 142107. <https://doi.org/10.1063/1.4917540>.
- (251) Murotani, H.; Akase, D.; Anai, K.; Yamada, Y.; Miyake, H.; Hiramatsu, K. Dependence of Internal Quantum Efficiency on Doping Region and Si Concentration in Al-Rich AlGa_N Quantum Wells. *Appl. Phys. Lett.* **2012**, *101* (4), 042110. <https://doi.org/10.1063/1.4739431>.
- (252) Liao, Y.; Thomidis, C.; Kao, C.; Moustakas, T. D. AlGa_N Based Deep Ultraviolet Light Emitting Diodes with High Internal Quantum Efficiency Grown by Molecular Beam Epitaxy. *Appl. Phys. Lett.* **2011**, *98* (8), 081110. <https://doi.org/10.1063/1.3559842>.
- (253) Banal, R. G.; Funato, M.; Kawakami, Y. Extremely High Internal Quantum Efficiencies from

- AlGaN/AlN Quantum Wells Emitting in the Deep Ultraviolet Spectral Region. *Appl. Phys. Lett.* **2011**, *99* (1), 011902. <https://doi.org/10.1063/1.3607306>.
- (254) Mickevičius, J.; Tamulaitis, G.; Shur, M.; Shatalov, M.; Yang, J.; Gaska, R. Internal Quantum Efficiency in AlGaN with Strong Carrier Localization. *Appl. Phys. Lett.* **2012**, *101* (21), 211902. <https://doi.org/10.1063/1.4767657>.
- (255) Bhattacharyya, A.; Moustakas, T. D.; Zhou, L.; Smith, David. J.; Hug, W. Deep Ultraviolet Emitting AlGaN Quantum Wells with High Internal Quantum Efficiency. *Appl. Phys. Lett.* **2009**, *94* (18), 181907. <https://doi.org/10.1063/1.3130755>.
- (256) Hao, G.-D.; Tamari, N.; Obata, T.; Kinoshita, T.; Inoue, S. Electrical Determination of Current Injection and Internal Quantum Efficiencies in AlGaN-Based Deep-Ultraviolet Light-Emitting Diodes. *Opt. Express* **2017**, *25* (16), A639. <https://doi.org/10.1364/OE.25.00A639>.
- (257) Dong, P.; Yan, J.; Zhang, Y.; Wang, J.; Zeng, J.; Geng, C.; Cong, P.; Sun, L.; Wei, T.; Zhao, L.; Yan, Q.; He, C.; Qin, Z.; Li, J. AlGaN-Based Deep Ultraviolet Light-Emitting Diodes Grown on Nano-Patterned Sapphire Substrates with Significant Improvement in Internal Quantum Efficiency. *J. Cryst. Growth* **2014**, *395*, 9–13. <https://doi.org/10.1016/j.jcrysgro.2014.02.039>.
- (258) Frankerl, C.; Hoffmann, M. P.; Nippert, F.; Wang, H.; Brandl, C.; Tillner, N.; Lugauer, H.-J.; Zeisel, R.; Hoffmann, A.; Davies, M. J. Challenges for Reliable Internal Quantum Efficiency Determination in AlGaN-Based Multi-Quantum-Well Structures Posed by Carrier Transport Effects and Morphology Issues. *J. Appl. Phys.* **2019**, *126* (7), 075703. <https://doi.org/10.1063/1.5100498>.
- (259) Kandaswamy, P. K.; Bougerol, C.; Jalabert, D.; Ruterana, P.; Monroy, E. Strain Relaxation in Short-Period Polar GaN/AlN Superlattices. *J. Appl. Phys.* **2009**, *106* (1), 013526. <https://doi.org/10.1063/1.3168431>.
- (260) Calarco, R.; Marso, M.; Richter, T.; Aykanat, A. I.; Meijers, R.; v.d. Hart, A.; Stoica, T.; Lüth, H. Size-Dependent Photoconductivity in MBE-Grown GaN-Nanowires. *Nano Lett.* **2005**, *5* (5), 981–984. <https://doi.org/10.1021/nl0500306>.
- (261) Ajay, A.; Lim, C. B.; Browne, D. A.; Polaczyński, J.; Bellet-Amalric, E.; Bleuse, J.; den Hertog, M. I.; Monroy, E. Effect of Doping on the Intersubband Absorption in Si- and Ge-Doped GaN/AlN Heterostructures. *Nanotechnology* **2017**, *28* (40), 405204. <https://doi.org/10.1088/1361-6528/aa8504>.
- (262) Lähnemann, J.; Flissikowski, T.; Wölz, M.; Geelhaar, L.; Grahn, H. T.; Brandt, O.; Jahn, U. Quenching of the Luminescence Intensity of GaN Nanowires under Electron Beam Exposure: Impact of C Adsorption on the Exciton Lifetime. *Nanotechnology* **2016**, *27* (45), 455706. <https://doi.org/10.1088/0957-4484/27/45/455706>.
- (263) Robins, L. H.; Bertness, K. A.; Barker, J. M.; Sanford, N. A.; Schlager, J. B. Optical and Structural Study of GaN Nanowires Grown by Catalyst-Free Molecular Beam Epitaxy. II. Sub-Band-Gap Luminescence and Electron Irradiation Effects. *J. Appl. Phys.* **2007**, *101* (11), 113506. <https://doi.org/10.1063/1.2736266>.
- (264) Songmuang, R.; Ben, T.; Daudin, B.; González, D.; Monroy, E. Identification of III–N Nanowire Growth Kinetics via a Marker Technique. *Nanotechnology* **2010**, *21* (29), 295605. <https://doi.org/10.1088/0957-4484/21/29/295605>.
- (265) Dimkou, I.; Di Russo, E.; Dalapati, P.; Houard, J.; Rochat, N.; Cooper, D.; Bellet-Amalric, E.; Grenier, A.; Monroy, E.; Rigutti, L. InGaN Quantum Dots Studied by Correlative Microscopy Techniques for Enhanced Light-Emitting Diodes. *ACS Appl. Nano Mater.* **2020**, *3* (10), 10133–10143. <https://doi.org/10.1021/acsanm.0c02106>.
- (266) Nakamura, S.; Pearton, S.; Fasol, G. *The Blue Laser Diode: The Complete Story*; Springer Berlin Heidelberg: Berlin, Heidelberg, 2000.
- (267) Pimpitkar, S.; Speck, J. S.; DenBaars, S. P.; Nakamura, S. Prospects for LED Lighting. *Nat. Photonics* **2009**, *3* (4), 180–182. <https://doi.org/10.1038/nphoton.2009.32>.
- (268) Deshpande, S.; Heo, J.; Das, A.; Bhattacharya, P. Electrically Driven Polarized Single-Photon Emission from an InGaN Quantum Dot in a GaN Nanowire. *Nat. Commun.* **2013**, *4* (1), 1675. <https://doi.org/10.1038/ncomms2691>.

- (269) Cho, J.-H.; Kim, Y. M.; Lim, S.-H.; Yeo, H.-S.; Kim, S.; Gong, S.-H.; Cho, Y.-H. Strongly Coherent Single-Photon Emission from Site-Controlled InGaN Quantum Dots Embedded in GaN Nanopyramids. *ACS Photonics* **2018**, *5* (2), 439–444. <https://doi.org/10.1021/acsp Photonics.7b00922>.
- (270) Chichibu, S.; Azuhata, T.; Sota, T.; Nakamura, S. Spontaneous Emission of Localized Excitons in InGaN Single and Multiquantum Well Structures. *Appl. Phys. Lett.* **1996**, *69* (27), 4188–4190. <https://doi.org/10.1063/1.116981>.
- (271) Chichibu, S. F.; Abare, A. C.; Minsky, M. S.; Keller, S.; Fleischer, S. B.; Bowers, J. E.; Hu, E.; Mishra, U. K.; Coldren, L. A.; DenBaars, S. P.; Sota, T. Effective Band Gap Inhomogeneity and Piezoelectric Field in InGaN/GaN Multiquantum Well Structures. *Appl. Phys. Lett.* **1998**, *73* (14), 2006–2008. <https://doi.org/10.1063/1.122350>.
- (272) Yang, T.-J.; Shivaraman, R.; Speck, J. S.; Wu, Y.-R. The Influence of Random Indium Alloy Fluctuations in Indium Gallium Nitride Quantum Wells on the Device Behavior. *J. Appl. Phys.* **2014**, *116* (11), 113104. <https://doi.org/10.1063/1.4896103>.
- (273) Vaxenburg, R.; Rodina, A.; Lifshitz, E.; Efros, A. L. The Role of Polarization Fields in Auger-Induced Efficiency Droop in Nitride-Based Light-Emitting Diodes. *Appl. Phys. Lett.* **2013**, *103* (22), 221111. <https://doi.org/10.1063/1.4833915>.
- (274) Iveland, J.; Martinelli, L.; Peretti, J.; Speck, J. S.; Weisbuch, C. Direct Measurement of Auger Electrons Emitted from a Semiconductor Light-Emitting Diode under Electrical Injection: Identification of the Dominant Mechanism for Efficiency Droop. *Phys. Rev. Lett.* **2013**, *110* (17), 177406. <https://doi.org/10.1103/PhysRevLett.110.177406>.
- (275) Chamard, V.; Schüllli, T.; Sztucki, M.; Metzger, T.; Sarigiannidou, E.; Rouvière, J.-L.; Tolan, M.; Adelman, C. Strain Distribution in Nitride Quantum Dot Multilayers. *Phys. Rev. B* **2004**, *69* (12), 125327. <https://doi.org/10.1103/PhysRevB.69.125327>.
- (276) Damilano, B.; Grandjean, N.; Dalmaso, S.; Massies, J. Room-Temperature Blue-Green Emission from InGaN/GaN Quantum Dots Made by Strain-Induced Islanding Growth. *Appl. Phys. Lett.* **1999**, *75* (24), 3751–3753. <https://doi.org/10.1063/1.125444>.
- (277) Bartel, T.; Dworzak, M.; Strassburg, M.; Hoffmann, A.; Strittmatter, A.; Bimberg, D. Recombination Dynamics of Localized Excitons in InGaN Quantum Dots. *Appl. Phys. Lett.* **2004**, *85* (11), 1946–1948. <https://doi.org/10.1063/1.1790599>.
- (278) Park, I.-K.; Kwon, M.-K.; Seo, S.-B.; Kim, J.-Y.; Lim, J.-H.; Park, S.-J. Ultraviolet Light-Emitting Diodes with Self-Assembled InGaN Quantum Dots. *Appl. Phys. Lett.* **2007**, *90* (11), 111116. <https://doi.org/10.1063/1.2712804>.
- (279) Smeeton, T. M.; Kappers, M. J.; Barnard, J. S.; Vickers, M. E.; Humphreys, C. J. Electron-Beam-Induced Strain within InGaN Quantum Wells: False Indium “Cluster” Detection in the Transmission Electron Microscope. *Appl. Phys. Lett.* **2003**, *83* (26), 5419–5421. <https://doi.org/10.1063/1.1636534>.
- (280) Coraux, J.; Favre-Nicolin, V.; Renevier, H.; Proietti, M. G.; Amstatt, B.; Bellet-Amalric, E.; Daudin, B. Quantitative Structural Characterization of GaN Quantum Dot Ripening Using Reflection High-Energy Electron Diffraction. *J. Appl. Phys.* **2007**, *101* (5), 056106. <https://doi.org/10.1063/1.2422902>.
- (281) Das, A.; Dimitrakopoulos, G. P.; Kotsar, Y.; Lotsari, A.; Kehagias, Th.; Komninou, Ph.; Monroy, E. Improved Luminescence and Thermal Stability of Semipolar (11-22) InGaN Quantum Dots. *Appl. Phys. Lett.* **2011**, *98* (20), 201911. <https://doi.org/10.1063/1.3588335>.
- (282) Gogneau, N.; Jalabert, D.; Monroy, E.; Sarigiannidou, E.; Rouvière, J. L.; Shibata, T.; Tanaka, M.; Gerard, J. M.; Daudin, B. Influence of AlN Overgrowth on Structural Properties of GaN Quantum Wells and Quantum Dots Grown by Plasma-Assisted Molecular Beam Epitaxy. *J. Appl. Phys.* **2004**, *96* (2), 1104–1110. <https://doi.org/10.1063/1.1759785>.
- (283) Figge, S.; Tessarek, C.; Aschenbrenner, T.; Hommel, D. InGaN Quantum Dot Growth in the Limits of Stranski-Krastanov and Spinodal Decomposition: InGaN Quantum Dots. *Phys. Status Solidi B* **2011**, *248* (8), 1765–1776. <https://doi.org/10.1002/pssb.201147165>.
- (284) Lefebvre, P.; Taliércio, T.; Morel, A.; Allègre, J.; Gallart, M.; Gil, B.; Mathieu, H.; Damilano, B.;

- Grandjean, N.; Massies, J. Effects of GaAlN Barriers and of Dimensionality on Optical Recombination Processes in InGaN Quantum Wells and Quantum Boxes. *Appl. Phys. Lett.* **2001**, *78* (11), 1538–1540. <https://doi.org/10.1063/1.1352664>.
- (285) Adelman, C.; Simon, J.; Feuillet, G.; Pelekanos, N. T.; Daudin, B.; Fishman, G. Self-Assembled InGaN Quantum Dots Grown by Molecular-Beam Epitaxy. *Appl. Phys. Lett.* **2000**, *76* (12), 1570–1572. <https://doi.org/10.1063/1.126098>.
- (286) Zhu, T.; El-Ella, H. A. R.; Reid, B.; Holmes, M. J.; Taylor, R. A.; Kappers, M. J.; Oliver, R. A. Growth and Optical Characterisation of Multilayers of InGaN Quantum Dots. *J. Cryst. Growth* **2012**, *338* (1), 262–266. <https://doi.org/10.1016/j.jcrysgr.2011.11.001>.
- (287) Andreev, A.; O'Reilly, E. Theory of the Electronic Structure of GaN/AlN Hexagonal Quantum Dots. *Phys. Rev. B* **2000**, *62* (23), 15851–15870. <https://doi.org/10.1103/PhysRevB.62.15851>.
- (288) Sarigiannidou, E.; Monroy, E.; Daudin, B.; Rouvière, J. L.; Andreev, A. D. Strain Distribution in GaN/AlN Quantum-Dot Superlattices. *Appl. Phys. Lett.* **2005**, *87* (20), 203112. <https://doi.org/10.1063/1.2123394>.
- (289) Himwas, C.; den Hertog, M.; Bellet-Amalric, E.; Songmuang, R.; Donatini, F.; Si Dang, L.; Monroy, E. Enhanced Room-Temperature Mid-Ultraviolet Emission from AlGaIn/AlN Stranski-Krastanov Quantum Dots. *J. Appl. Phys.* **2014**, *116* (2), 023502. <https://doi.org/10.1063/1.4887140>.
- (290) Leroux, M.; Grandjean, N.; Beaumont, B.; Nataf, G.; Semond, F.; Massies, J.; Gibart, P. Temperature Quenching of Photoluminescence Intensities in Undoped and Doped GaN. *J. Appl. Phys.* **1999**, *86* (7), 3721–3728. <https://doi.org/10.1063/1.371242>.
- (291) Rubanov, S.; Munroe, P. R. FIB-Induced Damage in Silicon. *J. Microsc.* **2004**, *214* (3), 213–221. <https://doi.org/10.1111/j.0022-2720.2004.01327.x>.
- (292) Dhara, S.; Datta, A.; Wu, C. T.; Chen, K. H.; Wang, Y. L.; Muto, S.; Tanabe, T.; Shen, C. H.; Hsu, C. W.; Chen, L. C.; Maruyama, T. Mechanism of Nanoblisters Formation in Ga⁺ Self-Ion Implanted GaN Nanowires. *Appl. Phys. Lett.* **2005**, *86* (20), 203119. <https://doi.org/10.1063/1.1931819>.
- (293) Wu, S.-E.; Hsueh, T.-H.; Liu, C.-P.; Sheu, J.-K.; Lai, W.-C.; Chang, S.-J. Focused Ion Beam Milled InGaN/GaN Multiple Quantum Well Nanopillars. *Jpn. J. Appl. Phys.* **2008**, *47* (4), 3130–3133. <https://doi.org/10.1143/JJAP.47.3130>.
- (294) Kandaswamy, P. K. *Al(Ga)N/GaN Nanostructures for Intersubband Optoelectronics in the near- and Mid-Infrared*; PhD thesis, 2010.
- (295) Rigutti, L. Laser-Assisted Atom Probe Tomography. In *Advances in Imaging and Electron Physics*; Elsevier, 2020; Vol. 213, pp 29–53. <https://doi.org/10.1016/bs.aiep.2019.11.003>.
- (296) Rigutti, L.; Venturi, L.; Houard, J.; Normand, A.; Silaeva, E. P.; Borz, M.; Malykhin, S. A.; Obraztsov, A. N.; Vella, A. Optical Contactless Measurement of Electric Field-Induced Tensile Stress in Diamond Nanoscale Needles. *Nano Lett.* **2017**, *17* (12), 7401–7409. <https://doi.org/10.1021/acs.nanolett.7b03222>.
- (297) Wei, W.; Jiang, K.; Wei, Y.; Liu, M.; Yang, H.; Zhang, L.; Li, Q.; Liu, L.; Fan, S. Measuring the Stress in Field-Emitting Carbon Nanotubes. *Nanotechnology* **2006**, *17* (8), 1994–1998. <https://doi.org/10.1088/0957-4484/17/8/033>.
- (298) Rigutti, L.; Vella, A.; Vurpillot, F.; Gaillard, A.; Sevelin-Radiguet, N.; Houard, J.; Hideur, A.; Martel, G.; Jacopin, G.; Luna Bugallo, A. D.; Deconihout, B. Coupling Atom Probe Tomography and Photoluminescence Spectroscopy: Exploratory Results and Perspectives. *Ultramicroscopy* **2013**, *132*, 75–80. <https://doi.org/10.1016/j.ultramic.2013.02.002>.
- (299) Chen, H.; Feenstra, R. M.; Northrup, J. E.; Zywiets, T.; Neugebauer, J.; Greve, D. W. Surface Structures and Growth Kinetics of InGaN(0001) Grown by Molecular Beam Epitaxy. *J. Vac. Sci. Technol. B Microelectron. Nanometer Struct.* **2000**, *18* (4), 2284. <https://doi.org/10.1116/1.1306296>.
- (300) Dimkou, I.; Houard, J.; Rochat, N.; Dalapati, P.; Di Russo, E.; Cooper, D.; Grenier, A.; Monroy, E.; Rigutti, L. A Photonic Atom Probe Analysis of the Effect of Extended and Point Defects on the Luminescence of InGaN/GaN Quantum Dots. *ArXiv210603649 Cond-Mat Physicsphysics*

2021.

- (301) Iveland, J.; Speck, J. S.; Martinelli, L.; Peretti, J.; Weisbuch, C. Auger Effect Identified as Main Cause of Efficiency Droop in LEDs. *SPIE Newsroom* **2014**. <https://doi.org/10.1117/2.1201406.005109>.
- (302) Wang, L.; Jin, J.; Mi, C.; Hao, Z.; Luo, Y.; Sun, C.; Han, Y.; Xiong, B.; Wang, J.; Li, H. A Review on Experimental Measurements for Understanding Efficiency Droop in InGaN-Based Light-Emitting Diodes. *Materials* **2017**, *10* (11), 1233. <https://doi.org/10.3390/ma10111233>.
- (303) Zhang, M.; Bhattacharya, P.; Guo, W. InGaN/GaN Self-Organized Quantum Dot Green Light Emitting Diodes with Reduced Efficiency Droop. *Appl. Phys. Lett.* **2010**, *97* (1), 011103. <https://doi.org/10.1063/1.3460921>.
- (304) Zhao, C.; Tang, C. W.; Lai, B.; Cheng, G.; Wang, J.; Lau, K. M. Low-Efficiency-Droop InGaN Quantum Dot Light-Emitting Diodes Operating in the “Green Gap.” *Photonics Res.* **2020**, *8* (5), 750. <https://doi.org/10.1364/PRJ.380158>.
- (305) Dussaigne, A.; Barbier, F.; Damilano, B.; Chenot, S.; Grenier, A.; Papon, A. M.; Samuel, B.; Ben Bakir, B.; Vaufrey, D.; Pillet, J. C.; Gasse, A.; Ledoux, O.; Rozhavskaia, M.; Sotta, D. Full InGaN Red Light Emitting Diodes. *J. Appl. Phys.* **2020**, *128* (13), 135704. <https://doi.org/10.1063/5.0016217>.
- (306) Bennett, S. E.; Saxey, D. W.; Kappers, M. J.; Barnard, J. S.; Humphreys, C. J.; Smith, G. D.; Oliver, R. A. Atom Probe Tomography Assessment of the Impact of Electron Beam Exposure on In_xGa_{1-x}N/GaN Quantum Wells. *Appl. Phys. Lett.* **2011**, *99* (2), 021906. <https://doi.org/10.1063/1.3610468>.
- (307) Riley, J. R.; Padalkar, S.; Li, Q.; Lu, P.; Koleske, D. D.; Wierer, J. J.; Wang, G. T.; Lauhon, L. J. Three-Dimensional Mapping of Quantum Wells in a GaN/InGaN Core–Shell Nanowire Light-Emitting Diode Array. *Nano Lett.* **2013**, *13* (9), 4317–4325. <https://doi.org/10.1021/nl4021045>.
- (308) Sánchez, A. M.; Gass, M.; Papworth, A. J.; Goodhew, P. J.; Singh, P.; Ruterana, P.; Cho, H. K.; Choi, R. J.; Lee, H. J. V-Defects and Dislocations in InGaN/GaN Heterostructures. *Thin Solid Films* **2005**, *479* (1), 316–320. <https://doi.org/10.1016/j.tsf.2004.11.207>.
- (309) Zhang, Y.; Zhou, X.; Xu, S.; Wang, Z.; Chen, Z.; Zhang, J.; Zhang, J.; Hao, Y. Effects of Growth Temperature on the Properties of InGaN Channel Heterostructures Grown by Pulsed Metal Organic Chemical Vapor Deposition. *AIP Adv.* **2015**, *5* (12), 127102. <https://doi.org/10.1063/1.4937127>.
- (310) Crawford, M. H. LEDs for Solid-State Lighting: Performance Challenges and Recent Advances. *IEEE J. Sel. Top. Quantum Electron.* **2009**, *15* (4), 1028–1040. <https://doi.org/10.1109/JSTQE.2009.2013476>.
- (311) Auf der Maur, M.; Pecchia, A.; Penazzi, G.; Rodrigues, W.; Di Carlo, A. Efficiency Drop in Green InGaN / GaN Light Emitting Diodes: The Role of Random Alloy Fluctuations. *Phys. Rev. Lett.* **2016**, *116* (2), 027401. <https://doi.org/10.1103/PhysRevLett.116.027401>.
- (312) Ivanov, S. V.; Shubina, T. V.; Komissarova, T. A.; Jmerik, V. N. Metastable Nature of InN and In-Rich InGaN Alloys. *J. Cryst. Growth* **2014**, *403*, 83–89. <https://doi.org/10.1016/j.jcrysgro.2014.06.019>.
- (313) Procion Analysis.
- (314) Hsu, C.-W.; Lundskog, A.; Karlsson, K. F.; Forsberg, U.; Janzén, E.; Holtz, P. O. Single Excitons in InGaN Quantum Dots on GaN Pyramid Arrays. *Nano Lett.* **2011**, *11* (6), 2415–2418. <https://doi.org/10.1021/nl200810v>.
- (315) Seguin, R.; Rodt, S.; Strittmatter, A.; Reißmann, L.; Bartel, T.; Hoffmann, A.; Bimberg, D.; Hahn, E.; Gerthsen, D. Multi-Excitonic Complexes in Single InGaN Quantum Dots. *Appl. Phys. Lett.* **2004**, *84* (20), 4023–4025. <https://doi.org/10.1063/1.1751214>.
- (316) Kremling, S.; Tessarek, C.; Dartsch, H.; Figge, S.; Höfling, S.; Worschech, L.; Kruse, C.; Hommel, D.; Forchel, A. Single Photon Emission from InGaN/GaN Quantum Dots up to 50 K. *Appl. Phys. Lett.* **2012**, *100* (6), 061115. <https://doi.org/10.1063/1.3683521>.
- (317) Dalapati, P.; Beainy, G.; Di Russo, E.; Blum, I.; Houard, J.; Moldovan, S.; Vella, A.; Vurpillot, F.;

- Le Biavan, N.; Hugues, M.; Chauveau, J. M.; Rigutti, L. In Situ Spectroscopic Study of the Optomechanical Properties of Evaporating Field Ion Emitters. *Phys. Rev. Appl.* **2021**, *15* (2), 024014. <https://doi.org/10.1103/PhysRevApplied.15.024014>.
- (318) Kingham, D. R. The Post-Ionization of Field Evaporated Ions: A Theoretical Explanation of Multiple Charge States. *Surf. Sci.* **1982**, *116* (2), 273–301. [https://doi.org/10.1016/0039-6028\(82\)90434-4](https://doi.org/10.1016/0039-6028(82)90434-4).
- (319) Zhao, X.; Alcalá, D. A.; McLain, M. A.; Maeda, K.; Potnis, S.; Ramos, R.; Steinberg, A. M.; Carr, L. D. Macroscopic Quantum Tunneling Escape of Bose-Einstein Condensates. *Phys. Rev. A* **2017**, *96* (6), 063601. <https://doi.org/10.1103/PhysRevA.96.063601>.
- (320) Di Russo, E.; Moyon, F.; Gogneau, N.; Largeau, L.; Giraud, E.; Carlin, J.-F.; Grandjean, N.; Chauveau, J. M.; Hugues, M.; Blum, I.; Lefebvre, W.; Vurpillot, F.; Blavette, D.; Rigutti, L. Composition Metrology of Ternary Semiconductor Alloys Analyzed by Atom Probe Tomography. *J. Phys. Chem. C* **2018**, *122* (29), 16704–16714. <https://doi.org/10.1021/acs.jpcc.8b03223>.
- (321) Russo, E. D.; Blum, I.; Houard, J.; Gilbert, M.; Da Costa, G.; Blavette, D.; Rigutti, L. Compositional Accuracy of Atom Probe Tomography Measurements in GaN: Impact of Experimental Parameters and Multiple Evaporation Events. *Ultramicroscopy* **2018**, *187*, 126–134. <https://doi.org/10.1016/j.ultramic.2018.02.001>.
- (322) Bonaf, B.; Cramer, R.; Speck, J. S. Nanometer Scale Composition Study of MBE Grown BGaN Performed by Atom Probe Tomography. *J. Appl. Phys.* **2017**, *121* (22), 225701. <https://doi.org/10.1063/1.4984087>.
- (323) Narukawa, Y.; Kawakami, Y.; Funato, M.; Fujita, S.; Fujita, S.; Nakamura, S. Role of Self-Formed InGaN Quantum Dots for Exciton Localization in the Purple Laser Diode Emitting at 420 Nm. *Appl. Phys. Lett.* **1997**, *70* (8), 981–983. <https://doi.org/10.1063/1.118455>.
- (324) Hangleiter, A.; Hitzel, F.; Netzel, C.; Fuhrmann, D.; Rossow, U.; Ade, G.; Hinze, P. Suppression of Nonradiative Recombination by V-Shaped Pits in GaInN / GaN Quantum Wells Produces a Large Increase in the Light Emission Efficiency. *Phys. Rev. Lett.* **2005**, *95* (12), 127402. <https://doi.org/10.1103/PhysRevLett.95.127402>.
- (325) Armstrong, A. M.; Bryant, B. N.; Crawford, M. H.; Koleske, D. D.; Lee, S. R.; Wierer, J. J. Defect-Reduction Mechanism for Improving Radiative Efficiency in InGaN/GaN Light-Emitting Diodes Using InGaN Underlayers. *J. Appl. Phys.* **2015**, *117* (13), 134501. <https://doi.org/10.1063/1.4916727>.
- (326) Haller, C.; Carlin, J.-F.; Jacopin, G.; Martin, D.; Butté, R.; Grandjean, N. Burying Non-Radiative Defects in InGaN Underlayer to Increase InGaN/GaN Quantum Well Efficiency. *Appl. Phys. Lett.* **2017**, *111* (26), 262101. <https://doi.org/10.1063/1.5007616>.
- (327) Weatherley, T.; Liu, W.; Osokin, V.; Alexander, D.; Taylor, R.; Carlin, J.-F.; Butté, R.; Grandjean, N. Imaging Non-Radiative Point Defects Buried in Quantum Wells Using Cathodoluminescence. *ArXiv210309702 Cond-Mat* **2021**.
- (328) Akasaka, T.; Gotoh, H.; Saito, T.; Makimoto, T. High Luminescent Efficiency of InGaN Multiple Quantum Wells Grown on InGaN Underlying Layers. *Appl. Phys. Lett.* **2004**, *85* (15), 3089–3091. <https://doi.org/10.1063/1.1804607>.

Scientific contributions

Journal Articles

- [1] (Submitted review) **A Photonic Atom Probe analysis of the effect of structural and point defects on the luminescence of InGaN/GaN QDs**
I. Dimkou, J. Houard, N. Rochat, P. Dalapati, E. Di Russo, D. Cooper, A. Grenier, E. Monroy, and L. Rigutti
- [2] **InGaN Quantum Dots Studied by Correlative Microscopy Techniques for Enhanced Light-Emitting Diodes**
Ioanna Dimkou, Enrico Di Russo, Pradip Dalapati, Jonathan Houard, Nevine Rochat, David Cooper, Edith Bellet-Amarlic, Adeline Grenier, Eva Monroy, and Lorenzo Rigutti
ACS Applied Nano Materials 3 (10), 10133-10143 (2020)
- [3] **Assessment of AlGaN/AlN superlattices on GaN nanowires as active region of electron-pumped ultraviolet sources**
I. Dimkou, A. Harikumar, F. Donatini, J. Lähnemann, M. I. den Hertog, C. Bougerol, E. Bellet-Amarlic, N. Mollard, A. Ajay, G. Ledoux, S. T. Purcell, and E. Monroy
Nanotechnology 31, 204001 (2020)
- [4] **Design of AlGaN/AlN Dot-in-a-wire Heterostructures for Electron-Pumped UV Emitters**
I. Dimkou, A. Harikumar, A. Ajay, F. Donatini, E. Bellet-Amarlic, A. Grenier, M. I. den Hertog, S. T. Purcell, and E. Monroy
physica status solidi (a) 217, 1900714 (2020)
- [5] **Internal quantum efficiency of AlGaN/AlN quantum dot superlattices for electron-pumped ultraviolet sources**
A. Harikumar, F. Donatini, C. Bougerol, E. Bellet-Amarlic, Q.-M. Thai, C. Dujardin, I. Dimkou, S. T. Purcell, and E. Monroy
Nanotechnology 31, (50), 505205 (2020)
- [6] **Multi-microscopy nanoscale characterization of the doping profile in a hybrid Mg/Ge-doped tunnel junction**
E. Di Russo, A. Mavel, V. Fan Arcara, B. Damilano, I. Dimkou, S. Vézian, A. Grenier, M. Veillerot, N. Rochat, G. Feuillet, B. Bonef, L. Rigutti, J.-Y. Duboz, E. Monroy, and D. Cooper
Nanotechnology 31, 465706 (2020)

Conferences

Personally presented in **bold**

- [1] **(Oral) High-resolution correlative techniques in the study of InGaN quantum dots by atom probe tomography combined with in-situ μ -PL**
Ioanna Dimkou, Enrico Di Russo, Pradip Dalapati, Jonathan Houard, Nevine Rochat, David Cooper, Edith Bellet-Amarlic, Adeline Grenier, Eva Monroy, and Lorenzo Rigutti
E-MRS Spring Meeting, Virtual Conference. 31st May- 3rd June 2021
- [2] **(Poster) Correlative microscopy of InGaN/GaN based UV LEDs: status and perspectives for the study of optically-active atom probe field emitters**
I. Dimkou, E. Di Russo, N. Rochat, D. Cooper, E. Bellet-Amarlic, L. Rigutti, E. Monroy, and A. Grenier
European APT workshop, Rouen, France. 12th-14th November 2019
- [3] **(Oral) AlGaN/AlN nanowires for electron-pumped UV emitters**
I. Dimkou, A. Ajay, E. Bellet-Amarlic, M. I. Den Hertog, F. Donatini, A. Grenier, S. T. Purcell, and E. Monroy
E-MRS Spring Meeting, Nice, France. 27th-31st May 2019

- [4] (Invited) III-nitride based nanowire photodetectors
M. Spies, I. Dimkou, S. Cuesta, A. Ajay, J. Lähnemann, E. Bellet-Almaric, M. I. den Hertog, and E. Monroy
PDI topical workshop on III-N nanowires, Berlin, Germany. 6th-7th June 2019
- [5] (Oral) Design of AlGa_N/AlN dot-in-a-wire heterostructures UV emitters
I. Dimkou, A. Ajay, E. Bellet-Almaric, M. I. Den Hertog, F. Donatini, N. Mollard, C. Bougerol, S. T. Purcell, and E. Monroy
13th International Conference on Nitride Semiconductors 2019 (ICNS-13), Bellevue, Washington, US. 7th-12st July 2019
- [6] (Oral) Design of AlGa_N/AlN dot-in-a-wire heterostructures UV emitters
I. Dimkou, A. Ajay, E. Bellet-Almaric, M. I. Den Hertog, F. Donatini, N. Mollard, C. Bougerol, S. T. Purcell, and E. Monroy
13th International Conference on Nitride Semiconductors 2019 (ICNS-13), Bellevue, Washington, US. 7th-12st July 2019
- [7] (Oral) AlGa_N/AlN dot-in-a-wire heterostructures for electron-pumped UV sources
I. Dimkou, A. Ajay, E. Bellet-Almaric, M. I. Den Hertog, F. Donatini, A. Grenier, S. T. Purcell, and E. Monroy
SPIE Optics+Photonics, San Diego, US. 11th-15st Aug. 2019
- [8] (Poster) Study of Al_xGa_{1-x}N/AlN ($0 \leq x \leq 0.1$) Quantum Dot Superlattices as the Active Region for Electron-Pumped Ultraviolet Sources
A. Harikumar, C. Bougerol, F. Donatini, E. Bellet-Almaric, I. Dimkou, G. Ledoux, S. T. Purcell, and E. Monroy
11th International Conference on Quantum Dots, Munich, Germany. (online) Dec. 7th-11th 2020
- [9] (Poster) Behavior of AlGa_N/AlN Qdots-in-wires under electron pumping for the implementation of efficient UV sources
A. Harikumar, I. Dimkou, F. Donatini, M. den Hertog, E. Bellet-Almaric, G. Ledoux, S. T. Purcell, and E. Monroy
11th International Conference on Quantum Dots, Munich, Germany. (online) Dec. 7th-11th 2020
- [10] (Invited) AlGa_N Nanostructures for Electron Beam Pumped UV Emitters
A. Harikumar, S. Cuesta, I. Dimkou, Q.-M. Thai, F. Donantini, Y. Curé, S. T. Purcell, Le Si Dang, and Eva Monroy
UK Nitrides Consortium (UKNC) Winter Meeting, UK. (online). 7th-8th Jan. 2021
- [11] (Poster) Study of Al_xGa_{1-x}N/AlN ($0 \leq x \leq 0.1$) Quantum Dot Superlattices as Active Region for Electron-Pumped UV Sources
A. Harikumar, F. Donatini, C. Bougerol, E. Bellet-Almaric, I. Dimkou, F. Rol, Q.-M. Thai, C. Dujardin, S. T. Purcell, and E. Monroy
SPIE Photonics West, US. (online) March 6th-11th 2021

Glossary

<u>Abbreviation</u>	<u>Definition</u>
a	lattice constant, deformation potential (2.3)
a_c1, a_c2	Conduction band deformation potentials
A	oscillation amplitude
A_i	Luttinger parameters
ARPES	angle-resolved photoemission spectroscopy
Å	Ångström
aDLD	advanced Delay Line Detector
a_i	base vectors
AFM	atom force microscopy
AlN	aluminium nitride
APT	atom probe tomography
a_s	lattice parameter of the substrate
B	detection bandwidth
C	carbon
c	lattice constant
c_0	lattice constant with zero strain
c_ij	elastic constants
C_(i,j,k,l)	stiffness constants
CB	conduction band
CBM	conduction-band maximum
CCD	charge coupled device
CH	crystal-field split-off valence subband
CL	cathodoluminescence
cps	counts per second
c_s	lattice parameter of the substrate
cw	continuous wavelength
C_9H_17Pt	(methylcyclopentadienyl)trimethyl platinum
D_1, D_2	conduction band deformation potentials
D_3, D_4, D_5	uniaxial valence band deformation potentials
DLD	delay line detector
d_z	thickness of the well
E	electric field
E_a	acceptor band
E_d	donor band
E_G	band gap energy
E_t	non-radiative recombination to mid-gap levels
e_ij	piezoelectric constants
EPUV	electron-pumped ultraviolet
EQE	external quantum efficiency

f	frequency
F	electrostatic force
FEG	field emission electron gun
FIB	focused ion beam
FlexTAP	flexible tomographic atom probe
FWHM	full width at half maximum
G	magnification
g(E)	density of states
GaAs	gallium arsenide
GaN	gallium nitride
GIS	gas injection system
HAADF	high-angle annular dark-field
HCP	hexagonal closed-packed
HH	heavy hole
h,k,l	Miller-Bravais
HR-XRD	high resolution x-ray diffraction
HVPE	hydride vapour phase epitaxy
I ₁	energy of the first ionization
InN	indium nitride
InP	indium phosphide
IQE	internal quantum efficiency
IR	infrared
ISB	intersubband
k _{α1}	x-ray emission line
k _B	Boltzmann constant
k _i	Ewald sphere radius
k _{x,y,z}	wavevector
L ₀	flight path of the ions
La-APT	laser-assisted atom probe tomography
LaWaTAP	laser-assisted wide-angle tomographic atom probe
LED	light emitting diodes
LH	light hole
LO	longitudinal optical
Lx, Ly, Lz	dimensions along x, y and z
m	mass
m+1	compression factor
m/n	mass over charge
m _{e0} , m _{h0}	free electron and hole mass
m*, m* _e , m* _h	effective mass, effective mass of electron and hole
MBE	molecular-beam epitaxy
MCP	microchannel plates
ML	monolayer
MOCVD	metalorganic chemical vapour deposition
MOVPE	metalorganic vapour-phase epitaxy
MQW	multi-quantum well
n _{x,y,z}	integer quantum number of each energy state

NW	nanowire
PAMBE	plasma-assisted molecular-beam epitaxy
PAP	photonic atom probe
PECS	precision etching and coating system
PFNC	nanocharacterisation platform
PL	photoluminescence
P_MQW	multi-quantum well period
P_PE	piezoelectric polarization
PSD	position sensitive detector
P_SP	spontaneous polarization
Pt	platinum
p _{x,y,z}	atomic orbital along x, y, z -axis
Q	detection efficiency (3.7), quality factor of resonance (3.5)
Q _a	activation energy
QCSE	quantum confined Stark effect
QD	quantum dot
QW	quantum well
R	curvature radius
RHEED	reflection high-energy electron diffraction
ROI	region of interest
S, s	detector and analysis surface
SAG	selective area growth
Sb	antimony
SEM	scanning electron microscopy
SF	stacking fault
Si	silicon
SiC	silicon carbide
SIMS	secondary ion mass spectroscopy
S-K	Stranski-Krastanov
SL	superlattice
STEM	scanning transmission electron microscopy
T	absolute temperature
T _{base}	base temperature
T _{crit}	critical temperature
TE	transverse-electric
TEM	transmission electron microscopy
THz	terahertz
TM	transverse-magnetic
TOF	time of flight
u	lattice parameter equals to b/c, where b is the bond-length in the c-direction
U _a , U _i	potential energy of a neutral and an ion
UHV	ultra-high vacuum
UV	ultraviolet
v	evaporation rate (Chapter 3)
V, V ₀	volume at atmospheric pressure (Chapter 2)
v ₀	vibration frequency (Chapter 3)

V_{at}	atomic volume of the charges
VB	valence band
VBM	valence-band maximum
V_{DC}	electric voltage
v_G	growth rate
$V(x,y,z)$	potential
W	tungsten or wolfram
$W(CO)_6$	tungsten hexacarbonyl
WL	wetting layer
WPE	wall-plug efficiency
wz	wurtzite
x	mole fraction
X,Y and x,y	impact on the detector and initial position on the tip of ions
XRD	x-ray diffraction
z	height along the z-axis
α, β	Varshni parameter
β	factor depending on the shape of the tip
Δ	width of the activation energy (Chapter 3)
ΔE	variation of the bandgap (2.3)
ΔE_{CB}	conduction-band offset
Δh	QD height
Δz	depth
$\epsilon_{(k,l)}$	strain
ϵ_{ij}	deformation tensor
η	strain of nanoscale field ion emitters

The aim of this thesis was to develop a methodology for the characterization of III-nitride nanostructures by correlative microscopy, correlating their structural and chemical features with their optical performance. As a first experiment, we describe the growth by plasma-assisted molecular beam epitaxy of AlGaIn/AlN quantum dot (QD) superlattices inserted in self-assembled GaN nanowires (NWs) for application in electron-pumped ultraviolet sources. The optical performance of superlattices on NWs is compared with the emission of multi-quantum wells. The NW ensembles attain internal quantum efficiency (IQE) in excess of 60% at room temperature. The IQE remains stable for high excitation power densities, up to 50 kW/cm². We demonstrate that the NW superlattice is long enough to collect the electron-hole pairs generated by an electron beam with an acceleration voltage $V_A = 5$ kV. These results are interesting for the application of such nanostructures to fabricate ultraviolet lamps. However, in view of difficulties associated to the sample preparation, we have decided to focus our correlative microscopy efforts on InGaIn/GaN Stransky-Krastanov QDs. In this case, microscopy specimens can be prepared by focused ion beam, and they present higher emission efficiency than AlGaIn/AlN NWs when optically pumped *in situ* in an atom probe tomography (APT) system.

Our correlative microscopy study of QDs combined high-resolution chemical and optical characterization by APT, *in-situ* microphotoluminescence, and *ex-situ* cathodoluminescence. We demonstrate that the information extracted by these techniques allows the precise modelling of the nanostructures, obtaining excellent agreement with the optical measurements. During the APT experiment, it was possible to resolve single-QD emission lines, which display a spectral shift assigned to the relaxation of elastic strain due to material evaporation. We have also studied the effect of extended and point defects on the luminescence of such QD structures. We observed that emission intensity is higher in the upper QD layers (closer to the surface) and it is not correlated with the dislocation density. This result highlights the relevance of inserting InGaIn underlayers to bury non-radiative point defects.

Keywords: GaN, AlN, nanowire, ultraviolet, InGaIn, quantum dots, correlative microscopy, luminescence, atom probe tomography, cathodoluminescence and photoluminescence.

L'objectif de cette thèse était de développer une méthodologie pour l'étude des nanostructures de semi-conducteurs nitrures par microscopie corrélative, en corrélant leurs caractéristiques structurales et chimiques avec leurs performances optiques. Comme première expérience, nous décrivons la croissance par épitaxie par faisceau moléculaire assistée par plasma de super-réseaux de boîtes quantiques (QD) AlGaIn/AlN insérés dans des nanofils (NW) de GaN auto-assemblés pour une application dans des sources ultraviolettes pompées par électrons. Les performances optiques des super-réseaux sur les NW sont comparées à l'émission de puits multi-quantiques. Les ensembles NW atteignent une efficacité quantique interne (IQE) supérieure à 60% à température ambiante. L'IQE reste stable pour des densités de puissance d'excitation élevées, jusqu'à 50 kW/cm². Nous démontrons que le super-réseau est suffisamment long pour collecter les paires électron-trou générées par un faisceau d'électrons avec une tension d'accélération $V_A = 5$ kV. Ces résultats sont intéressants pour l'application de telles nanostructures à la fabrication de lampes ultraviolettes. Cependant, compte tenu des difficultés liées à la préparation des échantillons, nous avons décidé de concentrer nos efforts de microscopie corrélative sur les QDs InGaIn/GaN Stransky-Krastanov. Dans ce cas, les échantillons de microscopie peuvent être préparés par faisceau d'ions focalisé, et ils présentent une efficacité d'émission plus élevée que les NWs AlGaIn/AlN lorsqu'ils sont injectés optiquement *in situ* dans un système de tomographie par sonde atomique (APT).

Notre étude en microscopie corrélative des boîtes quantiques (QDs) a combiné la caractérisation chimique et optique à haute résolution par APT, la micro-photoluminescence *in-situ* et la cathodoluminescence *ex-situ*. Nous démontrons que les informations extraites par ces techniques permettent la modélisation précise des nanostructures, obtenant un excellent accord avec les mesures optiques. Au cours de l'expérience APT, il a été possible de résoudre des raies d'émission des QDs uniques, qui présentent un décalage spectral attribué à la relaxation de la déformation élastique due à l'évaporation du matériau. Nous avons également étudié l'effet des défauts étendus et ponctuels sur la luminescence de telles structures QD. Nous avons observé que l'intensité d'émission est plus élevée dans les couches QD supérieures (plus proches de la surface) et qu'elle n'est pas corrélée à la densité de dislocation. Ce résultat met en évidence la pertinence d'insérer des sous-couches d'InGaIn pour enterrer les défauts ponctuels non radiatifs.

Mots clés : GaN, AlN, nanofil, ultraviolet, InGaIn, boîtes quantiques, microscopie corrélative, luminescence, tomographie par sonde atomique, cathodoluminescence et photoluminescence.